



MONASH University

Biomimetic nanomaterials as nanomedicine against amyloid diseases

Ibrahim Javed

Master of Philosophy (Pharmaceutical Chemistry)

A thesis submitted for the degree of ***Doctor of Philosophy*** at
Monash University in 2019

Drug Delivery, Disposition and Dynamics
Monash Institute of Pharmaceutical Sciences
Monash University (Parkville Campus)
381 Royal Parade, Parkville
Victoria 3052, Australia

Table of contents

Copyright notice	I
Abstract	II
Publications during enrolment	IV
Conference communications	V
Declaration of authorship	VI
Acknowledgement	IX
 Chapter 1: Introduction	 1
1 Introduction	2
1.1 Amyloid diseases	4
1.1.1 Type-2-Diabetes (T2D)	4
1.1.2 Alzheimer's disease	7
1.1.3 Parkinson's disease and other amyloid diseases	10
1.2 Amyloid proteins	12
1.2.1 Pathological amyloid proteins	12
1.2.1.1 Human islet amyloid polypeptide (IAPP)	12
1.2.1.2 Amyloid- β (A β)	14
1.2.1.3 α -Synuclein and prions	17
1.2.2 Functional amyloid proteins	18
1.2.2.1 Whey proteins: β -Lactoglobulin (bLg)	18
1.2.2.2 Whey proteins: Caseins	20
1.2.2.3 Bacterial amyloids : CsgA and FapC	22
1.3 Cross-talk between amyloid proteins	23
1.4 Nanoparticle-protein interactions	24
1.5 Nanomaterials against amyloid diseases	26
1.6 Zebrafish for amyloid research	28
1.7 References	31
 Chapter 2: Cofibrillization of pathogenic and functional amyloid proteins with gold nanoparticles against amyloidogenesis	 38
Declaration and rationale	39
Published manuscript	40
Supplementary information	47
 Chapter 3: In vivo mitigation of amyloidogenesis through functional-pathogenic double-protein coronae	 57
Declaration and rationale	58
Published manuscript	59
Supplementary information	67
 Chapter 4: Inhibition of amyloid beta toxicity in zebrafish with a chaperone-gold nanoparticle dual strategy	 79
Declaration and rationale	80
Published manuscript	81
Supplementary information	95
 Chapter 5: Summary and future directions	 111
5.1 Summary	112
5.2 Future directions	114

Copyright notice

© Ibrahim Javed (2019).

I certify that I have made all reasonable efforts to secure copyright permissions for third-party content included in this thesis and have not knowingly added copyright content to my work without the owner's permission.

Abstract

Amyloid diseases are a group of protein misfolding and aggregation disorders that influence the lifestyle and morbidity of millions of people worldwide. These diseases include type 2 diabetes (T2D), Alzheimer's disease (AD), Parkinson's disease (PD), Prions, Huntington's, arthritis, atherosclerosis and other cardiovascular or systemic amyloidosis where a protein specific to each of these disease misfolds and then self-assembles into β -sheets rich fibrils. Interestingly, the process of amyloid formation is not limited to pathogenic proteins but also functional proteins like β -lactoglobulin and caseins that render amyloid fibrils with similar atomic and mesoscopic structures as those of pathogenic amyloids. The mechanism of fibrillization and the distinct structure of a cross- β spine are ubiquitous across all pathogenic or functional amyloids, regardless of the peptide sequence, site of production and physiological function. Integrating this knowledge into consideration, the work compiled in this thesis presents innovative biomimetic approaches of synthesising nanomaterials with β -sheet rich or disordered whey protein coronas and then interfacing them with amyloid proteins to shut down the latter's fibrillization and toxicity, both *in vitro* and *in vivo*.

The content of the thesis is arranged as follows. The first chapter describes the co-fibrillization of bLg and human islet amyloid polypeptide (IAPP), facilitated via gold nanoparticles (AuNPs). The amyloid aggregation of IAPP is causative to pancreatic β -cell degeneration, which leads to the pathogenesis of T2D. Specifically, AuNPs of 8 nm in diameter were synthesised with bLg amyloid fragments that imparted a β -sheet rich corona on the surface of the AuNPs, which were subsequently embedded inside IAPP in amyloidosis. AuNPs embedded inside the IAPP amyloids enabled dark-field imaging, X-ray induced destruction and immune-recognition of IAPP amyloids by human T-cells. Next, bLg amyloid fragments were stabilized on the surface of multi-walled carbon nanotubes (MW-CNTs) and the CNTs were then encapsulated inside β -sheet rich bLg amyloid fragments. These functionalized CNTs completely inhibited the IAPP

fibrillization *in vitro* and *in vivo* in zebrafish embryos via the formation of pathogenic-functional protein coronae. This study further established zebrafish embryos as a fast and high-throughput *in-vivo* model system for screening the interactions between different nanomaterials and amyloid proteins. Finally, β -casein (β Cas) stabilised AuNPs of 5 nm in diameter were prepared to cloak the chaperone-like behavior of casein on AuNPs. β Cas AuNPs were interfaced against amyloid- β ($A\beta$) via their disordered or alpha helical moieties. $A\beta$ is a peptide whose aggregation is toxic to neuronal cells and leads to the pathogenesis of AD, a most devastating form of dementia. The chaperone-like activity of β Cas AuNPs was studied against $A\beta$ aggregation *in vitro* and *in vivo* in zebrafish larvae and adults. Zebrafish larvae provided a transparent and quick animal model to study the *in vivo* fibrillization of $A\beta$. $A\beta$ treated zebrafish developed AD-like symptoms that were rescued by β Cas AuNPs. Collectively, the findings in this thesis have provided fundamental understanding and a guidance to future research for biomimetic nanomaterials against amyloidosis. It also established zebrafish as a new lab rat for investigating amyloidosis which have so far been relying mostly on mouse models.

Publications during enrolment

1. Ibrahim Javed, Guotao Peng, Yanting Xing, Tianyu Yu, Mei Zhao, Aleksandr Kakinen, Ava Faridi, Clare L. Parish, Feng Ding, Thomas P. Davis, Pu Chun Ke, and Sijie Lin, Inhibition of amyloid beta toxicity in zebrafish with a chaperone-gold nanoparticle dual strategy. *Nat. Comm.*, 2019. 10(1): 3780.
2. Ibrahim Javed, Tianyu Yu, Guotao Peng, Antoni Sánchez-Ferrer, Ava Faridi, Aleksandr Kakinen, Mei Zhao, Raffaele Mezzenga, Thomas P Davis, Sijie Lin, and Pu Chun Ke, In Vivo Mitigation of Amyloidogenesis through Functional–Pathogenic Double-Protein Coronae. *Nano Lett.*, 2018. 18(9): 5797-5804.
3. Ibrahim Javed, Jiacheng He, Aleksandr Kakinen, Ava Faridi, Wen Yang, Thomas P Davis, Pu Chun Ke, and Pengyu Chen, Probing the aggregation and immune response of human islet amyloid polypeptides with ligand-stabilized gold nanoparticles. *ACS Appl. Mater. Interfaces*, 2019. 11(11): 10462-10471.
4. Ibrahim Javed, Yunxiang Sun, Jozef Adamcik, Bo Wang, Aleksandr Kakinen, Emily H Pilkington, Feng Ding, Raffaele Mezzenga, Thomas P Davis, and Pu Chun Ke, Cofibrillization of pathogenic and functional amyloid proteins with gold nanoparticles against amyloidogenesis. *Biomacromolecules*, 2017. 18(12): 4316-4322.
5. Pu Chun Ke, Emily H Pilkington, Yunxiang Sun, Ibrahim Javed, Aleksandr Kakinen, Guotao Peng, Feng Ding, and Thomas P Davis, Mitigation of Amyloidosis with Nanomaterials. *Adv. Mater.*, 2019: 1901690.
6. Aleksandr Kakinen, Yunxiang Sun, Ibrahim Javed, Ava Faridi, Emily H Pilkington, Pouya Faridi, Anthony W Purcell, Ruhong Zhou, Feng Ding, and Sijie Lin, Physical and toxicological profiles of human IAPP amyloids and plaques. *Sci. Bull.*, 2019. 64(1): 26-35.
7. Miaoyi Wang, Yunxiang Sun, Xueying Cao, Guotao Peng, Ibrahim Javed, Aleksandr Kakinen, Thomas P Davis, Sijie Lin, Jingquan Liu, and Feng Ding, Graphene quantum dots against human IAPP aggregation and toxicity in vivo. *Nanoscale*, 2018. 10(42): 19995-20006.
8. Miaoyi Wang, Ove JR Gustafsson, Ghizal Siddiqui, Ibrahim Javed, Hannah G Kelly, Thomas Blin, Hong Yin, Stephen J Kent, Darren J Creek, and Kristian Kempe, Human plasma proteome association and cytotoxicity of nano-graphene oxide grafted with stealth polyethylene glycol and poly (2-ethyl-2-oxazoline). *Nanoscale*, 2018. 10(23): 10863-10875.
9. Miaoyi Wang, Ove JR Gustafsson, Emily H Pilkington, Aleksandr Kakinen, Ibrahim Javed, Ava Faridi, Thomas P Davis, and Pu Chun Ke, Nanoparticle–proteome in vitro and in vivo. *J. Mater. Chem. B*, 2018. 6(38): 6026-6041.
10. Aleksandr Kakinen, Ibrahim Javed, Ava Faridi, Thomas P Davis, and Pu Chun Ke, Serum albumin impedes the amyloid aggregation and hemolysis of human islet amyloid polypeptide and alpha synuclein. *BBA Biomembrane*, 2018. 1860(9): 1803-1809.

11. Ava Faridi, Yunxiang Sun, Yutaka Okazaki, Guotao Peng, Jie Gao, Aleksandr Kakinen, Pouya Faridi, Mei Zhao, Ibrahim Javed, and Anthony W Purcell, Mitigating human IAPP amyloidogenesis in vivo with chiral silica nanoribbons. *Small*, 2018. 14(47): 1802825.
12. Miaoyi Wang, Ghizal Siddiqui, Ove JR Gustafsson, Aleksandr K  inen, Ibrahim Javed, Nicolas H Voelcker, Darren J Creek, Pu Chun Ke, and Thomas P Davis, Plasma Proteome Association and Catalytic Activity of Stealth Polymer - Grafted Iron Oxide Nanoparticles. *Small*, 2017. 13(36): 1701528.
13. Pu Chun Ke, Marc-Antonie Sani, Feng Ding, Aleksandr Kakinen, Ibrahim Javed, Frances Separovic, Thomas P Davis, and Raffaele Mezzenga, Implications of peptide assemblies in amyloid diseases. *Chem. Soc. Rev.*, 2017. 46(21): 6492-6531.

Conference communications

1. Hybridization of AuNPs with amyloids: exploiting amyloid fibrils for new science and engineering (11 Dec, 2016, ARC Centre of Excellence in Convergent Nano-Bio Science and Technology Annual Workshop 2016, Barossa Valley, Adelaide, Australia).
2. Amyloid-nanoparticle hybrids for nanomedicine against amyloidogenesis (5 July, 2017, 8th International Nanomedicine Conference, Coogee Beach, Sydney, Australia).
3. Biomimetic nanomaterials for corona-mediated nanomedicines against amyloid diseases (AsiaNano 2018, 29 Aug – 1 Sept, Qingdao, China).
4. Biomimetic nanomaterials for corona-mediated nanomedicines against amyloid diseases (27 July, 2018, 9th International Nanomedicine Conference, Coogee Beach, Sydney, Australia)
5. Biomimetic nanomaterials for corona-mediated nanomedicines against amyloid diseases (26 July, 2019, 14th Annual Graduate Research Symposium, MIPS).

Thesis including published works declaration

I hereby declare that this thesis contains no material which has been accepted for the award of any other degree or diploma at any university or equivalent institution and that, to the best of my knowledge and belief, this thesis contains no material previously published or written by another person, except where due reference is made in the text of the thesis.

This thesis includes **3** original papers published in peer reviewed journals. The core theme of the thesis is **Biomimetic nanomaterials as nanomedicines against amyloid diseases**. The ideas, development and writing up of all the papers in the thesis were the principal responsibility of myself, the student, working within the **Drug Delivery, Disposition and Dynamics, Monash Institute of Pharmaceutical Sciences** under the supervision of **Professor Thomas P. Davis** and **Dr Pu Chun Ke**.

The inclusion of co-authors reflects the fact that the work came from active collaboration between researchers and acknowledges input into team-based research.

In the case of **Chapter 2, 3** and **4** my contribution to the work involved the following:

Thesis Chapter	Publication Title	Status (published, in press, accepted or returned for revision, submitted)	Nature and % of student contribution	Co-author name(s) Nature and % of Co-author's contribution*	Co-author(s), Monash student Y/N*
2	Cofibrillization of pathogenic and functional amyloid proteins with gold nanoparticles against amyloidogenesis	Published	60%. Concept, experimental design, literature search, data collection/analysis and writeup	1) Yunxiang Sun; help in simulation 1% 2) Jozef Adamcik; help with experiment 1% 3) Bo Wang; help in simulation 1%	1)No 2)No 3)No 4)No 5)Yes 6)No 7)No

				4) Aleksandr Kakinen; help with experiment 1% 5) Emily H. Pilkington; help with experiment 1% 6) Feng Ding; help in simulation 1% 7) Raffaele Mezzenga; help in experiment 4% Thomas P. Davis; research supervision 10% 8) Pu Chun Ke; research supervision and manuscript preparation 20%	
3	In vivo mitigation of amyloidogenesis through functional–pathogenic double-protein coronae	Published	60%. Concept, experimental design, literature search, data collection/analysis and writeup	1) Tianyu Yu; help in experiment 1% 2) Guotao Peng; help in experiment 1% 3) Antoni Sánchez-Ferrer; help in experiment 2% 4) Ava Faridi; help in experiment 1% 5) Aleksandr Kakinen; manuscript proofreading 1% 6) Mei Zhao; help in experiment 1% 7) Raffaele Mezzenga; help in experiment 1% 8) Thomas P. Davis; research supervision 10% 9) Sijie Lin; help in experiment 2% 10) Pu Chun Ke; research supervision and	1)No 2)No 3)Yes 4)No 5)No 6)No 7)No 8)No

				manuscript preparation 20%	
4	Inhibition of amyloid beta toxicity in zebrafish with a chaperone-gold nanoparticle dual strategy	Accepted	60%. Concept, experimental design, literature search, data collection/analysis and writeup	1) Guotao Peng; help in experiment 1% 2) Yanting Xing; help in simulation 1% 3) Tianyu Yu; help in experiment 1% 4) Mei Zhao; help in experiment 1% 5) Aleksandr Kakinen; read the manuscript 1% 6) Ava Faridi; help in experiment 1% 7) Clare L. Parish; read the manuscript 1% 8) Feng Ding; help in simulation 1% 9) Thomas P. Davis; research supervision 10% 10) Pu Chun Ke; research supervision and manuscript preparation 21% 11) Sijie Lin; help in experiment 1%	1)No 2)No 3)No 4)No 5)No 6)Yes 7)No 8)No 9)No 10)No 11)No

I have renumbered sections of accepted or published papers in order to generate a consistent presentation within the thesis.

Student signature:

Date: 12/08/2019

The undersigned hereby certify that the above declaration correctly reflects the nature and extent of the student's and co-authors' contributions to this work. In instances where I am not the responsible author, I have consulted with the responsible author to agree on the respective contributions of the authors.

Main Supervisor signature:

Date: 12/08/2019

Acknowledgements

First, I would like to express my deepest gratitude and gratefulness to my doctoral supervisors Dr Pu Chun Ke and Professor Thomas Paul Davis. All the research, conducted and compiled in this thesis, would not be possible without their advisory support. During the tenure of my PhD, I have learned and acquired a number of skills that were not only required to complete my degree but also have tremendous value for my future career.

Next, I would like to thank our group members, Dr Aleksandr Kakinen, Dr Marvin Wang, Ava Faridi and Emily Pilkington, for your academic and social support. I also like to mention the valuable support from our collaborators, Dr Sijie Lin, Professor Raffaele Mezzenga and Dr. Feng Ding and Dr Pengyu Chen. It has been a great pleasure to work with all of you.

I would like to thank my panel members, Professor Colin Pouton, Dr Kristian Kempe and Dr Aleksandr Kakinen for your insights and constructive comments during my research work.

I would like to thank Dr Guotao Peng, Tianyu Yu, Mei Zhao, Yue Jiang, Yuan He, Xiaoxiao Wang, Dr Yunxiang Sun and Yanting Xing for your technical assistance.

Monash Institute of Pharmaceutical Sciences (MIPS), MIPS faculty scholarship, Monash International Postgraduate Research Scholarship (MIPRS), Monash Graduate Scholarship and Australian Research Training Program (RTP) are acknowledged for their financial support.

Last but not least, I would like to thank my family especially my parents, Mr and Mrs Javed for their unconditional support for me to pursue my dreams.

Chapter 1

Introduction

1. Introduction

Biomolecular self-assembly is a phenomenon that is of great pharmacological interest. In the cell, the self-assembly processes encompass the polymerisations of actins and tubulins into intermediate filaments; DNA and histones into chromatin; lipids, proteins and ion-channels into cellular membranes, and the pathological self-assembly of proteins from functional monomers to toxic oligomers, amyloid fibrils and plaques. The foundation of these processes relies on energy minimisation through either self-interactions between monomeric proteins or intermolecular interactions between monomers and ligands such as ions, chaperones, small organic molecules or biomacromolecules.² These interactions are driven kinetically and thermodynamically to achieve the stable forms of proteins that may either lead to biological functions, malfunctions, or the onset of amyloid diseases. The most widely studied amyloid diseases include type 2 diabetes (T2D), Alzheimer's (AD), Parkinson's (PD) and Huntington disease (HD). However, the term amyloid disease also encompasses a number of other protein misfolding diseases like arthritis, prion's disease, atherosclerosis, cardiovascular amyloidosis, system amyloidosis, and cerebral amyloid angiopathies. AD, PD and HD are neurodegenerative disorders and, together with T2D, influence the health state of over 400 million people worldwide. The proteins responsible for these diseases, i.e., human islet polypeptide (IAPP) for T2D, amyloid- β ($A\beta$) for AD and α -synuclein (αS) for Parkinson's, differ in their function, physiological location and sequence but share a common mechanism of β -sheet stacking to evolve into toxic oligomers and amyloid fibrils (**Fig. 1**).

When dissolved in aqueous solutions *in vitro*, amyloid proteins may take few hours (IAPP) to a few days ($A\beta$ and αS) to fibrillize into amyloid fibrils. However, under *in vivo* conditions where modulated pH, ionic strength, complex intra and extracellular environment and presence

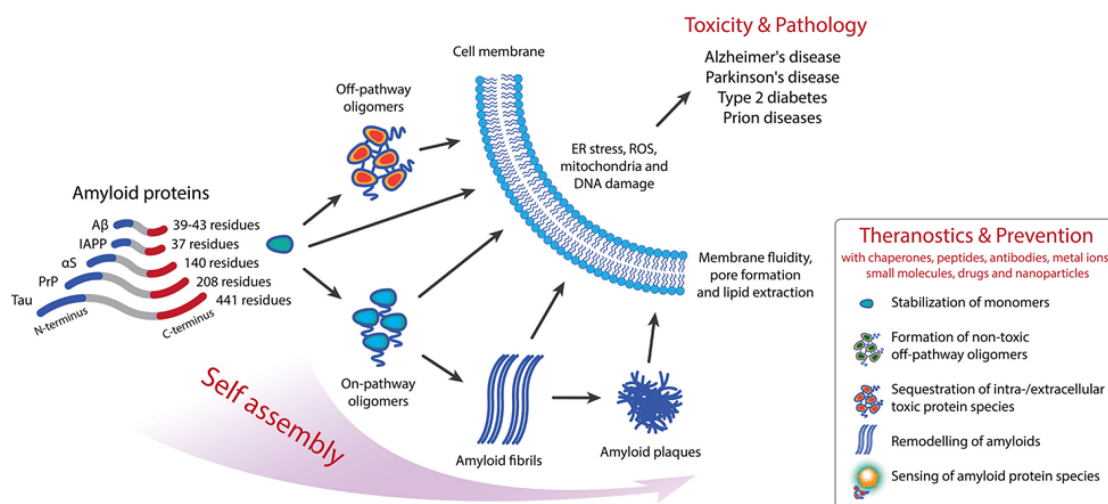


Figure 1. The pathological implications of peptide assemblies in amyloid diseases and therapeutic strategies against them. Amyloid proteins of different origins share a common mechanism of fibrillization and off-pathway oligomers induce their toxicity via membrane perturbation, endoplasmic reticulum (ER) stress, reactive oxygen species (ROS) production, among others. Reproduced from reference² with permission of the Royal Society of Chemistry.

of other biological molecules crowd or inhibit fibrillization, it may take decades for amyloid plaques to form.¹⁰

Biophysically, the protein fibrillization process is characterized by a lag phase, an elongation phase and a saturation phase. Nucleation of the monomers occurs during the lag phase. As the nucleated seeds or oligomers are considered as the most toxic species, therapeutic strategies are often designed to target the lag phase.¹¹ In the elongation phase, additional monomers are added to the seeds and protofilaments are formed. The saturation phase corresponds to the maturation, assembly and twisting of protofilaments to form mature amyloid fibrils. Apart from the primary nucleation, secondary nucleation may also occur that involves the interactions between monomers and already formed seeds, often through fragmentation.¹²

The work compiled in this thesis targets the disease models for T2D and AD. Hence this introduction will focus on T2D and AD and their associated peptides, i.e., IAPP and Aβ. Apart from pathological peptides, functional whey proteins used to construct nano-therapeutics and zebrafish as an *in vivo* model system for studying amyloidosis and nanomedicine against amyloidosis, are discussed.

1.1. Amyloid diseases

1.1.1. Type 2 Diabetes (T2D)

Diabetes is a group of metabolic disorders characterised by chronic hyperglycemia. The nutrients generated from the process of food digestion are majorly in the forms of glucose, proteins and lipids. Glucose is absorbed into the blood and later on consumed by cells for their daily energy needs. Insulin is a hormone, produced from β -cells in the islet of Langerhans in the pancreas, which facilitates the cellular uptake of glucose. Genetic deficiency of insulin or auto-immune destruction of β -cells leads to type 1 diabetes that is a medical emergency. However, a sedentary lifestyle and dietary habits can lead to either insulin resistance or reduced production of insulin from the pancreas, which results in chronic hyperglycemia and development of T2D, further associated with complications like retinopathies, arthritis, kidney failure, myocardial infarction (MI), cardiovascular complications and multiple organ failure. Current statistics suggest that there will be more than 500 million people suffering from T2D worldwide by 2028.¹³ Along with lifestyle and dietary habits, the etiology of T2D has been narrowed down to uric acid hypothesis, thrifty phenotype hypothesis and amyloid hypothesis.

Uric acid hypothesis (**Fig. 2**) explains the etiology of T2D based on total sugars intake, instead of caloric intake. Sugars like sucrose and fructose are metabolised to uric acid in the liver and released into the blood circulation. The uric acid generation is independent of caloric intake and appears to be associated with an even smaller amount of fructose intake in experimental rats.¹⁴ Fructose-induced uric acid generation further stimulates triglycerides accumulation in the liver, hepatic oxidative stress, fatty liver and mitochondrial dysfunction. Hyperuricemia is further linked to insulin resistance via several mechanisms: 1) accumulation of fats in the liver; 2) activation of NADPH oxidase in adipose tissues that generates oxidized lipids and stimulate inflammatory mediators like monocyte chemoattractant protein-1 (MCP-1); 3) direct scavenging of vascular-endothelial nitric oxide (NO) by uric acid or uric acid-generated

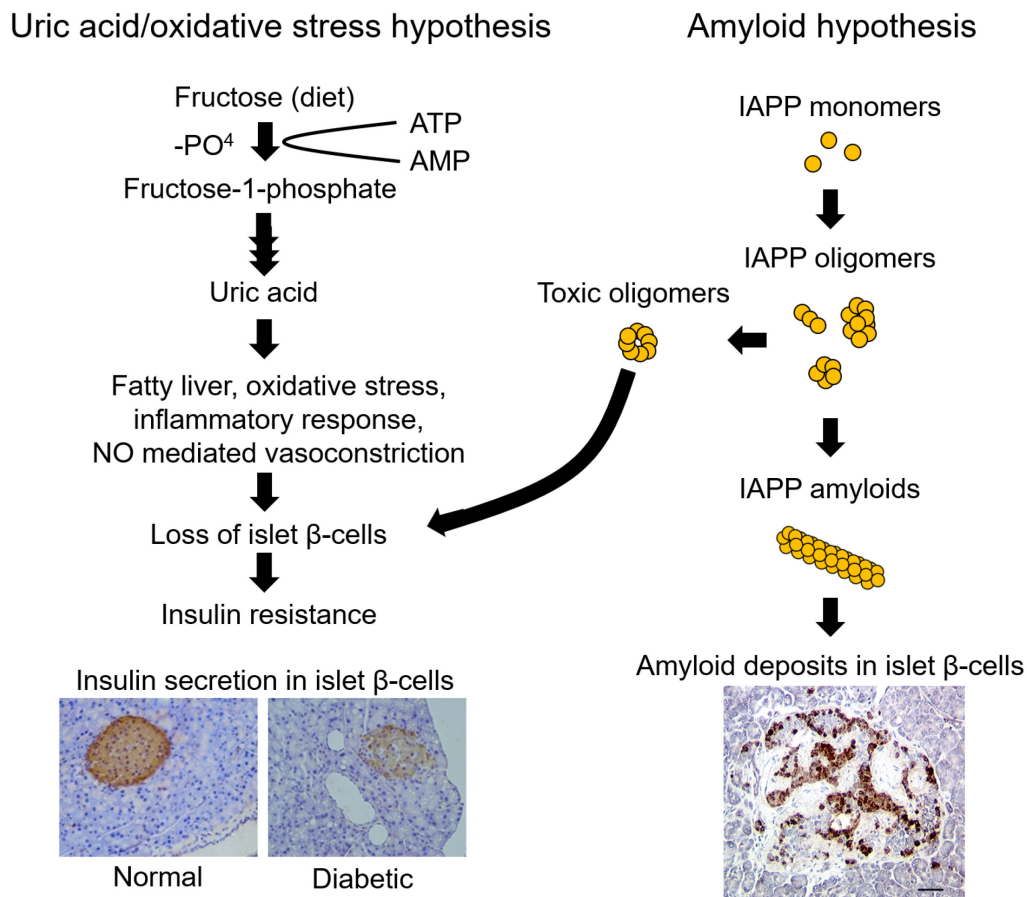


Figure 2. Schematic illustration explaining the uric acid and amyloid hypothesis for T2D. The microscopic images at the end of uric acid hypothesis represent immunostaining for insulin secretions from normal and uric acid treated diabetic rats.⁶ The microscopic images at the end of amyloid hypothesis represents IAPP amyloid deposition in islet capillaries of islet β -cells.⁸ Images reprinted with permission from *Plos* and *American Diabetes Association*.

oxidants that antagonize the insulin-generated NO; 4) uric acid induces oxidative stress in islet cells via hyalinosis, macrophage infiltration; and 5) expression of URAT-1 receptors on islet cells that facilitate uric acid uptake.¹⁵

Thrifty phenotype hypothesis is based on the fact that insulin is a growth hormone and maternal malnutrition results in poor fetal nutrition and poor development of islet cells mass. Thus fetus malnutrition leads to the development of insulin resistance. Such insulin resistance leads to T2D in adolescence.¹⁶

The amyloid hypothesis (**Fig. 2**) was proposed based on the observation of amylose like fibrillary deposits of proteins in the extracellular matrix of islet β -cells. The deposits were resolved to be proteinaceous in nature with their major component being a 37-residue peptide

that self-assembles with each other via β -sheets stacking. The peptide was named as amylin or later as human islet amyloid polypeptide (IAPP).¹⁷ There was evidence against the amyloid hypothesis based on the observation that severity of IAPP deposits was not correlated with disease conditions.¹⁸ IAPP amyloids were also observed in non-diabetic patients and were correlated with the normal aging process, while IAPP amyloids were not always observed in all diabetic patients.^{19, 20} However, extensive experimental and epidemiological evidence supports the amyloid hypothesis. Experimental mutation in rat IAPP increased the propensity of aggregation and early onset of T2D.²¹ Japanese population has a mutation in IAPP that promotes the peptide aggregation and makes the population more susceptible to diabetes.²² This conflict of amyloid hypothesis has been resolved by recent studies that revised the amyloid hypothesis and proposed that extracellular IAPP deposits are not responsible for the disease pathogenesis, but rather the toxic oligomers of IAPP that damage islet β -cells.^{23, 24}

A less established etiology is depression-induced diabetes. A few studies suggest that depression increases the chances for the onset of T2D up to 60%.²⁵ There was a bidirectional link between T2D and depression. Depression and frequent emotional disturbance lead to behavioral disorder, short episodes of hypo or hyperglycemia and abnormal brain neurochemistry that can be linked to T2D.²⁶ However, the exact mechanisms linking depression and T2D remain unclear.

High blood glucose levels are a hallmark of T2D. Chronic hyperglycemia results in the glycation of hemoglobin (Hb). Glycated hemoglobin (HbA1c) promotes the intracellular accumulation of ROS, changes membrane fluidity of red blood cells (RBCs), promotes aggregation of RBCs, increased blood viscosity, and occludes the smooth flow of blood in the microvasculature.

Current medicinal interventions against T2D include biguanides, e.g., metformin that is first-line T2D treatment. It acts by increasing the hepatic insulin sensitivity, aiding in cellular

consumption of glucose, reducing the hepatic glucose production and facilitating weight loss. Sulfonylureas, such as gliclazide and glimepiride, act by binding with specific receptors on β -cells to promote insulin secretion. Thiazolidinediones (e.g. pioglitazone) are less favoured therapeutic agents against T2D due to their adverse effects. They act by reducing insulin resistance and show a significant reduction in HbA1c levels. Insulin replacement therapy supplements the insulin levels in the body via exogenous insulin intake. Insulin is conjugated with protamine to prolong its action to a varying extent, i.e., Humulin 70/30.²⁷

1.1.2. Alzheimer's disease

Alzheimer's disease (AD) is a chronic neurodegenerative disorder characterised by the loss of neuronal mass and dementia. The characteristic histopathological hallmarks of the disease include amyloid deposits, neurofibrillary tangles, neuritic plaques and loss of neuronal cell. The causes of AD are poorly understood and usually believed to be inherited from parents through multiple genes. Other factors like history of brain injury, depression, behavioral issues and hypertension are also found to be involved in the onset of AD.²⁸ The initial symptoms are usually confused with aging or stress and the final diagnosis is made from autopsy for the presence of neuritic plaques and neurofibrillary tangles in neurocortex.

The underlying pathology for AD is the loss of synapses and neurons in the cerebral cortex and subcortical regions that leads to generalised atrophy of the brain in the temporal lobe, parietal lobe, frontal cortex and cingulate gyrus. Degenerative atrophy is also observed in the nuclei of the brain stem and locus coeruleus. Such atrophic reduction in the size of the brain is diagnosed via magnetic resonance imaging (MRI) and positron emission tomography (PET). Granulovacuolar degeneration is another histopathological characteristic of the AD brain. The pyramidal cells develop single or multiple vacuoles and each vacuole is loaded with granules. Although other cerebral lesions of AD are diffused in different structures of the brain, granulovacuolar degeneration is confined to the hippocampus.²⁹

The etiology of AD is based on the amyloid hypothesis that has been the subject of major research efforts (**Fig. 3A**). There are a few alternative AD hypotheses, i.e., the cholinergic hypothesis and the presenilin inhibition hypothesis, along with the amyloid hypothesis. All AD hypotheses are closely related to aging and the only differences are relatively increased histopathological hallmarks and worsened clinical symptoms. The presenilin hypothesis explains the development of AD on a genetic basis. Presenilin is a subunit protein of γ -secretase complex that has many other substrates along with amyloid precursor protein (APP). The genetic mutation in presenilin can reduce the flux of metabolic pathways of other substrates that leads to neuronal damage and death. However, this hypothesis lacks experimental support.³⁰

The cholinergic hypothesis is based on the fact that levels of acetylcholine (ACh), acetylcholine esterase and choline transferase are markedly reduced in the AD brain. M2 muscarinic and nicotinic receptors are down-regulated. The serotonin, γ -aminobutyric acid (GABA), somatostatin and norepinephrine levels are reduced and their respective receptors are down-regulated.³¹ The most of drugs licensed to treat the progressive symptoms of AD inhibits the breakdown of ACh by blocking acetylcholinesterase, increasing the life span of ACh. However, these inhibitors are not curative and do not prevent neuronal loss. The amyloid hypothesis explains neuronal loss and brain atrophy as a result of A β fibrillization, neurofibrillary tangles and τ -hyperphosphorylation. A typical A β plaque is 50-200 μ m in size that has an immunoreactive A β core surrounded by abnormal organelles, reactive astrocytes and microglia (**Fig. 3B**). Inflammatory activity is usually evident in and around the plaques, responsible for early neuronal death.⁹ A β is a cleavage product from APP, a transmembrane protein involved in neuronal growth and repair, exocytosis, cell adhesion, ion channels modulation and post-injury recovery.³⁰ Proteolytic cleavage of APP by γ -secretase results in the production of A β peptide that is essential for hippocampal-dependent memory function and acts as a neurotrophic factor to neurons. The imbalance between A β production and clearance results in accumulation

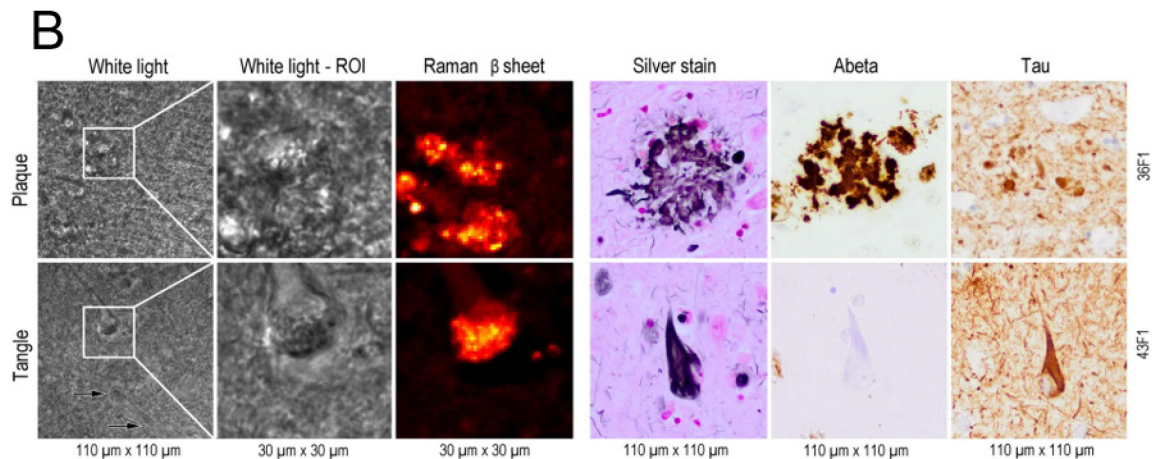
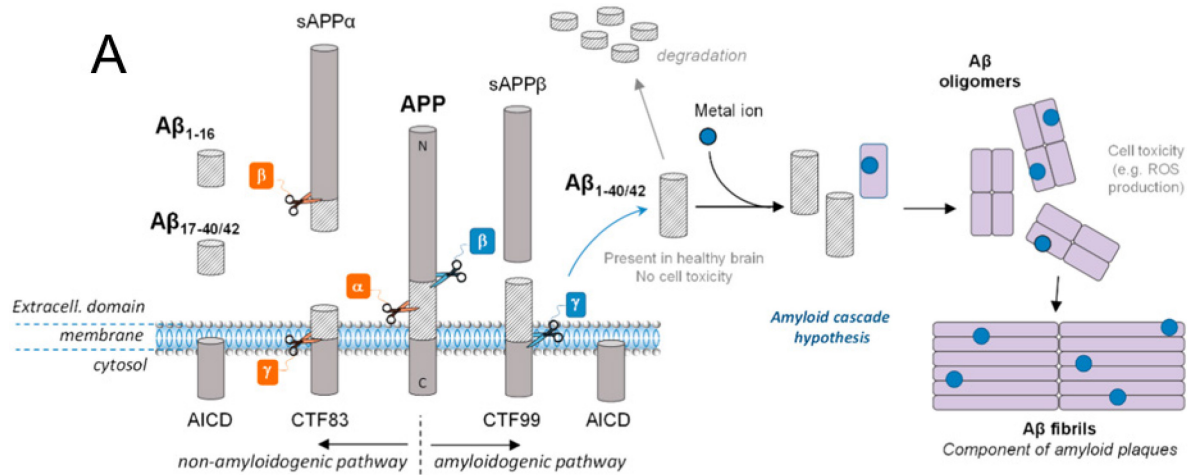


Figure 3. A) Amyloidogenic and non-amyloidogenic production of Aβ. When amyloid precursor protein (APP) is cleaved by α and then γ secretase, truncated non-amyloidogenic Aβ_{17-40/42} is produced. However, cleavage by β and then γ results in the production of amyloidogenic Aβ₄₂. Reproduced from reference⁵ with permission from Redox Biology. B presents Raman, silver-stained and immune-stained neuritic plaques (upper row) and neurofibrillary tangles (lower row) in the hippocampus of AD patients. The Aβ core is visible inside the neuritic plaques. Reproduced from reference⁹ with permission from Springer Nature.

of Aβ that further initiate misfolding and fibrillary aggregation of Aβ into amyloids. Along with extracellular Aβ deposits, there are intracellular τ-tangles in the brain of AD patients. τ undergoes phosphorylation and supports the cytoskeleton function of microtubules. In normal brain, microtubules bound and unbound fractions, as well as phosphorylated and dephosphorylated fractions of τ, are in balance. In AD, hyperphosphorylated and unbound fractions of τ are increased that are considered responsible to trigger misfolding and fibrillization of τ into tangled fibers. These tangles disrupt the normal function of intracellular transport in neurons and cause neuronal cell death.³²

In the context of anti-AD therapies, bapineuzumab was the first anti-A β antibody that targeted monomeric, oligomeric and fibrillary forms of A β .³³ In phase 2 trials, bapineuzumab showed insignificant results in amelioration of the cognitive-function decline in AD patients. Despite the failure of bapineuzumab, solanezumab was developed that targeted the soluble monomeric form of A β .³⁴ In phase 2 trial, solanezumab showed a dose-dependent increase in the plasma concentration of A β , a result that indicated clearance of A β burden from the brain. However, the antibody failed to produce significantly different results from placebo.³⁴ Gantenerumab is a human antibody that targets the amyloid form of A β . It has shown some reduction of A β plaques in double-blinded, randomized controlled trials, however, its efficacy in improving the cognitive decline is not yet studied. There are two ongoing phase-3 clinical trials for gantenerumab, evaluating its efficacy in prodromal and mild AD patients.³⁵

BACE1 and γ -secretase are the two enzymes involved in A β production by cleaving APP. BACE1 has many substrates along with APP and BACE1 knock out mice showed different CNS developmental abnormalities and functional alterations. Pioglitazone and rosiglitazone, two drugs used in T2D to control carbohydrate metabolism, were trialed to suppress BACE1 transcription.³⁶ Initial trials showed some improvement in AD patients but randomized trials in larger population showed no therapeutic efficacy. γ -secretase inhibitors also didn't show any significant difference in results and found to be associated with severe side effects like skin cancer and infections.³⁷

1.1.3. Parkinson's disease and other amyloid diseases

Parkinson's disease (PD) is a chronic neurodegenerative disorder characterised by a slow progression of motor and non-motor symptoms. The patients suffer from shaking, rigidity, behavioral issues, slow movements, difficulty in walking and thinking, resting tremors, postural instability and dementia. The risk factors are usually genetic or environmental. People exposed to pesticides, tobacco and industrial wastes or those who have a history of head injuries are

prone to early development of PD. The symptoms of the PD originate from the loss of dopaminergic neurons from midbrain and the substantia nigra regions of the brain resulting in low dopamine production in those regions. Histopathologically, proteins build up inside vacuoles, i.e., Lewy bodies, and α S amyloids deposits are observed in the surviving neurons of the PD brain.³⁸ Molecular pathophysiology of PD involves mitochondrial dysfunction, oxidative damage to lipids, proteins and DNA. Dysfunction of ubiquitin-proteasome system (UPS); a system that handles proteins, leads to proteolytic stress and toxic proteins build-ups like α S.³⁹

The etiology of PD is based on genetic mutations in α S that leads to increased propensity of α S aggregation and amyloid formation.⁴⁰ The physiological function of α S is poorly understood but it is known that the protein has the ability to bind with lipoproteins of cellular membranes which might be involved in the signal transduction for cytoskeleton and endocytosis regulation. The presence of α S in Lewy bodies indicates a direct involvement of α S in PD. Binding of α S to cell membranes induces structural changes and converts natively unfolded α S to an α -helical conformation. The α -helical form of α S has an increased propensity to aggregate and self-assemble into amyloids, and the process can be augmented by genetic factors like A30P mutation in α S. The subsequent aggregates of α S show a transition to β sheets that are detectable via thioflavin T (ThT) and Congo red histological staining. This phenomenon provides a basis for the amyloid hypothesis of PD that filamentous assembly of α S into β -sheets is sufficient and necessary for the death of dopaminergic neurons in the substantia nigra.⁴⁰ Another recent modification in this hypothesis suggests that oligomeric aggregates of α S are the toxic species and formation of filamentous aggregates is rather of a protective nature.^{40, 41}

Other amyloid diseases include Prion's disease and amyloid aggregation of proteins in the heart (immunoglobulins light chains), joints and kidneys (serum amyloid A), liver (transthyretin) and eye (keratoepithelin).⁴²⁻⁴⁴ Prion's disease is also called transmissible spongiform encephalitis

as it was initially transmitted to human from cattle and sheep. It is characterised by astrogliosis, vacuolation of the brain, neuronal apoptosis and presence of prion (PrP) amyloid as extra-neuronal aggregates. The uniqueness of Prion's disease is its infective nature and the resistance of PrP amyloid (the main infectious agent) to proteases and extreme heat.⁴⁵

1.2. Amyloid proteins

Amyloids are fibrillary aggregates of proteins made from the polymerisation of protein monomers via β -sheet stacking and hydrogen bonding. The term amyloid is derived from Amylo (starch) and oid (like) based on their resemblance to starch amylose and amylopectin that make linear and branched carbohydrate chains, respectively. Amyloid formation is common to pathological as well as functional or physiological proteins, under natural or artificial conditions.

1.2.1. Pathological amyloid proteins

1.2.1.1. Human islet amyloid polypeptide (IAPP)

IAPP is a 37-residue peptide that is synthesised, stored and secreted with insulin. The exact physiological function of IAPP is poorly understood, however, its involvement in gastric emptying, suppressing appetite and paracrine effect of shutting down insulin secretion has been implicated.⁴⁶ In T2D patients, the insulin and IAPP levels are spiked by high carbohydrate diet, thus a localised increased concentration of IAPP is considered responsible for triggering IAPP aggregation.

Structural elucidation of IAPP was difficult due to its propensity to aggregate. At low and neutral pH, IAPP exists as extended α -helical and kinked helical structures. Combination of sodium dodecyl sulfate (SDS) detergent, low concentration, pH and solution NMR helped to resolve the structure of IAPP (**Fig. 4A-C**). The N-terminus of IAPP exists as α -helices while the C-terminus exists as unstructured random-coils. The molecular structure of IAPP amyloid

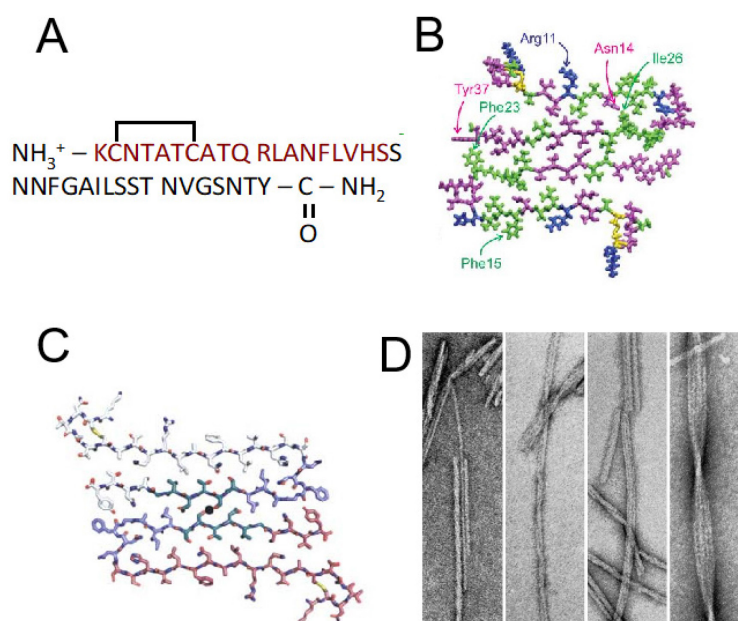


Figure 4. A) The peptide sequence of IAPP. Solid-state NMR (B) and X-ray crystallographic (C) structure of IAPP fibril. D) different morphologies of IAPP fibrils. Reproduced from reference¹⁻³ with permission from The American Chemical Society, John Wiley & Sons and Royal Society of Chemistry.

has been proposed based on different models. U-shaped fibrillar model, presented by Tycko et al., contends that the single molecule of IAPP adopts a U shape and then stacks onto the growing end of a U-shaped fibril.¹ Structural studies with disulfide-reduced IAPP led to a similar model but with a longer distance between consecutive monomers in a fibril.⁴⁷

The structure of IAPP fibrils was studied via transmission electron microscopy (TEM) and atomic force microscopy (AFM).^{48, 49} IAPP amyloids present significant polymorphism mesoscopically - ribbons, sheets, helical and twisted fibrils (**Fig. 4D**). The self-assembly of monomers leads to the formation of thin protofibrils (5 nm in diameter). The lateral association of protofibrils forms ribbons and sheets.

The toxic species of IAPP fibrillization were investigated by examining the cytotoxicity of 1) human IAPP monomers, 2) rat IAPP monomers (rat IAPP does not fibrillate and stays as monomers) and 3) human IAPP amyloids against human islet β -cells.^{24, 50, 51} From these three samples, only human IAPP monomers showed evident cytotoxicity and thus revealed that

human IAPP amyloids or rat IAPP monomers are not toxic. The human IAPP solution generated toxic oligomers during their incubation with β -cells. IAPP amyloids didn't induce toxicity, rather the cells were found decorated with IAPP amyloids. Furthermore, human IAPP monomers, together with rifampicin, were incubated with islet β -cells.⁵² Rifampicin can inhibit IAPP fibrilization but not the oligomeric aggregation of IAPP. This experiment supported the fact that toxic IAPP oligomers are not on-pathway to amyloid formation but rather off-pathway oligomers. The structure of toxic IAPP oligomers is still poorly understood. However, it is established to some extent that IAPP toxic oligomers are formed intracellularly. Gold NPs based molecular mimic of A β P toxic oligomers was synthesised and antibodies were raised against the mimic.⁵³ These anti-bodies were able to bind with the toxic oligomers of IAPP, A β , α S, prion and A β P. These results implied that 1) toxic oligomers from all these species have a similar structure, 2) mechanism of oligomer formation and disease induction can be similar across amyloid diseases, 3) the location of toxic oligomers can be traced using these antibodies, which was revealed to be intracellular based on *in vitro* and *in vivo* experiments.⁵⁴

1.2.1.2. Amyloid- β (A β)

A β peptide is produced by the cleavage of APP; a transmembrane protein whose function is poorly understood but found to be crucial for synaptic density and cognitive function.⁵⁵ A β peptide itself is found to be involved in memory function as A β knock-out mice presented impaired learning behaviour.⁵⁶ γ -secretase; an enzyme responsible for the cleavage of APP at different sites, generates a variety of functional (A β _{17-40/42}, A β ₁₋₁₆) and pathological (A β _{42/40}) isoforms of A β . The A β ₄₂ is the most amyloidogenic peptide and mostly referred to as A β . The primary sequence of an A β peptide possesses two hydrophobic regions that are predicted to adopt β -sheet structures, two turns and two hydrophilic regions that adopt an α -helical conformation.⁵⁷ The native structure of A β is difficult to elucidate due to the different structural transitions of the peptide in aqueous solution, organic solvent, different pH/buffer and detergent

solutions.⁵⁸ The mesoscopic structure of A β amyloid was studied via high field magic angle spinning NMR.⁵⁹ The structure revealed that dimer of A β molecules exists as s-shaped amyloid fold and contain 4 β -sheet strands and two hydrophobic cores.

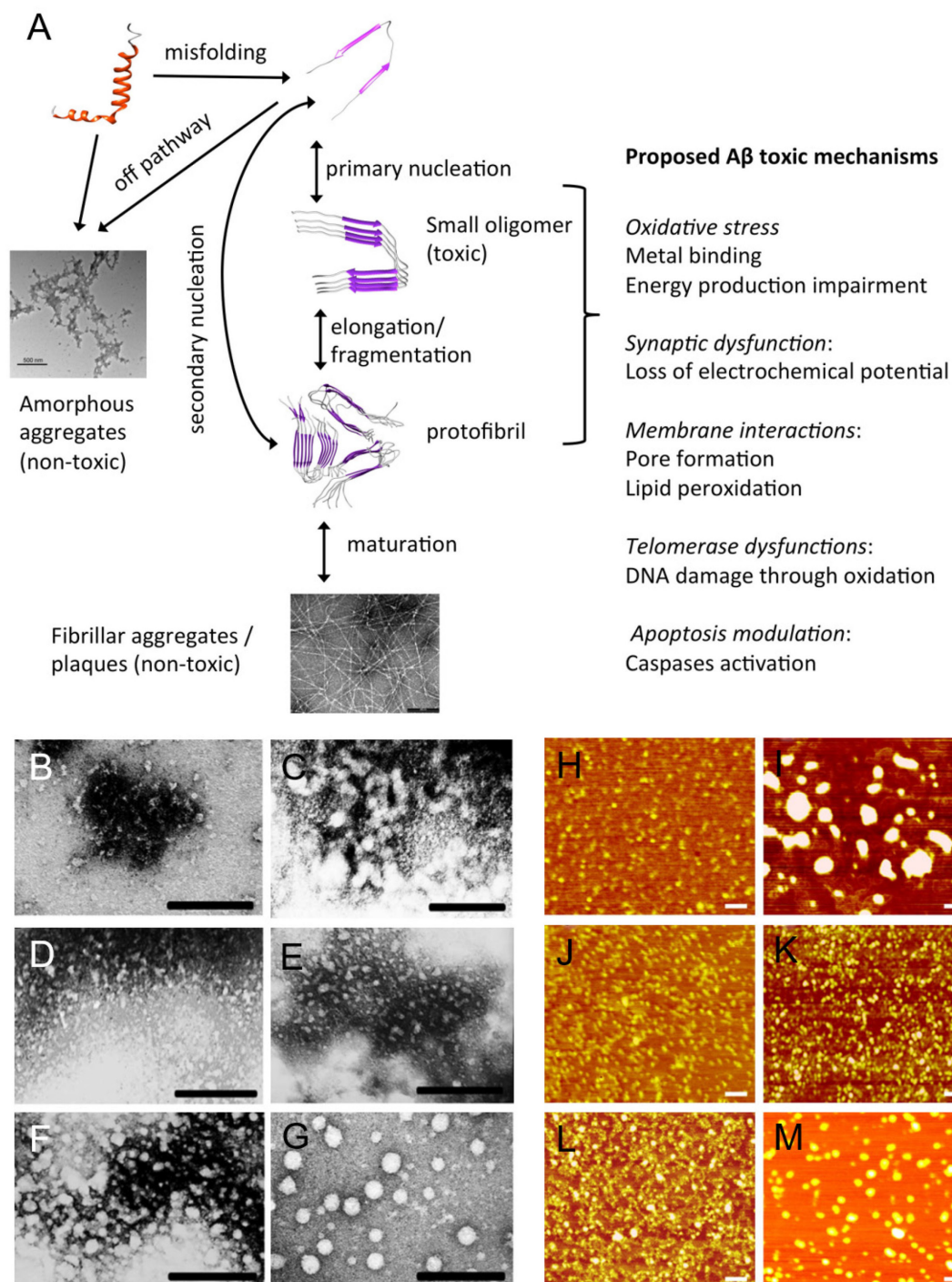


Figure 5. A β aggregation pathway (A) and toxic manifestations. TEM and AFM images of A β uncross-linked (B,H), cross-linked unfractionated (C,I), monomers (D,J), dimers (E,K), trimers (F,L) and tetramers (G,M) (scale bar: 100 nm). Reproduced from reference^{2,7} with permission from Royal Society of Chemistry and National Academy of Sciences (NAS).

The toxic species in A β fibrillization pathway is the small off-pathway oligomers (**Fig. 5A**). The structural study on A β oligomers was performed by Ono et al., who stabilised the oligomeric species by halting the fibrilization process at different stages, i.e., monomer, dimer, trimer and oligomers via photo-induced cross linking (**Fig. 5B-M**).⁷ The structural analysis revealed that intrinsic monomer of A β that dominantly possesses random coils, transitions into high-order structures in the dimer and trimer forms. The high-order structure of tetramer resembles closely the amyloid fibrils. The β -sheet contents were increased from 25% in monomers to 45% in tetramers.⁷ The oligomers presented a quasi-spherical morphology with their size increasing from 1.78 nm for dimers to 11 nm for tetramers. The neurotoxicity of trimers and tetramers was 3-fold higher than monomers in *in vitro* cell culture assays. However, different protocols used to develop the oligomers of amyloid proteins can result in different structures and toxicities. Therefore, it is difficult to present a unified structure and toxicity mechanisms for oligomers.⁶⁰

Like polymorphism in the structure of A β oligomers, different mechanisms have been proposed for the neuronal toxicity. As A β monomers have a high affinity for GM1 gangliosides and GM1-A β complex are found in the AD brain, it is therefore proposed that extracellular soluble oligomers are formed by the GM1 complex.⁶¹ Antibody, specific to on-pathway oligomers of A β , does not bind with GM1-A β complex. This implies that GM1 supports the formation of off-pathway toxic oligomers. These GM1-induced A β oligomers induced neuronal cell death by blocking nerve growth factor (NGF) receptors, activating down-stream c-Jun N-terminal kinase to induce NMDA-mediated loss of insulin receptors.⁶² A β oligomers that were produced through detergent stabilisation, i.e., incubation in SDS-PBS buffer, induced toxicity by impairing the calcium current and influencing the synaptic plasticity.⁶³ Presence of cytosolic GM1 and interaction of intracellular A β with different chaperone proteins can be responsible for intracellular oligomerization of A β .^{64, 65} Chaperone proteins like prefoldin and chaperonin are reported to promote and stabilize toxic A β oligomers in the cytoplasm.

1.2.1.3. α -Synuclein and prions

α S is a 140-residue presynaptic protein that is involved in dopaminergic neurotransmission, ER trafficking and synaptic vesicles and synaptic exocytosis.⁶⁶ In the intracellular space, α S is in equilibrium between membrane-unbound random-coil and membrane-bound alpha-helical conformation. α S is found to be the major component of Lewy body and neurites in the PD brain. The N-terminal domain of α S adopts an α -helical conformation, the central domain (NACore) is hydrophobic amyloidogenic region and the C-terminus is flexible with no structural inclination.⁶⁷ The mesoscopic architecture of α S amyloids consists of protofilaments formed via nucleated polymerisation.⁶⁸ This model describes the elongation of a protofilament by addition of partially folded monomers to the growing end of the filament via electrostatic and hydrophobic interactions. The protofilaments then assemble together in a lateral fashion to make protofibrils, each consisting of 2-3 protofilaments. Consistent with other amyloid proteins, the oligomeric form of α S is proposed to be the toxic species. Conway et al. compared the rate of disappearance of α S monomers vs. the appearance of α S amyloids.⁶⁹ The gap between the disappearance of monomers and the appearance of fibrils suggested the presence of non-fibrillary intermediates. These intermediates, when isolated and studied for morphology, revealed to be spheres (2-6 nm), chains of spheres or rings (4 nm in height). FTIR spectrophotometry revealed that α S oligomers contained antiparallel β -sheets that are contrary to the parallel β -sheet arrangement in amyloid fibrils.^{41, 64} The toxicity of α S has been explained by the interaction of α S with neuronal membranes. The N-terminus and NACore region of the peptide have the propensity to interact hydrophobically with lipid membranes, subsequently acting as a site of primary nucleation.⁷⁰ After adsorption on neuronal membranes, the α S conformation is transitioned through α -helical to β -sheet rich oligomers that favours the further adsorption of the α S peptide. This membrane supported nucleation of α S induces membrane permeability, pore formation and leakage of ions and neurotransmitters.⁷¹

Prion (PrP) is 253-residue protein, attached to the cell membrane via glycosyl phosphatidylinositol (GPI) anchor. The physiological role of PrP is unclear, however, has been found to be involved in neuroprotection against excitatory insults and starvations.⁷² The toxicity mechanism for PrP has been proposed as the primary nucleation of PrP oligomers on GPI anchored PrP. The PrP oligomeric complex, formed on the membrane, can be internalised to disrupt membrane fluidity and induce channel formation.^{73, 74}

1.2.2. Functional amyloid proteins

1.2.2.1. Whey proteins: β -Lactoglobulin (bLg)

bLg is a major component of bovine milk, constituting around 58% or 3.3 g/L of bovine whey proteins. The structure of bLg depends upon the pH. At pH 5-7, it exists as dimers that are aggregated to octamers at pH 3-5 and dissociated to monomers at pH below 3 or above 8.⁷⁵ It is an important constituent of neonatal food as a source of passive immunity and essential amino acid cysteine that is required to synthesise glutathione. The quaternary structure of bLg contains hydrophobic pockets that act as nano-carriers for retinols, fatty acids, vitamin D, cholesterol and flavor compounds.⁷⁶ The globular structure of bLg contains 7 major β -sheets which make the inner hydrophobic cores and hydrophobic nano-cavities.⁷⁷ It also contains a small proportion of α -helices that sits outside the globular structure and protects the reactive sulfhydryl group of Cys 122. Cys 122 is additional to two internal disulfide bridges. Upon heating, the sulfhydryl group is exposed to result in disulfide bridging with bLg or other whey proteins. If the β -sheet structure is digested, for example by heating, the hydrophobic segments re-anneal to gain stability. This reannealing is stabilised by hydrophobic-hydrophobic interactions with little contribution of the disulfide linkage.⁷⁷

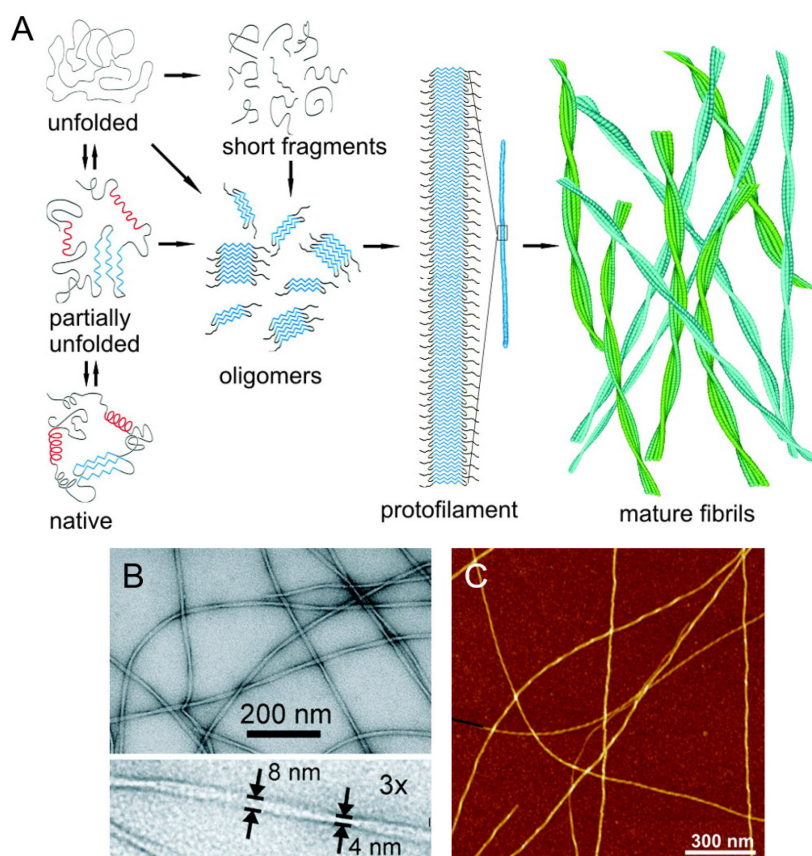


Figure 6. (A) Amyloid formation of bLg through oligomers and protofilaments. TEM (B) and AFM (C) images of bLg amyloids. Reproduced from reference⁴ with permission from American Chemical Society.

Another interesting property of bLg is amyloid formation (**Fig. 6**). When bLg solution is subjected to acid hydrolysis at high temperature, fine fibrillary amyloid structures are formed that are monoscopically similar to pathological amyloids. bLg amyloids are of great importance for materials science and also serve as a model for investigating the self-assembly of amyloid fibrils.^{78, 79} The process of amyloid formation starts from partially unfolded globular bLg. This partial unfolding is accelerated at high temperature (>90 °C). The partially unfolded globular protein undergoes fragmentation and these fragments interact via different intramolecular interactions like H-bonding, electrostatic and hydrophobic interactions, based on the sites that were not exposed in the native folded state.⁴ These interactions drive the process of oligomerisation of bLg and then through protofilaments to mature amyloids. Structural analysis of bLg amyloids has revealed a cross- β core composed of β -sheets that are stacked along the fibril axis.⁴

From the application perspective, bLg amyloid has demonstrated a great capacity in the purification of water from heavy metal ions and radioactive pollutants. bLg amyloids were adsorbed on activated carbon to make filters that removed $\text{KAu}(\text{CN})_2$, HgCl_2 , $\text{Pb}(\text{C}_2\text{H}_3\text{O}_2)_4$ and Na_2PdCl_4 with 99.98, 99.5, 99.97 and 99.84% efficiency, respectively.⁸⁰ Uranyl acetate and phosphorus-32, as radioactive wastes were removed with 99.35 and 99.88% efficiency. This high-efficiency filtration capacity of bLg amyloids is attributed to Cys-122 and metal binding pockets that are formed on and inside the amyloid structure.⁸⁰ The metal-binding capability of bLg amyloids was further exploited for crafting FeNPs-bLg amyloids hybrids.⁸¹ These hybrids, upon oral ingestion, were digested in the stomach and released bioavailable iron ions that showed a therapeutic potential in rat models of iron deficiency anemia. bLg amyloids have also found application in tissue engineering.⁸² Hybrids of hydroxyapatite and bLg amyloids provided an excellent template for bone growth and regeneration. The biocompatible properties of bLg amyloids supported human osteoblast cell adhesion. Such bLg hybrids are expected to replace the collagen-hydroxy apatite templates as biomimetic bones.⁸²

1.2.2.2. Whey proteins: Caseins

The caseins are a group of phosphorylated whey proteins (α_{S1} , α_{S2} , β and κ -caseins). They are responsible for the transport of a number of minerals including calcium and phosphate, required for bone growth in suckling infants.⁸³ In natural milk source, caseins exist as an aggregated micellar form (20-500 nm diameter) due to strong self-association and this micellar or supramolecular system is necessary for calcium delivery without calcification through the mammary glands. The intrinsic structure of casein is random coils and highly unstructured which are required for their dynamic physiology in mammary glands. Due to the lack of confined 3D conformation, caseins can adopt readily according to environmental factors like pH, temperature, concentration and presence of other ions and proteins.⁸⁴

The amyloid formation propensities of different casein isoforms are different. κ -casein micelles can be broken down to the monomers by addition of reducing agents.⁸⁵ The reduced monomers then self-assemble to amyloid fibrils at 37 °C and the process can be accelerated at a higher temperature, i.e., 60 °C. In milk, κ -casein exists in equilibrium between micellar and monomeric form. Even though the monomeric form of κ -casein constitutes only 10% of total κ -casein fraction, there has not been any observations of amyloids in milk. The reason lies in anti-amyloid properties of α and β -caseins. α and β -casein do not make fibrils at physiological or reducing conditions as for κ -casein. β -casein can make amyloid via acid hydrolysis while both α and β -caseins are strong inhibitors of amyloid formation at physiological conditions. Inhibition of κ -casein fibrillization by α and β -caseins is crucial for the stability of milk in mammary glands.^{85, 86}

Amyloid formation and inhibition activity of caseins are regarded as two-faced nature.⁸⁷ The amyloid inhibition activity of α and β -caseins are based on their chaperone-like behaviour. The chaperone-like behaviour is attributed to 1) open, flexible and dynamic conformational structure that is regarded as a molten globule, 2) the molten globular structure is further responsible for clustered and solvent-exposed hydrophobicity of casein, 3) existence as dynamic oligomeric or micellar forms and 4) their ability to bind with a wide range of partially folded and destabilised proteins. The reasons for this behavior lie in a high degree of proline residues, lack of disulfide linkage and a high degree of phosphorylation. Proline residues, i.e., 18% and 9% for β and α -casein respectively, and lack of disulfide linkages bestow them with hydrophobicity and an open/malleable conformation. Higher phosphorylation acts as a solubiliser of the casein chaperone complex after binding with target proteins, same as in heat shock (Hsp) chaperone proteins.^{87, 88}

1.2.2.3. Bacterial amyloids: CsgA and FapC

Bacterial amyloids were first discovered as extracellular organelles in uropathogenic strain of *Escherichia coli*.⁸⁹ It was later demonstrated that these curli-like fibers, originating from the surface of *E. coli*, have amyloid-like β -sheet stackings and they can bind with congo red and ThT dyes. *E. coli* use these amyloids for a number of physiological functions like interaction with host cells, biofilm formation, quorum sensing and evasion from drugs or host's immune system.⁹⁰ Later on, amyloid fibrils were discovered as a central component of biofilms in different other bacterial strains.⁹¹ Bacterial amyloids were found to provide a supporting network for the formation of a proteinaceous matrix and biofilm around the encapsulated bacterial community.

CsgA is the main component of curli amyloids in *E. coli*.⁹² CsgA amyloid formation is a tightly controlled process as compared to pathogenic amyloidosis. Therefore, a series of Csg proteins regulate the curli genesis in *E. coli*. CsgD controls the expression of CsgA, CsgG is involved in pore formation in the outer bacterial membrane and facilitates the excretion of CsgA and CsgC controls the pore formation activity of CsgG. Interestingly, all these components are not required to be produced from the same bacterial cell.⁹² X-ray fiber diffraction and solid state NMR has revealed a β -sheet stacking structure for CsgA amyloids. However, the structure of curli fibers made *in vitro* are not consistent with *in vivo* fibers as CsgC and CsgE can modulate or update the curli morphology depending upon the environmental conditions.⁹³ CsgB, the second component of curli fibers (CsgA:CsgB, 20:1) make differentially structured oligomers that serve as nucleators to control the mechanism and morphology of resulting CsgA fibrils.⁹⁴

FapC is the major amyloid component of *Pseudomonas*, expressed in *P. aeruginosa*, *P. fluorescence* and *P. putida*.⁹⁵ The molecular weight of a typical FapC protein from *P. aeruginosa* is 22.1 kDa. FTIR and CD data has revealed an amyloid-like β -sheet stacking structure of FapC with anti-parallel packing of β -sheets. However, the complete X-ray

crystallography or NMR-based structural elucidation for FapC amyloids have not yet been performed. X-ray fiber diffraction revealed the reflection at 4.7 Å.⁹⁶ Like curli amyloid, FapC fibrillization is controlled by a nucleator protein called FapB. FapB is found on the extracellular surface and in final fibrillized form of FapC, indicating that FapB is involved in triggering, accelerating and controlling the morphology of the mature FapC fibrils.⁹⁷ Additional members of the Fap family includes FapF that is involved in the transportation of FapC precursors through the membrane pores and FapA that acts as a chaperone to guide FapC through the periplasmic space.⁹⁸

1.3. Cross-talk between amyloid proteins

Protein misfolding diseases involve different proteins from different origins, synthesised to perform the different physiological functions. However, upon misfolding, they share a common aggregation mechanism (β -sheet stacking), mesoscopic structure and toxicity mechanism of membrane perturbation. The research into amyloid cross-talk started with clinical observations that diabetic patients are at higher risk of developing dementia.^{99, 100} Later on, clinical and histological studies revealed that there is an increased prevalence of IAPP and A β plaques in Alzheimer's and diabetic patients, respectively.¹⁰¹⁻¹⁰³ Such findings further fueled the histopathological studies to reveal IAPP amyloids in the frontal lobe, gray matter, perivascular spaces and mixed A β -IAPP plaques were observed in diabetic patients.¹⁰⁴ *In vitro* cross seeding studies suggested that IAPP can catalyze the oligomerisation of A β as they have similar cross- β spine.^{105, 106} Autopsy of pancreatic tissues from diabetic patients also revealed the presence of aggregated A β , both as standalone deposits and co-localised with IAPP plaques.¹⁰⁷ Further evidence for IAPP and A β cross-talk was established when Oskarsson et al. intravenously injected IAPP and A β amyloids into IAPP transgenic mice.¹⁰⁸ The results of this study revealed that both IAPP and A β amyloids were able to trigger the IAPP fibrillization in the pancreas of mice. Proximity ligation assay revealed co-localisation of A β and IAPP in pancreatic β -cells.

Similar cross-talk was also observed between α S and IAPP by Valbuena et al. who studied deposits of α S fibrils in the brain as well as in pancreatic β -cells of diabetic patients.¹⁰⁹ *In vitro* cross-reactivity assay between α S and IAPP revealed that preformed IAPP amyloids accelerated α S fibrillization and mixing IAPP and α S monomers resulted in co-aggregation of both peptides with fibrilization kinetics that was faster than individual fibrilization kinetics of α S and IAPP.¹¹⁰ α S and A β have also been found to increase the *in vivo* aggregation propensity of each other. Transgenic mice expressing both α S and A β presented severe neurodegeneration and distorted cognitive function revealing a link between α S and A β .¹¹¹ Cross-talk between prion and A β was also observed when A β transgenic mice were injected with prion and they showed early neurodegeneration and behavioral pathology.¹¹² All these studies indicate the cross-talk capabilities between different amyloid peptides can be attributed to their common fibrillization mechanism of cross- β stacking. Cross-talk between α S, driven by β -sheets stacking, is exploited to fabricate AuNPs sheets and pea-pods like strings that do not have direct biomedical implications but were used as printable electronics.^{113, 114}

The cross-talk between functional and pathological amyloids has been discovered between somatostatin and A β .¹¹⁵ Somatostatin is a growth hormone that is stored in presynaptic neurons in the form of amyloid granules. When released in the synaptic space, it was observed to interact and induce distinct oligomerisation of A β .

1.4. Nanoparticle-protein interactions

Nanoparticles (NPs) and nanomaterials offer various advantages over conventional therapeutic approaches that are not limited to therapeutic efficacy, superior dose-response relationship and drug targeting. However, there are still a few challenges like protein corona¹¹⁶ formation that are restricting the full implication of nanomedicine in clinical settings.¹¹⁷ Proteins are diverse biomacromolecules that are naturally designed to perform physiological functions. Even though the basic building blocks, i.e., amino acids, are the same for all the proteins distinct

polymerisation and self-association (disulfide linkage) of these amino acids enable the proteins to adopt a vast range of structural conformations. This further bestows the proteins with an ability to bind with metals, biomacromolecules or NPs via hydrophobic, hydrophilic, H-bonding, 3D electrostatic pockets and conformation driven interactions. Upon administration of NPs into a biological system and driven by thermodynamic fluctuations and energy minimisation, proteins immediately coat the surface of NPs to assume a protein corona, which determines the *in vivo* fate, therapeutic efficacy, targeting and clearance of the NPs.¹¹⁸⁻¹²⁰ The protein corona phenomenon also occurs in amyloidosis *in vitro* and *in vivo*, and may be exploited to inhibit amyloid aggregation and treat amyloid diseases.^{121, 122} Therefore, surface engineering and chemical modification of NPs can tune them to either avoid protein corona, preserving their intended therapeutic function, or to selectively bind with monomeric or oligomeric amyloid proteins in order to facilitate their clearance.¹²³ Factors controlling the corona formation include NPs surface, curvature, chemistry, incubation time, size of NPs and concentration, as reviewed by Wang et al.,¹¹⁷ Furthermore, *in vitro* vs. *in vivo* studies for protein corona reveal different results due to more realistic conditions for *in vivo* experiments that include blood flow dynamics, presence of cells like RBCs, WBCs and other macrophages that actively interact and opsonize the NPs. However, *in vivo* experiments for NPs-corona are challenging as the amount of NPs recovered post-administration are often too low for proteomics analysis. Furthermore, the *in vivo* dynamics of protein association with NPs is transient and complex. Upon administration, NPs are first coated with loosely bound and mostly abundant proteins, i.e., soft corona, that over time is competitively replaced with proteins that have higher affinity for the NP surface to render a hard corona.¹²⁴

Recently, the use of engineered NPs against amyloidosis has emerged as a therapeutic strategy, often exploiting the characteristics of the coronae of amyloid proteins. The interactions between the surface ligands of NPs and amyloid proteins are typically hydrophobic, electrostatic forces

as well as π -stacking. Although these interactions show promising results *in vitro*, however, there are few studies for *in vivo* inhibition of amyloidosis with nanomaterials.¹²⁵

1.5. Nanomaterials against amyloid diseases

Amyloid fibrils have good affinity for metal ions through residue coordination. Therefore, metal and metal oxide-based NPs have an intrinsic propensity for binding with amyloid proteins. The binding between NPs and amyloid proteins is controlled by competitive protein-protein vs. protein-NP interactions. If protein-NP interaction dominates then either the protein fibrillization is accelerated (as the proteins are accumulated in the vicinity of NPs) or inhibited (as proteins are sequestered by the ligand of NPs).^{126, 127} AuNPs are a typical nanomaterial whose interaction with amyloid proteins can be controlled by the nature of their surface ligands. Citrate- and polyethylene glycol (PEG)-conjugated AuNPs accelerated the fibrilization of IAPP, resulting from the conformational changes in IAPP induced by the AuNPs, from random coils to α -helices and then to β -sheets.¹²⁸ However, when the size of PEG was increased to 3,000 Da, the distance between the AuNP surface and IAPP molecules was increased, thus the acceleratory effect was diminished.¹²⁶ Similar NPs can also have different effects on different amyloid proteins. Citrate-capped AuNPs that showed acceleratory effect for IAPP slowed down insulin fibrillization and induced the formation of short and compact fibrils.¹²⁹ Similarly, changing the concentration of NPs can induce different effects on amyloid fibrillization. Lago et al., demonstrated that cationic polystyrene NPs accelerated the A β fibrillization at lower concentrations but inhibited the fibrillization at higher concentrations. This effect was explained on the basis of a balance between fibrillization of free peptides in the solution vs. surface-assisted nucleation and then fibrillization.¹³⁰ Curcumin-capped AuNPs were found to inhibit A β fibrillization.¹³¹ CdTe NPs interacted with A β via multiple binding sites to inhibit the peptide fibrillization.¹³² The hydrophobic surface of single-walled CNTs induced deposition of A β on their surface in a non-amyloid form. Oligomerisation of A β on the surface of single-

walled CNTs resulted in encapsulation of CNTs in an A β core.¹³³ *In silico* simulations revealed a β -barrel-like oligomeric assembly of A β that wrapped around the CNTs.¹³⁴ Further, for carbon-based nanomaterials, graphene quantum dots (GQDs) were explored against amyloidosis due to their small size, hydrophobic nature and strong binding with amyloid proteins. Through a combination of hydrophobic interaction, H-bonding, salt bridging and π -stacking, GQDs inhibited IAPP fibrillization *in vitro* and *in vivo* in zebrafish embryos. GQDs also converted IAPP peptides from on-pathway α -helices and β -hairpins to random coils.¹³⁵ In two separate experiments, GQDs inhibited *in vitro* A β fibrilization and crossed the blood brain barrier in zebrafish.¹³⁵ Kim et al. established the potential of GQDs in inhibiting α S fibrillization in *in vivo* mouse models, which prevented neuronal cell loss, Lewy neurite formation and mitochondrial dysfunction, the three pathogenic pathways of Parkinson's disease.¹³⁶ There are few *in vivo* studies regarding nanomaterials against amyloid disease. These include polymeric NPs ligated with KLVFF peptide that targeted A β and cleared the latter from the brain of an AD mouse model.¹³⁷ Lipoprotein-based NPs crafted from apolipoprotein E3 demonstrated a cross-talk ability with A β , and bound and cleared A β monomers from transgenic AD mice.¹³⁸ These *in vivo* studies for nanomaterial against amyloidosis had to overcome the complexity of the *in vivo* environments that could render NPs ineffective against amyloidosis. Another major challenge is the lack of suitable animal model systems to screen the therapies. Therapeutic modalities that show efficacy in mouse models have largely failed to show similar results in human clinical trials.¹³⁹ The pathologies of amyloid diseases are related to ageing and multiple pathophysiological pathways. The transgenic animal models developed so far usually offer single pathological pathways as their pharmacological target. It remains a challenge to establish an animal model with multiple pathophysiological pathways involved in the onset and progression of amyloid diseases.

1.6. Zebrafish for amyloid research

Amyloid diseases are related to the old age and *in vivo* fibrillization of amyloid fibrils. Amyloid plaques take a significantly longer period of time to appear in histological autopsies of patients. In comparison, transgenic mice models take around 1-2 years and mice that are directly injected with amyloid proteins usually take 6 months to develop the disease symptoms.^{140, 141} Zebrafish has emerged as a simplified and transparent model system that offers advantages in imaging and quick onset of disease phenotypes, properties which enable faster screening of therapeutic modalities. Furthermore, 70% of the human genome and 82% of disease-related genome have at least one orthologue gene in zebrafish.¹⁴² In terms of amyloid diseases, the protein machinery involved in the disease pathology is currently being discovered in zebrafish. For AD, zebrafish have demonstrated the presence of presenilin genes (psen1 and psen2) that are required for neuronal development, γ -secretase complexes for Notch signaling, amyloid precursor protein orthologues (APPa and APPb) for physical length and extension movement of the body, and apolipoprotein E and A β that are central protein components of the AD pathology.¹⁴³ Microinjection of human tau protein in zebrafish embryos has resulted in the development of hyperphosphorylated neurofibrillary tangles that are similar to that seen in AD patients. Two out of 6 genes that are associated with Parkinson's disease, i.e., ubiquitin carboxy-terminal hydrolase L1 (UCH-L1) and DJ-1 are expressed in adult and embryonic zebrafish.¹⁴⁴

Alongside the amyloid diseases-associated genes and proteins, zebrafish also express AD- and PD-associated neurotransmitters. Acetylcholine (ACh) is a cholinergic peripheral and central nervous system's neurotransmitter that is downregulated in AD due to loss of cholinergic neurons in basal forebrain and hippocampus. The cholinergic system has been studied via electrophysiology, histology and biochemistry in olfactory bulb, spinal cord, cerebellum and medulla oblongata of zebrafish. It is associated with learning behaviour in zebrafish.¹⁴⁵

Glutamate is an excitatory neurotransmitter that is involved in signal transduction between the neurons and plays an important role in learning and memory function. When released from the neuronal cells, it acts on metabotropic and ionotropic, e.g., N-methyl-D-aspartate (NMDA) receptors. Glutamatergic excitation of NMDA receptors activates the calcium uptake of neuronal cells. In AD, damaged neurons release an excess of glutamate that leads to overexposure of calcium to the surrounding neuronal cells. Zebrafish also revealed the presence of NMDA glutamate receptors in telencephalon; an analogue organ to human hippocampus.¹⁴⁶ NMDA receptors are associated with learning behaviour and memory function and zebrafish have demonstrated these abilities via inhibitory avoidance test with robust, long-lasting and NMDA receptors sensitive training. Glutamate transport activity has also been studied in zebrafish via sodium-dependent glutamate uptake in the zebrafish brain.¹⁴⁷

γ -aminobutyric acid (GABA) is an inhibitory neurotransmitter that maintains synaptic plasticity by countering the excitatory activity of glutamatergic neurotransmission. Tremors in PD are associated with GABAergic overexcitation. Zebrafish express GABAergic neurons in embryonic stages and in different cerebral regions of the adult, i.e., hypothalamus, olfactory bulb, telencephalon and tectum striatum.¹⁴⁸

Based on the expression of amyloid diseases related proteins, receptors and neurotransmitters, zebrafish can be a new lab rat for rapid screening of anti-amyloid therapeutic modalities. The third chapter of this thesis employs zebrafish larvae and adults as *in vivo* model systems to study A β toxicity and its mitigation with a chaperone casein-AuNP complex.

In concluding the literature review, it can be said that, despite the availability of a number of nanomaterial inhibitors against amyloid diseases, there remains a crucial need for complex, high-throughput and suitable model systems for research on amyloid diseases and anti-amyloid chemicals or nanomedicines. Zebrafish, in their different stages of life, i.e., embryos, larvae and adults, can be employed as new “lab rats” and an additional pre-clinical *in vivo* systems to

complement the AD, PD and T2D mouse models. Such zebrafish model systems have the potential to accommodate considerations of multiple pathogenic pathways in amyloidosis all at once. Furthermore, it has been understood that the protein coronae on the surfaces of nanomedicines can entail chaperone-like inhibition against amyloid fibrillization *in vivo*.

1.7. References

1. Luca, S.; Yau, W.-M.; Leapman, R.; Tycko, R., Peptide conformation and supramolecular organization in amylin fibrils: constraints from solid-state NMR. *Biochemistry* **2007**, *46* (47), 13505-13522.
2. Ke, P. C.; Sani, M.-A.; Ding, F.; Kakinen, A.; Javed, I.; Separovic, F.; Davis, T. P.; Mezzenga, R., Implications of peptide assemblies in amyloid diseases. *Chem. Soc. Rev.* **2017**, *46* (21), 6492-6531.
3. Wiltzius, J. J.; Sievers, S. A.; Sawaya, M. R.; Cascio, D.; Popov, D.; Riek, C.; Eisenberg, D., Atomic structure of the cross- β spine of islet amyloid polypeptide (amylin). *Protein Sci.* **2008**, *17* (9), 1467-1474.
4. Adamcik, J.; Mezzenga, R., Proteins fibrils from a polymer physics perspective. *Macromolecules* **2011**, *45* (3), 1137-1150.
5. Cheignon, C.; Tomas, M.; Bonnefont-Rousselot, D.; Faller, P.; Hureau, C.; Collin, F., Oxidative stress and the amyloid beta peptide in Alzheimer's disease. *Redox Biol.* **2018**, *14*, 450-464.
6. Jia, L.; Xing, J.; Ding, Y.; Shen, Y.; Shi, X.; Ren, W.; Wan, M.; Guo, J.; Zheng, S.; Liu, Y., Hyperuricemia causes pancreatic β -cell death and dysfunction through NF- κ B signaling pathway. *PLoS One* **2013**, *8* (10), e78284.
7. Ono, K.; Condon, M. M.; Teplow, D. B., Structure–neurotoxicity relationships of amyloid β -protein oligomers. *Proc. Natl. Acad. Sci. U.S.A.* **2009**, *106* (35), 14745-14750.
8. Bonner-Weir, S.; O'Brien, T. D., Islets in type 2 diabetes: in honor of Dr. Robert C. Turner. *Diabetes* **2008**, *57* (11), 2899-2904.
9. Michael, R.; Lenferink, A.; Vrensen, G. F.; Gelpi, E.; Barraquer, R. I.; Otto, C., Hyperspectral Raman imaging of neuritic plaques and neurofibrillary tangles in brain tissue from Alzheimer's disease patients. *Sci. Rep.* **2017**, *7* (1), 15603.
10. Hartl, F. U.; Hayer-Hartl, M., Converging concepts of protein folding in vitro and in vivo. *Nat. Struct. Mol. Biol.* **2009**, *16* (6), 574.
11. Lee, C.-C.; Nayak, A.; Sethuraman, A.; Belfort, G.; McRae, G. J., A three-stage kinetic model of amyloid fibrillation. *Biophys. J.* **2007**, *92* (10), 3448-3458.
12. Linse, S., Monomer-dependent secondary nucleation in amyloid formation. *Biophys. Rev.* **2017**, *9* (4), 329-338.
13. KAISER, A. B.; ZHANG, N.; DER PLUIJM, W. V., Global prevalence of type 2 diabetes over the next ten years (2018-2028). *Diabetes* **2018**, *67* (Supplement 1), 202-LB.
14. Nakagawa, T.; Hu, H.; Zharikov, S.; Tuttle, K. R.; Short, R. A.; Glushakova, O.; Ouyang, X.; Feig, D. I.; Block, E. R.; Herrera-Acosta, J., A causal role for uric acid in fructose-induced metabolic syndrome. *Am. J. Physiol. Renal Physiol.* **2006**, *290* (3), F625-F631.
15. Johnson, R. J.; Nakagawa, T.; Sanchez-Lozada, L. G.; Shafiu, M.; Sundaram, S.; Le, M.; Ishimoto, T.; Sautin, Y. Y.; Lanaspa, M. A., Sugar, uric acid, and the etiology of diabetes and obesity. *Diabetes* **2013**, *62* (10), 3307-3315.
16. Hales, C. N.; Barker, D. J., The thrifty phenotype hypothesis: Type 2 diabetes. *British Medical Bulletin* **2001**, *60* (1), 5-20.
17. Westermark, P.; Wernstedt, C.; O'Brien, T.; Hayden, D.; Johnson, K., Islet amyloid in type 2 human diabetes mellitus and adult diabetic cats contains a novel putative polypeptide hormone. *Am. J. Pathol.* **1987**, *127* (3), 414.
18. Clark, A.; Nilsson, M., Islet amyloid: a complication of islet dysfunction or an aetiological factor in Type 2 diabetes? *Diabetologia* **2004**, *47* (2), 157-169.
19. Westermark, P., The nature of amyloid in islets of Langerhans in old age. *Amyloidosis. Academic Press, London-New York-San Francisco* **1976**, 533-541.
20. Westermark, P., Fine structure of islets of Langerhans in insular amyloidosis. *Virchows Archiv A* **1973**, *359* (1), 1-18.
21. Matveyenko, A. V.; Butler, P. C., Islet amyloid polypeptide (IAPP) transgenic rodents as models for type 2 diabetes. *ILAR J.* **2006**, *47* (3), 225-233.
22. Seino, S.; Mellitus, S. G. o. C. A. o. G. F. i. D., S20G mutation of the amylin gene is associated with Type II diabetes in Japanese. *Diabetologia* **2001**, *44* (7), 906-909.

23. Mirzabekov, T. A.; Lin, M.-c.; Kagan, B. L., Pore formation by the cytotoxic islet amyloid peptide amylin. *J. Biol. Chem.* **1996**, *271* (4), 1988-1992.
24. Janson, J.; Ashley, R. H.; Harrison, D.; McIntyre, S.; Butler, P. C., The mechanism of islet amyloid polypeptide toxicity is membrane disruption by intermediate-sized toxic amyloid particles. *Diabetes* **1999**, *48* (3), 491-498.
25. Mezuk, B.; Eaton, W. W.; Albrecht, S.; Golden, S. H., Depression and type 2 diabetes over the lifespan: a meta-analysis. *Diabetes care* **2008**, *31* (12), 2383-2390.
26. Renn, B. N.; Feliciano, L.; Segal, D. L., The bidirectional relationship of depression and diabetes: a systematic review. *Clin. Psychol. Rev.* **2011**, *31* (8), 1239-1246.
27. Nourparvar, A.; Bulotta, A.; Di Mario, U.; Perfetti, R., Novel strategies for the pharmacological management of type 2 diabetes. *Trends Pharmacol. Sci.* **2004**, *25* (2), 86-91.
28. Burns, A.; Iliffe, S., Alzheimer's disease. *BMJ* **2009**, *338*, b158.
29. Köhler, C., Granulovacuolar degeneration: a neurodegenerative change that accompanies tau pathology. *Acta Neuropathologica* **2016**, *132* (3), 339-359.
30. Hardy, J., The amyloid hypothesis for Alzheimer's disease: a critical reappraisal. *J. Neurochem.* **2009**, *110* (4), 1129-1134.
31. Kandimalla, R.; Reddy, P. H., Therapeutics of neurotransmitters in Alzheimer's disease. *J. Alzheimers Dis.* **2017**, *57* (4), 1049-1069.
32. Ballatore, C.; Lee, V. M.-Y.; Trojanowski, J. Q., Tau-mediated neurodegeneration in Alzheimer's disease and related disorders. *Nat. Rev. Neurosci.* **2007**, *8* (9), 663.
33. Salloway, S.; Sperling, R.; Fox, N. C.; Blennow, K.; Klunk, W.; Raskind, M.; Sabbagh, M.; Honig, L. S.; Porsteinsson, A. P.; Ferris, S., Two phase 3 trials of bapineuzumab in mild-to-moderate Alzheimer's disease. *N. Engl. J. Med.* **2014**, *370* (4), 322-333.
34. Farlow, M.; Arnold, S. E.; Van Dyck, C. H.; Aisen, P. S.; Snider, B. J.; Porsteinsson, A. P.; Friedrich, S.; Dean, R. A.; Gonzales, C.; Sethuraman, G., Safety and biomarker effects of solanezumab in patients with Alzheimer's disease. *Alzheimer's Dement.* **2012**, *8* (4), 261-271.
35. Ostrowitzki, S.; Deptula, D.; Thurfjell, L.; Barkhof, F.; Bohrmann, B.; Brooks, D. J.; Klunk, W. E.; Ashford, E.; Yoo, K.; Xu, Z.-X., Mechanism of amyloid removal in patients with Alzheimer disease treated with gantenerumab. *Arch. Neurol.* **2012**, *69* (2), 198-207.
36. Miller, B. W.; Willett, K. C.; Desilets, A. R., Rosiglitazone and pioglitazone for the treatment of Alzheimer's disease. *Ann. Pharmacother.* **2011**, *45* (11), 1416-1424.
37. Ricciarelli, R.; Fedele, E., The amyloid cascade hypothesis in Alzheimer's disease: it's time to change our mind. *Curr. Neuropharmacol.* **2017**, *15* (6), 926-935.
38. Moore, D. J.; West, A. B.; Dawson, V. L.; Dawson, T. M., Molecular pathophysiology of Parkinson's disease. *Annu. Rev. Neurosci.* **2005**, *28*, 57-87.
39. Chung, K. K.; Dawson, V. L.; Dawson, T. M., The role of the ubiquitin-proteasomal pathway in Parkinson's disease and other neurodegenerative disorders. *Trends Neurosci.* **2001**, *24*, 7-14.
40. Goedert, M., Alpha-synuclein and neurodegenerative diseases. *Nat. Rev. Neurosci.* **2001**, *2*, 492.
41. Lashuel, H. A.; Hartley, D.; Petre, B. M.; Walz, T.; Lansbury Jr, P. T., Neurodegenerative disease: amyloid pores from pathogenic mutations. *Nature* **2002**, *418* (6895), 291.
42. Benson, M. D.; Uemichi, T., Transthyretin amyloidosis. *Amyloid* **1996**, *3* (1), 44-56.
43. Merlini, G.; Seldin, D. C.; Gertz, M. A., Amyloidosis: pathogenesis and new therapeutic options. *J. Clin. Oncol.* **2011**, *29* (14), 1924.
44. Kyle, R.; Bayrd, E., Amyloidosis: review of 236 cases. *Medicine* **1975**, *54* (4), 271-299.
45. Prusiner, S. B., Prions. *Proc. Natl. Acad. Sci. U.S.A.* **1998**, *95* (23), 13363-13383.
46. Lutz, T. A., Amylinergic control of food intake. *Physiol. Behav.* **2006**, *89* (4), 465-471.
47. Bedrood, S.; Li, Y.; Isas, J. M.; Hegde, B. G.; Baxa, U.; Haworth, I. S.; Langen, R., Fibril structure of human islet amyloid polypeptide. *J. Biol. Chem.* **2012**, *287* (8), 5235-5241.
48. Goldsbury, C.; Kistler, J.; Aebi, U.; Arvinte, T.; Cooper, G. J. S., Watching amyloid fibrils grow by time-lapse atomic force microscopy. *Journal of Molecular Biology* **1999**, *285* (1), 33-39.
49. Goldsbury, C. S.; Cooper, G. J. S.; Goldie, K. N.; Müller, S. A.; Saafi, E. L.; Gruijters, W. T. M.; Misur, M. P.; Engel, A.; Aebi, U.; Kistler, J., Polymorphic Fibrillar Assembly of Human Amylin. *Journal of Structural Biology* **1997**, *119* (1), 17-27.
50. Lorenzo, A.; Razzaboni, B.; Weir, G. C.; Yankner, B. A., Pancreatic islet cell toxicity of amylin associated with type-2 diabetes mellitus. *Nature* **1994**, *368* (6473), 756.

51. Konarkowska, B.; Aitken, J. F.; Kistler, J.; Zhang, S.; Cooper, G. J., The aggregation potential of human amylin determines its cytotoxicity towards islet β -cells. *FEBS J.* **2006**, *273* (15), 3614-3624.
52. Meier, J. J.; Kaye, R.; Lin, C.-Y.; Gurlo, T.; Haataja, L.; Jayasinghe, S.; Langen, R.; Glabe, C. G.; Butler, P. C., Inhibition of human IAPP fibril formation does not prevent β -cell death: evidence for distinct actions of oligomers and fibrils of human IAPP. *Am. J. Physiol. Endocrinol. Metab.* **2006**, *291* (6), E1317-E1324.
53. Kaye, R.; Head, E.; Thompson, J. L.; McIntire, T. M.; Milton, S. C.; Cotman, C. W.; Glabe, C. G., Common structure of soluble amyloid oligomers implies common mechanism of pathogenesis. *Science* **2003**, *300* (5618), 486-489.
54. Lin, C.-Y.; Gurlo, T.; Kaye, R.; Butler, A. E.; Haataja, L.; Glabe, C. G.; Butler, P. C., Toxic human islet amyloid polypeptide (h-IAPP) oligomers are intracellular, and vaccination to induce anti-toxic oligomer antibodies does not prevent h-IAPP-induced β -cell apoptosis in h-IAPP transgenic mice. *Diabetes* **2007**, *56* (5), 1324-1332.
55. Zheng, H.; Jiang, M.; Trumbauer, M. E.; Sirinathsinghji, D. J.; Hopkins, R.; Smith, D. W.; Heavens, R. P.; Dawson, G. R.; Boyce, S.; Conner, M. W.; Stevens, K. A.; Slunt, H. H.; Sisodia, S. S.; Chen, H. Y.; Van der Ploeg, L. H., beta-Amyloid precursor protein-deficient mice show reactive gliosis and decreased locomotor activity. *Cell* **1995**, *81* (4), 525-31.
56. Morley, J. E.; Farr, S. A.; Banks, W. A.; Johnson, S. N.; Yamada, K. A.; Xu, L., A physiological role for amyloid-beta protein: enhancement of learning and memory. *Journal of Alzheimer's disease : JAD* **2010**, *19* (2), 441-9.
57. Soto, C.; Brañes, M. C.; Alvarez, J.; Inestrosa, N. C., Structural determinants of the Alzheimer's amyloid β -peptide. *J. Neurochem.* **1994**, *63* (4), 1191-1198.
58. Vivekanandan, S.; Brender, J. R.; Lee, S. Y.; Ramamoorthy, A., A partially folded structure of amyloid-beta(1-40) in an aqueous environment. *Biochem. Biophys. Res. Commun.* **2011**, *411* (2), 312-6.
59. Colvin, M. T.; Silvers, R.; Ni, Q. Z.; Can, T. V.; Sergeyev, I.; Rosay, M.; Donovan, K. J.; Michael, B.; Wall, J.; Linse, S.; Griffin, R. G., Atomic Resolution Structure of Monomorphic A β 42 Amyloid Fibrils. *J. Am. Chem. Soc.* **2016**, *138* (30), 9663-74.
60. Dahlgren, K. N.; Manelli, A. M.; Stine, W. B.; Baker, L. K.; Krafft, G. A.; LaDu, M. J., Oligomeric and fibrillar species of amyloid- β peptides differentially affect neuronal viability. *J. Biol. Chem.* **2002**, *277* (35), 32046-32053.
61. Yamamoto, N.; Matsubara, E.; Maeda, S.; Minagawa, H.; Takashima, A.; Maruyama, W.; Michikawa, M.; Yanagisawa, K., A ganglioside-induced toxic soluble A β assembly its enhanced formation from A β bearing the arctic mutation. *J. Biol. Chem.* **2007**, *282* (4), 2646-2655.
62. Coulson, E. J., Does the p75 neurotrophin receptor mediate A β -induced toxicity in Alzheimer's disease? *J. Neurochem.* **2006**, *98* (3), 654-660.
63. Nimmrich, V.; Grimm, C.; Draguhn, A.; Barghorn, S.; Lehmann, A.; Schoemaker, H.; Hillen, H.; Gross, G.; Ebert, U.; Bruehl, C., Amyloid β oligomers (A β 1-42 globulomer) suppress spontaneous synaptic activity by inhibition of P/Q-type calcium currents. *J. Neurosci.* **2008**, *28* (4), 788-797.
64. Sakono, M.; Zako, T.; Ueda, H.; Yohda, M.; Maeda, M., Formation of highly toxic soluble amyloid beta oligomers by the molecular chaperone prefoldin. *FEBS J.* **2008**, *275* (23), 5982-5993.
65. Yuyama, K.; Yamamoto, N.; Yanagisawa, K., Accelerated release of exosome-associated GM1 ganglioside (GM1) by endocytic pathway abnormality: another putative pathway for GM1-induced amyloid fibril formation. *J. Neurochem.* **2008**, *105* (1), 217-224.
66. Burré, J.; Sharma, M.; Südhof, T. C., α -Synuclein assembles into higher-order multimers upon membrane binding to promote SNARE complex formation. *Proc. Natl. Acad. Sci. USA* **2014**, *111* (40), E4274-E4283.
67. Villar-Piqué, A.; Lopes da Fonseca, T.; Outeiro, T. F., Structure, function and toxicity of alpha-synuclein: the Bermuda triangle in synucleinopathies. *J. Neurochem.* **2016**, *139*, 240-255.
68. Ionescu-Zanetti, C.; Khurana, R.; Gillespie, J. R.; Petrick, J. S.; Trabachino, L. C.; Minert, L. J.; Carter, S. A.; Fink, A. L., Monitoring the assembly of Ig light-chain amyloid fibrils by atomic force microscopy. *Proc. Natl. Acad. Sci. USA* **1999**, *96* (23), 13175-13179.

69. Conway, K. A.; Lee, S.-J.; Rochet, J.-C.; Ding, T. T.; Williamson, R. E.; Lansbury, P. T., Acceleration of oligomerization, not fibrillization, is a shared property of both α -synuclein mutations linked to early-onset Parkinson's disease: Implications for pathogenesis and therapy. *Proc. Natl. Acad. Sci. USA* **2000**, *97* (2), 571-576.
70. Aisenbrey, C.; Borowik, T.; Byström, R.; Bokvist, M.; Lindström, F.; Misiak, H.; Sani, M.-A.; Gröbner, G., How is protein aggregation in amyloidogenic diseases modulated by biological membranes? *Eur. Biophys. J.* **2008**, *37* (3), 247-255.
71. Roberts, H.; Brown, D., Seeking a Mechanism for the Toxicity of Oligomeric α -Synuclein. *Biomolecules* **2015**, *5* (2), 282-305.
72. Llorens, F.; del Río, J. A., Unraveling the neuroprotective mechanisms of PrP(C) in excitotoxicity. *Prion* **2012**, *6* (3), 245-251.
73. Kristiansen, M.; Deriziotis, P.; Dimcheff, D. E.; Jackson, G. S.; Ovaa, H.; Naumann, H.; Clarke, A. R.; van Leeuwen, F. W.; Menéndez-Benito, V.; Dantuma, N. P., Disease-associated prion protein oligomers inhibit the 26S proteasome. *Mol. Cell* **2007**, *26* (2), 175-188.
74. Westergard, L.; Christensen, H. M.; Harris, D. A., The cellular prion protein (PrP C): its physiological function and role in disease. *BBA Mol. Basis. Dis.* **2007**, *1772* (6), 629-644.
75. Kontopidis, G.; Holt, C.; Sawyer, L., Invited review: β -lactoglobulin: binding properties, structure, and function. *J. Dairy Sci.* **2004**, *87* (4), 785-796.
76. Narayan, M.; Berliner, L. J., Fatty acids and retinoids bind independently and simultaneously to β -lactoglobulin. *Biochemistry* **1997**, *36* (7), 1906-1911.
77. Boland, M., 3 - Whey proteins. In *Handbook of Food Proteins*, Phillips, G. O.; Williams, P. A., Eds. Woodhead Publishing: 2011; pp 30-55.
78. Hamley, I. W., Peptide fibrillization. *Angew. Chem. Int. Ed.* **2007**, *46* (43), 8128-8147.
79. Jones, O. G.; Mezzenga, R., Inhibiting, promoting, and preserving stability of functional protein fibrils. *Soft Matter* **2012**, *8* (4), 876-895.
80. Bolisetty, S.; Mezzenga, R., Amyloid-carbon hybrid membranes for universal water purification. *Nature Nanotech.* **2016**, *11* (4), 365.
81. Shen, Y.; Posavec, L.; Bolisetty, S.; Hilty, F. M.; Nyström, G.; Kohlbrecher, J.; Hilbe, M.; Rossi, A.; Baumgartner, J.; Zimmermann, M. B., Amyloid fibril systems reduce, stabilize and deliver bioavailable nanosized iron. *Nature Nanotech.* **2017**, *12* (7), 642.
82. Li, C.; Born, A. K.; Schweizer, T.; Zenobi-Wong, M.; Cerruti, M.; Mezzenga, R., Amyloid-hydroxyapatite bone biomimetic composites. *Adv. Mater.* **2014**, *26* (20), 3207-3212.
83. Horne, D. S., Casein structure, self-assembly and gelation. *Curr. Opin. Colloid Interface Sci.* **2002**, *7* (5-6), 456-461.
84. McMahon, D. J.; Oommen, B. S., Casein micelle structure, functions, and interactions. In *Advanced Dairy Chemistry*, Springer: 2013; pp 185-209.
85. Thorn, D. C.; Meehan, S.; Sunde, M.; Rekas, A.; Gras, S. L.; MacPhee, C. E.; Dobson, C. M.; Wilson, M. R.; Carver, J. A., Amyloid fibril formation by bovine milk κ -casein and its inhibition by the molecular chaperones α S- and β -casein. *Biochemistry* **2005**, *44* (51), 17027-17036.
86. Thorn, D. C.; Ecroyd, H.; Sunde, M.; Poon, S.; Carver, J. A., Amyloid fibril formation by bovine milk α S2-casein occurs under physiological conditions yet is prevented by its natural counterpart, α S1-casein. *Biochemistry* **2008**, *47* (12), 3926-3936.
87. Thorn, D. C.; Ecroyd, H.; Carver, J. A., The two-faced nature of milk casein proteins: amyloid fibril formation and chaperone-like activity. *Aust. J. Dairy Technol.* **2009**, *64* (1), 34.
88. Guha, S.; Manna, T. K.; Das, K. P.; Bhattacharyya, B., Chaperone-like activity of tubulin. *J. Biol. Chem.* **1998**, *273* (46), 30077-30080.
89. Olsén, A.; Jonsson, A.; Normark, S., Fibronectin binding mediated by a novel class of surface organelles on Escherichia coli. *Nature* **1989**, *338* (6217), 652.
90. Chapman, M. R.; Robinson, L. S.; Pinkner, J. S.; Roth, R.; Heuser, J.; Hammar, M.; Normark, S.; Hultgren, S. J., Role of Escherichia coli curli operons in directing amyloid fiber formation. *Science* **2002**, *295* (5556), 851-855.
91. Larsen, P.; Nielsen, J. L.; Dueholm, M. S.; Wetzel, R.; Otzen, D.; Nielsen, P. H., Amyloid adhesins are abundant in natural biofilms. *Environ. Microbiol.* **2007**, *9* (12), 3077-3090.
92. Naiki, H.; Gejyo, F., Kinetic analysis of amyloid fibril formation. In *Methods Enzymol.*, Elsevier: 1999; Vol. 309, pp 305-318.

93. Shewmaker, F.; McGlinchey, R. P.; Thurber, K. R.; McPhie, P.; Dyda, F.; Tycko, R.; Wickner, R. B., The functional curli amyloid is not based on in-register parallel β -sheet structure. *J. Biol. Chem.* **2009**, *284* (37), 25065-25076.
94. Shu, Q.; Crick, S. L.; Pinkner, J. S.; Ford, B.; Hultgren, S. J.; Frieden, C., The E. coli CsgB nucleator of curli assembles to β -sheet oligomers that alter the CsgA fibrillization mechanism. *Proc. Natl. Acad. Sci. U.S.A.* **2012**, *109* (17), 6502-6507.
95. Dueholm, M. S.; Søndergaard, M. T.; Nilsson, M.; Christiansen, G.; Stensballe, A.; Overgaard, M. T.; Givskov, M.; Tolker-Nielsen, T.; Otzen, D. E.; Nielsen, P. H., Expression of Fap amyloids in *Pseudomonas aeruginosa*, *P. fluorescens*, and *P. putida* results in aggregation and increased biofilm formation. *Microbiologyopen* **2013**, *2* (3), 365-382.
96. Dueholm, M. S.; Petersen, S. V.; Sønderkær, M.; Larsen, P.; Christiansen, G.; Hein, K. L.; Enghild, J. J.; Nielsen, J. L.; Nielsen, K. L.; Nielsen, P. H., Functional amyloid in *Pseudomonas*. *Mol. Microbiol.* **2010**, *77* (4), 1009-1020.
97. Dueholm, M. S.; Otzen, D.; Nielsen, P. H., Evolutionary insight into the functional amyloids of the pseudomonads. *PLoS One* **2013**, *8* (10), e76630.
98. Rouse, S. L.; Hawthorne, W. J.; Berry, J.-L.; Chorev, D. S.; Ionescu, S. A.; Lambert, S.; Stylianou, F.; Ewert, W.; Mackie, U.; Morgan, R. M. L., A new class of hybrid secretion system is employed in *Pseudomonas* amyloid biogenesis. *Nature Com.* **2017**, *8* (1), 263.
99. U'Ren, R. C.; Riddle, M. C.; Lezak, M. D.; Bennington-Davis, M., The mental efficiency of the elderly person with type II diabetes mellitus. *J. Am. Geriatr. Soc.* **1990**, *38* (5), 505-510.
100. Ott, A.; Stolk, R.; Hofman, A.; van Harskamp, F.; Grobbee, D.; Breteler, M., Association of diabetes mellitus and dementia: the Rotterdam Study. *Diabetologia* **1996**, *39* (11), 1392-1397.
101. Luchsinger, J. A.; Tang, M.-X.; Stern, Y.; Shea, S.; Mayeux, R., Diabetes mellitus and risk of Alzheimer's disease and dementia with stroke in a multiethnic cohort. *Am. J. Epidemiol.* **2001**, *154* (7), 635-641.
102. Arvanitakis, Z.; Wilson, R. S.; Bienias, J. L.; Evans, D. A.; Bennett, D. A., Diabetes mellitus and risk of Alzheimer disease and decline in cognitive function. *Arch. Neurol.* **2004**, *61* (5), 661-666.
103. Janson, J.; Laedtke, T.; Parisi, J. E.; O'Brien, P.; Petersen, R. C.; Butler, P. C., Increased risk of type 2 diabetes in Alzheimer disease. *Diabetes* **2004**, *53* (2), 474-481.
104. Jackson, K.; Barisone, G. A.; Diaz, E.; Jin, L. w.; DeCarli, C.; Despa, F., Amylin deposition in the brain: a second amyloid in Alzheimer disease? *Ann. Neurol.* **2013**, *74* (4), 517-526.
105. Krotee, P.; Griner, S. L.; Sawaya, M. R.; Cascio, D.; Rodriguez, J. A.; Shi, D.; Philipp, S.; Murray, K.; Saelices, L.; Lee, J., Common fibrillar spines of amyloid- β and human islet amyloid polypeptide revealed by microelectron diffraction and structure-based inhibitors. *J. Biol. Chem.* **2018**, *293* (8), 2888-2902.
106. N Fawver, J.; Ghiwot, Y.; Koola, C.; Carrera, W.; Rodriguez-Rivera, J.; Hernandez, C.; T Dineley, K.; Kong, Y.; Li, J.; Jhamandas, J., Islet amyloid polypeptide (IAPP): a second amyloid in Alzheimer's disease. *Curr. Alzheimer Res.* **2014**, *11* (10), 928-940.
107. Miklossy, J.; Qing, H.; Radenovic, A.; Kis, A.; Vilen, B.; László, F.; Miller, L.; Martins, R. N.; Waeber, G.; Mooser, V., Beta amyloid and hyperphosphorylated tau deposits in the pancreas in type 2 diabetes. *Neurobiol. Aging* **2010**, *31* (9), 1503-1515.
108. Oskarsson, M. E.; Paulsson, J. F.; Schultz, S. W.; Ingelsson, M.; Westermark, P.; Westermark, G. T., In vivo seeding and cross-seeding of localized amyloidosis: a molecular link between type 2 diabetes and Alzheimer disease. *Am. J. Pathol.* **2015**, *185* (3), 834-846.
109. Martinez-Valbuena, I.; Amat-Villegas, I.; Valenti-Azcarate, R.; del Mar Carmona-Abellan, M.; Marcilla, I.; Tuñón, M.-T.; Luquin, M.-R., Interaction of amyloidogenic proteins in pancreatic β cells from subjects with synucleinopathies. *Acta Neuropathologica* **2018**, *135* (6), 877-886.
110. Horvath, I.; Wittung-Stafshede, P., Cross-talk between amyloidogenic proteins in type-2 diabetes and Parkinson's disease. *Proc. Natl. Acad. Sci. U.S.A.* **2016**, *113* (44), 12473-12477.
111. Masliah, E.; Rockenstein, E.; Veinbergs, I.; Sagara, Y.; Mallory, M.; Hashimoto, M.; Mucke, L., β -Amyloid peptides enhance α -synuclein accumulation and neuronal deficits in a transgenic mouse model linking Alzheimer's disease and Parkinson's disease. *Proc. Natl. Acad. Sci. U.S.A.* **2001**, *98* (21), 12245-12250.

112. Morales, R.; Estrada, L. D.; Diaz-Espinoza, R.; Morales-Scheihing, D.; Jara, M. C.; Castilla, J.; Soto, C., Molecular cross talk between misfolded proteins in animal models of Alzheimer's and prion diseases. *J. Neurosci.* **2010**, *30* (13), 4528-4535.
113. Lee, J.; Bhak, G.; Lee, J. H.; Park, W.; Lee, M.; Lee, D.; Jeon, N. L.; Jeong, D. H.; Char, K.; Paik, S. R., Free-standing gold-nanoparticle monolayer film fabricated by protein self-assembly of α -Synuclein. *Angew. Chem. Int. Ed.* **2015**, *54* (15), 4571-4576.
114. Lee, D.; Choe, Y. J.; Choi, Y. S.; Bhak, G.; Lee, J.; Paik, S. R., Photoconductivity of pea-pod-type chains of gold nanoparticles encapsulated within dielectric amyloid protein nanofibrils of α -Synuclein. *Angew. Chem. Int. Ed.* **2011**, *50* (6), 1332-1337.
115. Wang, H.; Muiznieks, L. D.; Ghosh, P.; Williams, D.; Solarski, M.; Fang, A.; Ruiz-Riquelme, A.; Pomes, R.; Watts, J. C.; Chakrabartty, A., Somatostatin binds to the human amyloid β peptide and favors the formation of distinct oligomers. *Elife* **2017**, *6*, e28401.
116. Cedervall, T.; Lynch, I.; Lindman, S.; Berggård, T.; Thulin, E.; Nilsson, H.; Dawson, K. A.; Linse, S., Understanding the nanoparticle-protein corona using methods to quantify exchange rates and affinities of proteins for nanoparticles. *Proc. Natl. Acad. Sci. U.S.A.* **2007**, *104* (7), 2050-2055.
117. Wang, M.; Gustafsson, O. J.; Pilkington, E. H.; Kakinen, A.; Javed, I.; Faridi, A.; Davis, T. P.; Ke, P. C., Nanoparticle-proteome in vitro and in vivo. *J. Mater. Chem. B* **2018**, *6* (38), 6026-6041.
118. Ke, P. C.; Lin, S.; Parak, W. J.; Davis, T. P.; Caruso, F., A decade of the protein corona. *ACS Nano* **2017**, *11* (12), 11773-11776.
119. Lundqvist, M.; Stigler, J.; Cedervall, T.; Berggård, T.; Flanagan, M. B.; Lynch, I.; Elia, G.; Dawson, K., The evolution of the protein corona around nanoparticles: a test study. *ACS Nano* **2011**, *5* (9), 7503-7509.
120. Lundqvist, M.; Stigler, J.; Elia, G.; Lynch, I.; Cedervall, T.; Dawson, K. A., Nanoparticle size and surface properties determine the protein corona with possible implications for biological impacts. *Proc. Natl. Acad. Sci. U.S.A.* **2008**, *105* (38), 14265-14270.
121. Javed, I.; Yu, T.; Peng, G.; Sánchez-Ferrer, A.; Faridi, A.; Kakinen, A.; Zhao, M.; Mezzenga, R.; Davis, T. P.; Lin, S., In vivo mitigation of amyloidogenesis through functional-pathogenic double-protein coronae. *Nano Lett.* **2018**, *18* (9), 5797-5804.
122. Pilkington, E. H.; Gustafsson, O. J.; Xing, Y.; Hernandez-Fernaund, J.; Zampronio, C.; Kakinen, A.; Faridi, A.; Ding, F.; Wilson, P.; Ke, P. C., Profiling the serum protein corona of fibrillar human islet amyloid polypeptide. *ACS Nano* **2018**, *12* (6), 6066-6078.
123. Casals, E.; Pfaller, T.; Duschl, A.; Oostingh, G. J.; Puentes, V., Time evolution of the nanoparticle protein corona. *ACS Nano* **2010**, *4* (7), 3623-3632.
124. Hadjidemetriou, M.; Kostarelos, K., Nanomedicine: evolution of the nanoparticle corona. *Nature Nanotech.* **2017**, *12* (4), 288.
125. Ke, P. C.; Pilkington, E. H.; Sun, Y.; Javed, I.; Kakinen, A.; Peng, G.; Ding, F.; Davis, T. P., Mitigation of Amyloidosis with Nanomaterials. *Adv. Mater.* **2019**, 1901690.
126. Javed, I.; He, J.; Kakinen, A.; Faridi, A.; Yang, W.; Davis, T. P.; Ke, P. C.; Chen, P., Probing the aggregation and immune response of human islet amyloid polypeptides with ligand-stabilized gold nanoparticles. *ACS Appl. Mater. Interfaces* **2019**, *11* (11), 10462-10471.
127. Gladysz, A.; Abel, B.; Risselada, H. J., Gold-induced fibril growth: the mechanism of surface-facilitated amyloid aggregation. *Angew. Chem. Int. Ed.* **2016**, *55* (37), 11242-11246.
128. Wang, S.-T.; Lin, Y.; Todorova, N.; Xu, Y.; Mazo, M.; Rana, S.; Leonardo, V.; Amdursky, N.; Spicer, C. D.; Alexander, B. D., Facet-dependent interactions of islet amyloid polypeptide with gold nanoparticles: Implications for fibril formation and peptide-induced lipid membrane disruption. *Chem. Mater.* **2017**, *29* (4), 1550-1560.
129. Hsieh, S.; Chang, C.-w.; Chou, H.-h., Gold nanoparticles as amyloid-like fibrillogenesis inhibitors. *Colloids Surf. B* **2013**, *112*, 525-529.
130. Cabaleiro-Lago, C.; Quinlan-Pluck, F.; Lynch, I.; Dawson, K. A.; Linse, S., Dual effect of amino modified polystyrene nanoparticles on amyloid β protein fibrillation. *ACS Chem. Neurosci.* **2010**, *1* (4), 279-287.
131. Palmal, S.; Maity, A. R.; Singh, B. K.; Basu, S.; Jana, N. R.; Jana, N. R., Inhibition of amyloid fibril growth and dissolution of amyloid fibrils by curcumin-gold nanoparticles. *Chem.: Eur. J.* **2014**, *20* (20), 6184-6191.

132. Yoo, S. I.; Yang, M.; Brender, J. R.; Subramanian, V.; Sun, K.; Joo, N. E.; Jeong, S. H.; Ramamoorthy, A.; Kotov, N. A., Inhibition of amyloid peptide fibrillation by inorganic nanoparticles: functional similarities with proteins. *Angew. Chem. Int. Ed.* **2011**, *50* (22), 5110-5115.
133. Luo, J.; Wärmländer, S. K.; Yu, C.-H.; Muhammad, K.; Gräslund, A.; Abrahams, J. P., The A β peptide forms non-amyloid fibrils in the presence of carbon nanotubes. *Nanoscale* **2014**, *6* (12), 6720-6726.
134. Fu, Z.; Luo, Y.; Derreumaux, P.; Wei, G., Induced β -barrel formation of the Alzheimer's A β 25–35 oligomers on carbon nanotube surfaces: Implication for amyloid fibril inhibition. *Biophys. J.* **2009**, *97* (6), 1795-1803.
135. Wang, M.; Sun, Y.; Cao, X.; Peng, G.; Javed, I.; Kakinen, A.; Davis, T. P.; Lin, S.; Liu, J.; Ding, F., Graphene quantum dots against human IAPP aggregation and toxicity in vivo. *Nanoscale* **2018**, *10* (42), 19995-20006.
136. Kim, D.; Yoo, J. M.; Hwang, H.; Lee, J.; Lee, S. H.; Yun, S. P.; Park, M. J.; Lee, M.; Choi, S.; Kwon, S. H., Graphene quantum dots prevent α -synucleinopathy in Parkinson's disease. *Nature Nanotech.* **2018**, *13* (9), 812.
137. Luo, Q.; Lin, Y.-X.; Yang, P.-P.; Wang, Y.; Qi, G.-B.; Qiao, Z.-Y.; Li, B.-N.; Zhang, K.; Zhang, J.-P.; Wang, L., A self-destructive nanosweeper that captures and clears amyloid β -peptides. *Nature Com.* **2018**, *9* (1), 1802.
138. Song, Q.; Huang, M.; Yao, L.; Wang, X.; Gu, X.; Chen, J.; Chen, J.; Huang, J.; Hu, Q.; Kang, T., Lipoprotein-based nanoparticles rescue the memory loss of mice with Alzheimer's disease by accelerating the clearance of amyloid-beta. *ACS Nano* **2014**, *8* (3), 2345-2359.
139. Reardon, S., Frustrated Alzheimer's researchers seek better lab mice. *Nature* **2018**, *563*, 611-612.
140. Nakamura, S.; Murayama, N.; Noshita, T.; Annoura, H.; Ohno, T., Progressive brain dysfunction following intracerebroventricular infusion of beta1–42-amyloid peptide. *Brain Res.* **2001**, *912* (2), 128-136.
141. Oakley, H.; Cole, S. L.; Logan, S.; Maus, E.; Shao, P.; Craft, J.; Guillozet-Bongaarts, A.; Ohno, M.; Disterhoft, J.; Van Eldik, L., Intraneuronal β -amyloid aggregates, neurodegeneration, and neuron loss in transgenic mice with five familial Alzheimer's disease mutations: potential factors in amyloid plaque formation. *J. Neurosci.* **2006**, *26* (40), 10129-10140.
142. Howe, K.; Clark, M. D.; Torroja, C. F.; Torrance, J.; Berthelot, C.; Muffato, M.; Collins, J. E.; Humphray, S.; McLaren, K.; Matthews, L., The zebrafish reference genome sequence and its relationship to the human genome. *Nature* **2013**, *496* (7446), 498.
143. Newman, M.; Ebrahimie, E.; Lardelli, M., Using the zebrafish model for Alzheimer's disease research. *Front. Genet.* **2014**, *5*, 189.
144. Best, J.; Alderton, W. K., Zebrafish: an in vivo model for the study of neurological diseases. *Neuropsych. Dis Treat.* **2008**, *4* (3), 567.
145. Park, E.; Lee, Y.; Kim, Y.; Lee, C.-J., Cholinergic modulation of neural activity in the telencephalon of the zebrafish. *Neurosci. Lett.* **2008**, *439* (1), 79-83.
146. Nam, R.-H.; Kim, W.; Lee, C.-J., NMDA receptor-dependent long-term potentiation in the telencephalon of the zebrafish. *Neurosci. Lett.* **2004**, *370* (2-3), 248-251.
147. Rico, E. P.; de Oliveira, D. L.; Rosemberg, D. B.; Mussulini, B. H.; Bonan, C. D.; Dias, R. D.; Wofchuk, S.; Souza, D. O.; Bogo, M. R., Expression and functional analysis of Na⁺-dependent glutamate transporters from zebrafish brain. *Brain Res. Bull.* **2010**, *81* (4-5), 517-523.
148. Kim, Y.-J.; Nam, R.-H.; Yoo, Y. M.; Lee, C.-J., Identification and functional evidence of GABAergic neurons in parts of the brain of adult zebrafish (*Danio rerio*). *Neurosci. Lett.* **2004**, *355* (1-2), 29-32.

Chapter 2

Cofibrillization of pathogenic and functional amyloid proteins with gold nanoparticles against amyloidogenesis

Declaration

This chapter was published as Ibrahim Javed, Yunxiang Sun, Jozef Adamcik, Bo Wang, Aleksandr Kakinen, Emily H Pilkington, Feng Ding, Raffaele Mezzenga, Thomas P Davis, and Pu Chun Ke, Cofibrillization of pathogenic and functional amyloid proteins with gold nanoparticles against amyloidogenesis. *Biomacromolecules*, 2017. 18(12): 4316-4322.

Rationale

The rationale for the design of this project is based on cross-interaction and co-fibrillization of bLg and IAPP amyloids, facilitated by AuNPs. IAPP amyloids are formed naturally, under physiological conditions. In contrast, bLg forms functional amyloids under acidic conditions and at high temperature. Despite fibrillization under different conditions, there are striking similarities between the mesoscopic structure and β -sheet organization of these two types of amyloid fibrils. Therefore, it was hypothesized in this chapter, that cross-seeding between bLg amyloid-fragments and IAPP should be feasible, and should lead to a co-structure further involving AuNPs, the substrate of bLg amyloid fragments. The interaction between AuNPs and IAPP amyloids was exploited for *in vitro* toxicity mitigation, X-ray induced destruction, immunorecognition and dark-field imaging of IAPP amyloids.

Cofibrillization of Pathogenic and Functional Amyloid Proteins with Gold Nanoparticles against Amyloidogenesis

Ibrahim Javed,[†] Yunxiang Sun,^{‡,⊥} Jozef Adamcik,^{§,⊥} Bo Wang,[‡] Aleksandr Kakinen,[†] Emily H. Pilkington,[†] Feng Ding,^{*,‡,⊥} Raffaele Mezzenga,^{§,⊥} Thomas P. Davis,^{*,‡,⊥} and Pu Chun Ke^{*,†,⊥}

[†]ARC Centre of Excellence in Convergent Bio-Nano Science and Technology, Monash Institute of Pharmaceutical Sciences, Monash University, 381 Royal Parade, Parkville, Victoria 3052, Australia

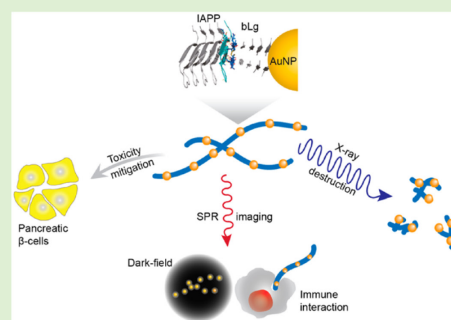
[‡]Department of Physics and Astronomy, Clemson University, Clemson, South Carolina 29634, United States

[§]Food & Soft Materials, Department of Health Science & Technology, ETH Zurich, Schmelzbergstrasse 9, LFO, E23, 8092, Zurich, Switzerland

[⊥]Department of Chemistry, University of Warwick, Gibbet Hill, Coventry, CV4 7AL, United Kingdom

Supporting Information

ABSTRACT: Biomimetic nanocomposites and scaffolds hold the key to a wide range of biomedical applications. Here we show, for the first time, a facile scheme of cofibrillizing pathogenic and functional amyloid fibrils via gold nanoparticles (AuNPs) and their applications against amyloidogenesis. This scheme was realized by β -sheet stacking between human islet amyloid polypeptide (IAPP) and the β -lactoglobulin “corona” of the AuNPs, as revealed by transmission electron microscopy, 3D atomic force microscopy, circular dichroism spectroscopy, and molecular dynamics simulations. The biomimetic AuNPs eliminated IAPP toxicity, enabled X-ray destruction of IAPP amyloids, and allowed dark-field imaging of pathogenic amyloids and their immunogenic response by human T cells. In addition to providing a viable new nanotechnology against amyloidogenesis, this study has implications for understanding the *in vivo* cross-talk between amyloid proteins of different pathologies.



INTRODUCTION

The aggregation of proteins and peptides into cross-beta fibrils is a ubiquitous phenomenon associated with neurodegenerative disorders and type 2 diabetes, the amyloid diseases debilitating more than 5% of the global population.^{1,2} Although much progress has been made in the past decades toward understanding the molecular and mesoscopic structures of protein fibrils as well as their fibrillization kinetics and toxicity, there is a crucial lack of strategies for probing the aggregation of amyloid proteins *in situ*, despite their relevance to elucidating the pathologies of amyloid diseases and to the development of effective therapeutics.^{1,3}

Nanoparticles (NPs) of metals, semiconductors, and oxides possess distinct optical, electrical, magnetic and catalytic properties. The small size of NPs also enables their cellular translocation, biocirculation, and drug delivery. Accordingly, designing biomimetic nanocomposites and scaffolds holds great promise for bioremediation, diagnosis, and disease intervention. Recently, Moore et al. examined the effects of gold NPs (AuNPs) on Alzheimer's disease amyloid- β protein aggregation, and found that both the NP size and surface chemistry modulated the extent of protein aggregation, while the NP charge influenced the aggregate morphology.⁴ Gladysz et al. succeeded in interfacing AuNPs and amyloid proteins,⁵

revealing that the amyloid aggregation of human islet amyloid polypeptide (IAPP) and prion protein SUP35 hinged on a balance between peptide-NP and peptide-peptide interactions. Hamley et al. demonstrated labeling of (Ala)10-(His)6 amyloid fibrils with AuNPs.⁶ Collectively, these studies demonstrated the feasibility of exploiting NP-protein interactions against amyloidogenesis, an emerging field at the frontiers of materials, medicine, physical sciences, and bioengineering.

IAPP is a 37-residue peptide involved in glycemic control, but its aggregation into amyloids and plaques is a hallmark of type 2 diabetes, a metabolic disease and a global epidemic. By contrast, β -lactoglobulin (bLg) is a natural whey protein that hydrolyzes into small peptide fragments upon heating and acid exposure (pH 2), and subsequently self-assembles into functional bLg amyloid fibrils.^{7,8} Efficient *in vitro* iron delivery and wastewater purification have been recently demonstrated using bLg amyloids,^{9,10} pointing to the untapped potential of this biomaterial.

To develop biomimetic NPs against amyloidogenesis, we synthesized AuNPs using sonicated bLg amyloids as a β -sheet

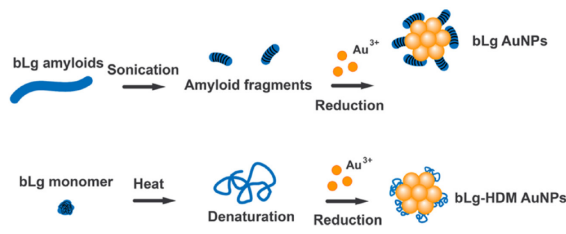
Received: September 19, 2017

Revised: October 31, 2017

Published: November 2, 2017

rich template (bLg AuNPs, ~ 8 nm in diameter; Scheme 1 and Figure 1), which were then cofibrillized with pathogenic IAPP.

Scheme 1. Synthesis of AuNPs Stabilized by Sonicated bLg Amyloids (bLg AuNPs) and Heat-Denatured bLg Monomers (bLg-HDM AuNPs)



In addition, we synthesized AuNPs stabilized by heat-denatured bLg monomers (bLg-HDM AuNPs, ~ 6 nm in diameter; Scheme 1 and Figure 1), which had a low β -sheet content. The use of AuNPs in this study was motivated by their biocompatibility as well as their potential for drug delivery, biosensing, and photothermal therapy.^{11,12} Following the synthesis, we examined the AuNPs within the context of IAPP fibrillization, toxicity, dark-field imaging, and destruction by localized heating of the AuNPs using X-rays. Collectively, our results implicated bLg-AuNPs as a new nanomedicine against amyloidogenesis.

EXPERIMENTAL METHODS

Synthesis of Gold Nanoparticles (AuNPs). bLg amyloids were formed according to our reported method.¹³ Probe sonicated bLg amyloids (5 mL, 1 mg/mL) were introduced into the refluxing solution (10 mL) of HAuCl₄ (0.5 mM), and 200 μ L of NaBH₄ (0.2 M) was added into the mixture 30 min later. Heating was stopped after

ruby red-colored AuNPs were synthesized and kept on overnight stirring. bLg-HDM AuNPs were synthesized following the same method as with the bLg amyloid fragments. The bLg-capped AuNPs were purified via centrifugal filtration. The concentrations of the AuNPs were derived according to the literature.¹⁴

Synthesis of AuNP-IAPP Hybrids. Human islet amyloid polypeptide (IAPP; 37 residues, 2–7 disulfide bridge, 3.9 kDa, > 95% pure by HPLC) was obtained in lyophilized monomeric form from AnaSpec, and prepared in Milli-Q water at a stock concentration of 200 μ M at room temperature with mixing immediately prior to use. AuNPs were cofibrillated with IAPP by incubating different concentrations of the NPs with 25 μ M of the peptide under ambient conditions for 24 h. bLg AuNPs (0.083 mM) were also incubated with 25 μ M Amyloid β (1–42) obtained from AnaSpec, for 72 h in Milli-Q water before TEM visualization.

Transmission Electron Microscopy and Energy-Dispersive X-ray Spectroscopy. Transmission electron microscopy (TEM) and EDX spectral mapping were performed on an FEI Tecnai F20 transmission electron microscope, operated at 200 kV with the samples adsorbed on a glow discharged (15 s) 400 mesh Formvar-coated copper grid. Samples (25 μ M of IAPP, 0.083 mM or 0.11 mM of AuNPs) were then stained with 1% uranyl acetate for visualization.

Dynamic Light Scattering. Zeta potential and hydrodynamic size were acquired for the two types of AuNPs in aqueous solution (0.1 mM) at room temperature (Malvern Zetasizer). The stability of the AuNPs was evaluated by incubating the AuNPs (0.5 mM) with different concentrations of NaCl at 37 °C for 4 h and then analyzed for aggregation (Table S2).

Circular Dichroism Spectroscopy. Circular dichroism (CD) spectra of the two types of AuNPs (0.25 mM) were obtained for the wavelength range of 190–240 nm with a 0.5 nm step size at room temperature. The data was converted from mean residue ellipticity (θ) to deg-cm²-dmol⁻¹ and the protein secondary structure was estimated by DichroWeb, using Contin as reference program and reference set4.¹⁵ In addition, the CD spectra of bLg AuNPs associated IAPP amyloids before and after X-ray irradiation were acquired.

Thioflavin T Assay. IAPP fibrillization in the presence of the two types of AuNPs was analyzed by a thioflavin T (ThT) assay. The assay

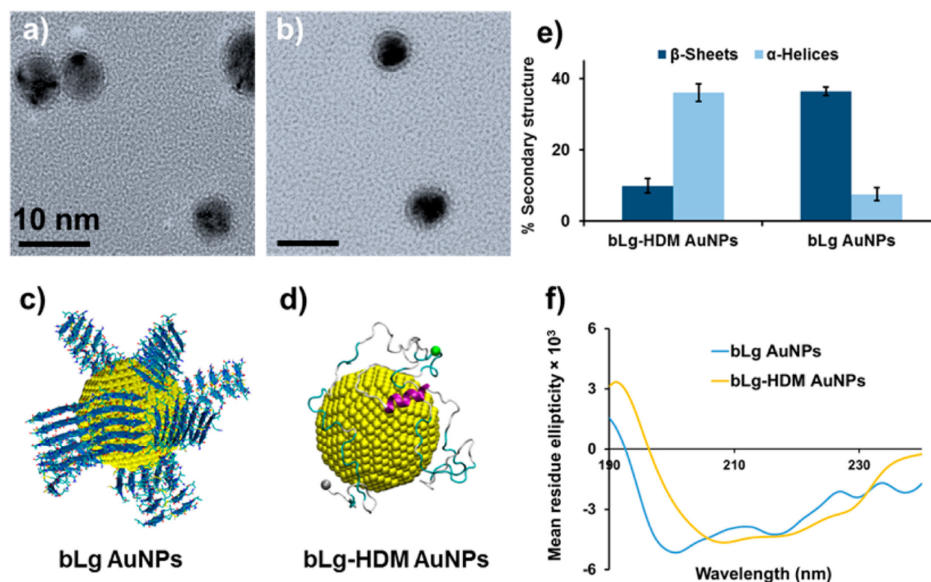


Figure 1. Transmission electron microscopy (a,b) and discrete molecular simulations (c,d) show bLg AuNPs and bLg-HDM AuNPs. Circular dichroism spectroscopy indicates high β -sheet content in bLg AuNPs but not in bLg-HDM AuNPs (e,f). Scale bars in a,b: 10 nm. bLg amyloids of LACQCL (blue) coated on AuNPs (yellow spheres, 4 nm in diameter) (c). Full-length bLg molecules bound to an AuNP in the denatured state (d). Alpha-helices: purple, beta-sheets: orange, turns: cyan, coils: gray. C $_{\alpha}$ atoms in N- and C-termini: gray and green beads (d).

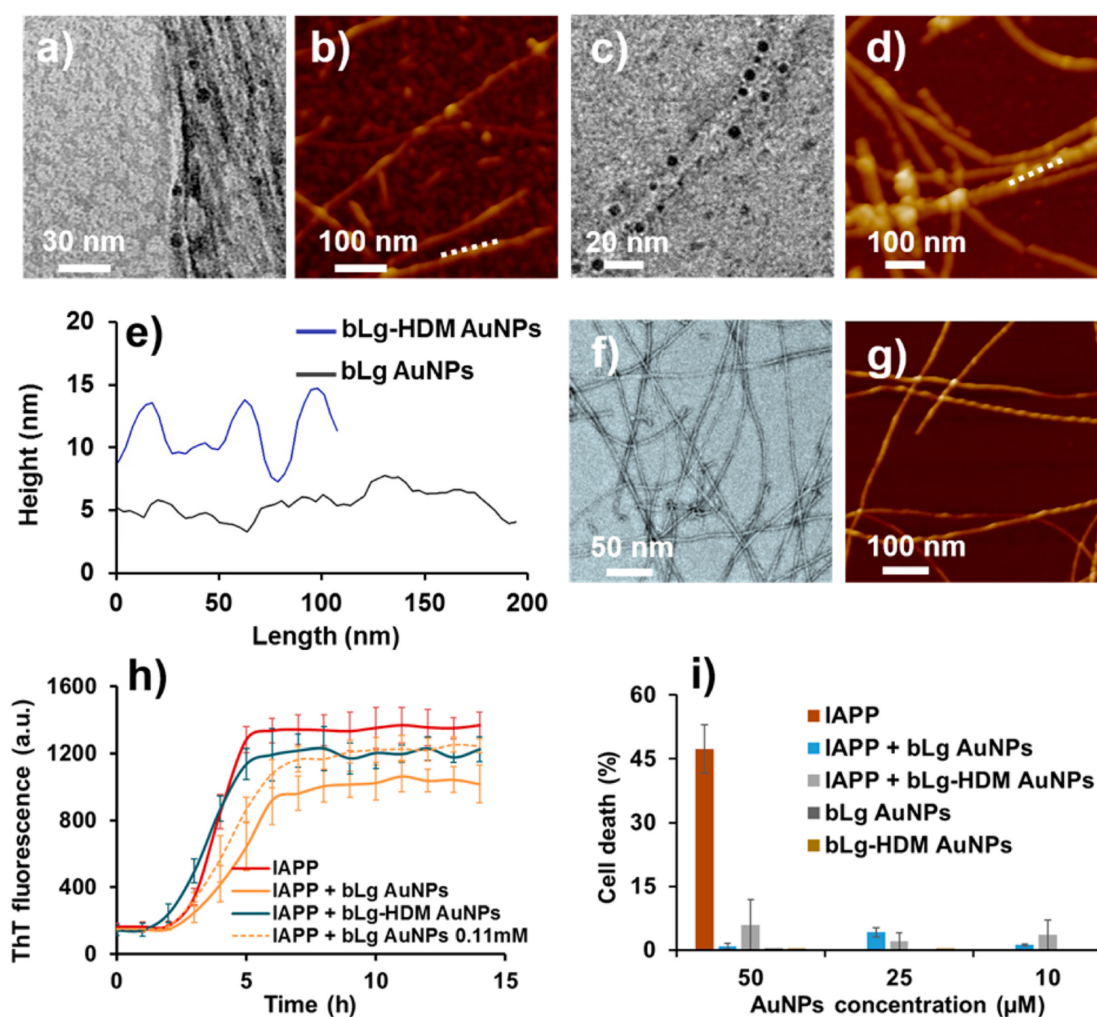


Figure 2. Transmission electron microscopy (a,c) and atomic force microscopy (b,d) show bLg AuNPs and bLg-HDM AuNPs incubated with IAPP after 24 h of cofibrillization. The AFM height scans of the IAPP fibrils (e) correspond to panels b and d (white dashed lines). The height variations of the blue trace indicate adsorption of bLg-HDM AuNPs, while the relatively flat contour of the black trace suggests intercalation of bLg AuNPs with IAPP fibrils, in agreement with the TEM image in panel a. While transmission electron microscopy showed the electron densities of IAPP fibrils incubated with the AuNPs (dark spots, a,c), 3D atomic force microscopy revealed topologies of the IAPP fibrils in the presence of the AuNPs (b,d). The IAPP fibrils appeared intercalated with bLg AuNPs (a) while surface-adsorbed with bLg-HDM AuNPs (c). The IAPP control is shown in panels f and g. The effects of the AuNPs on IAPP fibrillization were evaluated by a thioflavin T kinetic assay (h), where the IAPP control (25 μ M) displayed standard sigmoidal kinetics while the AuNPs (0.083 mM, unless specified otherwise) affected the kinetics as also summarized in Table S1. The toxicity induced by IAPP (fixed at 25 μ M) in pancreatic β TC6 cells was fully eliminated in the presence of the AuNPs at 10–50 μ M (i).

was performed under ambient conditions with 100 μ L of total reaction volume per well, consisting of 25 μ M ThT dye, 25 μ M of IAPP and 0.083 mM or 0.11 mM of AuNPs in a 96 well-plate. The kinetic assay was carried out for 14 h with excitation and emission wavelengths of 440 and 485 nm at 25 $^{\circ}$ C. The kinetic parameters of lag time, fibrillation rate constant (k) and time to reach the half of fibrillization ($t_{1/2}$) were calculated from the ThT data.¹⁶ The measurements were performed with 4 repeats for each sample condition and data was presented as mean \pm standard deviation.

Atomic Force Microscopy. Aliquots of 20 μ L of AuNP-IAPP solution (IAPP concentration: 25 μ M, AuNPs: 0.083 mM, incubated 24 h) were deposited on freshly cleaved mica, left to adsorb for 2 min at room temperature, rinsed with Milli-Q water, and gently dried with pressurized air. The samples were scanned on Nanoscope VIII Multimode Scanning Force Microscopes (Bruker) covered with an

acoustic hood to minimize vibrational noise. The AFM was operated in tapping mode under ambient conditions using commercial silicon nitride cantilevers (Bruker). All AFM images were flattened to remove background curvature using the Nanoscope Analysis 1.5 software and no further image processing was carried out.

Cytotoxicity Assay. The IAPP control and the AuNPs with IAPP were incubated with human embryonic kidney 293 (HEK293) cells or pancreatic β TC6 cells (acquired from ATCC) in DMEM supplemented with 15% FBS and 1% penicillin/streptomycin at 37 $^{\circ}$ C, 5% CO₂. End point cytotoxicity was determined by the percentage of propidium iodide (PI) positive cells after 24 h. The experiment was performed in triplicate.

Dark-Field Imaging. bLg AuNPs-IAPP hybrids were incubated for 30 min with human plasma proteins or CEM.NKR-CCR5 human T cells, obtained from the Department of Microbiology and Immunol-

ogy, The Peter Doherty Institute for Infection and Immunity, The University of Melbourne. The samples were then mounted between a glass slide and a coverslip sandwiched with a double-sided tape and visualized by a dark-field microscope (CytoViva).

X-ray-Induced Destruction of AuNP-IAPP Hybrids. IAPP as well as bLg AuNPs-IAPP hybrids were irradiated with X-rays using a Bruker D8 advanced X-ray generator. The X-rays (Cu source, Type Gaussian) were generated at 125 W energy (25 kV and 5 mA) and directed to the center of the sample holder with an $8 \times 8 \mu\text{m}$ slit. Samples were exposed for 100 s with a dose of $300 \mu\text{Sv/h}$. The exposed samples were immediately prepared for TEM after the X-ray treatment.

RESULTS AND DISCUSSION

Synthesis and Characterizations of bLg AuNPs and bLg-HDM AuNPs. Sonicated bLg fragments coated AuNPs via electrostatic interaction and surface adsorption, which prevented flocculation of the AuNPs against NaCl up to 2 M in concentration (Figure S1b, Supporting Information or SI). The AuNPs were monodisperse, but occasionally contained more than one NP per unit. The high stability of the bLg AuNPs (stable in water for at least 2 months of storage at 4°C) is essential for their biological applications without evoking destabilization through ligand exchange.¹¹ The hydrolyzed bLg fragments were $\sim 6 \text{ kDa}$.¹⁷ The 1–2 nm thick “coronas” of the bLg AuNPs (Figure 1a) were rich in β -sheets ($>35\%$), resulting from bLg amyloids during the synthesis as corroborated by circular dichroism (CD) analysis (Figure 1e). In the CD spectra of bLg AuNPs, the negative peak absorbance around 218 nm indicates β -sheet conformation, whereas in the case of bLg-HDM AuNPs, the broad negative peak from 225 to 208 nm represents α -helices as the dominant conformation (Figure 1f). The presence of α -helices in the AuNPs could be due to heat-induced conversion of β -sheets.¹⁸

All-atom discrete molecular dynamics (DMD) simulations, a rapid and predictive molecular dynamics algorithm,^{19,20} were employed to provide a molecular insight into the corona formation of bLg fragments and denatured full-length bLg on the surface of AuNPs.²¹ According to prior analysis of bLg amyloid formation and its binding with AuNPs,^{9,22} the amyloid-forming segment ¹¹⁷LACQCL¹²² from the native bLg sequence was chosen to model the AuNP-binding bLg amyloids, as described in the SI. The sequence is one of the most amyloidogenic regions in the native bLg sequence according to the zipperDB server, which estimates the propensity of a given 6- or 7-residue sequence in forming the steric zipper cross- β conformation,^{18,23} and contains two cysteines with strong binding affinity for AuNPs. We first evaluated the binding between a single sonicated bLg fibril (a two-layer β -sheet formed by 10 peptides with the molecular mass of $\sim 6 \text{ kDa}$ as identified experimentally,¹⁷ Figure S2) and a 4 nm spherical AuNP, where protein–AuNP interactions were adopted from the GoLP force field (Methods, Figure S2b).²⁴ The cross- β fibrils bound the AuNP in two modes, with either the fibril interface being parallel or perpendicular to the AuNP surface (Figure S2d,e). With more cross- β fibrils added to the system, formation of fibril “coronas” was observed due to strong fibril–AuNP binding and interfibril interactions on the AuNP surface (Figure 1c). The interaction between a heat-denatured bLg monomer and an AuNP was also simulated at 350 K, where the unfolded protein was found to bind and spread over the AuNP surface with the native helices retained (Figure 1d, Figure S3), consistent with the CD measurement (Figure 1e,f).

Fibrillization of Pathogenic IAPP in the Presence of bLg AuNPs and bLg-HDM AuNPs. Upon incubation with IAPP monomers in the aqueous phase, bLg AuNPs appeared within the contours of the IAPP fibrils indicating intercalation of the NPs with the fibrils (Figure 2a). By contrast, bLg-HDM AuNPs, consisting of AuNPs stabilized by heat-denatured bLg monomers, protruded out of the fibril contours resulting from surface adsorption of the NPs onto the IAPP fibrils upon their incubation (Figure 2c). Ligand exchange between the protein coating of bLg AuNPs and free IAPP monomers (prior to fibrillization) was unfavorable, due to strong binding between bLg fragments and AuNPs, as reflected by the high stability of the NPs against salt (Figure S1b) and time. The association between the bLg AuNPs and IAPP fibrils was confirmed by energy-dispersive X-ray (EDX) mapping of the IAPP hybrids, which displayed a prominent elemental peak of Au (Figure S4). Three-dimensional atomic force microscopy (3D AFM) and AFM height scans (Figure 2e) further revealed intercalation (Figure 2b) or adsorption (Figure 2d) of AuNPs with respect to IAPP fibrils, consistent with the observations by transmission electron microscopy (TEM). It is necessary to mention that the IAPP fibrils alone were a mixture of different structural morphologies—many of the fibrils possessed the morphology of a twisted ribbon with a certain periodicity and handedness (Figure 2f,g), while the IAPP fibrils assembled in the presence of intercalated AuNPs did not display a distinct periodicity. This suggests a reduced cooperativity in the self-assembly of IAPP in the presence of the AuNPs.

The effects of the AuNPs on IAPP fibrillization were examined by a thioflavin T (ThT) kinetic assay (Figure 2h). The parameters of lag time, aggregation rate constant (k) and time to reach half of the fibrillization ($t_{1/2}$) were derived from the ThT data (Table S1).¹⁶ As bLg AuNPs mostly intercalated with IAPP during fibrillization, they notably prolonged the lag time due to the inclusion of AuNPs in IAPP self-assembly. The intercalation observed for IAPP and bLg AuNPs at $\leq 0.083 \text{ mM}$ (see ref 14 for calculation of AuNP concentration) was absent at 0.11 mM , as the NPs became adsorbed onto the fibril surfaces (Figure S5a). This can be understood as bLg AuNPs of high concentrations interacted more strongly among themselves, hence compromising NP-peptide interaction to favor peptide–peptide interaction.⁵ However, such interaction was not observed for α -helix rich bLg-HDM AuNPs at all concentrations, indicating the intercalation of bLg AuNPs with IAPP was not merely kinetic driven, but through β -sheet stacking. Accordingly, the kinetic parameters for the case of bLg-HDM AuNPs resembled that of the IAPP control (Table S1). Time-dependent TEM imaging further revealed the dynamic processes of IAPP interacting with the AuNPs (Figure S6), where IAPP–AuNP binding and cofibrillization started to occur within the first hour. In addition, both AuNPs were found adsorbed onto preformed IAPP fibrils (Figure S7a,b), suggesting that cofibrillization occurred prior to the saturation phase. Moreover, the association between bLg AuNPs and amyloidogenic proteins was found to be independent from peptide sequence or charge, as it occurred for both cationic IAPP and anionic amyloid- β (1–42) (Figure S5b,c), further pointing to the role of β -sheet stacking in rendering the hybrid architectures.

To understand how bLg AuNPs were embedded within IAPP fibrils, docking simulations between model fibrils²⁵ of IAPP and bLg fragment were performed. Briefly, the β -sheets in two fibrils were prealigned in parallel or antiparallel by shifting

each residue, followed by DMD simulations for structural relaxation and binding energy estimation. The binding mode with the highest binding affinity was selected (Figure 3). The

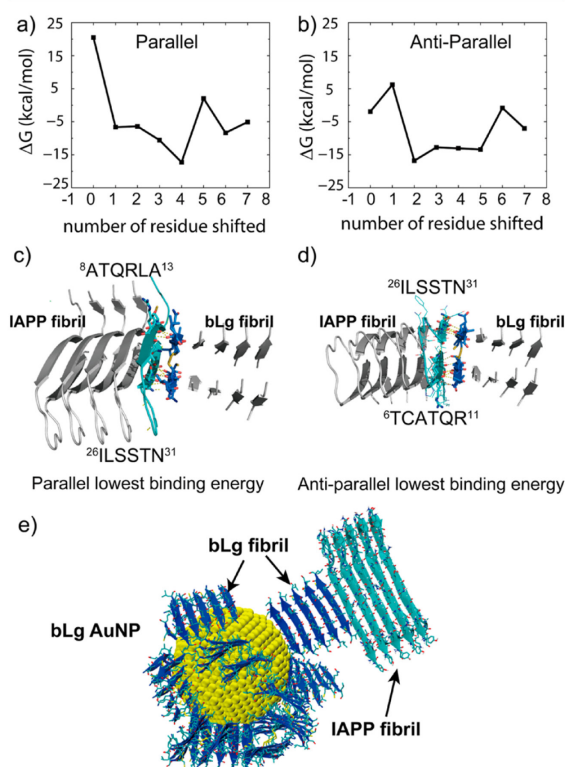


Figure 3. Docking analysis between LACQCL and IAPP fibrils. The binding energy, ΔG , between the double-layered LACQCL and u-shaped IAPP fibrils, was plotted as a function of the number of shifted residues in parallel (a) and antiparallel (b) alignments, respectively. The equilibrated snapshot structures with the corresponding lowest binding energies in parallel and antiparallel are shown in panels c and d. In both cases, similar regions in the IAPP bound to the LACQCL fibril, with the parallel alignment showing a slightly stronger binding affinity. A schematic of a bLg AuNP (4 nm) stacking with IAPP fibrils is illustrated in panel e. bLg fibrils: blue. IAPP fibrils: cyan.

two segments of $^8\text{ATQRLA}^{13}$ and $^{26}\text{ILSSTN}^{31}$ facing each other in the IAPP amyloid fibril were found to bind the double-layered LACQCL fibril in parallel by extensive backbone hydrogen bonding as well as side-chain polar and hydrophobic interactions (Figure 3c). These two IAPP segments partially overlapped with the two amyloidogenic segments of IAPP, $^{13}\text{ANFLVH}^{18}$, and $^{22}\text{NFGAILS}^{28}$, whose amyloid structures belonged to the class 2 and class 7 steric zippers assuming a parallel, up–up, face-to-back and antiparallel, up–up, face-to-back packing of β sheets, respectively.^{23,26} To confirm the fibrillization interactions of IAPP and bLg amyloids, we performed a ThT assay of IAPP in the presence of bLg amyloid seeds that were obtained by ultrasonication of mature bLg amyloids (Figure S8). The enhanced ThT fluorescence and saturation plateau indicated the stimulatory effect of bLg amyloid seeds on IAPP fibrillization. Based on these observations and DMD simulations, we propose that IAPP fibrillization could be initiated by the existing bLg amyloid

fragments on the AuNP surface, where the bLg fibrils had one of the fibril-growth interfaces bound to the 4 nm AuNP and the other one solvent-exposed and ready for cofibrillization (Figure 3e).

Applications of Cofibrillization against Amyloidogenesis. The two types of the AuNPs and the AuNP-IAPP hybrids were shown to be highly biocompatible with insulin-producing pancreatic βTC6 cells (Figure 2i) and human embryonic kidney (HEK293) cells (data not shown) and, most importantly, fully eliminated IAPP toxicity likely through sequestration of toxic IAPP oligomers and protofibrils with bLg. The AuNP-IAPP hybrids, with the coating of human plasma proteins (Figure 4a) to mimic the scenario of IAPP in circulation,²⁷ were clearly visible on dark-field microscopy via the surface plasmon resonance (SPR) of the AuNPs (CytoViva, Figure 4b). IAPP is synthesized and secreted by pancreatic islets for glycemic control, and has been found in the brain, heart and kidneys,^{28,29} in addition to their presence in circulation.³⁰ In the present study, phagocytosis of the hybrids by CEM.NKR-CCR5 human T cells was observed with dark-field microscopy (Figure 4c,d), circumventing the need of antibody labeling for immunogenic clearance of amyloid species in circulation.³¹ Furthermore, X-ray irradiation of IAPP hybridized with bLg AuNPs induced potent destruction of the amyloid structures through localized heating of AuNPs (Figure 4e,f). Such effect was not observed for IAPP amyloids in the absence of AuNPs (Figure S9). It has been shown in the literature that X-ray irradiation of AuNPs resulted in localized hyperthermia (41–46 °C), which was exploited for targeted photothermal therapy of cancer without harming normal tissue.^{32,33} As the generated heat was highly confined to the bLg AuNPs embroidered inside IAPP fibrils, this scheme is not expected to induce significant damage to a cellular environment. The destructed IAPP fibrils were in the form of small aggregates. The β -sheet contents of IAPP-bLg AuNP hybrids were markedly reduced as a result of X-ray irradiation, from 34% to 5%, while the unordered contents were increased from 39% to 69% (Figure 4g,h), indicating that the destructed IAPP aggregates contained minimal toxic and β -sheet rich IAPP oligomers.³⁴

bLg AuNPs prolonged the lag time to accommodate their intercalation within the IAPP fibrils. Such intercalation may be understood from the surfactant-like nature of amyloidogenic peptides, as the β -sheets of IAPP protofibrils/fibrils sought to minimize their exposure to the aqueous environment (and hence free energy) by interfacing the bLg β -sheets on the NP surfaces.¹³ For bLg-HDM AuNPs, the lack of β -sheets (Figure 1e) coupled with their high zeta potential (Table S2) encouraged NP adsorption onto the IAPP fibrils. The short lag time (Figure 2h, Table S1) associated with bLg-HDM AuNPs may be attributed to heat-induced bLg denaturation and increased hydrophobicity, and hence increased affinity of bLg-HDM AuNPs for an IAPP “halo” to facilitate fast fibrillization.⁵

CONCLUSION

Taken together, this study offers biomimetic AuNPs of coupling functional and pathogenic amyloids for toxicity elimination, X-ray-induced destruction and dark-field imaging of phagocytosis of amyloid proteins, three new strategies for the detection and mitigation of amyloidogenesis associated with a number of human diseases.^{31,35} The novel synthesis schemes may be extended to the construction of other types of amyloid-

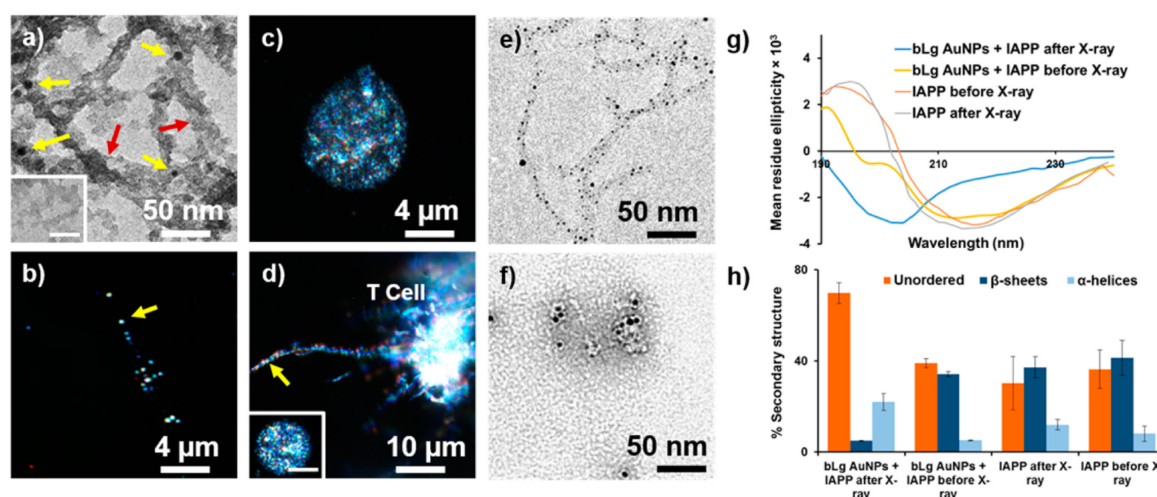


Figure 4. Transmission electron microscopy and dark-field microscopy of bLg AuNP-IAPP hybrids coated with human plasma proteins (a,b: 24 h incubation; inset in a: plasma proteins without IAPP). Dark-field microscopy of human T cells (c) and human T cells phagocytosing a bLg AuNP-IAPP hybrid (d); inset in d: a T cell in the presence of IAPP fibrils. Scale bar: 4 μm. Yellow arrows: AuNPs. Red arrows: human plasma proteins. Destruction of IAPP amyloids via localized X-ray heating of bLg AuNPs before (e) and after (f) X-ray irradiation. CD spectra and corresponding secondary structures of IAPP control and IAPP hybridized with bLg AuNPs before and after X-ray irradiation (g,h).

metal biomimetics for biosensing. Furthermore, the molecular mechanism of β -sheet stacking between two amyloid species may have implications for understanding the *in vivo* cross-talk between proteins of different pathogenic origins that has so far eluded a biophysical underpinning.³⁶

■ ASSOCIATED CONTENT

Supporting Information

The Supporting Information is available free of charge on the ACS Publications website at DOI: 10.1021/acs.biomac.7b01359.

DMD simulation methodologies, Tables S1–2, and Figures S1–9 (PDF)

■ AUTHOR INFORMATION

Corresponding Authors

*E-mail: thomas.p.davis@monash.edu.

*E-mail: fding@clemson.edu.

*E-mail: pu-chun.ke@monash.edu.

ORCID

Feng Ding: 0000-0003-1850-6336

Raffaele Mezzenga: 0000-0002-5739-2610

Thomas P. Davis: 0000-0003-2581-4986

Pu Chun Ke: 0000-0003-2134-0859

Author Contributions

[†]These authors contributed equally to this work.

Notes

The authors declare no competing financial interest.

■ ACKNOWLEDGMENTS

This work was supported by ARC Project No. CE140100036 (Davis), NSF CAREER grant CBET-1553945 (Ding), NIH R35GM119691 (Ding), and Monash Institute of Pharmaceutical Sciences (Ke).

■ REFERENCES

- (1) Ke, P. C.; Sani, M.-A.; Ding, F.; Kakinen, A.; Javed, I.; Separovic, F.; Davis, T. P.; Mezzenga, R. *Chem. Soc. Rev.* **2017**, *46*, 6492–6531.
- (2) Knowles, T. P.; Vendruscolo, M.; Dobson, C. M. *Nat. Rev. Mol. Cell Biol.* **2014**, *15*, 384–396.
- (3) Maillet, M.; Van Berlo, J. H.; Molkenin, J. D. *Nat. Rev. Mol. Cell Biol.* **2013**, *14*, 38–48.
- (4) Moore, K. A.; Pate, K. M.; Soto-Ortega, D. D.; Lohse, S.; van der Munnik, N.; Lim, M.; Jackson, K. S.; Lyles, V. D.; Jones, L.; Glasgow, N.; et al. *J. Biol. Eng.* **2017**, *11*, 5.
- (5) Gladysz, A.; Abel, B.; Risselada, H. J. *Angew. Chem., Int. Ed.* **2016**, *55*, 11242–11246.
- (6) Hamley, I. W.; Kirkham, S.; Dehsorkhi, A.; Castelletto, V.; Adamcik, J.; Mezzenga, R.; Ruokolainen, J.; Mazzuca, C.; Gatto, E.; Venanzi, M.; et al. *Biomacromolecules* **2014**, *15*, 3412–3420.
- (7) Nyström, G.; Fernández-Ronco, M. P.; Bolisetty, S.; Mazzotti, M.; Mezzenga, R. *Adv. Mater.* **2016**, *28*, 393–393.
- (8) Bolisetty, S.; Boddupalli, C. S.; Handschin, S.; Chaitanya, K.; Adamcik, J.; Saito, Y.; Manz, M. G.; Mezzenga, R. *Biomacromolecules* **2014**, *15*, 2793–2799.
- (9) Bolisetty, S.; Mezzenga, R. *Nat. Nanotechnol.* **2016**, *11*, 365–371.
- (10) Shen, Y.; Posavec, L.; Bolisetty, S.; Hilty, F. M.; Nyström, G.; Kohlbrecher, J.; Hilbe, M.; Rossi, A.; Baumgartner, J.; Zimmermann, M. B.; Mezzenga, R. *Nat. Nanotechnol.* **2017**, *12*, 642–647.
- (11) Javed, I.; Hussain, S. Z.; Shahzad, A.; Khan, J. M.; Rehman, M.; Usman, F.; Razi, M. T.; Shah, M. R.; Hussain, I. *Colloids Surf., B* **2016**, *141*, 1–9.
- (12) Van de Broek, B.; Devoogdt, N.; D'Hollander, A.; Gijs, H.-L.; Jans, K.; Lagae, L.; Muyldermans, S.; Maes, G.; Borghs, G. *ACS Nano* **2011**, *5*, 4319–4328.
- (13) Jung, J.-M.; Savin, G.; Pouzot, M.; Schmitt, C.; Mezzenga, R. *Biomacromolecules* **2008**, *9*, 2477–2486.
- (14) Chanana, M.; Rivera-Gil, P.; Correa-Duarte, M. A.; Liz-Marzán, L. M.; Parak, W. J. *Angew. Chem., Int. Ed.* **2013**, *52*, 4179–4183.
- (15) Whitmore, L.; Wallace, B. A. *Biopolymers* **2008**, *89*, 392–400.
- (16) Cabaleiro-Lago, C.; Quinlan-Pluck, F.; Lynch, I.; Lindman, S.; Minogue, A. M.; Thulin, E.; Walsh, D. M.; Dawson, K. A.; Linse, S. J. *Am. Chem. Soc.* **2008**, *130*, 15437–15443.
- (17) Lara, C.; Adamcik, J.; Jordens, S.; Mezzenga, R. *Biomacromolecules* **2011**, *12*, 1868–1875.

- (18) Narhi, L. O.; Philo, J. S.; Li, T.; Zhang, M.; Samal, B.; Arakawa, T. *Biochemistry* **1996**, *35*, 11447–11453.
- (19) Ding, F.; Tsao, D.; Nie, H.; Dokholyan, N. V. *Structure* **2008**, *16*, 1010–1018.
- (20) Zhou, Y.; Karplus, M. *Nature* **1999**, *401*, 400–403.
- (21) Wang, B.; Seabrook, S. A.; Nedumpully-Govindan, P.; Chen, P.; Yin, H.; Waddington, L.; Epa, V. C.; Winkler, D. A.; Kirby, J. K.; Ding, F.; et al. *Phys. Chem. Chem. Phys.* **2015**, *17*, 1728–1739.
- (22) Akkermans, C.; Venema, P.; van der Goot, A. J.; Gruppen, H.; Bakx, E. J.; Boom, R. M.; van der Linden, E. *Biomacromolecules* **2008**, *9*, 1474–1479.
- (23) Sawaya, M. R.; Sambashivan, S.; Nelson, R.; Ivanova, M. I.; Sievers, S. A.; Apostol, M. I.; Thompson, M. J.; Balbirnie, M.; Wiltzius, J. J.; McFarlane, H. T.; et al. *Nature* **2007**, *447*, 453.
- (24) Hughes, Z. E.; Wright, L. B.; Walsh, T. R. *Langmuir* **2013**, *29*, 13217–13229.
- (25) Luca, S.; Yau, W.-M.; Leapman, R.; Tycko, R. *Biochemistry* **2007**, *46*, 13505–13522.
- (26) Soriaga, A. B.; Sangwan, S.; Macdonald, R.; Sawaya, M. R.; Eisenberg, D. *J. Phys. Chem. B* **2016**, *120*, S810–S816.
- (27) Pilkington, E. H.; Xing, Y.; Wang, B.; Kakinien, A.; Wang, M.; Davis, T. P.; Ding, F.; Ke, P. C. *Sci. Rep.* **2017**, *7*, 2455.
- (28) Gong, W.; Liu, Z.; Zeng, C.; Peng, A.; Chen, H.; Zhou, H.; Li, L. *Kidney Int.* **2007**, *72*, 213–218.
- (29) Srodulski, S.; Sharma, S.; Bachstetter, A. B.; Brelsfoard, J. M.; Pascual, C.; Xie, X. S.; Saatman, K. E.; Van Eldik, L. J.; Despa, F. *Mol. Neurodegener.* **2014**, *9*, 30.
- (30) Despa, S.; Margulies, K. B.; Chen, L.; Knowlton, A. A.; Havel, P. J.; Taegtmeyer, H.; Bers, D. M.; Despa, F. *Circ. Res.* **2012**, *110*, 598–608.
- (31) Richards, D. B.; Cookson, L. M.; Berges, A. C.; Barton, S. V.; Lane, T.; Ritter, J. M.; Fontana, M.; Moon, J. C.; Pinzani, M.; Gillmore, J. D.; et al. *N. Engl. J. Med.* **2015**, *373*, 1106–1114.
- (32) Chatterjee, D. K.; Diagaradjane, P.; Krishnan, S. *Ther. Delivery* **2011**, *2*, 1001–1014.
- (33) Jain, S.; Hirst, D.; O'sullivan, J. *Br. J. Radiol.* **2012**, *85*, 101–113.
- (34) Laganowsky, A.; Liu, C.; Sawaya, M. R.; Whitelegge, J. P.; Park, J.; Zhao, M.; Pensalfini, A.; Soriaga, A. B.; Landau, M.; Teng, P. K.; et al. *Science* **2012**, *335*, 1228–1231.
- (35) Masters, S. L.; Dunne, A.; Subramanian, S. L.; Hull, R. L.; Tannahill, G. M.; Sharp, F. A.; Becker, C.; Franchi, L.; Yoshihara, E.; Chen, Z.; et al. *Nat. Immunol.* **2010**, *11*, 897–904.
- (36) Jackson, K.; Barisone, G. A.; Diaz, E.; Jin, L. w.; DeCarli, C.; Despa, F. *Ann. Neurol.* **2013**, *74*, S17–S26.

Supporting Information

Co-fibrillization of pathogenic and functional amyloid proteins with gold nanoparticles against amyloidogenesis

Ibrahim Javed,[†] Yunxiang Sun,^{§,‡} Jozef Adamcik,^{‡,‡} Bo Wang,[§] Aleksandr Kakinen,[†] Emily H. Pilkington,[†] Feng Ding,^{,§} Raffaele Mezzenga,[‡] Thomas P. Davis,^{*,†,¶} and Pu Chun Ke^{*,†}*

[†]ARC Centre of Excellence in Convergent Bio-Nano Science and Technology, Monash Institute of Pharmaceutical Sciences, Monash University, 381 Royal Parade, Parkville, VIC 3052, Australia

[§]Department of Physics and Astronomy, Clemson University, Clemson, SC 29634, USA

[‡]Food & Soft Materials, Department of Health Science & Technology, ETH Zurich, Schmelzbergstrasse 9, LFO, E23, 8092, Zurich, Switzerland

[¶]Department of Chemistry, University of Warwick, Gibbet Hill, Coventry, CV4 7AL, United Kingdom

Discrete molecular dynamics simulations

Discrete molecular dynamics is a unique type of molecular dynamics algorithm with significantly enhanced sampling efficiency¹, which has been extensively used model nanoparticle-biomolecules interactions.^{2, 3, 4} Detailed descriptions of the DMD method can be found elsewhere.^{1, 5} We applied a united atom representation - i.e., explicitly modelling all polar hydrogen and heavy atoms - to model the proteins and fibrils. The interatomic interactions included *van der Waals*, solvation, electrostatic interactions and H-bonding. The solvation energy was estimated with the Lazaridis-Karplus implicit solvent model, EEF1.⁶ The distance- and angular-dependent hydrogen bond interactions were modelled using a reaction-like algorithm.⁷ Screened electrostatic interactions were modelled by the Debye-Hückel approximation.⁸ A Debye length of 1 nm was used by assuming a water dielectric constant of

80 and a monovalent electrolyte concentration of 0.1 M. The Anderson's thermostat was used for the constant-temperature simulations.

Choice of amyloid-forming sequences in bLg

Mass-spectroscopy experiments showed that bLg amyloid fibrils were formed by a range of short peptide segments, which correlated with their hydrophobicity.⁹ In this study, we chose the 6-residue segment ¹¹⁷LACQCL¹²², which has high hydrophobicity and corresponds to a short beta-strand in the native structure of bLg (Figure S2). Typically, a 6 or 7-residue sequence window has been used as a minimal length of amyloid peptides with amyloid-like aggregation behavior – e.g., GNNQQNY from yeast prion, sup35;¹⁰ NFGAIL from IAPP;¹¹ and KLVFFAE from amyloid- β .¹² Additionally, it has also been shown in many cases sub-peptides corresponding to the amyloid core sequence of an amyloidogenic protein/peptide often share similar properties with the full-length protein/peptide, such as structure and cytotoxicity.^{13, 14} Moreover, the LACQCL sequence contains two cysteines (three other cysteines are scattered in the full sequence or do not participate in the fibril⁹ that are known to have strong affinity for Au, as confirmed by our binding simulations. Therefore, our choice of LACQCL captures the essential properties of AuNP coating with bLg and its subsequent co-fibrillization with IAPP.

Molecular systems in DMD simulations

We adopted the recently developed Au molecular mechanics force field¹⁵ to model a spherical AuNP with a diameter of 40 Å that comprising 1,865 Au Atoms. The AuNP force field included both physical and chemical absorptions, aromatic and “image” charge interactions. The polarization was modelled by attaching a charged virtual particle ($-0.3e$) to each metal ($0.3e$) atom with a fixed bond length (1.0 Å) as implemented in the GoIP force field.¹⁵ Only the electrostatic interaction was taken into account for the virtual particle.

The known crystallography structure of native bLg was obtained from the RCSB Protein Data

Bank with the PDB code 3NPO.¹⁶ The sequence of bLg amyloid-forming fragment LACQCL was picked based on previous mass spectrometry studies of bLg amyloids prepared at high temperature and low pH.^{9, 17} Model bLg amyloids were subsequently built as double-layer β sheets with 10 peptides based on the zipperDB amyloid model of short peptides.¹⁸ The double-layered IAPP protofibril model was generated based on the zipperDB energy landscape and the solid-state NMR constraints from the Tycko group,¹⁹ which comprised 10 IAPP monomers. The basic and acidic residues of the IAPP (fibril) were assigned charges corresponding to their titration states at physiological condition (pH=7.4) – i.e., Arg and Lys residues were assigned +1e, Asp and Glu were assigned -1e, while His was neutral. Counter ions (Cl⁻) were added to maintain the net charge of the systems zero and account for possible counter-ion condensation. All the fibril structures were energy minimized prior to the simulations.

Binding of single bLg amyloids with AuNP

The binding mechanism of each single protofibril with a 4 nm AuNP was probed. Specifically, five independent simulations with different initial inter-molecular orientations were carried out for each type of the protofibrils. As shown in Figure S2, the LACQCL protofibril could bind the AuNP with two different interfaces: having the fibril growth axis perpendicular to (mode 1; Figure S6d) and parallel to the AuNP surface (mode 2; Figure S2e). In mode 1, the LACQCL protofibril had one of the two fibril growth surfaces anchored on the AuNP surface. The mode 2 of the LACQCL protofibril had the beta-strand ends along the fibril surface contact the AuNP surface. In short, the protofibril formed by LACQCL could bind the surface of AuNP by more than one mode. For each type of the amyloid fibrils, we also computed the average binding energy of each binding mode as the energy difference between bound and unbound states (Figure S2).

Binding of heat-denatured bLg monomers with AuNP

To investigate the interaction between full-length and heat-denatured bLg and AuNP, DMD simulations of a bLg monomer and a 4 nm AuNP at ~350 K were performed. The bLg monomer was firstly placed 1.5 nm away from the AuNP (Figure S3c). As shown in Figure S3, the native structure of bLg mainly adopts β -sheets (~40%) and helices (~16%). Both β -sheet and helical structures were lost in less than 10 ns simulations at 350 K. However, the helical region (from D130 to K141) refolded when the bLg were bound on the AuNP surface (Figure S3f). Residues other than the helical region (D130 to K141) mainly assumed random coils and covered the AuNP surface (Figure S3c, f). The evolution of each residue's distance to the AuNP surface (Figure S3b, C α atom of each residue was used in the calculation) revealed that most bLg residues bound the AuNP surface in less than 50 ns. This indicates that bLg monomers bound AuNPs at 350 K mostly in random coils, with residues D130-K141 retaining their native helical structure.

Binding of multiple bLg amyloids with AuNP

To investigate the self-assembly of multiple amyloids on the AuNP surface, we randomly placed 10 decameric protofibrils on the surface of an AuNP initially separated from each other. For each fibril type, we performed five independent DMD simulations. In all cases, the protofibrils could assemble by moving around the AuNP surface and by inter-amyloid interactions, leaving the open surface region of the AuNP available for additional amyloid fibrils to bind. As a result, amyloids are expected to fully cover the AuNP surface rendering a 'hard' amyloid-AuNP corona. Only the amyloids with binding mode 1 (Figure S2) had their fibril growth interface exposed and available for potential "seeding" of amyloid growth.

Docking between IAPP and bLg fibrils using DMD simulations

The model structures of the IAPP fibril derived from solid-state NMR¹⁹ and the double-layer LACQCL fibril were used in the docking simulation. The β sheets from the two types of

amyloids were pre-aligned in parallel or anti-parallel by shifting each residue. For each initial alignment, 25 ns DMD simulations were performed for structural relaxation and binding energy estimation. The binding energy, ΔG , was estimated as the potential energy difference between the complex after equilibration and the unbound state (Figure 3). The lowest binding energy corresponded to a parallel binding between $^8\text{ATQRLA}^{13}$ and $^{26}\text{ILSSTN}^{31}$ of the IAPP and bLg fibril.

Table S1. IAPP fibrillation kinetic parameters in the presence of the two types of AuNPs.

Sample	Lag Time (min)	k (min ⁻¹)	t _{1/2} (min)
IAPP control	168.3 ± 26.3	0.03 ± 0.001	230 ± 5
bLg AuNPs (0.083 mM)	232.1 ± 31.4	0.04 ± 0.009	285 ± 7
bLg AuNPs (0.11 mM)	181.4 ± 29.9	0.03 ± 0.005	240 ± 15
bLg-HDM AuNPs	113.6 ± 22.7	0.02 ± 0.001	225 ± 13

Table S2. Hydrodynamic sizes and zeta potentials of the two types of AuNPs.

AuNPs	Hydrodynamic Size (nm)	Zeta potential (mV)
bLg-AuNPs	24 ± 3	-15.8 ± 2.4
bLg-HDM AuNPs	20 ± 3	-21.6 ± 2.1

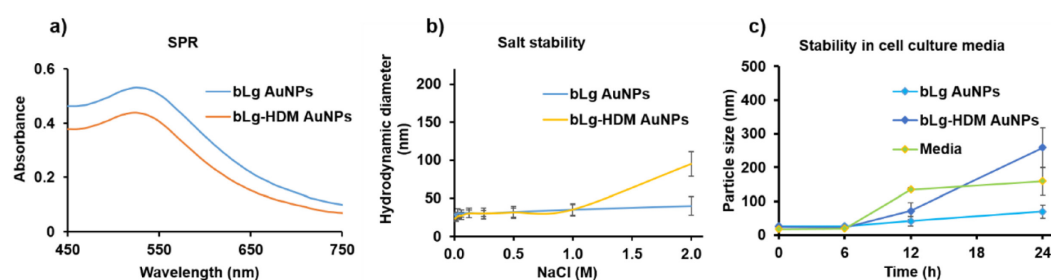


Figure S1. Characteristic surface plasmon resonance (SPR) peaks of the AuNPs at ~550 nm (a). Stability of the AuNPs against NaCl (b). AuNPs stability in cell culture media enriched with 15% fetal bovine serum (FBS) (c).

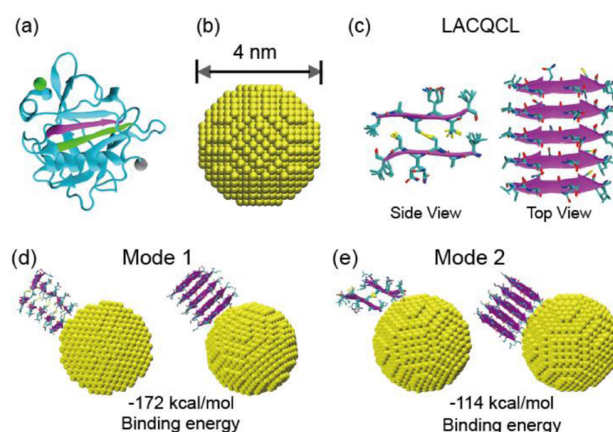


Figure S2. The molecular structures used in the DMD simulations. (a) The structure of the bLg (PDB ID: 3NPO) in cartoon representation with the C α atoms in the N- and C-termini shown as grey and green beads, respectively. Two of the experimentally-identified amyloid-forming fragments, 112 LACQCL 117 and 21 SLAMAAS 27 , are colored in purple and green, respectively. (b) The structure of AuNP with a diameter of 4 nm is shown in sphere representation. (c) The model structure of decameric protofibrils formed by 10 LACQCL. The peptides are shown in two different views (Side and Top). The binding modes of the protofibril formed by LACQCL (d, e) on the AuNP surface are shown in two different views. The LACQCL protofibril can directly bind AuNP with two different interfaces: one has the fibril growth axis perpendicular to the AuNP surface (mode 1; d), and the other has the fibril growth axis parallel to the AuNP surface (mode 2; e).

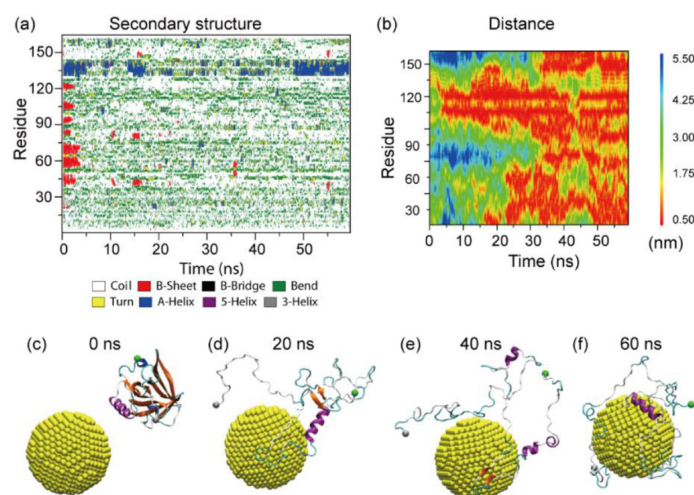


Figure S3. Coating of a bLg monomer on an AuNP at 350 K. (a) Time evolution of the secondary structure of each amino acid in full-length bLg (162 residues) at the surface of the 4 nm AuNP. (b) Time evolution of each residue's distance to the AuNP surface ($C\alpha$ atom of each residue is used in calculation). (c-f) Snapshots along the simulation trajectory at 0, 20, 40 and 60 ns. The protein structures are shown as cartoons with α helices displayed in purple, β sheets in orange, turns in cyan, and coils in grey. The $C\alpha$ atoms in the N- and C-termini are shown as grey and green beads, respectively.

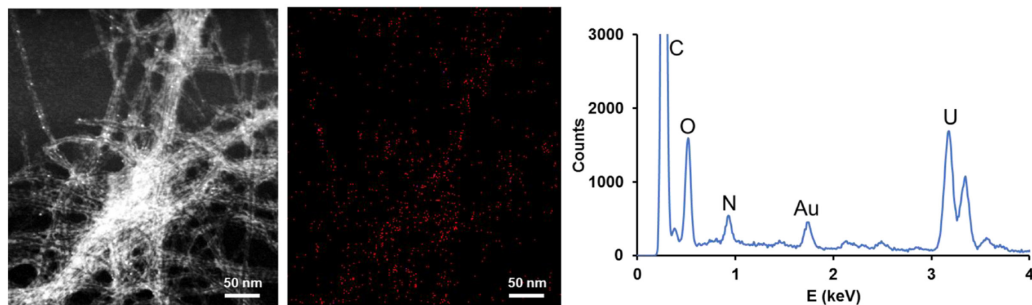


Figure S4. Energy-dispersive X-ray spectroscopic (EDX) mapping of bLg AuNPs in IAPP fibrils (middle), showing the peak of element Au (right) for the TEM image (HAADF mode) on the far left.

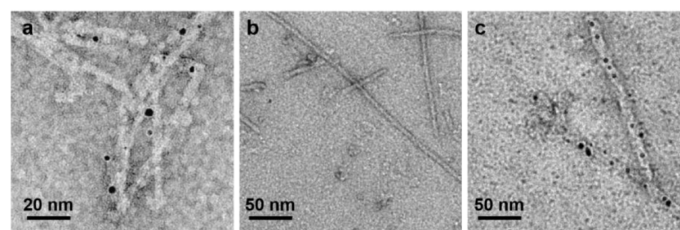


Figure S5. (a) bLg AuNPs (0.11 mM) adsorbed on IAPP fibril surfaces. Amyloid- β (1-42) incubated alone (b) and in the presence of bLg AuNPs (c). Incubation: 48 h.

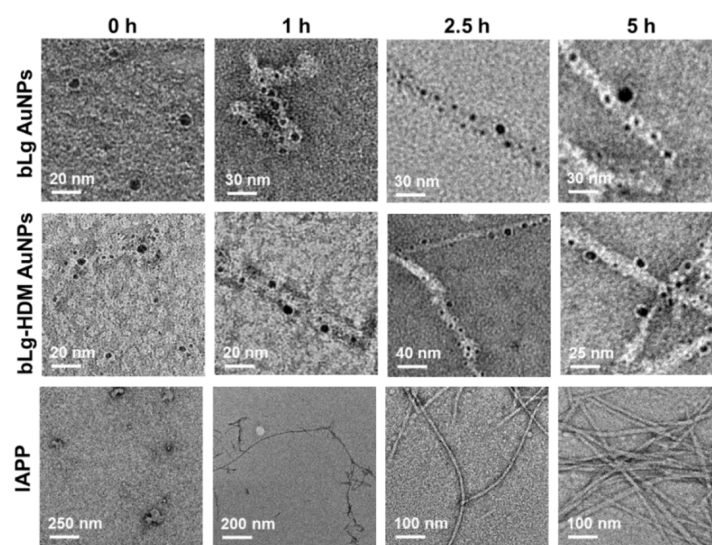


Figure S6. TEM imaging of the AuNPs incubated with IAPP. The interactions between the AuNPs and IAPP started to occur within the first hour, while intercalation of bLg AuNPs with IAPP appeared largely complete within 5 h.

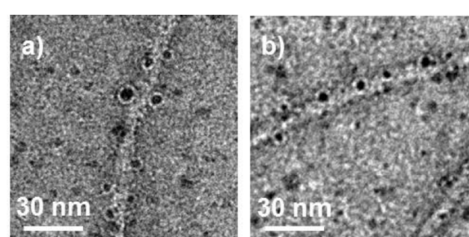


Figure S7. TEM imaging of bLg AuNPs (a) and bLg-HDM AuNPs (b) incubated for 4 h with preformed IAPP fibrils (2 day old).

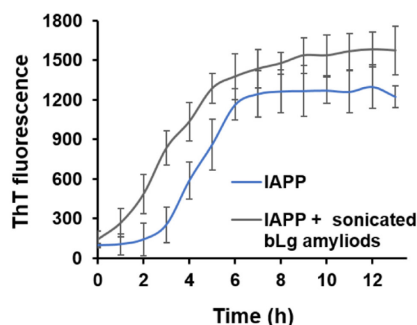


Figure S8. ThT assay of seeding IAPP monomers with sonicated bLg amyloids.

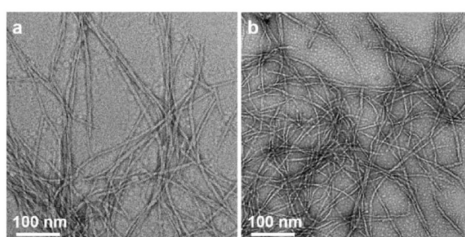


Figure S9. IAPP fibrils before (a) and after (b) X-ray irradiation.

References:

1. Ding, F.; Tsao, D.; Nie, H.; Dokholyan, N. V. *Structure* **2008**, *16*, 1010-1018.
2. Radic, S.; Nedumpully-Govindan, P.; Chen, R.; Salonen, E.; Brown, J. M.; Ke, P. C.; Ding, F. *Nanoscale* **2014**, *6*, 8340-8349.
3. Nedumpully-Govindan, P.; Gurzov, E. N.; Chen, P.; Pilkington, E. H.; Stanley, W. J.; Litwak, S. A.; Davis, T. P.; Ke, P. C.; Ding, F. *Phys. Chem. Chem. Phys.* **2016**, *18*, 94-100.
4. Wang, B.; Seabrook, S. A.; Nedumpully-Govindan, P.; Chen, P.; Yin, H.; Waddington, L.; Epa, V. C.; Winkler, D. A.; Kirby, J. K.; Ding, F. *Phys. Chem. Chem. Phys.* **2015**, *17*, 1728-1739.
5. Shirvanyants, D.; Ding, F.; Tsao, D.; Ramachandran, S.; Dokholyan, N. V. *J. Phys. Chem. B* **2012**, *116*, 8375-8382.
6. Lazaridis, T.; Karplus, M. *Curr. Opin. Struc. Biol.* **2000**, *10*, 139-145.
7. Ding, F.; Borreguero, J. M.; Buldyrey, S. V.; Stanley, H. E.; Dokholyan, N. V. *Proteins: Structure, Function, and Bioinformatics* **2003**, *53*, 220-228.
8. Debye, P.; Hückel, E. *Physikalische Zeitschrift* **1923**, *24*, 185-206.
9. Akkermans, C.; Venema, P.; van der Goot, A. J.; Gruppen, H.; Bakx, E. J.; Boom, R. M.; van der Linden, E. *Biomacromolecules* **2008**, *9*, 1474-1479.
10. Nelson, R.; Sawaya, M. R.; Balbirnie, M.; Madsen, A. Ø.; Riek, C.; Grothe, R.; Eisenberg, D. *Nature* **2005**, *435*, 773-778.
11. Marshall, K. E.; Serpell, L. C. *Soft Matter* **2010**, *6*, 2110-2114.
12. Lu, K.; Jacob, J.; Thiagarajan, P.; Conticello, V. P.; Lynn, D. G. *J. Am. Chem. Soc.* **2003**, *125*, 6391-6393.
13. Rodriguez, J. A.; Ivanova, M. I.; Sawaya, M. R.; Cascio, D.; Reyes, F. E.; Shi, D.; Sangwan, S.; Guenther, E. L.; Johnson, L. M.; Zhang, M. *Nature* **2015**, *525*, 486-490.
14. Krotee, P.; Rodriguez, J. A.; Sawaya, M. R.; Cascio, D.; Reyes, F. E.; Shi, D.; Hattne, J.; Nannenga, B. L.; Oskarsson, M. E.; Philipp, S. *eLife* **2017**, *6*, e19273.
15. Hughes, Z. E.; Wright, L. B.; Walsh, T. R. *Langmuir* **2013**, *29*, 13217-13229.

16. Loch, J.; Polit, A.; Górecki, A.; Bonarek, P.; Kurpiewska, K.; Dziedzicka- Wasylewska, M.; Lewiński, K. *J. Mol. Recognit.* **2011**, 24, 341-349.
17. Bolisetty, S.; Mezzenga, R. *Nat. Nanotech.* **2016**, 11, 365-371.
18. Goldschmidt, L.; Teng, P. K.; Riek, R.; Eisenberg, D. *Proc. Nat. Acad. Sci. USA* **2010**, 107, 3487-3492.
19. Luca, S.; Yau, W.-M.; Leapman, R.; Tycko, R. *Biochemistry* **2007**, 46, 13505-13522.

Chapter 3

In vivo mitigation of amyloidogenesis through functional–pathogenic double- protein coronae

Declaration

This chapter was published as Ibrahim Javed, Tianyu Yu, Guotao Peng, Antoni Sánchez-Ferrer, Ava Faridi, Aleksandr Kakinen, Mei Zhao, Raffaele Mezzenga, Thomas P Davis, Sijie Lin and Pu Chun Ke, In Vivo Mitigation of Amyloidogenesis through Functional–Pathogenic Double-Protein Coronae. *Nano Lett.*, 2018. 18(9): 5797-5804.

Rationale

After studying the *in vitro* interaction as described in the previous chapter, this chapter was designed to study *in vivo* interactions between bLg amyloid-fragments coated CNTs and IAPP in aggregation through the formation of pathogenic-functional coronae. bLg amyloid-fragments coated AuNPs possessed a particle size comparable to the thickness of IAPP fibrils. This was one of the major rationales discussed for the co-fibrillization effect, rather than inhibitory effect, observed for AuNPs against IAPP. In this chapter, it was hypothesized that coating of bLg amyloid-fragments on larger surfaces like CNTs, should enable sequestration of oligomeric and protofibrillar IAPP to inhibition IAPP fibrilization. Furthermore, to fill a crucial need for *in vivo* model systems for research on anti-amyloidosis, this chapter detailed the use of zebrafish embryos as a quasi-*in vivo* system to study bLg amyloid-fragments coated CNTs against IAPP fibrilization. Zebrafish embryos were employed, developed and characterised as an imaging friendly *in vivo* model system to study IAPP toxicity and its mitigation with functionalised CNTs.

In Vivo Mitigation of Amyloidogenesis through Functional–Pathogenic Double-Protein Coronae

Ibrahim Javed,^{†,‡,§} Tianyu Yu,[‡] Guotao Peng,[‡] Antoni Sánchez-Ferrer,[§] Ava Faridi,[†] Aleksandr Kakinen,[†] Mei Zhao,[‡] Raffaele Mezzenga,^{§,||} Thomas P. Davis,^{*,†,||} Sijie Lin,^{*,‡,||} and Pu Chun Ke^{*,†,||}

[†]ARC Centre of Excellence in Convergent Bio-Nano Science and Technology, Monash Institute of Pharmaceutical Sciences, Monash University, 381 Royal Parade, Parkville, Victoria 3052, Australia

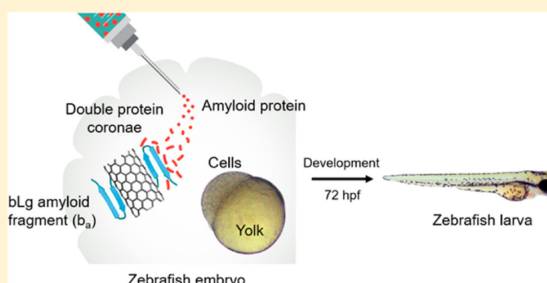
[‡]Biomedical Multidisciplinary Innovation Research Institute, Shanghai East Hospital, State Key Laboratory of Pollution Control and Resource Reuse, Shanghai Institute of Pollution Control and Ecological Security, College of Environmental Science and Engineering, Tongji University, 1239 Siping Road, Shanghai 200092, China

[§]Department of Health Sciences & Technology, ETH Zurich, Schmelzbergstrasse 9, LFO, E23, 8092 Zurich, Switzerland

Supporting Information

ABSTRACT: Amyloid diseases are global epidemics with no cure available. Herein, we report a first demonstration of in vivo mitigation of amyloidogenesis using biomimetic nanotechnology. Specifically, the amyloid fragments (b_a) of β -lactoglobulin, a whey protein, were deposited onto the surfaces of carbon nanotubes (b_a CNT), which subsequently sequestered human islet amyloid polypeptide (IAPP) through functional-pathogenic double-protein coronae. Conformational changes at the b_a –IAPP interface were studied by Fourier transform infrared, circular dichroism, and X-ray scattering spectroscopies. b_a CNT eliminated the toxic IAPP species from zebrafish embryos, as evidenced by the assays of embryonic development, cell morphology, hatching, and survival as well as suppression of oxidative stress. In addition to IAPP, b_a CNT also displayed high potency against the toxicity of amyloid- β , thereby demonstrating the broad applicability of this biomimetic nanotechnology and the use of an embryonic zebrafish model for the high-throughput screening of a range of amyloidogenesis and their inhibitors in vivo.

KEYWORDS: Amyloidogenesis, IAPP, amyloid β , zebrafish, carbon nanotubes, amyloid diseases



Amyloid diseases are modern epidemics that impact more than 6% of the global population and are characterized by deposits of amyloid fibrils and plaques in the brain and pancreas as well as other bodily organs.¹ The development of such aberrant biological substances is consequential to the fibrillization of amyloid proteins such as amyloid- β ($A\beta$), associated with Alzheimer's disease, and human islet amyloid polypeptide (IAPP), associated with type 2 diabetes (T2D), from the nucleation of monomers into oligomers and the elongation of oligomers into amyloid fibrils. Regardless of their physiological and pathological origins, the oligomeric forms of amyloid proteins are believed to be the major toxic species.^{2,3} Such oligomers show a propensity of partitioning in lipid membranes in a porin-like fashion to alter the fluidity and integrity of the cell.^{4,5} Amyloid fibrils, in addition, can extract lipids from membranes through hydrophobic interactions.⁶ The fibrillization of amyloid proteins, furthermore, has been found to stimulate the production of reactive oxygen species (ROS) to trigger cell degeneration.¹

A common mitigation strategy against amyloidogenesis is to minimize the population of the toxic oligomeric species by

pitching protein-inhibitor interaction against protein–protein interaction.^{7–10} Hydrogen bonding and hydrophobic interaction as well as the π stacking of cross- β amyloid proteins are not only responsible for the self-assembly but also postulated as a reason for the cross-talk between pathogenic–pathogenic or functional–pathogenic amyloid proteins.^{11–13} Such interactions have recently been exploited for the development of therapeutics against amyloidogenesis,¹⁰ the construction of three-dimensional nanoarchitectures,¹⁴ and cross-talk between pathogenic amyloid proteins in which parent seeds transferred the toxic and structural polymorphs to daughter fibrils.^{15,16}

β -Lactoglobulin (bLg) is a functional whey protein that, under high temperature and low pH, self-assembles into amyloid fibrils of similar morphology to that of IAPP or $A\beta$.¹⁷ This class of functional amyloid has shown potential as versatile substrates or scaffolds for tissue engineering, iron fortification, and water purification.^{18–20} To exploit the cross-talk and medicinal

Received: June 16, 2018

Revised: August 5, 2018

Published: August 8, 2018

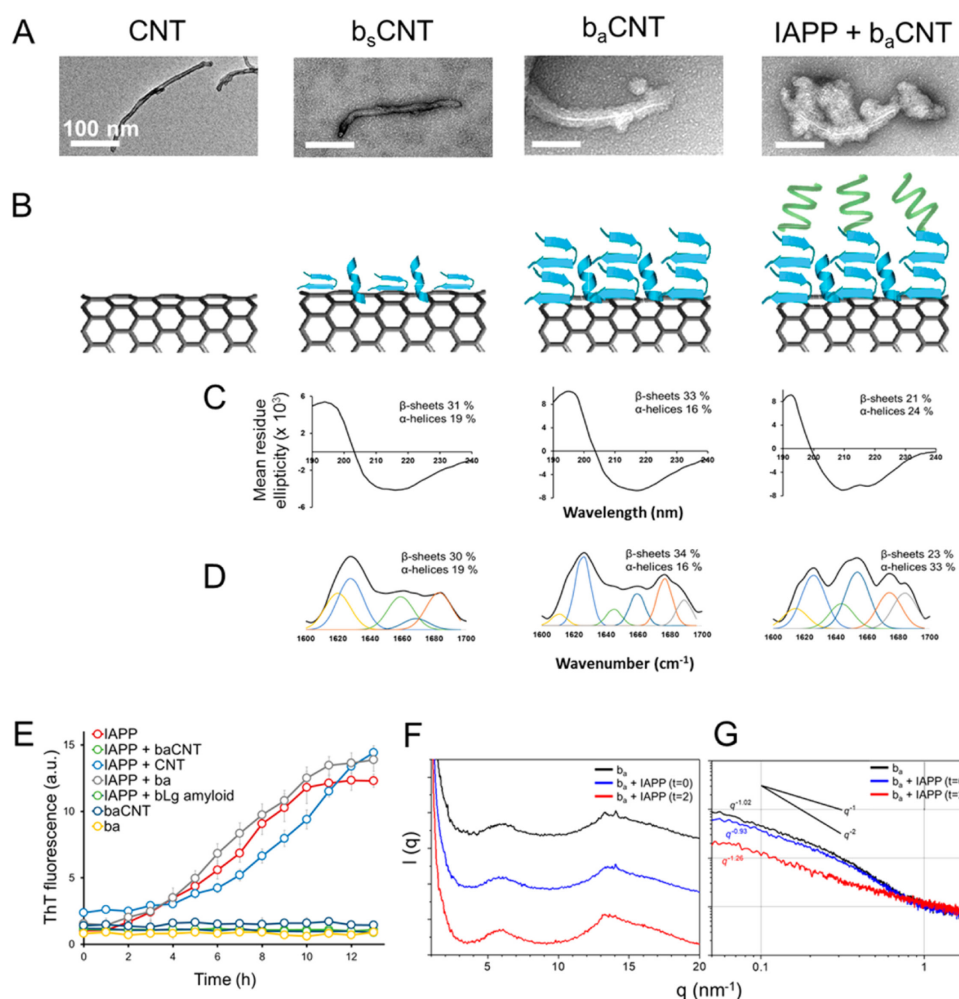


Figure 1. Synthesis scheme of CNTs functionalized with bLg amyloid corona, their surface properties, and interaction with IAPP in fibrillization. (A) TEM images of the synthesized materials and their associations with IAPP. Pristine multiwalled carbon nanotubes (CNTs) of 10–20 nm diameter were sonicated with bLg amyloid fragments (b_a). Sonication deposited an initial layer of ~ 10 nm on the CNTs (b_s CNT) and stabilized their dispersion in water. Further heating of this dispersion resulted in coalescence of surrounding b_a on the CNT surfaces, resulting in a b_a corona of ~ 30 – 50 nm on the b_a CNT surfaces. b_a CNT further captured IAPP in the form of small protruding aggregates. Scale bars: 100 nm. (B) Graphical illustration of the materials preparations. The structures of the coronae were studied with (C) CD spectroscopy and (D) FTIR amide-I band deconvolution, revealing that a relatively larger proportion of β -sheet rich corona was imparted by b_a on the CNT surfaces. After the sequestering of IAPP, the overall secondary structure of the corona was shifted toward the α helix. (E) ThT kinetic assay revealed complete inhibition of IAPP ($50 \mu\text{M}$) fibrillization by b_a CNT ($50 \mu\text{M}$ with respect to b_s). CNTs and b_a inhibited IAPP fibrillization, and no ThT fluorescence was observed in the controls of b_s CNTs or b_a alone. (F) WAXS intensity profiles of dry samples of b_a , b_a plus IAPP ($t = 0$ h), and b_a plus IAPP ($t = 2$ h). (G) SAXS intensity profiles of the water dispersions of b_a , b_a plus IAPP ($t = 0$ h), and b_a plus IAPP ($t = 2$ h).

potentials of functional bLg amyloid, we interfaced bLg amyloid fragments (abbreviated as b_a) with IAPP to capture the toxic IAPP species for mitigating IAPP amyloidogenesis in vivo. Multiwalled carbon nanotubes (CNTs) were employed as a model hydrophobic substrate to host a b_a layer, or a protein “corona”,²¹ on the tube surfaces via hydrophobic interaction and π stacking. The nonspecific binding of CNTs and A β has been previously examined in silico, in which the protein β -sheets wrapped around the CNT surfaces to reduce the latter’s surface energy in the aqueous phase.²² Such coronae afforded by proteins and other natural amphiphiles provided both the ability

to suspend in water and a new biological identity to their carbon-based nanomaterial substrates.^{23,24}

In the present study, the biomimetic constructs of a b_a corona adsorbed on a CNT surface (b_a CNT) displayed a high portion of β -sheets, which subsequently inhibited toxic IAPP species at the early stage of IAPP fibrillization. As a high-throughput model system, zebrafish embryos were developed and comprehensively characterized for screening the toxicities of amyloid proteins IAPP and A β as well as their mitigation by b_a CNT. This study first demonstrated the feasibility of in vivo mitigation of amyloidogenesis with a facile biomimetic nanotechnology and the use of a nanoliter sample volume for the induction of

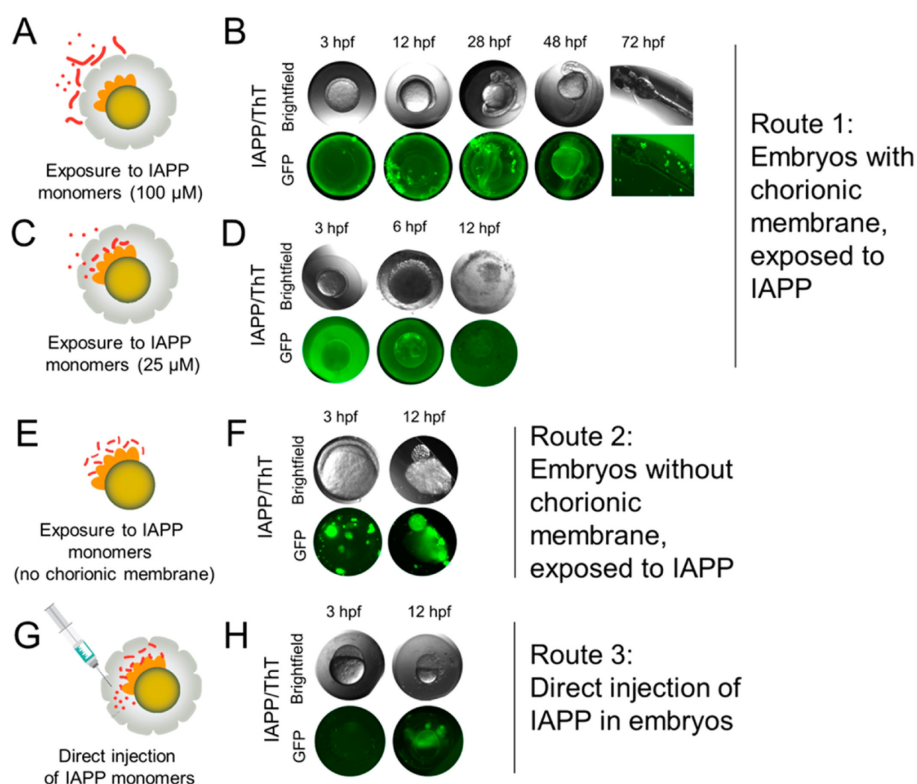


Figure 2. Toxicity of IAPP fibrillization in zebrafish embryos. IAPP peptide monomers were exposed to zebrafish embryos via three different routes, and embryonic development was monitored in the bright-field and GFP channel of a fluorescence microscope until successful hatching on the fourth day. Controls of embryos injected with equal amounts of ThT presented no fluorescence. (A) Exposure of a zebrafish embryo with chorionic membrane to IAPP of 100 μ M. (B) IAPP aggregated on the membranes without penetrating through the chorionic pores. To induce peptide–chorion interaction, (C) IAPP concentration was decreased to 25 μ M in the outer solution, and (D) ThT fluorescence indicated penetration of IAPP into the perivitelline space. (E) In the case of unprotected embryos, (F) IAPP induced toxicity within the first 12 h of development. (G) Direct injection of IAPP into the perivitelline space of embryos bypassed the chorionic barrier and resulted in direct interactions of the peptide with the lipid membranes of cells, as indicated by (H) ThT fluorescence and the toxic arrest of embryonic development at 12 hpf.

amyloid protein toxicity, two major technical advancements for the rapid screening of amyloidogenesis and their inhibitors toward a cure for amyloid diseases.¹

Sonicated bLg amyloid fragments (b_a) were adsorbed on the CNT (~ 20 nm in diameter) surfaces to render a protein corona of $\sim 30 \pm 5$ nm (Figure 1A). The elemental composition of pristine CNTs was determined by X-ray photoelectron spectroscopy (XPS), which contained mostly carbon (97.2%) as well as small traces of impurities of O ($2.6 \pm 0.1\%$) and Si ($0.2 \pm 0.0\%$). bLg amyloids were first synthesized by overnight heating (80 $^{\circ}$ C, pH 2) of 2% aqueous solution of bLg monomers, and the amyloid fibrils were then broken down to small fragments by probe sonication (Figure S1). The CNTs were embedded inside a thick coat of b_a in a two-step process: first, a layer of $\sim 10 \pm 3$ nm of b_a was deposited on the CNTs by sonication (b_s CNT), and subsequent heating (70 $^{\circ}$ C for 30 min at pH 4.3) grew the initial layer to ca. 50 ± 7 nm, resulting in b_a CNT (Figure 1A,B). The sizes of the CNTs before and after deposition of the b_a corona were measured directly from transmission electron microscopy (TEM). Sonication exposed the hydrophobic cores of the protein species, b_s in this case, to facilitate their binding with the hydrophobic CNTs,²⁵ while heating induced free proteins in the solution to coalesce on the already adsorbed

protein layer, increasing the protein content on the CNT surfaces from 67% to 76% for b_a CNT (Figure S2A). Dynamic light scattering (DLS) revealed that the hydrodynamic radius of b_a CNT was increased by ~ 9 nm from b_s CNT after heating (Table S1). The protein secondary structure of the b_a corona was estimated by circular dichroism (CD) and Fourier transform infrared (FTIR) spectroscopies, revealing a β -sheet content of 33–34% (Figure 1C,D), comparable to that of bLg amyloid ($\sim 40\%$)^{10,26} prior to sonication and deposition onto CNTs. The thickening of b_s CNT into b_a CNT by heating did not induce major effects on the secondary structure of the b_a corona.

A thioflavin T (ThT) kinetic assay revealed that b_a CNT completely inhibited IAPP fibrillization at equimolar concentrations (for IAPP and b_a) (Figure 1E). Changes in the b_a CNT surface charge indicated the adsorption and physical state of IAPP on the CNTs. Specifically, the ζ potential for IAPP peptide and mature fibrils was +15.8 and +65.3 mV, respectively. Upon incubation with IAPP, the ζ potential of b_a CNT changed from -18.4 to -12.5 mV (Table S1), indicating association of cationic IAPP with b_a CNT. CD and FTIR spectra revealed that IAPP assumed a β -sheet rich conformation upon fibrillization (Figure S2B,C). When incubated with IAPP, large protruding aggregates of IAPP were observed on the b_a CNT surfaces by

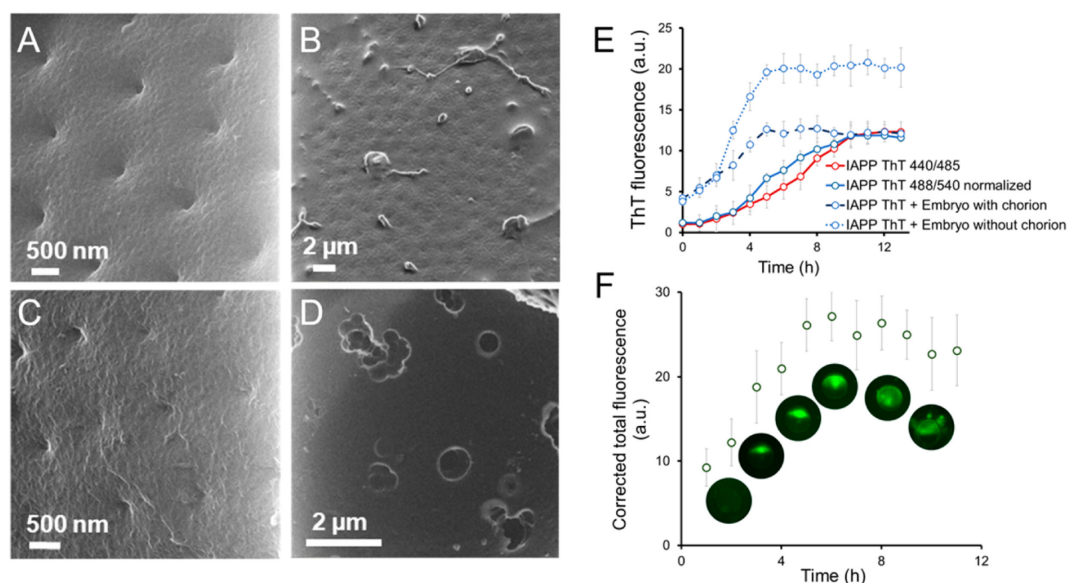


Figure 3. Amyloidogenic interactions and fibrillization kinetics of IAPP with zebrafish embryos. (A–D) IAPP–embryonic interactions were examined by helium-ion microscopy (HIM). (A) When embryos were developed in IAPP of 25 μ M, IAPP trespassed through the pores of chorionic membranes. (B) In the presence of IAPP of 100 μ M, the peptide aggregated on the outer surfaces of the embryos. (C) In contrast, unobstructed clear pores can be seen in control embryos. (D) The chorionic membrane of an embryo was cut open to assess IAPP interacting with the underlying embryonic cell. IAPP toxicity is indicated by morphological changes in the embryonic cellular membrane. (E) ThT kinetic assay of IAPP fibrillization in the presence of embryos, with and without chorionic membranes, i.e., the first and second routes of exposure. IAPP: 25 μ M; ThT: 50 μ M. The shape of ThT kinetic curve (excitation/emission: 440 nm/485 nm) recorded on a plate-reader is comparable to that acquired via the GFP channel (excitation/emission: 488 nm/540 nm). The ThT fluorescence intensity in the GFP channel was normalized by multiplying by a factor of 5 for the comparison. (F) Fibrillization kinetics of IAPP with the third route of exposure (direct injection) was measured by microinjecting 5 nL of IAPP (50 μ M) and ThT (100 μ M) inside embryos.

TEM (Figure 1A), rendering an elevated α -helix content compared to that of b_2 CNT (Figure 1C,D). It has been shown in the literature that protein or lipid interfaces can trigger conformational changes or oligomerization in the adsorbed protein.^{27,28} Sonication and heat-induced adsorption of b_a on the CNTs exposed their hydrophobic cores,^{29,30} while IAPP bound b_2 CNT via hydrogen bonding and hydrophobic interaction, converting the protein from random coils to the α -helical conformation (Figure S2B,C versus Figure 1C,D). This is in contrast to our previous study,¹⁰ in which spherical gold nanoparticles (AuNPs, 5 nm) coated by b_a intercalated inside IAPP fibrils during fibrillization. This difference may be attributed to the significantly different morphologies and aspect ratios of CNTs (>25) and AuNPs (\sim 1). It is conceivable that b_a on the tubular CNT substrate assumed more directional orientations than on spherical AuNPs, thereby allowing surface adsorption of disordered IAPP monomers but preventing that of cross- β IAPP protofibrils from inhibiting IAPP fibrillization.

To assess how IAPP might affect the structure of b_a , a wide-angle X-ray scattering (WAXS) experiment was performed on dry samples containing b_a (without CNTs) after the immediate addition of IAPP (b_a -IAPP at $t = 0$) and 2 h of incubation (b_a -IAPP at $t = 2$). Samples containing b_a displayed two peaks characteristic of inter and intra β -sheet distances at $q = 6.0$ and 13.4 nm^{-1} ($d_{\beta\text{-sheet}} = 1.1 \text{ nm}$ and $d_{\beta\text{-strand}} = 4.7 \text{ \AA}$, respectively) (Figure 1F). No differences due to the presence of CNTs were observed on the β -sheet secondary structure from the WAXS analysis (Figure S3A). Thus, no major changes at the molecular level were observed in b_a after the addition of IAPP.

Additionally, small-angle X-ray scattering (SAXS) experiment was conducted on water dispersions containing b_a , after immediate introduction of IAPP (b_a -IAPP at $t = 0$) and 2 h of incubation (b_a -IAPP at $t = 2$). No differences due to the presence of CNTs were observed on the β -sheet secondary structure from the SAXS analysis (Figure S3B). No significant changes in the scattering profiles were observed between the genitor samples and after adding IAPP at 0 h (Figure 1G). After 2 h of incubation with IAPP, b_a exhibited different SAXS intensity profiles compared with the corresponding genitor systems. This indicates that IAPP interacted with the b_L species (tubular β sheets) building up different colloidal particles but maintaining the initial secondary structures.

The recent failure of the phase-3 trial of solanezumab at Eli Lilly and the general lack of clinical success in the field of amyloidogenesis may be partially attributed to a deficiency in anti-amyloidogenesis strategies and a lack of easily accessible, economic in vivo models.³¹ Zebrafish (*Danio rerio*) share 70% of their genome and 84% of their disease-related genes with humans and are a preeminent vertebrate model for toxicology, pharmacology, and genetics research.³² Zebrafish larvae display neuropathological and behavioral phenotypes that are quantifiable and relate to those seen in humans and have been applied to many studies of Huntington's, Alzheimer's, and Parkinson's diseases.^{33,34} Here, we first developed zebrafish embryos as an in vivo model for screening nanoscale inhibitors against amyloid protein toxicity. The fibrillization and interaction of IAPP with zebrafish embryos were tracked by tagging the IAPP protofibrils and fibrils with the β -sheet affinitive ThT dye and visualized

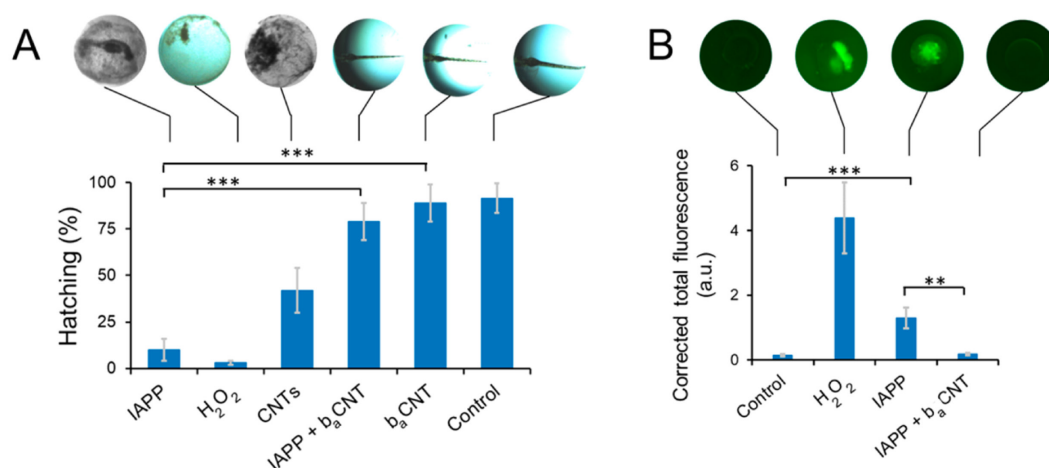


Figure 4. IAPP toxicity mitigation via functional-pathogenic double coronae on CNTs. (A) IAPP along with b_aCNT were injected inside zebrafish embryos and mitigation of IAPP toxicity was observed in terms of hatching survival of embryos on the third day post fertilization (72 hpf). b_aCNT protected the embryos from IAPP toxicity (triple asterisks indicate $p < 0.005$), while b_aCNT were biocompatible with the embryos and induced no toxicity. (B) ROS assay further confirmed the oxidative stress resulted from IAPP interaction with embryos and its mitigation by b_aCNT. ROS generation by IAPP was significantly higher than the control.

under the green fluorescence protein (GFP) channel of a fluorescence microscope (Figure S4). To determine the optimal method for assessing IAPP toxicity, zebrafish embryos were exposed to IAPP monomers via three different routes, and their efficacies were assessed.

First, embryos (3 h post-fertilization, hpf) were developed with intact chorionic membranes in 100 μ M of IAPP solution (Figure 2A). When traced by ThT (100 μ M), IAPP was found to aggregate on the surfaces of chorionic membranes and was unable to penetrate through the chorionic pores. Therefore, no toxicity was observed in the embryos (Figure 2B). However, when embryos with chorionic membranes were developed in IAPP solution of 25 μ M (Figure 2C), the peptide penetrated through the chorionic membranes to interact with the underlying embryonic cells to induce toxicity (Figure 2D). Compared to an IAPP of 100 μ M, in which peptide–peptide interaction was dominant to form aggregates, peptide–chorion interaction was evident at IAPP of 25 μ M in concentration, showing diffused ThT fluorescence in the perivitelline space at 3 hpf. Fibrillizing IAPP interacted with the underlying embryos at 6 hpf and toxic arrest of embryonic development was observed at 12 hpf (Figure 2D).

In the second route of exposure, embryos without chorionic membranes were developed in IAPP solution of different concentrations (Figure 2E). The IC₅₀ value of IAPP was reduced to 25 ± 12.5 μ M, as assessed by the percent hatching of the embryos on the third day post-fertilization (dpf). Fibrillating IAPP interacted with the cellular mass of the embryos immediately after mixing (Figure 2F). At 12 hpf, the dividing cells inside the embryos shrank to small globular masses, and the embryos lost viability. Strong ThT fluorescence, indicating IAPP amyloid aggregation, was associated with dead embryonic cells resulting from their exposure to IAPP.

In the third route of exposure, different concentrations of IAPP (5 nL of 2 to 100 μ M) were directly injected inside the perivitelline space of embryos (Figure 2G). The IC₅₀ value of IAPP was found to be 5.6 ± 1.7 μ M, the lowest for the three routes of exposure. ThT fluorescence indicated that IAPP

aggregated on the lipid membranes of the embryonic cells (Figure 2H, fluorescence image on the right) and toxic arrest of embryonic development was observed at 12 hpf.

Helium ion microscopy (HIM) was used to further visualize the interaction of IAPP with chorion and lipid membranes of embryonic cells. HIM imaging of zebrafish chorions revealed a porous morphology with an average pore size of ~ 200 nm (Figure 3A), which led to the hypothesis that IAPP monomers could penetrate through the pores to induce toxicity to the underlying embryonic cells. In the first route of exposure, in which IAPP was exposed to embryos with chorionic membranes, IAPP of 100 μ M in concentration formed large fibrillary aggregates outside the membrane pores and was not able to penetrate (Figure 3B). However, at an IAPP concentration of 25 μ M, the chorionic pores were less visible due to trespassing IAPP aggregates (Figure 3C). To visualize the interaction of IAPP with the lipid membranes of underlying embryonic cells, which is relevant to the second and third routes of IAPP administration, embryos treated with the direct micro-injection of IAPP were cut open to reveal the embryonic cells. IAPP elicited toxicity to the embryonic cells, as evidenced in the form of holes, swelling, and morphological irregularities in the membranes (Figure 3D).

The IAPP fibrillization kinetics for the three routes of exposure was recorded. In the first case, the chorionic membranes significantly enhanced the fibrillization (50 μ M IAPP) and shortened the lag time. However, the saturation phase remained the same as the control (Figure 3E). This is understandable because polysaccharides are the major component of zebrafish chorions and have been previously observed to accelerate oligomerization of α -synuclein and A β .^{35,36} In the second case of no chorion, exposure of the lipid membranes of embryonic cells to IAPP resulted in faster fibrillization and a higher saturation plateau, suggesting consumption of available monomers or oligomeric seeds and early formation of mature fibrils (Figure 3E).³⁷ In the third case of direct injection, IAPP monomers (12.5 μ M) and ThT (25 μ M) were microinjected inside the perivitelline space of embryos to observe IAPP

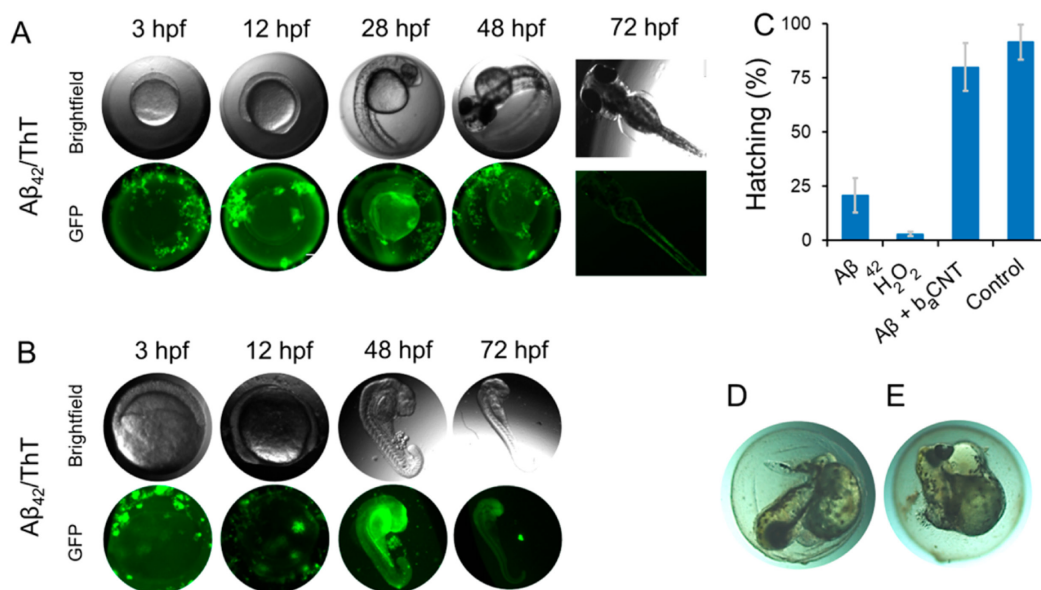


Figure 5. A β toxicity mitigation via functional-pathogenic double coronae on CNTs. Development of embryo was monitored (A) with and (B) without chorionic membrane inside a solution of fibrillating A β 42. Similar to IAPP, A β was not able to penetrate through the chorionic pores at a 100 μ M concentration. However, the IC₅₀ value of A β was 100 ± 25 μ M when embryos were directly exposed to A β solution. (C) b_aCNTs were able to sequester the toxicity of A β in the embryo. (D, E) Phenotypically strange development was observed for the embryo when injected with sub-toxic concentration (5 μ M) of A β .

fibrillization kinetics inside the chorionic fluids (Figure 3E). The saturation phase was reached at ~ 6 h for all three cases. Overall, the third route of exposure appeared to be the most efficient with sample volume (5 nL) and most facile in terms of execution (i.e., microinjection of samples directly into the perivitelline space of embryos).

The interaction between mature IAPP fibrils and developing zebrafish embryos was also studied by injecting the ThT-tagged fibrils (100 μ M of both IAPP and ThT, 24 h of maturation) inside the perivitelline space of embryos at 3 hpf (Figure S5A). No toxicity was observed based on the development and survival of the embryos (Figure S5B). The development of the embryos treated with IAPP fibrils was comparable to the control. However, hatching was significantly delayed by 48 ± 5 h compared to the control, suggesting a possible interaction between IAPP fibrils and the hatching enzyme, a zinc metalloprotease.³⁸ This is plausible because metals, especially zinc, interact strongly with IAPP to alter the latter's fibrillization and toxicity.^{39,40} In comparison, no fluorescence was observed for control embryos microinjected with ThT (Figure S5B).

Peptide-based inhibitors have shown efficacies in the inhibition of IAPP aggregation both in vitro and with transgenic animal models.^{41–47} bLg amyloids are functional and biocompatible and yet possess a similar morphology as IAPP fibrils;^{10,18} hence, they may serve as an inhibitor against IAPP toxicity. However, in vivo administration of full-length bLg amyloids is unfeasible due to their large dimensions (micrometers in length) compared to blood vasculature, and b_a itself did not elicit a notable inhibitory effect on IAPP fibrillization (Figure 1E). Accordingly, b_a was stabilized on CNT surfaces in this study, simultaneously improving the biocompatibility of CNTs while enabling inhibitory interaction with IAPP. The embryonic zebrafish system was employed to translate the mitigation

potential of b_aCNT against IAPP toxicity in vivo. Direct microinjection (route 3) was adopted because this mode of exposure allowed the use of ultrasmall sample volumes without the interference from chorionic membranes. b_aCNT were injected together with IAPP at equimolar concentrations of 10 μ M (i.e., higher than the IC₅₀ value of 5.7 μ M). b_aCNT eliminated IAPP toxicity and restored the hatching survival of IAPP-treated embryos to 85%, while b_aCNT themselves displayed no toxicity to the embryos (Figure 4A).

The above toxicity study was augmented by a ROS assay (Figure 4B). Specifically, IAPP monomers were mixed with 2',7'-dichlorodihydrofluorescein diacetate (H₂DCFDA) dye, immediately before being microinjected into the perivitelline space. ROS generation, resulting from membrane disruption of embryonic cells, was observed for IAPP. However, consistent with the hatching survival assay, no ROS species were detected when IAPP was incubated with b_aCNT.

To evaluate the mitigation potential of b_aCNT, A β was introduced to elicit toxicity in zebrafish embryos. Similar to IAPP, fibrillating A β (100 μ M) was not able to penetrate through the chorionic pores of embryos but aggregated on chorionic membranes (Figure 5A). However, when chorionic membranes were removed and embryos were exposed, A β of 100 ± 25 μ M was toxic to the embryos. In comparison to IAPP, the fibrillization of A β was slower, and the embryos survived the 3rd through the 6th somite stages at 12 hpf, after which the embryo development was arrested at the 20th somite stage at 48 hpf, and ThT fluorescence was observed from the anterior of the larvae (Figure 5B). The IC₅₀ value of A β , when injected directly inside the perivitelline space, was determined to be 7.4 ± 0.84 μ M. In comparison, Donnini et al. reported a cerebral angiopathic effect of wild-type A β peptide in zebrafish embryos at 2.5 μ M, in which the IC₅₀ value was determined to be 6.1 μ M,

comparable to that determined by our current approach.⁴⁸ b_aCNT were then injected together with A β at equimolar concentrations of 15 μ M (i.e., higher than the MIC values), and b_aCNT rescued ($p < 0.005$) the embryos from A β toxicity (Figure 5C). Abnormal phenotypic development of embryos was observed, when the embryos were microinjected with A β at 5 μ M that was just below the IC₅₀ value (Figure 5D,E), which can explain well the A β -induced neurovascular degeneration and cerebral senescence observed by Donnini et al.⁴⁸ These agreements with literature further validated our current methodologies. It should be noted that the functional-pathogenic double protein coronae on CNTs, as delineated for the in-solution characterizations (Figure 1B), do not encompass all possible protein-protein interactions under in vivo conditions, in which the chorionic sac also contained zebrafish hatching enzyme 1 (ZHE1), glycoprotein subunits, and different forms of metabolites during embryonic development.^{49–52} However, because b_a was rich in β -sheets and therefore possessed a higher affinity for amyloid proteins,^{10,53,54} the binding of b_a with IAPP through H-bonding and hydrophobic and electrostatic interactions as well as β -sheet stacking should dominate the nonspecific interactions (“soft corona”) between b_a and the other proteins and enzymes. This robust mitigation potential of b_aCNT against amyloid proteins was corroborated by additional ThT and viability assays (Figure S6), in which the presence of human plasma proteins and fetal bovine serum (FBS) did not compromise the potency of b_aCNT from inhibiting IAPP aggregation and toxicity. This latter aspect also points to the promise of exploiting the b_aCNT nanotechnology in biological fluids beyond the chorionic sac.

In summary, we have developed a facile, potent biomimetic nanotechnology against amyloidogenesis in vivo. This nanotechnology consisted of CNTs coated with a cross- β -sheet-rich, functional corona of whey protein bLg amyloid fragments (b_a), which consequently acquired a pathogenic protein corona by sequestering amyloid protein IAPP or A β . No IAPP fibrillization inhibition was observed for b_a alone (Figure 1E), justifying the role of the CNT substrates in orienting the adsorbed amyloid fragments and subsequently capturing the pathogenic protein from on-pathway fibrillization. In contrast to b_aCNT, bLg monomer-coated CNTs (b_mCNT) (Figure S7A), possessing no cross- β -sheet component, displayed a much-lower efficiency in inhibiting IAPP fibrillization (Figure S7B versus Figure 1E). In addition, an embryonic zebrafish assay through direct microinjection, i.e., the third route of exposure, has been developed into a high-throughput platform for screening amyloidogenesis and its mitigation by b_aCNT in vivo. Consistent with the ThT assay, b_mCNT, being nontoxic itself (Figure S8A), was not able to rescue zebrafish embryos from the toxicity elicited by IAPP, as evidenced by both the hatching and the ROS assays (Figure S8A,B versus Figure 4). This further vindicates the crucial role of the cross- β component in b_a and the architecture of b_aCNT in effective amyloidogenesis mitigation. Other major advantages of this assay include high fecundity and transparency of the zebrafish organism as well as an ultra-small sample volume (5 nL). IAPP at high concentrations was dominated by peptide-peptide interaction, and no toxicity was induced to zebrafish embryos. Reducing the peptide concentration promoted peptide-chorion interaction, and the peptide penetrated through the chorionic pores to elicit toxicity to embryonic cells through continued aggregation. This embryonic model system is therefore suited for examining amyloidogenesis with realistic dosage. b_aCNT protected zebrafish embryos from the

toxicities of both IAPP and A β , as evidenced by hatching-survival and ROS-generation assays. Together, this study opens the door to the rapid screening of the toxicities of a wide range of amyloid proteins and facilitates the development of potent, bioinspired nanotechnologies^{55–57} against amyloidogenesis in vivo.

■ ASSOCIATED CONTENT

Supporting Information

The Supporting Information is available free of charge on the ACS Publications website at DOI: 10.1021/acs.nanolett.8b02446.

Additional details of experimental methods. Figures showing additional TEM, TGA, WAXS and SAXS, ThT, viability, and IAPP embryonic assay data. A table showing ζ -potential and dynamic light scattering data. (PDF)

■ AUTHOR INFORMATION

Corresponding Authors

*E-mail: thomas.p.davis@monash.edu. Phone: +61-03-99039260.

*E-mail: lin.sijie@tongji.edu.cn. Phone: +86-21-65982325.

*E-mail: pu-chun.ke@monash.edu. Phone: +61-03-99039267.

ORCID

Ibrahim Javed: 0000-0003-1101-5614

Raffaele Mezzenga: 0000-0002-5739-2610

Thomas P. Davis: 0000-0003-2581-4986

Sijie Lin: 0000-0002-6970-8221

Pu Chun Ke: 0000-0003-2134-0859

Author Contributions

P.C.K., I.J., S.L., and T.P.D. designed the project. I.J. and P.C.K. wrote the manuscript. I.J. performed syntheses, CD, FTIR, ThT, TGA, XPS, ζ potential, and DLS measurements and analyses. I.J., T.Y., G.P., M.Z., and S.L. developed and performed the embryonic assays. A.S.F. and R.M. performed SAXS and WAXS experiments and analyses. A.K. and I.J. conducted TEM and prepared the illustrations. A.F. performed the cell culture and viability assay. All authors agreed on the presentation of the manuscript.

Notes

The authors declare no competing financial interest.

■ ACKNOWLEDGMENTS

This work was supported by ARC project no. CE140100036 and the Recruitment Program of “1000plan Youth” and Startup Funds from Tongji University (Lin). T.P.D. is thankful for the award of an ARC Australian Laureate Fellowship. I.J. acknowledges the support of Monash International Postgraduate Research Scholarship (MIPRS). TEM imaging was performed at Bio21 Advanced Microscopy Facility, University of Melbourne. HIM imaging was performed at the MCFP platform, University of Melbourne by Dr. Babak Nasr. I.J. and S.L. thank the Shanghai Science and Technology Commission “Belt and Road” initiative program, grant no. 17230743000.

■ REFERENCES

- (1) Ke, P. C.; Sani, M.-A.; Ding, F.; Kakinen, A.; Javed, I.; Separovic, F.; Davis, T. P.; Mezzenga, R. *Chem. Soc. Rev.* **2017**, *46* (21), 6492–6531.

- (2) Cao, P.; Abedini, A.; Wang, H.; Tu, L.-H.; Zhang, X.; Schmidt, A. M.; Raleigh, D. P. *Proc. Natl. Acad. Sci. U. S. A.* **2013**, *110* (48), 19279–19284.
- (3) Haataja, L.; Gurlo, T.; Huang, C. J.; Butler, P. C. *Endocr. Rev.* **2008**, *29* (3), 303–316.
- (4) Ritzel, R. A.; Meier, J. J.; Lin, C.-Y.; Veldhuis, J. D.; Butler, P. C. *Diabetes* **2007**, *56* (1), 65–71.
- (5) Kayed, R.; Sokolov, Y.; Edmonds, B.; McIntire, T. M.; Milton, S. C.; Hall, J. E.; Glabe, C. G. *J. Biol. Chem.* **2004**, *279* (45), 46363–46366.
- (6) Sparr, E.; Engel, M. F.; Sakharov, D. V.; Sprong, M.; Jacobs, J.; de Kruijff, B.; Höppener, J. W.; Antoinette Killian, J. *FEBS Lett.* **2004**, *577* (1–2), 117–120.
- (7) Cabaleiro-Lago, C.; Lynch, I.; Dawson, K.; Linse, S. *Langmuir* **2010**, *26* (5), 3453–3461.
- (8) Cabaleiro-Lago, C.; Quinlan-Pluck, F.; Lynch, I.; Dawson, K. A.; Linse, S. *ACS Chem. Neurosci.* **2010**, *1* (4), 279–287.
- (9) Linse, S.; Cabaleiro-Lago, C.; Xue, W.-F.; Lynch, I.; Lindman, S.; Thulin, E.; Radford, S. E.; Dawson, K. A. *Proc. Natl. Acad. Sci. U. S. A.* **2007**, *104* (21), 8691–8696.
- (10) Javed, I.; Sun, Y.; Adamcik, J.; Wang, B.; Kakinen, A.; Pilkington, E. H.; Ding, F.; Mezzenga, R.; Davis, T. P.; Ke, P. C. *Biomacromolecules* **2017**, *18* (12), 4316–4322.
- (11) Morales, R.; Moreno-Gonzalez, I.; Soto, C. *PLoS Pathog.* **2013**, *9* (9), e1003537.
- (12) Maury, C. J. *Intern. Med.* **2009**, *265* (3), 329–334.
- (13) Morales, R.; Estrada, L. D.; Diaz-Espinoza, R.; Morales-Scheihing, D.; Jara, M. C.; Castilla, J.; Soto, C. *J. Neurosci.* **2010**, *30* (13), 4528–4535.
- (14) Lee, J.; Bhak, G.; Lee, J. H.; Park, W.; Lee, M.; Lee, D.; Jeon, N. L.; Jeong, D. H.; Char, K.; Paik, S. R. *Angew. Chem., Int. Ed.* **2015**, *54* (15), 4571–4576.
- (15) García-Ayllón, M.-S.; Small, D. H.; Avila, J.; Sáez-Valero, J. *Front. Mol. Neurosci.* **2011**, *4*, 1–9.
- (16) Krotee, P.; Rodriguez, J. A.; Sawaya, M. R.; Cascio, D.; Reyes, F. E.; Shi, D.; Hattne, J.; Nannenga, B. L.; Oskarsson, M. E.; Philipp, S. *eLife* **2017**, *6*, e19273.
- (17) Adamcik, J.; Jung, J.-M.; Flakowski, J.; De Los Rios, P.; Dietler, G.; Mezzenga, R. *Nat. Nanotechnol.* **2010**, *5* (6), 423–428.
- (18) Nyström, G.; Fong, W.-K.; Mezzenga, R. *Biomacromolecules* **2017**, *18* (9), 2858–2865.
- (19) Bolisetty, S.; Mezzenga, R. *Nat. Nanotechnol.* **2016**, *11* (4), 365.
- (20) Li, C.; Adamcik, J.; Mezzenga, R. *Nat. Nanotechnol.* **2012**, *7* (7), 421–427.
- (21) Cedervall, T.; Lynch, I.; Lindman, S.; Berggård, T.; Thulin, E.; Nilsson, H.; Dawson, K. A.; Linse, S. *Proc. Natl. Acad. Sci. U. S. A.* **2007**, *104* (7), 2050–2055.
- (22) Fu, Z.; Luo, Y.; Derreumaux, P.; Wei, G. *Biophys. J.* **2009**, *97* (6), 1795–1803.
- (23) Castagnola, V.; Zhao, W.; Boselli, L.; Lo Giudice, M.; Meder, F.; Polo, E.; Paton, K.; Backes, C.; Coleman, J.; Dawson, K. *Nat. Commun.* **2018**, *9* (1), 1577.
- (24) Monopoli, M. P.; Åberg, C.; Salvati, A.; Dawson, K. A. *Nat. Nanotechnol.* **2012**, *7* (12), 779–786.
- (25) Matsuura, K.; Saito, T.; Okazaki, T.; Ohshima, S.; Yumura, M.; Iijima, S. *Chem. Phys. Lett.* **2006**, *429* (4), 497–502.
- (26) Gosal, W. S.; Clark, A. H.; Pudney, P. D.; Ross-Murphy, S. B. *Langmuir* **2002**, *18* (19), 7174–7181.
- (27) Sethuraman, A.; Vedantham, G.; Imoto, T.; Przybycien, T.; Belfort, G. *Proteins: Struct., Funct., Genet.* **2004**, *56* (4), 669–678.
- (28) Roach, P.; Farrar, D.; Perry, C. C. *J. Am. Chem. Soc.* **2005**, *127* (22), 8168–8173.
- (29) Lara, C.; Adamcik, J.; Jordens, S.; Mezzenga, R. *Biomacromolecules* **2011**, *12* (5), 1868–1875.
- (30) Li, C.; Bolisetty, S.; Chaitanya, K.; Adamcik, J.; Mezzenga, R. *Adv. Mater.* **2013**, *25* (7), 1010–1015.
- (31) The Lancet. Alzheimer's disease: expedition into the unknown. *Lancet* **2016**, *388* (10061), 2713.
- (32) Howe, K.; Clark, M. D.; Torroja, C. F.; Torrance, J.; Berthelot, C.; Muffato, M.; Collins, J. E.; Humphray, S.; McLaren, K.; Matthews, L.; et al. *Nature* **2013**, *496* (7446), 498.
- (33) Kalueff, A. V.; Stewart, A. M.; Gerlai, R. *Trends Pharmacol. Sci.* **2014**, *35* (2), 63–75.
- (34) Best, J.; Alderton, W. K. *Neuropsych. Dis. Treat.* **2008**, *4* (3), 567–576.
- (35) Das, P. K.; Dean, D. N.; Fogel, A. L.; Liu, F.; Abel, B. A.; McCormick, C. L.; Kharlampieva, E.; Rangachari, V.; Morgan, S. E. *Biomacromolecules* **2017**, *18* (10), 3359–3366.
- (36) Munishkina, L. A.; Cooper, E. M.; Uversky, V. N.; Fink, A. L. *J. Mol. Recognit.* **2004**, *17* (5), 456–464.
- (37) Cabaleiro-Lago, C.; Szczepankiewicz, O.; Linse, S. *Langmuir* **2012**, *28* (3), 1852–1857.
- (38) Okada, A.; Sano, K.; Nagata, K.; Yasumasu, S.; Ohtsuka, J.; Yamamura, A.; Kubota, K.; Iuchi, I.; Tanokura, M. *J. Mol. Biol.* **2010**, *402* (5), 865–878.
- (39) Nedumpully-Govindan, P.; Ding, F. *Sci. Rep.* **2015**, *5*, 8240.
- (40) Ge, X.; Kakinen, A.; Gurzov, E. N.; Yang, W.; Pang, L.; Pilkington, E. H.; Govindan-Nedumpully, P.; Chen, P.; Separovic, F.; Davis, T. P.; et al. *Chem. Commun.* **2017**, *53* (68), 9394–9397.
- (41) Raleigh, D.; Zhang, X.; Hastoy, B.; Clark, A. J. *Mol. Endocrinol.* **2017**, *59* (3), R121–R140.
- (42) Sivanessam, K.; Shu, I.; Huggins, K. N.; Taterek-Nossol, M.; Kapurniotu, A.; Andersen, N. H. *FEBS Lett.* **2016**, *590* (16), 2575–2583.
- (43) Wijesekara, N.; Ahrens, R.; Wu, L.; Ha, K.; Liu, Y.; Wheeler, M.; Fraser, P. *Diabetes, Obes. Metab.* **2015**, *17* (10), 1003–1006.
- (44) Wang, H.; Abedini, A.; Ruzsicska, B.; Raleigh, D. P. *Biochemistry* **2014**, *53* (37), 5876–5884.
- (45) Potter, K. J.; Scrocchi, L. A.; Warnock, G. L.; Ao, Z.; Younker, M. A.; Rosenberg, L.; Lipsett, M.; Verchere, C. B.; Fraser, P. E. *Biochim. Biophys. Acta, Gen. Subj.* **2009**, *1790* (6), 566–574.
- (46) Scrocchi, L. A.; Chen, Y.; Waschuk, S.; Wang, F.; Cheung, S.; Darabie, A. A.; McLaurin, J.; Fraser, P. E. *J. Mol. Biol.* **2002**, *318* (3), 697–706.
- (47) Westermark, P.; Grimelius, L. *Acta Pathol. Microbiol. Scand., Sect. A* **1973**, *81* (3), 291–300.
- (48) Donnini, S.; Solito, R.; Cetti, E.; Corti, F.; Giachetti, A.; Carra, S.; Beltrame, M.; Cotelli, F.; Ziche, M. *FASEB J.* **2010**, *24* (7), 2385–2395.
- (49) Okada, A.; Sano, K.; Nagata, K.; Yasumasu, S.; Ohtsuka, J.; Yamamura, A.; Kubota, K.; Iuchi, I.; Tanokura, M. *J. Mol. Biol.* **2010**, *402* (5), 865–878.
- (50) Xia, T.; Zhao, Y.; Sager, T.; George, S.; Pokhrel, S.; Li, N.; Schoenfeld, D.; Meng, H.; Lin, S.; Wang, X.; Wang, M.; Ji, Z.; Zink, J. I.; Mädler, L.; Castranova, V.; Lin, S.; Nel, A. E. *ACS Nano* **2011**, *5* (2), 1223–1235.
- (51) Huang, S. M.; Xu, F.; Lam, S. H.; Gong, Z.; Ong, C. N. *Mol. Biosyst.* **2013**, *9* (6), 1372–1380.
- (52) Lin, S.; Zhao, Y.; Ji, Z.; Ear, J.; Chang, C. H.; Zhang, H.; Lowkam, C.; Yamada, K.; Meng, H.; Wang, X.; et al. *Small* **2013**, *9* (9–10), 1776–1785.
- (53) Lee, J.; Bhak, G.; Lee, J. H.; Park, W.; Lee, M.; Lee, D.; Jeon, N. L.; Jeong, D. H.; Char, K.; Paik, S. R. *Angew. Chem., Int. Ed.* **2015**, *54* (15), 4571–4576.
- (54) Amit, M.; Yuran, S.; Gazit, E.; Reches, M.; Ashkenasy, N. *Adv. Mater.* **2018**, 1707083.
- (55) Gao, N.; Sun, H.; Dong, K.; Ren, J.; Duan, T.; Xu, C.; Qu, X. *Nat. Commun.* **2014**, *5*, 3422.
- (56) Geng, J.; Li, M.; Ren, J.; Wang, E.; Qu, X. *Angew. Chem., Int. Ed.* **2011**, *50* (18), 4184–4188.
- (57) Li, M.; Yang, X.; Ren, J.; Qu, K.; Qu, X. *Adv. Mater.* **2012**, *24* (13), 1722–1728.

In vivo mitigation of amyloidogenesis through functional-pathogenic double protein coronae

*Ibrahim Javed,[†] Tianyu Yu,[§] Guotao Peng,[§] Antoni Sánchez-Ferrer,[‡] Ava Faridi,[†] Aleksandr Kakinen,[†]
Mei Zhao,[§] Raffaele Mezzenga,[‡] Thomas P. Davis,^{*,†} Sijie Lin^{*,§} and Pu Chun Ke^{*,†}*

[†]ARC Centre of Excellence in Convergent Bio-Nano Science and Technology, Monash Institute of
Pharmaceutical Sciences, Monash University, 381 Royal Parade, Parkville, VIC 3052, Australia

[§]Biomedical Multidisciplinary Innovation Research Institute, Shanghai East Hospital, State Key
Laboratory of Pollution Control and Resource Reuse, Shanghai Institute of Pollution Control and
Ecological Security, College of Environmental Science and Engineering, Tongji University, 1239
Siping Road, Shanghai 200092, China

[‡]Department of Health Sciences & Technology, ETH Zurich, Schmelzbergstrasse 9, LFO, E23, 8092,
Zurich, Switzerland

Email: lin.sijie@tongji.edu.cn; thomas.p.davis@monash.edu; pu-chun.ke@monash.edu

Phone: +86-21-65982325; +61-03-99039260; +61-03-99039267

MATERIALS & METHODS

Syntheses of b_a CNT and b_m CNT

β -lactoglobulin (bLg) amyloids were first prepared by overnight heating of bLg (Sigma-Aldrich, MW: 18.4 kDa) solution (2%) at 80 °C and pH 2, and then probe-sonicated at 40% of full intensity (20 kHz, 750 W) for 2 h to obtain bLg amyloid fragments (b_a). Aqueous dispersion of multi-walled carbon nanotubes (Nanostructured & Amorphous Materials, Inc.; purity 95+ %; outer diameter: 10-20 nm; length: 0.5-2 μ m) at a concentration of 0.2 mg/mL were first probe-sonicated at 20% of full intensity for 10 min. b_a (0.2%) was added into CNTs immediately after

sonication, and the dispersion was adjusted to pH 4.3 and further sonicated for 30 min (ice bath for 4 °C) to obtain b_sCNT. The dispersion was then centrifuged (9,200 RCF; 30 min; 4 °C) to separate large aggregates, and the supernatant was adjusted to pH 4.3 and subjected to heating at 70 °C for 20 min to obtain b_aCNT. In addition, b_mCNT was synthesized by the same procedures, except replacing b_a with monomeric bLg.

Thioflavin T (ThT) assay

A ThT kinetic assay was used to monitor IAPP fibrillization in the presence of pristine and functionalized CNTs. 200 µg of human islet amyloid polypeptide (IAPP1-37; MW: 3904.5 Da; AnaSpec) was weighed on a microbalance and dissolved in 200 µL of deionized water to make a stock solution, which was used to make further dilutions for experiments. In a 96 well plate, 100 µL (50 µM) of IAPP, ThT dye (100 µM), and b_aCNT/b_mCNT (50 µM with respect to bLg) were incubated for 13 h at 28 °C. ThT fluorescence was monitored (excitation/emission: 440 nm/485 nm) at 1 h intervals (PerkinElmer EnSpire 2300). Controls were performed with IAPP alone, or with pristine CNTs and b_a at equivalent concentrations. ThT dye was incubated with pristine CNTs, b_aCNT/b_mCNT, bLg amyloids and b_a under comparable conditions, but without IAPP, as controls. The effect of human plasma proteins on b_aCNT inhibition of IAPP aggregation was measured by an additional ThT assay. The molar ratio of IAPP to plasma proteins was adjusted from 1:1 to 2:1 and 4:1. Details of the blood protein collection method are described in a previous publication.¹ Blood was collected from a healthy donor after obtaining informed consent for any experimentation in this study, in accordance with the University of Melbourne Human ethics approval 1443420 and the Australian National Health and Medical Research Council Statement on Ethical Conduct in Human Research. All experiments were performed in compliance with the relevant laws and institutional guidelines of Monash University Occupational Health & Safety.

FTIR, TGA, CD and DLS measurements

Fourier transformed infrared spectroscopy (FTIR) and thermogravimetric analysis (TGA) were performed with freeze-dried b_aCNT, IAPP, b_aCNT and IAPP incubated for 13 h at comparable concentrations as for the ThT assay. IAPP incubated with b_aCNT was purified from un-adsorbed IAPP by centrifugation. FTIR was performed with a Shimadzu IRtracer-100 with a GladiATR-10 accessory. Around 1 mg of sample was placed in the holder and FTIR spectra were recorded in the 1600-1700 cm⁻¹ amide I band. The peak was de-convoluted with LabSolutions IR and peak fitting was performed to quantify the percentage secondary structures. For TGA, 1 mg of sample was placed in the holder (PerkinElmer Pyris 1) and analysis was performed from 50 °C to 700 °C with a heating rate of 10 °C/min, under a continuous flow of nitrogen (1 mL/min). Circular dichroism (CD) spectroscopy was performed in addition to FTIR, to analyze the secondary structural changes in the corona of b_aCNT, before or after IAPP adsorption. IAPP, b_aCNT and IAPP incubated with b_aCNT were pipetted into CD cuvettes at a concentration of 0.5 mg/mL with respect to the protein contents and CD spectra were recorded from 190 to 240 nm with a 0.5 nm step size at room temperature. The data was analyzed via Dichroweb and Contin/reference set 4 was used to estimate the percentage secondary structures.² The zeta potential and hydrodynamic size of the samples were measured by dynamic light scattering (DLS) under ambient conditions (Malvern Instruments).

Small- and wide-angle X-ray scattering (SAXS, WAXS)

Simultaneous SAXS and WAXS experiments were performed using a Rigaku MicroMax-002⁺ microfocused beam (4 kW, 45 kV, 0.88 mA) to obtain direct information on the SAXS and WAXS reflections. The Cu K_α radiation ($\lambda_{\text{Cu K}\alpha} = 1.5418 \text{ \AA}$) was collimated by three pinhole (0.4, 0.3, and 0.8 mm) collimators. The scattered X-ray intensity was detected by a Fuji Film BASMS 2025 imaging plate system (15.2 × 15.2 cm², 50 μm resolution) and a two-dimensional Triton-200 X-ray detector (20 cm diameter, 200 μm resolution), for WAXS and SAXS regions,

respectively. An effective scattering vector range of $0.05 \text{ nm}^{-1} < q < 20 \text{ nm}^{-1}$ was obtained, where q is the scattering wave vector defined as $q = 4\pi \sin \theta / \lambda_{\text{Cu K}\alpha}$, with a scattering angle of 2θ .

X-ray photoelectron spectroscopy

The elemental composition of pristine CNTs was analyzed by X-ray photoelectron spectroscopy (XPS; ESCA LAB 220i-XL Thermo VG Scientific U.K.). XPS data files were processed using the application CasaXPS software (version 2.3.13). Mean values +/- deviations were calculated based on three measurements on different spots.

Zebrafish embryos as a toxicity model for screening amyloidogenesis

The AB wild-type zebrafish (*Danio rerio*) was maintained at $28 \pm 0.5 \text{ }^{\circ}\text{C}$ on a 14 h:10 h light/dark cycle in a fish breeding circulatory system (Haisheng, Shanghai, China). Embryos were produced by adult spawning triggered by first light in the morning. All experiments with zebrafish embryos were performed in Holtfreter's buffer³. Microinjections were performed at 5 nL each time, unless specified, under a 20 psi injection pressure by a pneumatic microinjection system (PV830 Pneumatic Picopump, WPI). First, imaging of ThT-tagged amyloids was performed in the green fluorescence protein (GFP) channel by a fluorescence microscope (EVOS FL Auto, Life Technologies). IAPP or A β ₄₂ (Human A β 1-42; MW: 4514.1 Da; AnaSpec) and bLg (50 μM) were fibrillized into amyloids in the absence and presence of ThT dye (50 μM). A drop of fibrillized amyloid solution was placed in a 96 well plate and visualized. ThT tagged amyloids were visible in the GFP channel, while no fluorescence was observed for ThT or amyloid alone. IAPP (100 μM , fibrillized with 100 μM of ThT) was injected (5 nL) inside embryos at 3 h post fertilization (hpf). The embryos were placed in 100 μL of Holtfreter's buffer inside a 96 well plate and their development was monitored for 3 consecutive days in bright field and the GFP channel. Control embryos were injected with 5 nL

of buffer or ThT dye (100 μ M) with a microinjector (PV830 Pneumatic Picopump, WPI). The experiment first involved immersion of embryos inside IAPP or A β solutions. Different concentrations of IAPP or A β (12.5 to 200 μ M) were dissolved in buffer and 200 μ L of each protein solution was placed in a 96 well plate. Embryos at 3 hpf with and without chorions were then immersed in the solutions. The chorionic membranes were removed under a microscope by tweezers inside buffer.

A ThT kinetic assay of IAPP fibrillization was performed in the presence of the embryos, with and without chorionic membranes, observed through the GFP channel (excitation/emission: 488/540 nm). 200 μ L of solution containing one embryo, 50 μ M of IAPP and 100 μ M of ThT was incubated at 28 °C and the fluorescence was recorded for 13 h at a 1 h interval. IAPP alone in buffer and ThT with embryos, with and without chorionic membranes, were measured as controls. For the ThT assay inside the embryos, 5 nL of IAPP (50 μ M) and ThT (100 μ M) were injected in the chorionic fluids, and ThT fluorescence was recorded with the EVOS microscope and analyzed by ImageJ for corrected fluorescence.

Amyloid toxicity mitigation in an embryonic zebrafish model

Minimum inhibitory concentrations (MIC) for IAPP and A β against zebrafish embryos were obtained by dissolving different concentrations of IAPP and A β (2 to 100 μ M) in buffer and 5 nL of the solution was injected inside the perivitelline space of 3 hpf embryos. For the sequestration experiment, 5 nL of buffer containing 10 or 15 μ M of IAPP or A β and CNTs of equivalent concentrations (with respect to b_a or b_m on the CNT surfaces) were injected inside the chorionic fluids. The treated embryos were placed in 200 μ L of buffer in a 96 well plate and toxicity mitigation was studied in the context of hatching survival of embryos on the 3rd day of fertilization. Embryos injected with 5 nL of buffer were used as controls. For imaging,

5 nL of buffer with 10 μ M of IAPP and 20 μ M of ThT dye was injected with and without b_aCNT and ThT fluorescence images were recorded with the EVOS fluorescence microscope.

Reactive oxygen species (ROS) generation

ROS generation assay was performed with 2',7'-dichlorodihydrofluorescein diacetate (H₂DCFDA) dye. 5 nL of buffer, containing 10 μ M of IAPP (with or without 10 μ M of b_aCNT or b_mCNT) and 20 μ M of H₂DFCDA dye was injected inside chorionic fluids of zebrafish embryos. The embryos were incubated in 200 μ L of buffer in a 96 well plate at 28 °C for 12 h. ROS generation was characterized by imaging the embryos in the GFP channel and images were analyzed in ImageJ for corrected total ROS fluorescence.

Helium ion microscopy (HIM) and transmission electron microscopy (TEM)

HIM was used to image the interaction of fibrillizing IAPP and zebrafish embryos. Embryos with chorionic membranes were incubated inside 100 and 25 μ M of IAPP monomers dissolved in buffer, at 28 °C. After 6 h of incubation, the buffer was replaced by 2.5 % paraformaldehyde to fix the embryos. The embryos were left in paraformaldehyde solution for 2 h under ambient conditions and then at 4 °C overnight. Afterwards, the embryos were transferred into ethanol by gradually replacing the paraformaldehyde solution with 20, 40, 60, 80 and 100 % ethanol, with 2 h incubation at room temperature for each step. Embryos preserved in 100 % ethanol were further subjected to critical point drying with liquid CO₂. Dried embryos were positioned on a carbon tape and imaged with HIM (Zeiss Orion NanoFab), operating at a 0.6 to 0.8 pA beam current and a 0.2 s dwell time. To image the interaction of IAPP with lipid membranes of embryonic cells, chorionic membranes of the embryos treated with 25 μ M of IAPP were ruptured with tweezers under an optical microscope, prior to HIM imaging.

TEM imaging of CNTs, b_aCNT, b_mCNT, and b_aCNT or b_mCNT with IAPP (24 h incubation) was performed by drying a drop of sample on formvar-coated copper grids and negative

staining was done with 1 % uranyl acetate. TEM images were captured by a Tecnai G2 F20 transmission electron microscope (FEI, Eindhoven, The Netherlands) operated at 200 kV.

Cell culture and in vitro viability assay

Pancreatic β TC-6 (ATCC) beta cells were cultured in complete Dulbecco's modified Eagle's medium (DMEM) with 15% fetal bovine serum (FBS). A 96 well plate (Costar black, clear bottom) was coated with 70 μ L Poly-L-lysine (Sigma, 0.01%), incubated at 37 °C for 30 min and cells at a density of \sim 70,000 cells per well in 200 μ L DMEM with 15% FBS were added to the wells. Cells were incubated for 48 h at 37 °C and 5% CO₂ to reach \sim 80% confluency. The cell culture medium was then refreshed with 1 μ M propidium iodide dye (PI, excitation/emission: 535 nm/617 nm) in DMEM and incubated for 30 min. Fresh IAPP, b_aCNT and IAPP in the presence of b_aCNT (20 μ M final concentration of each sample) were added into the wells. All samples were examined in triplicate and measured by Operetta (PerkinElmer) in a live cell chamber (37 °C, 5% CO₂) after 7 h of treatment. The percentage of dead cells (PI-positive) relative to total cell count was determined by a built-in bright-field mapping function of Harmony High-Content Imaging and Analysis software (PerkinElmer). The measurement was conducted at 5 reads per well and performed in triplicate. Untreated cells were recorded as controls.

Statistical analysis

The data was presented as mean \pm standard deviation. The experiments were performed in triplicate. The level of significance was determined by one-way ANOVA followed by Turkey's test and p value < 0.05 was considered as statistically significant. The group size was 20 embryos and three groups per sample were used for experiments.

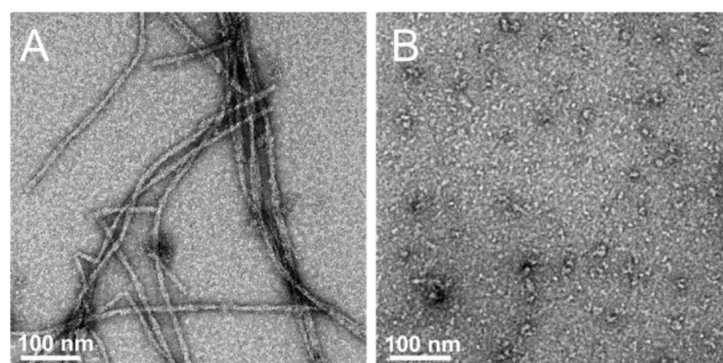


Figure S1. (A) bLg amyloids and (B) sonicated fragments of bLg amyloids.

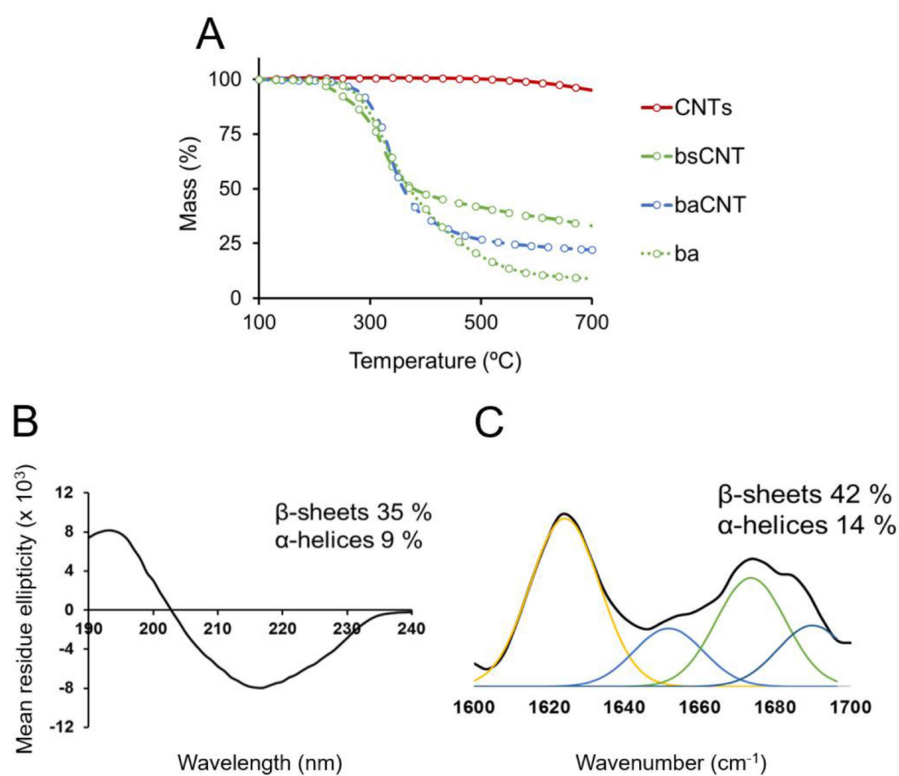


Figure S2. (A) TGA analysis of b_s CNT (CNTs coated with an initial thin layer of b_a via sonication) and b_a CNT (heating of b_s CNT to obtain a b_a corona on CNT), pristine CNTs and b_a as the controls. (B) CD spectroscopy and (C) FTIR amide I band deconvolution for the secondary structure of mature IAPP fibrils.

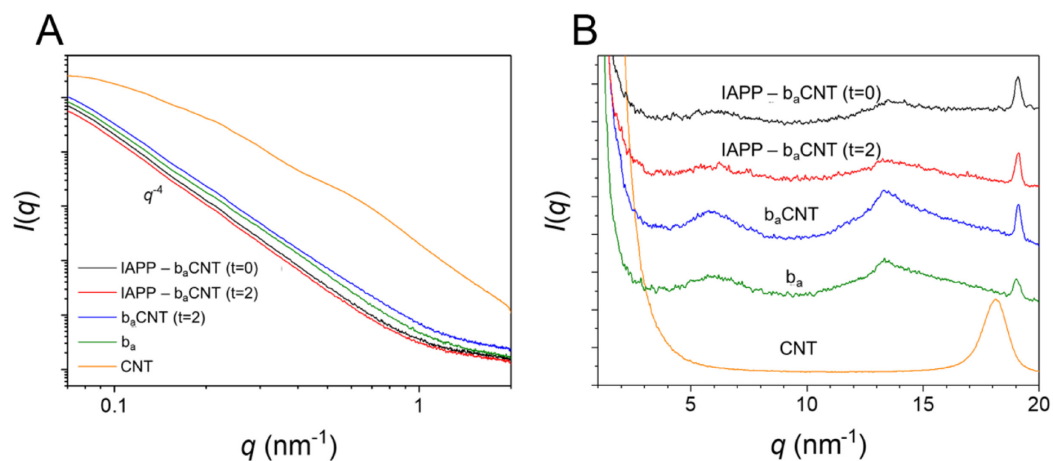


Figure S3. (A) The WAXS intensity profiles of IAPP- b_a CNT ($t=0$) (black), IAPP- b_a CNT ($t=2$) (red), b_a @CNTs (blue), b_a (green), and CNTs (orange). (B) The SAXS intensity profiles of IAPP- b_a CNT ($t=0$) (black), IAPP- b_a CNT ($t=2$) (red), b_a CNT (blue), b_a (green), and CNTs (orange). The presence of CNTs showed no effect on the β -sheet secondary structure.

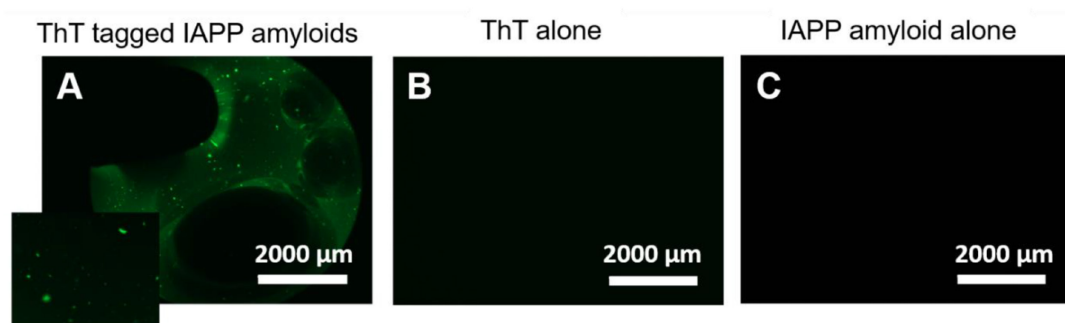


Figure S4. (A) ThT tagged IAPP amyloids (100 μM of ThT and IAPP; incubated for 24 h) were visible under the GFP channel, while ThT alone (B) or IAPP alone (C) were invisible.

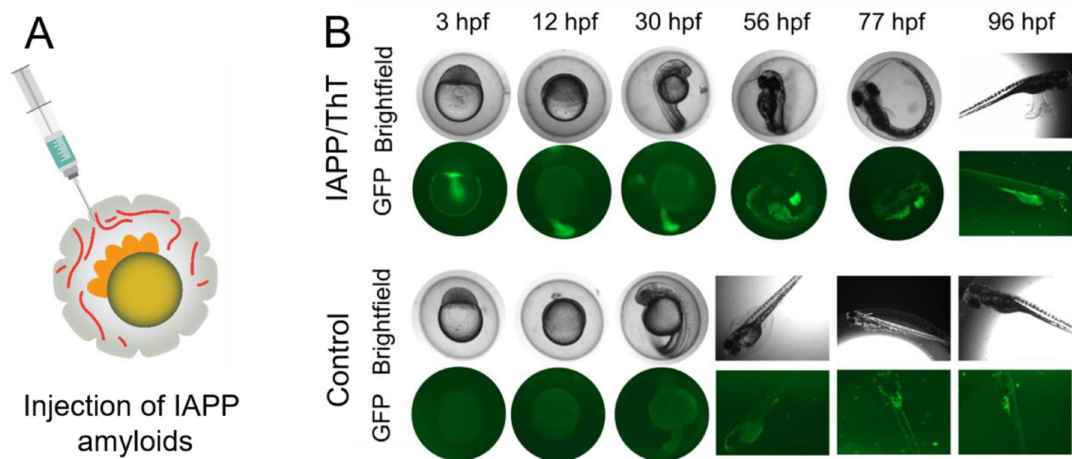


Figure S5. Toxicity of mature IAPP in zebrafish embryos. (A) Illustration of mature IAPP (100 μ M peptide, with 100 μ M of ThT dye) injected inside 3 hpf zebrafish embryos. (B) Controls of embryos injected with equal amounts of ThT presented no fluorescence. Hatching in IAPP amyloid treated embryos was significantly delayed compared to the control.

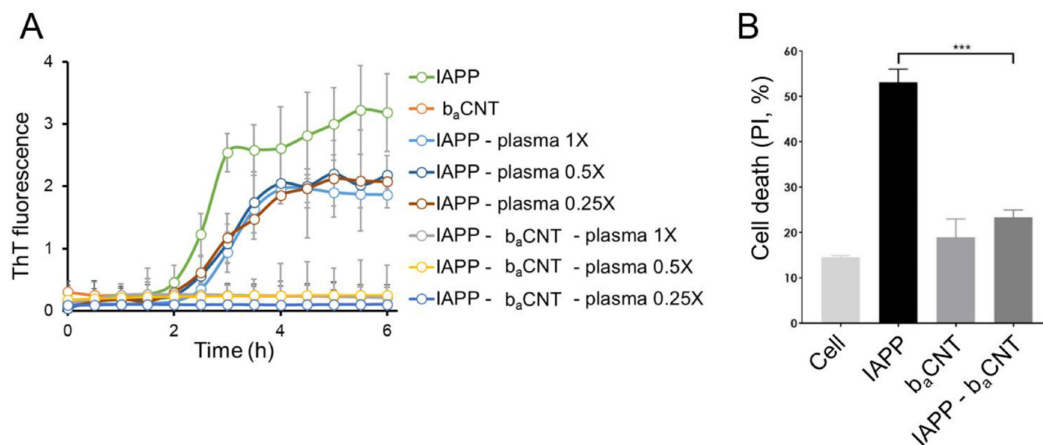


Figure S6. (A) ThT kinetic assay on b_aCNT inhibition of IAPP aggregation, in the presence of plasma proteins. IAPP/plasma protein molar ratio: 1:1, 2:1 and 4:1. IAPP concentration: 50 μ M. (B) β TC6 pancreatic beta cell mortality induced by IAPP, in the presence of b_aCNT. IAPP final concentration: 20 μ M. b_a/IAPP molar ratio: 1:1. Incubation: 7 h.

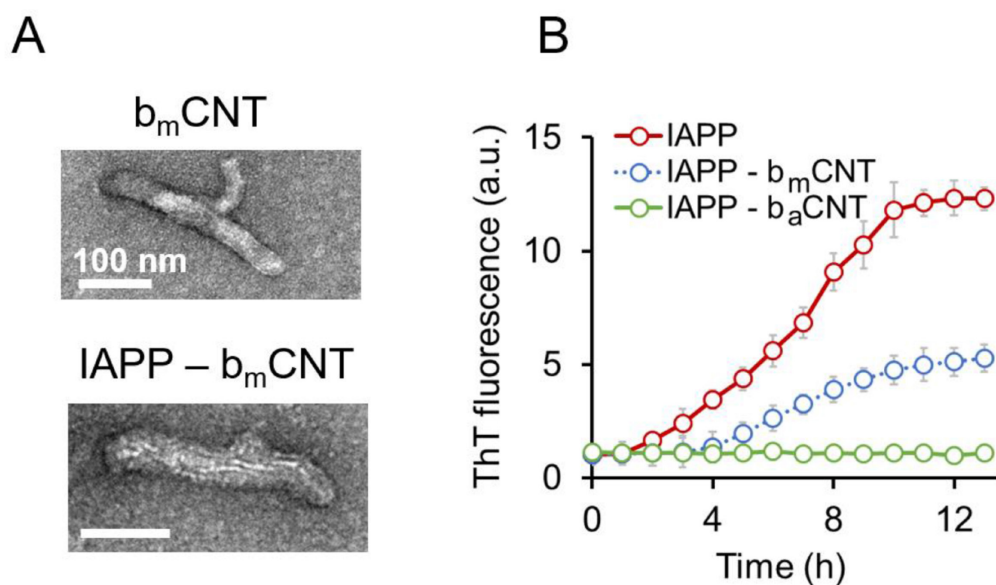


Figure S7. (A) TEM imaging of bLg monomer-coated CNTs (b_mCNT) and b_mCNT incubated with IAPP for 24 h. Scale bars: 100 nm. (B) ThT assay of IAPP fibrillization in the presence of b_mCNT vs. b_aCNT. IAPP: 50 μM. b_m: 50 μM. b_a: 50 μM.

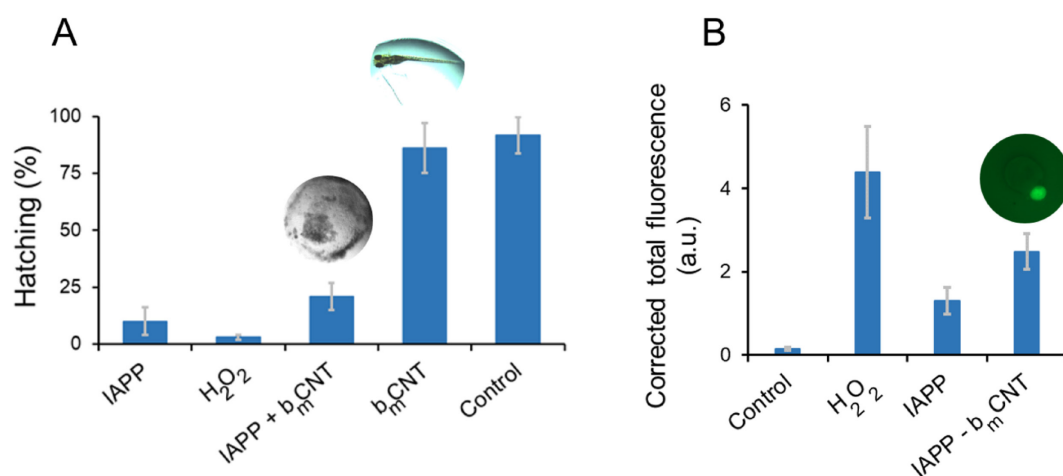


Figure S8. (A) IAPP and b_mCNT were injected inside zebrafish embryos and no significant mitigation of IAPP toxicity was observed in terms of hatching survival of embryos on the 3rd day post fertilization (72 hpf). (B) No significant reduction of IAPP-elicited ROS production was observed with b_mCNT after 12 h of incubation. IAPP: 10 μM. b_m: 10 μM.

Table S1. Zeta potential and hydrodynamic size of b_s@CNT before and after IAPP incubation.

Sample	Hydrodynamic diameter (nm)	Zeta potential (mV)
b _s CNT	165.8 ± 13.4	-11.8 ± 3.2
b _a CNT	184.1 ± 15.2	-18.4 ± 2.4
IAPP + b _a CNT	516.1 ± 53.9	-12.5 ± 2.1
IAPP monomer	46.1 ± 5.3	15.8 ± 4.2
IAPP amyloid	568.9 ± 87.3	65.3 ± 3.6
b _a	11.5 ± 2.1	-9.5 ± 1.8
Pristine CNTs	3236 ± 438.2	-15.1 ± 2.2

*Subscripts: s - sonication, and a - amyloid fragments.

References

- (1) Wang, M.; Siddiqui, G.; Gustafsson, O. J.; Käkinen, A.; Javed, I.; Voelcker, N. H.; Creek, D. J.; Ke, P. C.; Davis, T. P. *Small* **2017**, 13, (36), 1701528.
- (2) Whitmore, L.; Wallace, B. A. *Biopolymers* **2008**, 89, (5), 392-400.
- (3) Lin, S.; Zhao, Y.; Xia, T.; Meng, H.; Ji, Z.; Liu, R.; George, S.; Xiong, S.; Wang, X.; Zhang, H. *ACS Nano* **2011**, 5, (9), 7284-7295.

Chapter 4

Inhibition of amyloid beta toxicity in zebrafish with a chaperone-gold nanoparticle dual strategy

Declaration

This chapter was published as Ibrahim Javed, Guotao Peng, Yanting Xing, Tianyu Yu, Mei Zhao, Aleksandr Kakinin, Ava Faridi, Clare L. Parish, Feng Ding, Thomas P. Davis, Pu Chun Ke and Sijie Lin, Inhibition of amyloid beta toxicity in zebrafish with a chaperone-gold nanoparticle dual strategy. *Nat. Comm.* 2019. 10(1): 3780.

Rationale



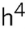



After studying the interplay between bLg amyloid-fragments and IAPP in the previous two chapters, this chapter was designed to study the *in vivo* mitigation of A β -induced neurotoxicity with biomimetic AuNPs. The compositional protein of the corona was changed from bLg to β -Casein (β Cas). β Cas forms amyloid under similar conditions to bLg. However, in native monomeric state, β Cas possesses an unfolded and melted conformation. This structure bestows β Cas with a chaperone-like capacity, which was expected to be particularly suitable for inhibiting the self-assembly of amyloid proteins IAPP, A β and α S. Accordingly, in this chapter, β Cas in its native monomeric form was employed to exploit its chaperone-like activity against A β fibrillization. The chaperone-like activity of β Cas was coupled with the blood-brain-barrier translocation capacity of AuNPs to mitigate A β -induced Alzheimer's-like symptoms in both larval and adult zebrafish. Larval and adult zebrafish were developed and characterised as facile and high-throughput *in vivo* model system to study A β -induced neurotoxicity. This, again, fulfilled the crucial need for establishing facile, high-throughput, alternative *in vivo* models to mouse models for evaluating amyloid diseases and anti-amyloidosis nanomedicines.

ARTICLE

<https://doi.org/10.1038/s41467-019-11762-0>

OPEN

Inhibition of amyloid beta toxicity in zebrafish with a chaperone-gold nanoparticle dual strategy

Ibrahim Javed ^{1,2}, Guotao Peng ², Yanting Xing³, Tianyu Yu², Mei Zhao², Aleksandr Kakinen¹, Ava Faridi¹, Clare L. Parish⁴, Feng Ding ³, Thomas P. Davis ^{1,5}, Pu Chun Ke ¹ & Sijie Lin ²

Alzheimer's disease (AD) is the most prevalent form of neurodegenerative disorders, yet no major breakthroughs have been made in AD human trials and the disease remains a paramount challenge and a stigma in medicine. Here we eliminate the toxicity of amyloid beta ($A\beta$) in a facile, high-throughput zebrafish (*Danio rerio*) model using casein coated-gold nanoparticles (β Cas AuNPs). β Cas AuNPs in systemic circulation translocate across the blood brain barrier of zebrafish larvae and sequester intracerebral $A\beta_{42}$ and its elicited toxicity in a nonspecific, chaperone-like manner. This is evidenced by behavioral pathology, reactive oxygen species and neuronal dysfunction biomarkers assays, complemented by brain histology and inductively coupled plasma-mass spectroscopy. We further demonstrate the capacity of β Cas AuNPs in recovering the mobility and cognitive function of adult zebrafish exposed to $A\beta$. This potent, safe-to-use, and easy-to-apply nanomedicine may find broad use for eradicating toxic amyloid proteins implicated in a range of human diseases.

¹ARC Centre of Excellence in Convergent Bio-Nano Science and Technology, Monash Institute of Pharmaceutical Sciences, Monash University, 381 Royal Parade, Parkville, VIC 3052, Australia. ²College of Environmental Science and Engineering, Biomedical Multidisciplinary Innovation Research Institute, Shanghai East Hospital, Shanghai Institute of Pollution Control and Ecological Security, Key Laboratory of Yangtze River Water Environment, Tongji University, 1239 Siping Road, Shanghai 200092, China. ³Department of Physics and Astronomy, Clemson University, Clemson, SC 29634, USA. ⁴The Florey Institute of Neuroscience and Mental Health, The University of Melbourne, 30 Royal Parade, Parkville, VIC 3052, Australia. ⁵Australian Institute for Bioengineering and Nanotechnology, The University of Queensland, Brisbane, Qld 4072, Australia. Correspondence and requests for materials should be addressed to F.D. (email: fding@clemson.edu) or to T.P.D. (email: thomas.p.davis@monash.edu) or to P.C.K. (email: pu-chun.ke@monash.edu) or to S.L. (email: lin.sijie@tongji.edu.cn)

The aggregation of proteins into amyloid fibrils and plaques, under abnormal physiological conditions, is a phenomenon common to a range of human amyloid diseases including amyloid beta (A β) for Alzheimer's disease (AD), α -synuclein for Parkinson's disease (PD), and human islet amyloid polypeptide for type 2 diabetes (T2D)¹. The amyloid hypothesis regards oligomers as the most toxic species², where protofibrils or oligomers of amyloid proteins are proposed to induce local inflammation, failed autophagy, and membrane perturbation that are responsible for the further loss of neuronal or pancreatic β -cells mass^{3,4}.

AD is a primary form chronic neurodegenerative disorder and a major cause of dementia, impairing 46 million people worldwide⁵. The pathological origin of AD is highly debatable, but is believed to be associated with a range of health, genetics, environmental and lifestyle factors, as well as inflammation^{6–9}. The etiology of AD includes a number of events that precede A β plaque formation, such as autophagy or endosomal dysfunction¹⁰, endoplasmic reticulum stress¹¹, oxidative stress or hypoxia, vasculature and mitochondrial dysfunction¹², and prior history of bacterial infections¹³. A β ₄₂ is one of the two most abundant peptide species derived from amyloid precursor protein (APP) through proteolysis and, alongside tau, is strongly associated with the pathology of AD¹⁴. Despite much research over the past decades devoted to understanding the origin, diagnosis and prevention of AD, there is a glaring lack of success against A β amyloidosis marked by recent withdrawals of clinical trials with Eli Lilly, Pfizer, and Biogen^{15–17}. This indicates failures in current anti-amyloid therapeutic approaches, compounded by a lack of suitable in vivo models for high throughput screening^{18,19}, further justifying the urgency for developing alternative strategies against AD.

Among the common strategies against amyloidosis, peptides, small molecules, monoclonal antibodies and, more recently, engineered nanoparticles, have shown various degrees of promise as inhibitors^{20–27}. For in vivo applications, these inhibitors are designed to satisfy—partially or fully—the following criteria: minimal toxicity, good circulation/repeated dosing, good translocation efficacy across the blood brain barrier (BBB), as well as capabilities in targeting and further eliminating toxic oligomers, protofibrils, and fibrils of amyloid proteins. β casein (β Cas), a whey protein, along with α _{s1} casein, possesses a chaperone-like activity, similarly to small heat-shock proteins and extracellular clusterin. This activity of the caseins arises from the following: (1) a lack of tertiary structure and solvent-exposed hydrophobicity with well separated hydrophilic regions, (2) existence as heterogeneous oligomers, (3) dynamics and malleable protein regions, and (4) ability to bind with a wide range of partially folded proteins preventing their aggregation²⁸. One factor that attributes to these properties is the presence of a high percentage of proline residues, i.e., 18% in the case of β Cas, and no disulfide bonds that provide them with an open and flexible conformation²⁹. The chaperone-like behavior of β Cas and α _{s1} caseins shields the amyloidogenic regions and naturally prevents the amyloidosis of α _{s2} and κ -casein in mammary glands or milk while inhibiting the amyloidosis of insulin and A β ₄₀ in vitro^{30–32}. Structurally, monomeric caseins are mostly disordered, but tend to form micelles mediated by hydrophobic and electrostatic interactions²⁸.

Here, we devise a facile method of coating β Cas onto gold nanoparticles (AuNPs). We systemically deliver the β Cas AuNPs via intracardial administration to mitigate the toxicity of A β ₄₂ induced in the brain of zebrafish larvae and adults (*Danio rerio*). β Cas AuNPs sequester toxic A β ₄₂ in the brain of zebrafish larvae and adults through a nonspecific, chaperone-like manner. No such mitigation is obtained with caseins alone, indicating the

essential role of the AuNPs in delivering the protein. This demonstrates the inhibition potential of a chaperone protein integrated with a biocompatible nanomaterial against Alzheimer's-like symptoms. The established zebrafish model also opens the door to economically viable, high-throughput in vivo screening of emerging nanomedicines targeting a wide range of amyloid diseases.

Results and discussion

Scheme of study. Different fractions of caseins, e.g., α _{s1} and β , have a known potential for surface-assisted sequestration and colloidal inhibition of A β ₄₀ and insulin amyloid formation^{31,32}. Herein, β Cas with an intrinsic chaperone-like activity³³ was coated on AuNPs by NaBH₄-assisted reduction of Au. Synthesis of the β Cas AuNPs was optimized at room temperature to obtain ~5 nm in size for efficient BBB translocation while preserving the random coil structure of β Cas that is required for its chaperone activity³⁰. β Cas AuNPs were then characterized for their inhibitory activity against A β ₄₂ (abbreviated as A β from hereon) fibrillization in vitro. For in vivo translation, an A β toxicity model was developed in zebrafish larvae by cerebroventricular injection of A β . The biodistribution and translocation of β Cas AuNPs across the larval zebrafish BBB were then determined after introducing the nanoparticles into the bloodstream via intracardiac injection. Finally, A β and β Cas AuNPs were co-administered via cerebroventricular and intracardiac injections into zebrafish larvae, and alleviations of A β -induced behavioral symptoms were quantified. In addition, A β -induced behavioral pathology and cognitive dysfunction in adult zebrafish were rescued by β Cas AuNPs, further implicating the chaperone potential of β Cas AuNPs against A β toxicity in vivo.

In vitro interaction of β Cas AuNPs and A β . A β was fibrillized in vitro from random coils to β -sheet rich amyloid fibrils within 48 h at 37 °C. A thioflavin T (ThT) assay was used to study the fibrillization kinetics (Fig. 1a), while transmission electron microscopy (TEM) (Fig. 1b) and circular dichroism (CD) spectroscopy were employed to investigate fibril formation and secondary structural transitions of A β (Fig. 1c, d). β Cas AuNPs (Fig. 1e) often clustered together after binding with A β (Fig. 1f) and prevented β -sheet formation of the peptide (Fig. 1a). The presence of A β coronae on β Cas AuNPs was evident from TEM imaging (Fig. 1f inset). The secondary structure of β Cas AuNPs was predominantly random coils that transitioned into α helices in A β - β Cas AuNPs complex (Fig. 1g, d). β Cas formed micelles of ~100 nm in size in the aqueous medium (Fig. 1h). Upon incubation with A β , β Cas (in the absence of the AuNPs) induced an early onset of fibrillization as revealed by the ThT assay (Fig. 1a), which can be attributed to the fast nucleation of A β promoted by β Cas micelles in vicinity³⁴. However, A β fibrillization was not inhibited and random aggregates of the peptide were observed under TEM (Fig. 1i). CD spectroscopy indicated that the α -helix rich structure of β Cas was converted to β -sheets in β Cas + A β aggregates due to A β fibrillization (Fig. 1j, d). The hydrodynamic diameters of β Cas AuNPs and β Cas were increased from 7.5 ± 2.6 and 156.3 ± 34.4 nm to 39.3 ± 5.4 and 496.1 ± 114 nm ($n = 3$), respectively (Fig. 1k and Supplementary Table 1). The zeta potential of β Cas AuNPs was markedly elevated from -11.7 ± 1.8 to -33.7 ± 2.1 mV ($n = 3$), indicating adsorption of anionic A β onto the surfaces of β Cas AuNPs (Supplementary Table 1). Clusterization of β Cas AuNPs was confirmed by hyperspectral imaging (HSI), where the surface plasmon resonance (SPR) of β Cas AuNPs was red shifted from 490 ± 21 to 601 ± 24 nm ($n = 3$) upon aggregation and light illumination (Supplementary Fig. 1A–C). As oligomers/protofibrils are the main toxic species

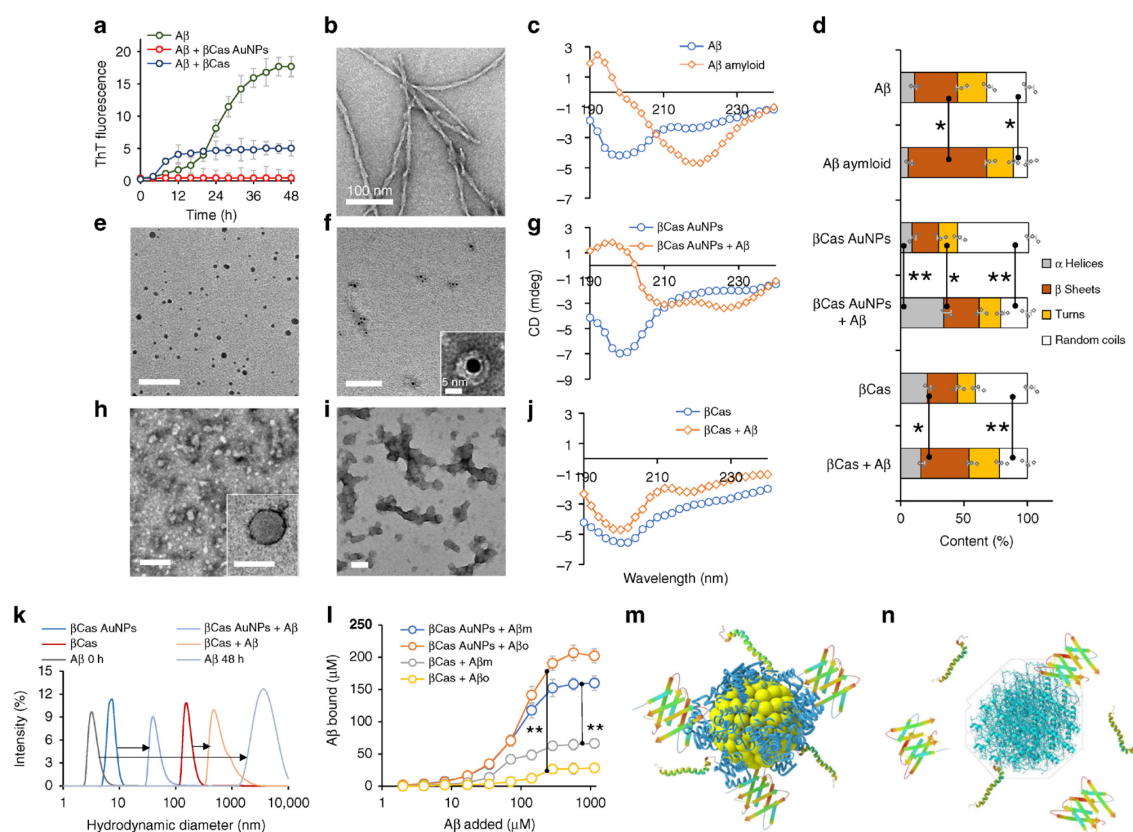


Fig. 1 In vitro inhibitory interactions between β Cas AuNPs and β Cas with A β . **a** ThT assay of A β alone (50 μ M) and in the presence of β Cas AuNPs (equivalent to 6.25 μ M of β Cas) and β Cas (6.25 μ M) ($n = 4$). β Cas AuNPs completely inhibited while β Cas decreased ($p < 0.005$) the lag time and plateau ThT fluorescence of A β fibrillization. **b** TEM image of fibrillized A β . **c** CD spectra of A β (100 μ M) before and after fibrillization indicate conformation change from random coils (198 nm peak) to β -sheets (220 nm peak). **d** Secondary structure of A β (100 μ M) fibrillized with and without β Cas AuNPs or β Cas ($n = 4$). TEM images of β Cas AuNPs before (**e**) and after incubation with A β (**f**; inset shows A β corona on a β Cas AuNP). **g** CD spectra of β Cas AuNPs before and after incubation with A β . TEM images of β Cas before (**h**) and after (**i**) incubation with A β . **j** Appearance of a negative peak at 218 nm in CD spectra of β Cas + A β indicates limited A β fibrillization into β -sheets. After binding with A β , the α -helix contents of β Cas AuNPs were decreased significantly ($p < 0.05$) from 56 to 21%; while in the case of β Cas, α -helices decreased from 41 to 22% ($p < 0.005$) and β -sheets increased from 24 to 38% ($p < 0.05$). **k** Hydrodynamic radius of A β before and after fibrillization in the presence and absence of β Cas AuNPs or β Cas. **l** Quantification of binding capacity of β Cas AuNPs or β Cas with A β m or A β o ($n = 4$). β Cas AuNPs (6.25 μ M β Cas equivalent) were able to bind up to 152.3 ± 13.4 and 190.7 ± 10.9 μ M of A β m and A β o. β Cas (6.25 μ M) was only able to adsorb 62.4 ± 3.4 and 26.4 ± 4.6 μ M of A β m and A β o, indicating a significant ($p < 0.005$) increase in A β binding capacity of β Cas in the form of β Cas AuNPs. **m**, **n** Enhanced binding of A β m and A β o with β Cas promoted by the AuNP substrate. Scale bars in TEM images is 100 nm, while F inset is 5 nm. Error bars represent the standard deviation. Source data are provided as a Source Data file

of amyloid proteins¹⁴, interactions of β Cas AuNPs with A β monomers (A β m) and A β oligomers (A β o) were also examined. The in vitro binding between A β o/m and β Cas or β Cas AuNPs was further quantified by a bicinchoninic acid assay (BCA) and thermogravimetric analysis (TGA). β Cas or β Cas AuNPs were incubated with different concentrations of A β m or A β o for 48 h and centrifuged to remove free A β . The centrifuged pellets containing A β m or A β o bound to β Cas or β Cas AuNPs were subjected to analysis (Supplementary Fig. 1D). The maximum binding capacity between A β and β Cas (6.25 μ M) was quantified to be 62 and 26 μ M for A β m and A β o, respectively (Fig. 1l). However, when β Cas AuNPs (containing 6.25 μ M β Cas) were exposed to A β , the maximum binding capacity was increased to 152 and 190 μ M for A β m and A β o, respectively. Similar results were obtained with TGA, where no difference in the TGA curve was observed when the concentration of A β was increased beyond

0.3 and 0.06 mM for β Cas AuNPs and β Cas, respectively, suggesting binding saturations (Supplementary Fig. 1E). The differential binding of β Cas and β Cas AuNPs with A β m/o is illustrated in Fig. 1m, n.

The high affinity of β Cas AuNPs for A β o can be attributed to the ability of β Cas to bind with misfolded/molten globules of proteins²⁸. To further investigate the differential binding of β Cas AuNPs with A β o and A β m, we incubated β Cas AuNPs with preformed A β o and A β m for 3 h and separated them from unbound A β o/m via centrifugal washing. The UV-SPR spectra of β Cas AuNPs were significantly suppressed upon incubation with A β o as compared to A β m (Supplementary Fig. 2A). Similarly, the fluorescence of neutral red-conjugated AuNPs (NR- β Cas AuNPs) was suppressed when incubated with A β o (Supplementary Fig. 2B). This indicates increased adsorption of A β o than A β m by β Cas AuNPs, as further confirmed by TEM imaging of corona

formation on the nanoparticles (Supplementary Fig. 2C). Furthermore, CD results indicated similar secondary structural distributions of A β and A β - β Cas AuNPs complex. Thus, the α helices in A β - β Cas AuNPs complex can be attributed to the A β corona on β Cas AuNPs (Supplementary Fig. 2D, E). Incubation of β Cas AuNPs with A β m did not present any difference in the secondary structure of β Cas AuNPs. That, together with the UV-SPR, fluorescence and TEM results, confirmed the high affinity of β Cas AuNPs for A β .

DMD simulations of β Cas binding with AuNP and A β monomer/oligomer. To gain a molecular insight into the adsorption of β Cas onto an AuNP surface (i.e., the formation of a β Cas AuNP “corona”) and the inhibition mechanism of β Cas AuNPs against A β aggregation, discrete molecular dynamics (DMD) simulations—an accurate and rapid molecular dynamics algorithm widely used to study the structure and dynamics of large molecular systems^{35,36}—were performed (Fig. 2). The binding of a β Cas monomer with an AuNP (4 nm in diameter), an A β monomer and an A β oligomer were examined (Supplementary Methods), and the control simulations included an isolated β Cas, an A β monomer, and an A β oligomer. We first computed secondary structure contents from equilibrium simulations (e.g., radius of gyration in Supplementary Fig. 3A and number of hydrogen bond in Supplementary Fig. 5A indicated simulations reaching steady states) and used them to estimate the expected CD spectra for different molecular systems (Fig. 2b). The predicted CD spectra agreed well with the experimental results (Fig. 1c, g, j, d) in terms of secondary structural changes. As expected, β Cas was intrinsically disordered with unstructured coils as the dominant secondary structure. Upon binding the

AuNP, β Cas exhibited increased coil and decreased helix and sheet contents both in silico (Fig. 2b inset) and in vitro (Fig. 1g, j, d). Analysis identified several specific binding sites of β Cas for the AuNP, such as residues His65, Phe67, Lys122, Met124, and His159 (the upper panel in Fig. 2a). Based on clustering analysis of the structural ensemble from multiple independent DMD simulations (Supplementary Methods), representative binding structures of β Cas monomers with the AuNP were obtained (Supplementary Fig. 3B), where individual β Cas partially covered the AuNP. To form a monolayer protein corona, at least three β Cas molecules were required to fully coat the AuNP surface (Fig. 2c, estimated by covering the NP surface with randomly selected centroid structures from top ten clusters shown in Supplementary Fig. 3B). When β Cas bound to an A β monomer, the overall contents of ordered helices and sheets increased while coils decreased (Fig. 2b), in agreement with the experiments (Fig. 1c, j, d). Residues in β Cas that had strong binding with the A β monomer did not overlap with those preferred to bind the AuNP (Fig. 2a). This result suggests that β Cas AuNP could still bind to A β monomers, as illustrated by the β Cas-AuNP complex where A β -binding residues were exposed (Fig. 2c, with the protein surface color-coded according to their binding probabilities with the A β monomer). Although we did not perform simulations for the binding of A β with β Cas AuNP, due to the prohibitively large system, we expected similar trends of secondary structure changes as observed in the experiments (Fig. 1d). Representative structures of the binding complexes obtained from the simulations (Supplementary Fig. 4A) suggest that β Cas could bind A β and form either β sheets or helices (Supplementary Fig. 4B), which in turn inhibited A β aggregation by sequestering A β in solution or capping A β fibrils from elongation. Moreover, simulations of β Cas with a preformed cross- β A β oligomer

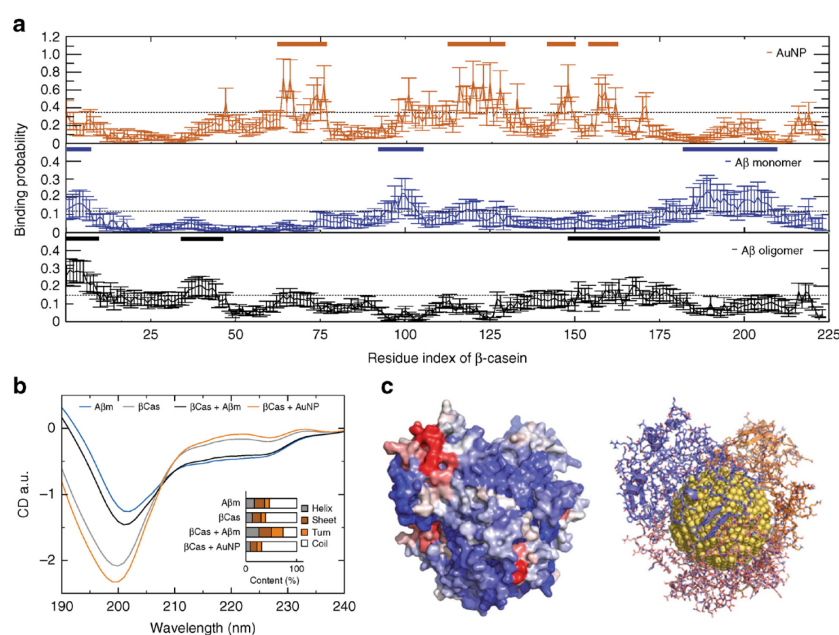


Fig. 2 DMD simulations of β Cas binding with AuNP, A β monomer, and oligomer. **a** Binding probabilities of β Cas with an AuNP, an A β monomer and an A β oligomer, where high-binding is defined as residues with binding probabilities above one standard deviation from the average (dash lines). β Cas high-binding residue regions with AuNP and with A β monomer/oligomer are highlighted with bars (inset). **b** Predicted CD spectra of secondary structure contents (inset) derived from simulations. **c** Predicted β Cas-AuNP corona structures comprised of three β Cas proteins on an AuNP surface (right) and corresponding molecular surfaces of the proteins (left) are shown to highlight their binding with an A β monomer, where each β Cas residue was colored from purple (low) to red (high) according to its binding probability with A β monomer as in panel A middle. Source data are provided as a Source Data file

indicate that the β Cas-AuNP complex could bind A β oligomer (Fig. 2a) and the strong binding between β Cas and A β oligomer (Supplementary Fig. 5D) inhibited further growth of the initial oligomer (i.e., inset of Supplementary Fig. 5E) into an extended β -sheet structure via conformational rearrangements. Taken together, our simulations were not only consistent with the ensemble measurements *in vitro*, but also uncovered the molecular mechanism for the formation of the β Cas AuNP complex and their inhibition of A β aggregation via either sequestering of A β monomers or capping of A β fibril elongation. In addition, the binding of A β with a bare AuNP is presented in Supplementary Fig. 6. Approximating the binding affinity and energy differences between the complex (β Cas + AuNP, A β + AuNP) and individual components (β Cas, A β) from DMD simulations (Fig. 2 and Supplementary Fig. 6) revealed that the binding of β Cas with the AuNP was significantly stronger than the binding of A β with the AuNP ($\Delta\Delta G \sim -194 \text{ kcal mol}^{-1}$) (Supplementary Table 2). Hence, replacement of β Cas corona with A β was energetically unfavorable.

Development of A β toxicity model in zebrafish larvae. Zebrafish larvae express human orthologues of A β , APP, and γ -secretase components (PSENEN³⁷, NCTN³⁸, APH1b³⁷) 24 h after hatching³⁹. Gene knockout or chemical inhibitors may create an imbalance among these protein components to result in neurological and behavioral abnormalities^{40,41}. Here, an A β toxicity model was developed using zebrafish larvae (5 days old) by injecting A β into the cerebroventricular space (Fig. 3a and Supplementary Fig. 7). *In vivo* oligomerization of A β into toxic oligomeric species induced pathological features in zebrafish larvae after 5 days of A β treatment (Fig. 3b). Different concentrations of A β were injected into the larvae and no lethality was observed even with the highest concentration of A β , at 1200 fM per larva. However, reduced locomotion of the larvae was notable in a concentration dependent manner, with nonresponsive mobility and a loss of balance at higher A β concentrations ($\geq 75 \text{ fM}$) (Fig. 3c). The nonresponsiveness of the larvae was recorded using tapping as a stimulus and loss of balance was observed as a tilt of the larvae from the normal horizontal axis to the imbalanced vertical axis (Supplementary Videos 1–3). The larvae injected with 10, 50, and 100 fM A β were characterized on an automated zebrafish behavior analysis system, to quantify total distance traveled and frequency of movement during the 1 h recording period. Observations were made on the third (Supplementary Fig. 8A) and fifth (Fig. 3d) day post treatment with A β . Significant reductions in both total distance traveled and frequency of movements were noted, in a concentration-dependent manner on the fifth day, in A β -treated larvae compared to untreated control. To visualize the presence of A β fibrils in the brain of the larvae, Congo red dye was injected in the cerebroventricular space of zebrafish larvae (Fig. 3e) on the third (Supplementary Fig. 8B) and fifth day post injection of A β (Fig. 3f). Significantly increased fluorescence was observed from the brain of the A β -injected larvae on the fifth day post injection. By comparison, Congo red dye was injected in untreated control and no fluorescence was observed (Fig. 3g). A β amyloid formation in the brain of zebrafish larvae was further confirmed by matrix assisted laser desorption/ionization (MALDI) analysis. Five days post injection with A β , the larvae heads were excised after euthanization, homogenized in phosphate-buffered saline (PBS) buffer and analyzed by MALDI. A peak corresponding to the molecular weight of A β was observed at 4538.1 m/z^{-1} (Fig. 3h). A β treated larvae were further fixed, cryo-sectioned and stained with Congo red. A β plaques were observed using the red fluorescence protein (RFP) channel

of a microscope (Fig. 3i). No red fluorescence was observed in untreated control (Fig. 3j).

Biodistribution of β Cas AuNPs in zebrafish larvae. The bio-distribution of β Cas AuNPs was characterized by conjugating the AuNPs with NR dye and injecting the AuNPs via the intracardiac route (Fig. 4a). Whole-mount imaging was performed under the RFP channel of a fluorescence microscope at 0.5, 6, and 12 h after injection in order to trace the biodistribution of NR- β Cas AuNPs in different regions of the larvae (Fig. 4b). No fluorescence was observed from the dorsal or lateral view of the larvae in the control (Supplementary Fig. 9). The zebrafish BBB is a double-layered membrane separating cerebral blood vessels from brain tissues. Alongside tight junctions, zebrafish BBB expresses occluding, claudins and p-glycoproteins and thus possesses a selectivity against xenobiotics^{42,43}. In the present study, upon intracardiac injection of NR- β Cas AuNPs into larvae, bright red fluorescence was observed from the brain after 0.5 h, indicating translocation of β Cas AuNPs across the BBB (Fig. 4c). At 6 h after injection, the fluorescence from the cerebral region was decreased while it was recorded in the liver. However, the fluorescence was diminished from the liver at 12 h. β Cas AuNPs were detectable by HSI and the SPR signals of the AuNPs were recorded from the brain sections of the larvae, prepared 0.5 h post injection of β Cas AuNPs (Fig. 4d). However, no AuNPs or SPR were detected from the brain of untreated control. Finally, inductively coupled plasma mass spectroscopy (ICP-MS) was performed to further quantify the presence of AuNPs in the brain. The larvae treated with intracardiac injection of β Cas AuNPs were euthanized at 0.5, 0.6, and 12 h and their heads were homogenized and quantified for Au in the brain and trunks. The concentration of Au was the highest in the brain at 0.5 h while decreased to the lowest level at 12 h (Fig. 4e). A correlation of AuNPs injected in the heart and delivered across the brain is shown in Fig. 4f. Injection of 1.5, 3, and 6 ng Au equivalent AuNPs via the heart delivered around 0.15, 0.45, and 0.5 ng of AuNPs to the brain, indicating that injection of $>3 \text{ ng}$ of AuNPs did not increase the delivery of AuNPs to the cerebral region. TEM images of microtome slices of the zebrafish larval brain also showed the presence of β Cas AuNPs in the intracellular space (Supplementary Fig. 10).

Apart from the brain, 5 nm β Cas AuNPs (conjugated with NR dye) also distributed to the fins and were imaged while circulating inside the microvasculature of zebrafish larvae (Supplementary Fig. 11). In contrast to β Cas AuNPs, NR-conjugated β Cas micelles (4.5 ng) were not able to translocate across the BBB and, instead, accumulated in the liver 6 and 12 h post injection (Supplementary Fig. 12) due to their larger sizes.

Mitigation of A β toxicity and pathological symptoms. Mitigation of A β toxicity was first assessed *in vitro* with SH-SY5Y neuronal cells. β Cas AuNPs were able to sequester A β toxicity against SH-SY5Y cells in the viability assay (Supplementary Fig. 13A). Helium ion microscopy (HIM) revealed morphological damage induced by A β to the SH-SY5Y cells and their recovery by β Cas AuNPs (Supplementary Fig. 13B, C). For *in vivo*, A β toxicity was induced in the zebrafish larvae by cerebroventricular injection of A β and was relieved by intracardiac injection of β Cas AuNPs. Specifically, β Cas AuNPs were administered at different time intervals post A β injection and the exposed larvae were studied for their behaviors 3 (Supplementary Fig. 14) and 5 days (Fig. 5a) post A β injection. β Cas AuNPs completely relieved the symptoms when treated within 2 h of A β injection, as indicated by the total distance traveled, movement frequency and trajectories during 1 h of observation. Administration of β Cas AuNPs, 6 h after A β treatment, partially alleviated the behavioral

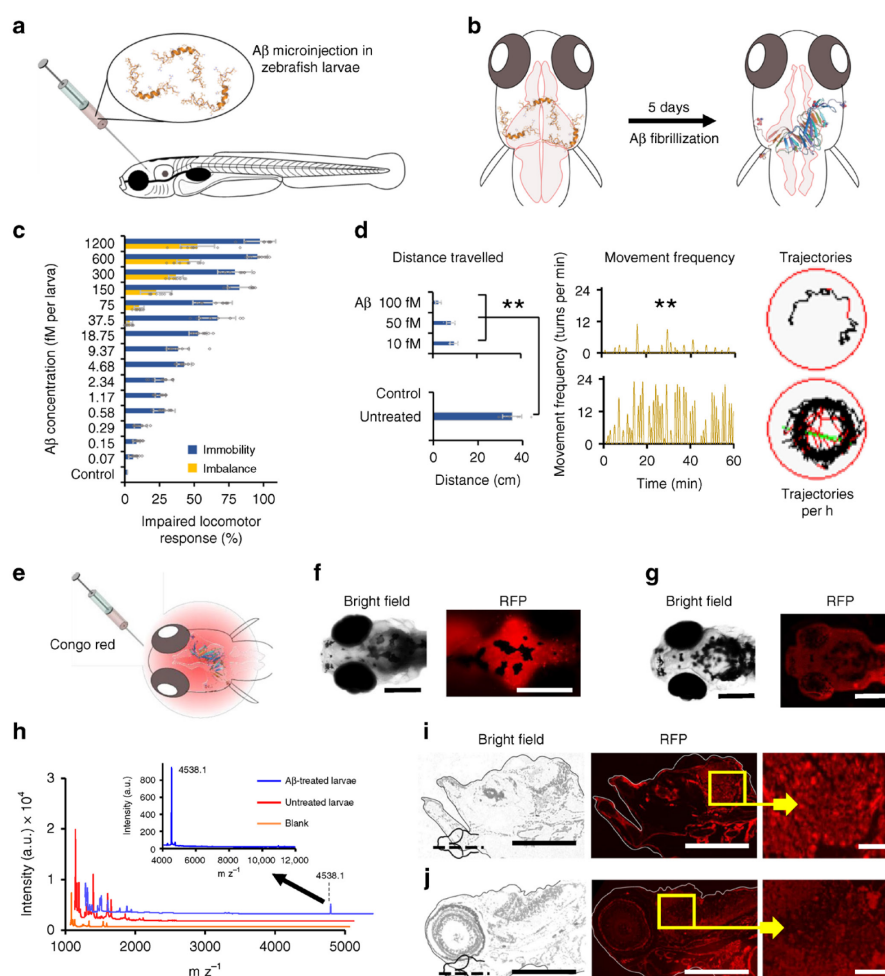


Fig. 3 Aβ toxicity in zebrafish (*Danio rerio*) larvae. **a** Five-day-old zebrafish larvae were treated with Aβ and developed pathological symptoms (**b**). **c** Disruptive locomotive behavior was recorded in terms of percentage of larvae who failed to respond upon tapping (blue bars) and unable to maintain horizontal swimming position (orange bars) ($n = 10$). **d** The behavior of the larvae was further recorded on an automated zebrafish behavior monitoring system for 1 h at 5 days post Aβ treatment ($n = 10$). Total distance traveled along with movement frequency was significantly decreased compared to untreated control ($p < 0.005$). Representative trajectories of 100 fM Aβ treated and untreated larvae inside a single well of a 96-well plate, during 1 h of observation. **e** Five days after Aβ (100 fM) treatment, larvae were further treated with Congo red (100 fM) via cerebroventricular injection. Whole mount larvae were imaged under the RFP channel 6 h after Aβ treatment. **f** Significant fluorescence was retained in the cerebral region of larvae on the fifth day post Aβ treatment. **g** Congo red injected in untreated larva was not retained in the cerebral region. **h** MALDI detection of Aβ in the brain of zebrafish larvae, 5 days post Aβ injection ($n = 10$, Mean \pm SD). Five days after cerebroventricular injection of Aβ, the heads of zebrafish larvae were excised after euthanization. The heads were homogenized in Holfreter's buffer and subjected to MALDI-TOF/TOF analysis. Peak corresponding to Aβ molecular weight was observed at 4538.1 mz^{-1} . Untreated larvae and matrix alone were used as controls. **i** Congo red-stained thin section (sagittal) of Aβ treated larvae brain tissue. Bright red spots were observed in the cerebral region of larvae, corresponding to the Aβ amyloid or plaque formation. **j** In thin sections of the brain tissue of untreated larvae (negative control), no red spots were observed. Scale bars in all images are 200 μm , while in **i** and **j** inset are 20 μm . Error bars represent the standard deviation. Source data are provided as a Source Data file

symptoms. However, treatment with βCas AuNPs 12 h after Aβ injection did not rescue the larvae from Aβ toxicity, indicating the neurotoxicity of Aβ had been initiated. This observation correlates with the nucleation and oligomerization of Aβ into toxic species around 12 h, as indicated by the ThT kinetic assay (Fig. 1a). In contrast, βCas micelles failed to rescue the larvae from Aβ toxicity even injected 2 h after Aβ administration. βCas AuNPs and βCas as controls did not induce any behavioral abnormalities in zebrafish larvae (Supplementary Fig. 15). In

addition, citrate-capped AuNPs failed to rescue the larvae from Aβ toxicity, implicating that βCas, but not AuNPs was mainly responsible for toxicity mitigation (Fig. 5a).

Microtome slices of the brain tissues of zebrafish larvae, treated with Aβ and βCas AuNPs, were prepared on the fifth day post Aβ treatment and stained with Congo red. No amyloid plaque formation was observed (Fig. 5b), indicating elimination of Aβ species by βCas AuNPs. Immunohistochemistry (IHC) (Fig. 5c) and polarized light microscopy (Fig. 5d) further confirmed

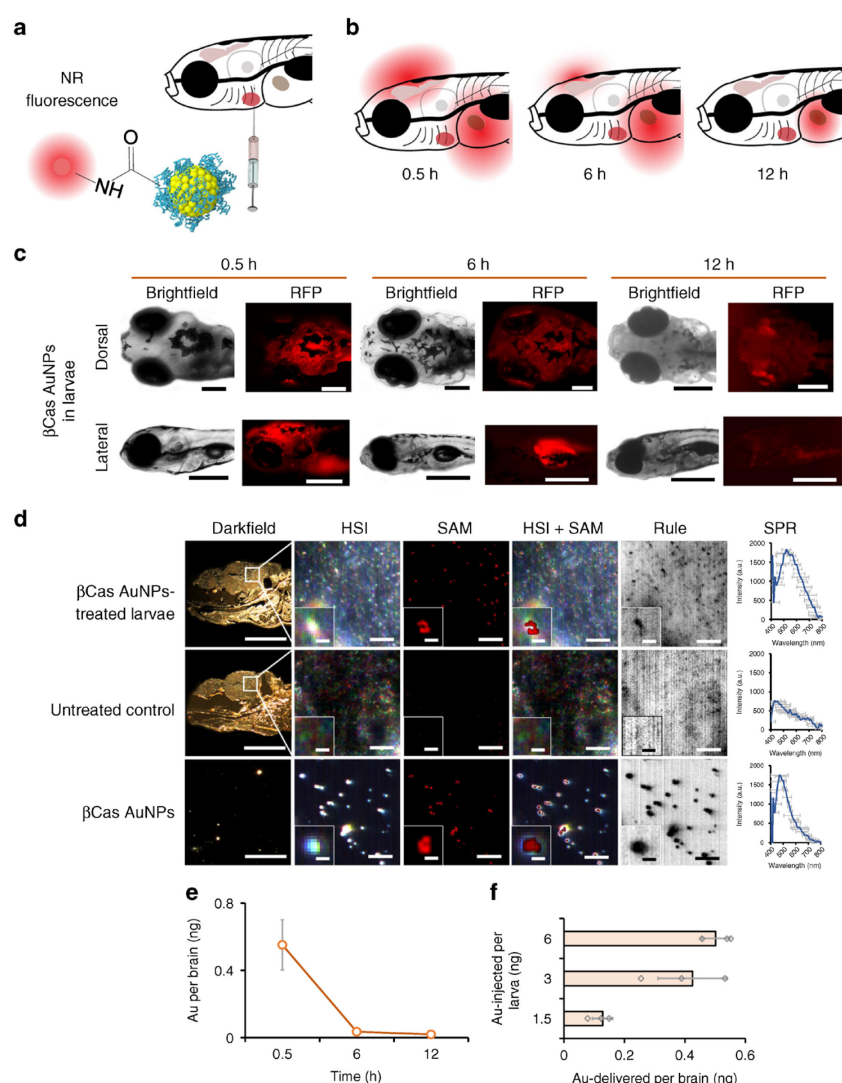


Fig. 4 In vivo biodistribution of β Cas AuNPs in zebrafish larvae. **a** β Cas AuNPs were conjugated with neutral red and injected to zebrafish larvae (5 day old) via the intracardiac route in a dose equivalent to 3 ng Au per 4.5 ng β Cas. **b** Labeled β Cas AuNPs were traced for in vivo distribution at 0.5, 6, and 12 h in dorsal and lateral positions (**c**). Bright fluorescence was observed from the brain 0.5 h after AuNP administration. However, fluorescence was eliminated from the cerebral region in 6 h, while it took 12 h to eliminate from the body (scale bars: 200 μ m). **d** Tissue microtome of zebrafish brain was subjected to HSI imaging. Spectral angular mapping (SAM) images were built from HSI by scanning against the β Cas AuNPs spectral library. SAM and Rule images colored the pixels as red and black, respectively, that have matching spectra of β Cas AuNPs. Zebrafish larvae with β Cas AuNPs in the brain presented black spots in Rule images and red pixels in SAM images. SPR spectra with peak ~530 nm were observed in the brain of β Cas AuNPs treated larvae. No such spectra were recorded for control larva (scale bars: darkfield 200 μ m; HSI, SAM, HSI + SAM, Rule: 10 μ m; inset scale bar: 2 μ m; scale bar for β Cas AuNPs: 10 μ m, inset scale bar: 0.5 μ m). **e** ICP MS analysis, where the AuNP concentration was the highest in the larval brain at 0.5 h, i.e., equivalent to 0.6 ± 0.1 ng of Au, and dropped to 0.05 ± 0.01 and 0.02 ± 0.008 ng at 6 and 12 h, respectively ($n = 10$). **f** Dose-response relationship between the amount of AuNPs injected vs. the amount of AuNPs delivered across the brain ($n = 10$). Significantly ($p < 0.05$) increased amount of Au was delivered when intracardiac dose of AuNPs was increased from 1.5 to 3 ng equivalent. However, increasing the dose from 3 to 6 ng did not improve AuNP delivery across the BBB, indicating a dose saturation. Error bars represent the standard deviation. Source data are provided as a Source Data file

deposition of A β amyloids in the brain tissues of zebrafish larvae, but not in β Cas AuNPs-treated or untreated control larvae. The positive controls of fibrillized A β analyzed by IHC and polarized light microscopy were shown in Supplementary Fig. 16.

In addition to the behavioral symptoms, the neurotransmitters associated with A β toxicity and reactive oxygen species (ROS)

were quantified and loss of synaptophysin was imaged (Fig. 6), to vindicate the potency of β Cas AuNPs against the toxicity of A β . Zebrafish are reported to possess cholinergic, glutamatergic and GABAergic neurotransmission that change in response to neurological dysfunction⁴⁴. The acetylcholine esterase (AChE) and glutamate (GLT) levels were therefore assayed in A β and

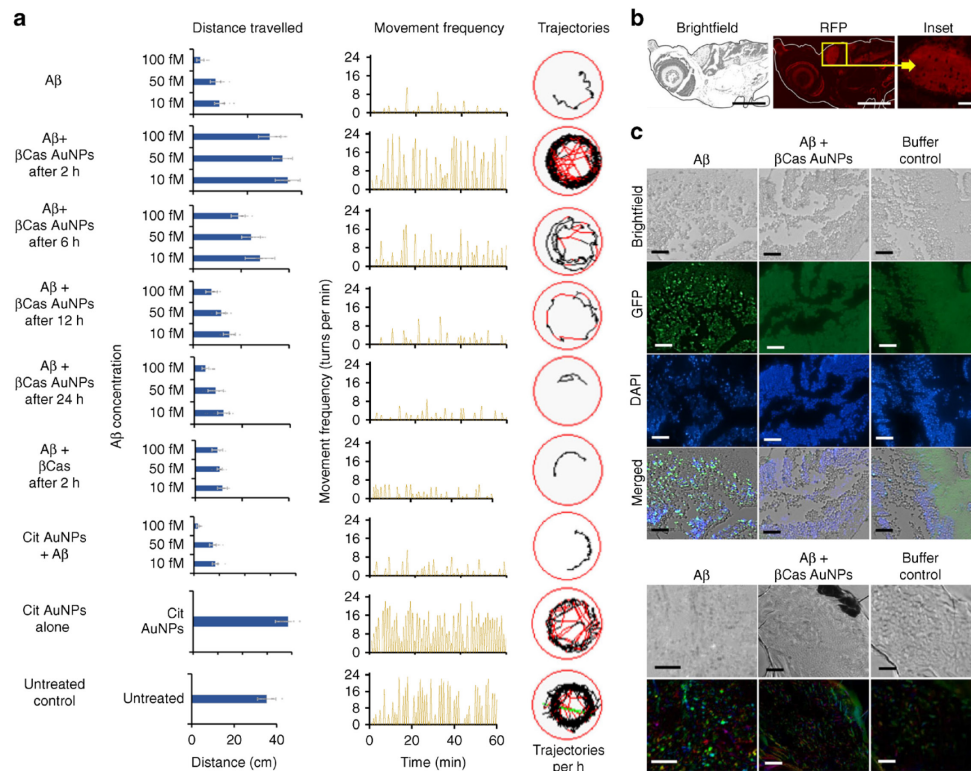


Fig. 5 Mitigation of A β toxicity in zebrafish larvae with β Cas AuNPs. **a** A β peptide was injected into the cerebroventricular space at 10, 50, and 100 fM concentrations ($n = 20$, mean \pm SD). Zebrafish larvae were monitored on an automated behavior monitoring system at fifth day post A β treatment and parameters of total distance traveled, movement frequency and trajectory path were observed for 1 h. Significant ($p < 0.005$) difference in the behavior of the larvae was observed on the fifth day post treatment. β Cas AuNPs injected, via the intracardiac route 2 and 6 h after the A β treatment, rescued the larvae from A β toxicity and from developing Alzheimer's-like symptoms. Representative trajectories of the larvae are displayed in the far-right column. Treating the larvae with β Cas AuNPs, 12 and 24 h post A β treatment, failed to protect the larvae from developing A β toxicity. **b** Zebrafish larvae, treated with β Cas AuNPs 2 h after A β treatment were fixed, sliced and stained with Congo red to image any A β fibrils that could have formed. Tissue slices of the brain section did not present any red fluorescence, indicating no A β fibril formation in β Cas AuNPs treated larvae (scale bars: 200 μ M; inset scale bar: 20 μ M). Furthermore, immunohistochemistry (IHC) (**c**) and polarized light microscopy (apple green birefringence of amyloid) (**d**) revealed deposition of aggregated A β in the larval brain while no A β deposition was observed in β Cas AuNPs or buffer treated larvae (Scale bars: IHC, 30 μ M; polarized light microscopy, 50 μ M). Error bars represent the standard deviation. Source data are provided as a Source Data file

A β + β Cas AuNPs treated larvae. The heads were separated from the euthanized larvae, homogenized and used for the assays to minimize interference from the trunks. The biomarkers were first evaluated on the fifth day post A β (6 fM per larva) treatment. AChE levels in the Alzheimer's affected brain are known to be decreased⁴⁵, however, here no significant differences in the AChE activity (0.10 ± 0.02 a.u. per brain) or GLT level (17.9 ± 1.2 nm per brain) were observed compared to untreated control (0.09 ± 0.01 a.u. for AChE and 19.7 ± 1.2 nm for GLT per brain) with 6 fM A β . As severe cases of Alzheimer's presence increased levels of AChE⁴⁶, the biomarker assay was performed with 600 fM A β and the AChE levels were found to increase twofold compared to the control, i.e., 0.22 ± 0.01 a.u. AChE per brain (Fig. 6a). AChE levels were close to the control in the larvae treated with β Cas AuNPs (3 ng Au equivalent) + A β (600 fM). β Cas AuNPs and β Cas, as controls, did not elicit any impact on the AChE levels. Similar results were observed for GLT, where β Cas AuNPs reduced the GLT level from 29.2 ± 5.08 to 18.1 ± 3.07 nm per brain (Fig. 6b). According to the literature, the A β_{42} concentration in the gray and white matter of the brain of AD patients is 1.3 and 0.25 nm mg^{-1} , respectively⁴⁷. Tg2576 mice models of AD present

$\sim 1600\text{--}1700$ fM mg^{-1} of A β_{42} after developing the disease symptoms⁴⁸. However, the wet weight of whole zebrafish larva is ~ 1 mg and its brain is 4–5 times smaller than its body weight⁴⁹. Considering this physiological relevance of the body weight, A β_{42} was injected in zebrafish larvae over a concentration range of 0.07–1200 fM per larva and based on locomotor response (Fig. 3c) 100 fM was selected for further experiments. However, 100 fM of A β concentration did not produce any difference in neurotransmitter levels that are usually disturbed in severe cases of AD⁴⁶. Therefore, A β of 600 fM was used to observe any possible fluctuations in neurotransmitters.

ROS generation was quantified by a direct measurement of dichlorofluorescein diacetate (DCF) fluorescence from the larval brain (Fig. 6c, d). It has been shown in literature that oligomeric amyloid proteins directly interacted with cell membranes to induce cytotoxicity by membrane disruption and subsequent ROS generation¹⁴. A β were injected in the cerebroventricular space and their associated toxicity was determined by ROS generation, in comparison with the positive control of H₂O₂. The samples were mixed with DCF prior to microinjection in larvae. The corrected total (CT) fluorescence from H₂O₂ and A β treated

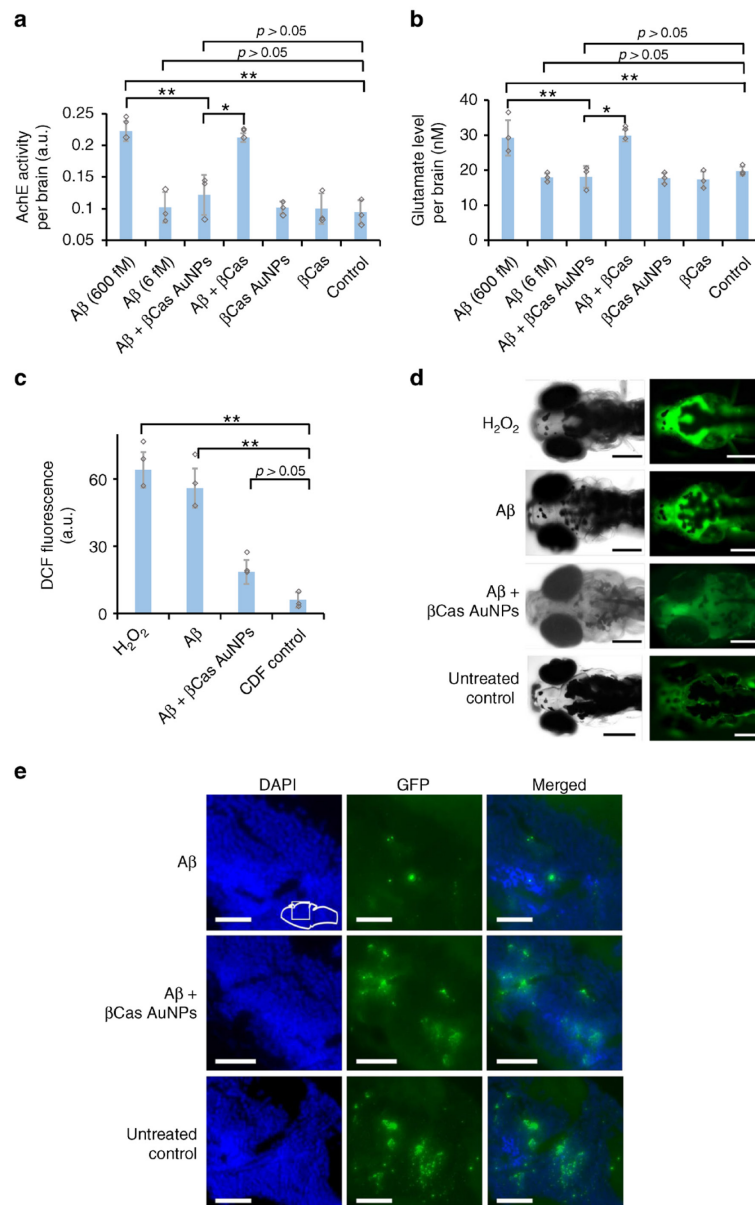


Fig. 6 Neurotransmitters and reactive oxygen species (ROS) in the brain of Aβ treated larvae. The biomarkers were measured 5 days post Aβ treatment. Cerebrovascular injection of Aβ peptide at 6 fM per larvae did not significantly ($p > 0.05$) influence the AChE (**a**) and GLT (**b**) levels in zebrafish larvae ($n = 10$). However, increasing the Aβ dose to 600 fM significantly increased ($p < 0.05$) AChE and GLT levels. βCas AuNPs (3 ng Au per 4.5 ng βCas), injected 2 h post Aβ treatment, significantly ($p < 0.005$) reduced the AChE and GLT levels on the 5th day post Aβ (600 fM) treatment. βCas micelles (dose equivalent to βCas in 3 ng βCas AuNPs), in comparison, failed to improve ($p > 0.05$) the biomarker levels. **c** ROS generation was significantly ($p < 0.005$) high in Aβ treated (600 fM) larvae. ROS generation was suppressed in βCas AuNPs treated larvae and close to control ($n = 10$). **d** Representative images of zebrafish larvae expressing DCF/ROS fluorescence when treated with H₂O₂, Aβ, Aβ + βCas AuNPs, and Aβ + βCas. **e** Larvae's brain sections were stained for synaptophysin. Aβ-treated larvae presented loss of synaptophysin indicating neurodegeneration. Scale bars in all images are 200 μm. Error bars represent the standard deviation. Source data are provided as a Source Data file

larvae were 41 ± 7.9 and 42.9 ± 8.7 , respectively. However, upon treatment with βCas AuNPs, the CT fluorescence was reduced to 14.5 ± 5.4 , comparable to DCF as negative control (8 ± 3.4). Synaptophysin-based neurodegeneration, an indicator for neuronal synapsis, was also imaged via immunostaining (Fig. 6e). Aβ

treated larvae presented a significant loss of synaptophysin as compared to Aβ + βCas AuNPs or untreated control larvae.

In this study, zebrafish larvae is developed and used as a simple, in vivo visual model to study Aβ fibrillization, toxicity, behavioral pathology, neurodegeneration, and biodistribution

and nano-chaperone activity of β Cas AuNPs. These advantages can be employed to screen or study the efficacy, pharmacokinetics and pharmacology of anti-Alzheimer's drugs, specifically nano-chaperone based therapeutic modalities. However, despite possessing a vertebrate nervous system, zebrafish larvae still develop cognitive and learning functions. Therefore, the behavioral pathology observed in this study may not be clinically equivalent to Alzheimer's symptoms. To study the A β toxicity and chaperone activity of β Cas AuNPs, adult zebrafish was employed to offer a more advanced in vivo model with a cognitive capacity⁵⁰. Microinjection of A β (1 μ L, 50 μ M) in adult zebrafish produced behavioral toxicity (Fig. 7a, b), A β aggregation in brain (Fig. 7c) and clinically relevant Alzheimer's-like symptoms (Fig. 7d–f). Retro-orbital microinjection (1 μ L, 0.5 mM) of β Cas AuNPs, 2 h post A β treatment, rescued the adult zebrafish from developing the cognitive dysfunction.

Expression of human orthologues of A β -associated neuronal machinery at 24 h post fertilization suggests suitability of zebrafish for AD modeling^{39,51}. Macro-organization of the brain and cellular morphology of zebrafish are parallel to vertebrates and have led to studies of neurobehavioral pharmacology and stress-induced behavior⁵². In addition, exogenous microinjection or genetic overexpression of Tau in zebrafish has resulted in intracellular tangle formation and abnormalities in the animal's development and swimming behaviors^{53,54}. These, together with our observations, support A β toxicity induction and AD modeling in zebrafish, especially within the context of cerebral deposition of A β and their associated behavioral pathology.

Intracardiac injection of β Cas AuNPs mitigated the toxicity of cerebroventricularly injected A β_{42} in a new, high-throughput zebrafish model. This remarkable capacity of eliminating toxic A β and rescuing the animal from AD-like symptoms was evidenced by in vitro assays of ThT, CD, and TEM, in silico

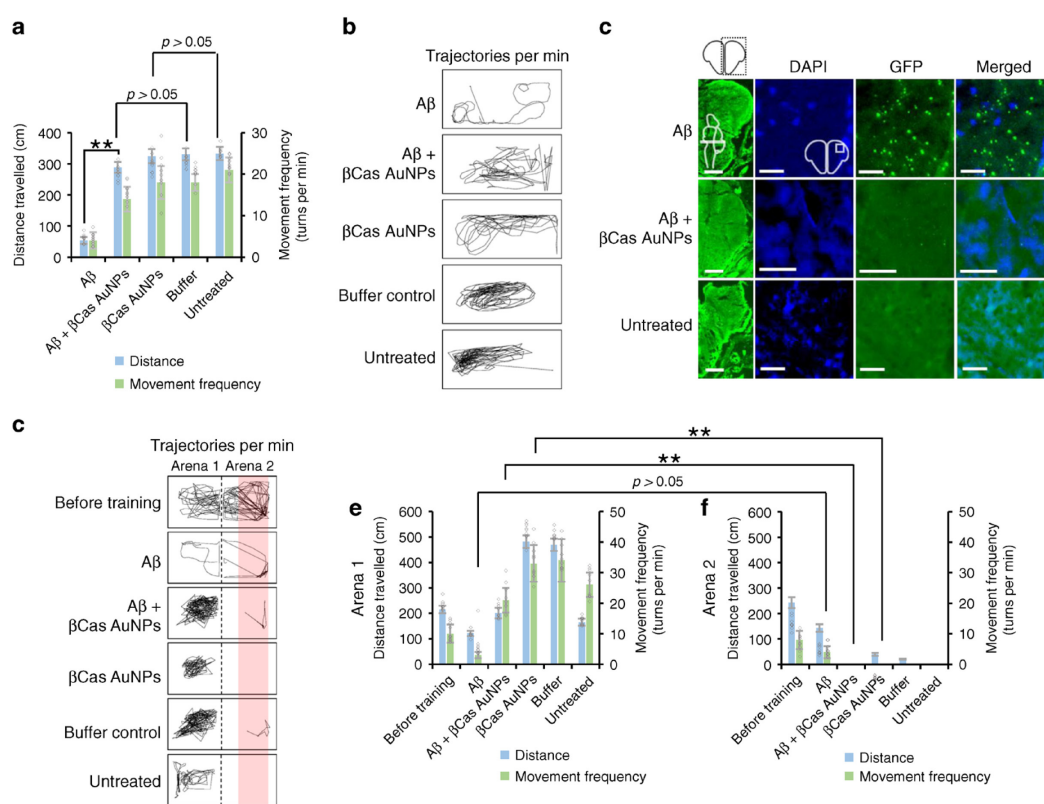


Fig. 7 Mitigation of A β toxicity and Alzheimer's-like symptoms in adult zebrafish with β Cas AuNPs. **a** Adult zebrafish (10 months old) were microinjected (cerebroventricular) with A β (1 μ L, 50 μ M) and observed for behavioral pathologies at 2 weeks post injection ($n = 4$, SD \pm mean). To study the mitigation with β Cas AuNPs, β Cas AuNPs were microinjected (retro-orbital, 1 μ L, 0.5 mM) 2 h prior to A β treatment. A β induced significant reduction in total distance traveled and movement frequency in adult zebrafish while β Cas AuNPs were able to rescue the symptoms. Movement trajectories are presented in **(b)**. Observations were made for 1 min, three times at a 2 h interval for each fish ($n = 3$). **c** IHC was performed on adult zebrafish brain sections to image the A β deposition. The first column represents the right cerebral brain of adult zebrafish in the GFP channel (Scale bars: 200 μ M). DAPI, GFP, and merged images at higher magnifications revealed A β plaque deposition in A β treated but not in A β + β Cas AuNPs, or untreated control (Scale bars: 20 μ M). Furthermore, cognitive behavior of adult zebrafish was analyzed. **f** Zebrafish were trained to avoid swimming into the right half (Arena 2) of the swimming tank (1 L) that was labeled red and attached with a source of electric shock (9 V) (Supplementary Fig. 17). After training, the electric source was removed and the cognitive memory of the fish to remain in arena 1 and to avoid arena 2 was assessed for a period of 2 min ($n = 3$, three times for each fish at a 2 h interval). The movement trajectories of the fish in arena 1 vs. arena 2 are presented in panel F. Comparative analysis of distance traveled and movement frequency of the fish in arena 1 **(d)** vs. arena 2 **(e)** revealed cognitive dysfunction of A β -treated fish that were unable to avoid arena 2. However, β Cas AuNPs treated, buffer control and untreated control fish were able to avoid swimming into arena 2. Error bars represent the standard deviation. Source data are provided as a Source Data file

examination of A β - β Cas AuNP binding, *ex vivo* assays of microtome, HSI, ICP-MS, and MALDI analyses of A β impaired zebrafish brain, *in vivo* assays of ROS, behavior and neurological dysfunction biomarkers of zebrafish larvae, and cognition of adult zebrafish. The binding between A β and β Cas was mediated by nonspecific interactions via the residues of the whey protein that were free from engagement with the AuNP surface. Adsorption of β Cas onto an AuNP surface enabled trafficking of β Cas across the zebrafish larvae BBB where β Cas was then capable of efficiently binding A β for elimination. Furthermore, β Cas AuNPs induced no harmful effects on the development of healthy zebrafish, owing to the biocompatibility of both the chaperone-like protein and the AuNPs. As this nano-formulation meets all key criteria for a potent *in vivo* amyloidosis inhibitor, it holds the promise to be further developed into safe-to-use, preventative nanomedicines against the pathologies of AD and other debilitating human amyloid diseases. Although zebrafish lack advanced cognitive capacity as possessed by rodents, they can serve as a robust, economic, and high-throughput alternative to complement neurological mouse models that are no longer deemed sufficient¹⁹.

Methods

Animal husbandry and ethics statement. The AB wild-type zebrafish (*Danio rerio*) was maintained in a fish breeding circulatory system (Haisheng, Shanghai, China) at 28 \pm 0.5 °C with a 14 h light: 10 h dark cycle. The embryos were produced by adult spawning. For spawning, two pairs of male and female were placed in tank with shallow water. The male and female were separated by a removable partition and kept overnight. The spawning was triggered by removing the partition with first light in the morning and embryos were collected 2 h later, washed with 0.5 ppm methylene blue and placed in petri dish with Holtfreter's buffer. The healthy embryos at the same developmental stage were selected and developed to 5-day-old larvae for further measurement. All the experiments were performed with larvae in Holtfreter's buffer²⁵. Tricaine (0.4% in Holtfreter's buffer) was used for anesthesia. When required, larvae were euthanized by placing in 0.01% tricaine in Holtfreter's buffer for 10 min that was pre-chilled at 4 °C. The excision of head from the trunk was performed under an optical stereomicroscope with a sharp surgical blade. All zebrafish experiments were performed in accordance to the ethical guidelines of Tongji University and the protocols were approved by the Animal Center of Tongji University (Protocol #TJLAC-019-113). All *in vitro* and other experiments were performed in compliance with the relevant ethics, laws, and institutional guidelines of Monash University Occupational Health & Safety.

Synthesis of β Cas AuNPs. HAuCl₄ (1 mM, PBS pH 6) was heated at 40 °C and while stirring at 1000 rpm, added with an equal volume of β Cas in PBS (pH 6) at the concentration of 1 mg mL⁻¹. The heating continued for 10 min and 100 μ L of 0.5 mM NaBH₄ was added dropwise to the reaction mixture. The solution turned wine red indicating the formation of β Cas AuNPs. Heating was stopped after 2 h while the reaction was kept on stirring for overnight. β Cas AuNPs were purified by centrifugal filtration with 100 kDa spin filters. AuNPs were washed 3 \times with deionized water, transferred to PBS (pH 7.4) and stored at 4 °C for further experimentation. After purification, the β Cas concentration in β Cas AuNPs was determined by the BCA method⁵⁶. Citrate-capped AuNPs (Cit AuNPs) were synthesized via a reported method⁵⁷. Briefly, a solution of HAuCl₄ (10 mL, 1 mM) was brought to boiling at 120 °C and then 1 mL (10 mM) trisodium citrate was added dropwise. The solution turned to wine red, indicating the formation of Cit AuNPs. The solution was brought to room temperature, purified via centrifugal washing with deionized water and stored in dark for further use.

Neutral red (NR) dye was conjugated to β Cas and β Cas AuNPs for tracing their biodistributions in zebrafish larvae. The dye was conjugated via 1-ethyl-3-(3-dimethylaminopropyl)carbodiimide (EDC) coupling. Briefly, 2 mL of 6.25 μ M of β Cas or equivalent concentration of β Cas AuNPs was stirred overnight with 18 μ M of EDC, 23 μ M of N-hydroxysuccinimide (NHS), and 14 μ M of the NR dye. The NR-conjugated β Cas or β Cas AuNPs were purified via centrifugal filtration, transferred to PBS (pH 7.4) and stored for *in vivo* assays.

ThT kinetic assay. A β was treated with hexafluoro-2-propanol (HFIP) to break-down pre-existing small aggregates. Specifically, 0.5 mg of A β (Anaspec Inc., purity \geq 95%) was dissolved in 500 μ L of HFIP, incubated for 3 h, aliquoted to different concentrations and dried to evaporate the HFIP. The dried A β was dissolved in 0.01% NH₄OH for dissolution purpose and left in the open for 20 min to evaporate NH₄OH, leaving behind the aqueous solution of A β that was used for further experiments. For the thioflavin T (ThT) assay, a 50 μ L aqueous solution of 50 μ M A β and 100 μ M of ThT were incubated with or without β Cas (6.25 μ M) or equivalent concentration of β Cas AuNPs in a 96-well plate. The ThT fluorescence

was recorded with excitation at 445 nm and emission at 488 nm, at 30 min intervals for 48 h.

Transmission electron microscopy. A β was mixed with β Cas or β Cas AuNPs in the same ratio as for the ThT assay and incubated for 48 h. After incubation, a drop of each sample was placed on a glow discharged, carbon coated copper grid and blotted after 1 min. The sample-coated grid was negatively stained with 1% uranyl acetate that was blotted after 30 s. The grid was dried in vacuum and visualized with a Technai F20 transmission electron microscope operated at a voltage of 200 kV.

CD spectroscopy, hydrodynamic size, and zeta potential. The secondary structural contents of β Cas, β Cas AuNPs, A β m, A β o, A β fibrillized w/o β Cas or β Cas AuNPs were determined by CD spectroscopy. In all, 200 μ L of the sample was pipetted into a CD cuvette and the concentration of A β was 100 μ M while β Cas and β Cas AuNPs were 12.5 μ M β Cas equivalent in all CD measurements. The incubation time was 48 h at 37 °C and the incubation medium was deionized water. CD spectra were recorded from 190 to 240 nm with a 1 nm step size. The acquired data were presented in the unit of millidegrees (mdeg). Percentage secondary structure contents were determined by analyzing the CD data via Dichroweb with Contin/reference set 4⁵⁸. The hydrodynamic diameter and zeta potential of the AuNPs were measured with dynamic light scattering under ambient conditions (Malvern Instruments). The concentrations and incubation conditions were the same as for the CD experiments.

Binding capacity (BCA, TGA, TEM, CD, UV-SPR, and fluorescence microscopy). The binding capacity between A β and β Cas or β Cas AuNPs was determined via a BCA assay⁵⁶ and TGA. Briefly, 6.25 μ M of β Cas or equivalent β Cas AuNPs were incubated with varying concentrations of A β m (monomers) or A β o (oligomers) ranging from 2 to 1137 μ M. Incubation time was 48 h at 37 °C in deionized water. HFIP-treated A β was considered as A β m while A β m incubated in water for 12 h at 4 °C was considered as A β o. After incubation, the samples were centrifuged at 17,300 \times g for 30 min and the pellets were redispersed in 10 μ L of deionized water and subjected to BCA protein content quantification. The BCA binding efficacy was presented in terms of the amount of A β bound to β Cas or β Cas AuNPs. For TGA analysis, the pellet dispersed in 10 μ L water was placed as a drop on a platinum pan. The samples were held at 80 °C for 30 min and then scanned from 80 to 800 °C at a scanning rate of 10 °C min⁻¹ under a constant flow of nitrogen of 1 mg mL⁻¹. For A β m and A β o, 10 μ L of 1 mg mL⁻¹ of the peptide was placed on a TGA pan and scanned under the same conditions.

To assess binding affinity, β Cas AuNPs or NR- β Cas AuNPs (12.5 μ M β Cas equivalent) were incubated with preformed A β o or A β m (100 μ M) for 3 h at 37 °C and unbound A β m/o was removed via centrifugal washing thrice (25,000 \times g for 10 min at 4 °C). CD and TEM were performed as described above in the respective sections. UV-SPR for β Cas AuNPs and fluorescence spectra (NR- β Cas AuNPs, excitation at 470 nm) were recorded with a microplate reader.

Cellular toxicity. SH-SY5Y (ATCC® CRL-2266™) human bone marrow neuroblastoma cells were cultured in Dulbecco's Modified Eagle Medium: Nutrient Mixture F-12 (DMEM/F12) with 10% fetal bovine serum (FBS). A 96-well plate (Costar black/clear bottom) was coated with 70 μ L of poly-L-lysine (Sigma, 0.01%) and incubated at 37 °C for 30 min. After removing poly-L-lysine, the wells were washed by PBS thrice. Cells (~50,000 cells per well per 200 μ L medium) were added to the wells and incubated at 37 °C with 5% CO₂ for 24 h to reach ~70–80% of confluency. The cell culture medium was then refreshed with 1 μ M propidium (PI) dye in DMEM/F12 with 10% FBS and incubated for another 30 min. A β was freshly dissolved in 0.005% NH₄OH buffer, in the presence or absence of β Cas AuNPs and added to the wells with final concentration of 20 and 50 μ M for A β and β Cas AuNPs, respectively. Cellular toxicity was recorded by Operetta (PerkinElmer, 20 \times PlanApo microscope objective, numerical aperture: 0.7) in a live cell chamber (37 °C, 5% CO₂) after 15 h of treatment. The percentage of dead cells (PI-positive) to total cell count was determined by a built-in bright-field mapping function of Harmony High-Content Imaging and Analysis software (PerkinElmer). The measurement was performed in triplicate and conducted at five reads per well. Untreated cells were recorded as control.

Helium ion microscopy. SH-SY5Y neuronal cells were incubated with A β in the presence or absence of β Cas AuNPs as described for the cellular toxicity assay. The incubation was performed for 2 h at 37 °C and then stabilized by 2.5% paraformaldehyde. The samples were incubated at 4 °C overnight. The paraformaldehyde/medium was replaced with gradient concentrations of ethanol in the five steps of 20%, 40%, 60%, 80%, and 95%, respectively, with ~2 h of rest time at each gradient. In all, 30 μ L suspension of cells was air-dried on a carbon tape and the morphologies of the cells were visualized by HIM (Orion NanoFab, Zeiss, USA). Untreated cells were used as control.

Microinjection of A β , β Cas, β Cas AuNPs, and Cit AuNPs in zebrafish larvae. HFIP-treated A β (10 μ g) was dissolved in PBS (pH 7.4) to make a stock solution of

100 μ M. Dilutions of 0.07–1200 fM of A β per 5 nL were made in PBS and injected (5 nL injection volume) into the cerebroventricular space of 5 days old zebrafish larvae. PBS alone was used as negative control. For microinjection, zebrafish larvae were anesthetized by adding 2 drops of 0.4% tricaine in petri dish and waited until the larvae stopped moving in response to tapping on the table. The larvae were positioned on a 1% agarose gel plate and microinjected with A β peptide. Microinjections were performed with a fine calibrated needle of a pneumatic microinjection system (PV830 Pneumatic Picopump, WPI) operated under 20 psi of injection pressure. The tip of the glass capillary needle was inserted in the ventricular space, across the dorsal soft skin tissue. The tip was ensured not to penetrate more than 0.1–0.3 mm across the center meeting point of left and right telencephalon (Supplementary Video 4). β Cas and β Cas AuNPs were administered under similar conditions via intracardiac microinjection (Supplementary Video 5). The original as-synthesized β Cas AuNPs solution contained 1 and 1.5 ng of Au and β Cas per 5 nL. The original β Cas AuNPs solution was concentrated 3 \times and redispersed in PBS. A 5 nL of this solution was microinjected into zebrafish larvae via the intracardiac route and each 5 nL contained 3 ng of Au per 4.5 ng (37.5 μ M mL⁻¹) of β Cas in the form of β Cas AuNPs. β Cas solution of equivalent concentration was prepared in PBS for microinjection. For dose dependent delivery of β Cas AuNPs in cerebral tissues, the original β Cas AuNPs solution was concentrated to 1.5, 3, and 6 \times , and dispersed in PBS prior to intracardiac microinjection to zebrafish larvae. Cit AuNPs were concentrated to equal concentration as β Cas AuNPs and microinjected into the larvae with the same protocol.

Zebrafish larvae behavioral pathology. Larval response to tapping stimuli in a 96-well plate was observed. The 96-well plate was tapped gently at the rate of 1 per sec and the larvae unable to move after five consecutive stimuli were counted as nonresponsive. Furthermore, the larvae losing their horizontal swimming position at higher doses of A β were also counted and the percentage of the larvae losing response to stimuli and their swimming position was calculated. The swimming behavior of zebrafish larvae was observed with an automated zebrafish behavior recording system ZebraBox (Viewpoint) and characterized in terms of total distance traveled by the larvae in a 96-well plate and range of the movement that was >90°, clockwise or counter clockwise, were counted. Representative trajectories of the movement were also recorded by built-in sensors. The observation period was 1 h. The number of larvae in each group was 20 and 3 groups were used for each sample. The larvae treated with β Cas or β Cas AuNPs, 2 h after A β treatment, were monitored for behavioral pathology with the same method.

Fluorescence imaging, IHC, and polarized light microscopy. Whole mount larval imaging was performed under the brightfield (BF) and RFP channels of a stereomicroscope (Olympus MVX10). For imaging of A β in the cerebral region, the A β treated larvae (100 fM, cerebroventricular microinjection) was microinjected with 100 fM of Congo red on the third and fifth day post A β treatment. The larvae were placed in Holtfreter's buffer for 6 h to allow staining of the amyloids. The larvae were anesthetized immediately prior to imaging with 0.4% tricaine, and positioned in dorsal or lateral view in a drop of 1% low-melting agarose gel. The cerebral region, fin and mid-vascular region of the larvae were imaged with the same method. The biodistribution of NR-conjugated β Cas or β Cas AuNPs was imaged by following the same method 0.5, 6, and 12 h post- β Cas or β Cas AuNPs treatment via intracardiac microinjection. The microinjection volume was 5 nL with a dose of 4.5 ng for β Cas (37.5 μ M) or β Cas AuNPs equivalent to 4.5 ng β Cas.

For Congo red staining of the sliced sections of the zebrafish larvae, A β (100 fM) treated larvae were first fixed in 2.5% paraformaldehyde for 12 h at 4 °C. Microtome slices of zebrafish larvae were prepared by embedding the larvae into paraffin. The paraffin-embedded larvae were cut into thin slices of 5 μ M via microtome and slices were placed in a hot water bath (40 °C) for removal of any wrinkles. The slices were then mounted on glass slides and dried. Slide mounted slices were dewaxed by treating with (1) xylene for 2 h, (2) absolute ethanol for 15 min, and (3) 75% ethanol for 5 min and then rinsed with deionized water. The slices were treated with 0.5% Congo red stain in 50% ethanol for 20 min, rinsed with water, differentiated with 1% NaOH solution in 50% ethanol (5–10 dips) and again rinsed with water. The slices were then dehydrated with 95% ethanol (3 min) and 2 dips in 100% ethanol (each 3 min) and cleared with 2 dips in xylene (each 3 min). The samples were finally sealed with neutral gum and imaged with an optical microscope.

For IHC, 5 μ M thick sections of zebrafish larvae were mounted on glass slides as for Congo red staining. The dried sections were washed in PBS (pH 7.4) and TritonX-100 (0.05% in PBS) for 5 min each. A drop (50 μ L, 2 μ g mL⁻¹) of primary antibody (Anti-amyloid β 42, mouse monoclonal, Anaspec, AS-55922) was placed on each section on the glass slides and incubated at 4 °C overnight. Primary antibodies were washed away from the sections by dipping in PBS and TritonX-100 (0.05% in PBS) for 5 min. Sections were incubated with a drop (50 μ L, 2 μ g mL⁻¹) of secondary antibody (Goat anti-mouse HiLyte™ Fluor 488—labeled, Anaspec, AS-61057-05-H488) for 6 h at room temperature. The secondary antibodies were washed away by dipping the slides in TritonX-100 (0.05% in PBS) for 5 min. Slides were dried, mounted with a cover slip using a drop of 50% glycerol and imaged under a fluorescence microscope (Nikon Ti-Eclipse). The larvae's brain sections were immunostained for synaptophysin with the same method using primary (50 μ L, 2 μ g mL⁻¹ of anti-Synaptophysin antibody, abcam, Cat# ab32594) and

secondary antibodies (50 μ L, 2 μ g mL⁻¹ of Goat Anti-Rabbit IgG H&L, Alexa Fluor® 488, abcam, Cat# ab150081).

Polarized light microscopy was performed on the Congo red-stained larvae tissue sections. The slides were imaged for birefringence under an Abrio polarization microscope. A drop (50 μ L, 20 μ M) of fibrillized A β was placed and dried on a glass slide. The dried sample was processed same as for larva tissue sections for immunostaining and polarized light microscopy and used as control.

Darkfield HSI. Zebrafish larvae at 0.5 h post treatment with intracardiac microinjection of β Cas AuNP (3 ng Au per 4.5 ng β Cas equivalent) were euthanized and fixed in 2.5% paraformaldehyde for 12 h and then sliced to thin sections, dehydrated and mounted on glass slides with the same procedure as described for fluorescence microscopy. HSI was performed with a CytoViva darkfield microscope equipped with a pixelFly CCD camera. ENVI 4.8 software was used to capture and process the images and to acquire AuNPs spectra. The darkfield images were captured and then scanned for HSI for β Cas AuNPs treated larvae, untreated control larvae and β Cas AuNPs alone. β Cas AuNPs alone as control were used to acquire the spectral library of AuNPs by selecting ~1500 pixels with region of interest function of ENVI 4.8. Spectral libraries obtained from β Cas AuNPs and a mean spectral signature was generated. The mean spectral signature of β Cas AuNPs was used to filter against the selected pixels (~1000) from β Cas AuNPs treated and untreated control larval images to generate spectral angular mapping images. Rule images were obtained by matching the pixel spectra from β Cas AuNPs against β Cas AuNPs or untreated larval images. Rule images darkened the pixels with matching spectra of β Cas AuNPs. All images were normalized against lamp spectra. For HSI imaging of β Cas AuNPs and β Cas AuNPs incubated with A β , the AuNPs were incubated with A β at the same ratio as for ThT for 48 h. A drop of each sample was placed on a glass slide covered with a slip. Darkfield images and SPR spectra of the AuNPs were obtained by scanning ~1500 pixels for each sample.

TEM imaging of brain tissues. For TEM analysis of tissues, zebrafish larvae were injected with 3 ng Au per 4.5 ng β Cas equivalent β Cas AuNPs via intracardiac microinjection as described above, euthanized and fixed in 2.5% glutaraldehyde 0.5 h post treatment. The larvae were treated with 1% osmium tetroxide for 4 h (4 °C) and then washed three times with 0.1 M PBS buffer (pH 7.4), 15 min each. The larvae were then treated with 1% citrate in 0.1 M PBS buffer (pH 7.4, 20 °C) for 2 h and again washed three times with 0.1 M PBS (pH 7.4), at 15 min each. After that the larvae were dehydrated by treating with 50, 60, 70, 80, 90, and 100% ethanol, at 15 min each. Following that the larvae were treated with acetone: 812 embedding agent (1:1) and then with 812 embedding agent, both for overnight and then baked at 60 °C for 4 h for polymerization of embedding resin. The larvae were finally sliced into ultra-thin sections of 60–80 nm with Diatome ultra 45°. The sections were double stained with 2% solutions of uranyl acetate and lead citrate, 15 min each, dried overnight and then imaged with a transmission electron microscope (Technai G2 20 TWIN) operated at 80 kV.

Inductively coupled plasma-mass spectrometry. Delivery of β Cas AuNPs across the larvae's brain was quantified with ICP-MS analysis. Zebrafish larvae were microinjected with 1.3, 3, and 6 ng Au equivalent β Cas AuNPs via the intracardiac route with the same method as described above. The larvae were euthanized 0.5, 6, and 12 h post microinjection and their heads were excised and homogenized in PBS (pH 7.4) in a Teflon-glass homogenizer (70 Hz for 1 min). Brain or trunk homogenate was made up to 1 mL with PBS (pH 7.4), added with 9 mL of 68% HNO₃ and digested by stepwise heating at 100, 150, 170, and 190 °C for 30, 30, 30, and 90 min, respectively. The dried and digested layer was dissolved in 1 mL of 4% HNO₃ and analyzed with ICP-MS (Agilent 7700) for quantification of Au. The instrument was operated under 0.75 MPa Ar pressure and a standard calibration was made with Au spiked PBS samples, digested in the same way as the larval samples. Untreated larvae and PBS alone were used as negative controls. The number of larvae in each group was 20 and 3 groups per sample were used for analysis.

Matrix-assisted laser desorption ionization-time of flight mass spectrometry (MALDI TOF MS). Saturated solution of sinapinic acid (SA) was prepared in ethanol and 1 μ L of the sample was dried on a ground steel MALDI plate. Another saturated solution of SA was prepared in acetonitrile and trifluoroacetic acid (30:70, v/v) and mixed with the zebrafish larvae head homogenate at a 1:1 ratio. In all, 0.5 μ L of this mixture was applied to previously dried SA layer. The dried layer was analyzed by a Bruker ultraflexxtreme MALDI-TOF/TOF in the linear positive mode. The instrument was calibrated using protein calibration standards I and II. A total of 8000 shots were gathered across the sample spots using Flexcontrol software (3.4) in the range of 1–20 kDa. The acquired spectra were processed by baseline subtraction and peak picking using Flexanalysis software (3.4).

Biomarkers and ROS assay. Acetylcholine esterase (AChE) and glutamate (GLT) levels were measured as biomarkers for neurodegeneration. Briefly, zebrafish larvae treated with A β , A β + β Cas, and A β + β Cas AuNPs were euthanized and their heads were excised from the trunks. The heads were homogenized in PBS (pH 7.4)

and AchE and GLT levels were estimated using assay kits according to reported literature^{59,60}.

For ROS assay, A β (100 fM) were injected to the cerebroventricular space of zebrafish larvae and 2,7'-DCF (5 nL of 2 μ M) was injected 5 days post A β treatment. The whole mount larvae were imaged under the green fluorescence protein channel of an optical microscope 1 h after DCF treatment. For β Cas AuNPs, the nanoparticles were injected 2 h post A β treatment followed by the same procedure. H₂O₂ (5 nL of 0.1%) was used as positive control and injected 3 h prior to DCF microinjection in positive control larvae. DCF fluorescence was quantified by excising the head from the trunk of euthanized larvae, homogenizing in PBS buffer (50 μ L, pH 7.4) and reading the DCF fluorescence with a microplate reader with excitation/emission at 495 nm/529 nm.

Microinjection in adult zebrafish. Adult zebrafish at the age of 10 mth were used for the cognition experiment. The fish was maintained, before and during the experiment, as described in the "Animal husbandry and ethics statement" section. For microinjection, adult fish were anesthetized with ice chilled tricaine (0.01% in Holtfreter's buffer for 20 s). Cerebroventricular microinjection of A β (1 μ L, 50 μ M) was performed via 1 μ L Hamilton glass syringes. A β peptide was injected in between the right and left telencephalon and the needles did not penetrate more than 1 mm (Supplementary Video 6). The fish were held in place via a forcep. The syringes were washed with 70% ethanol and 1 \times PBS twice, in between the injections. For the group with A β with β Cas AuNPs, β Cas AuNPs were injected 2 h prior to the injection of A β . β Cas AuNPs (1 μ L, 0.5 mM, 20 psi injection pressure) were slowly introduced into the systemic circulation of the fish via retro-orbital microinjection (7 o'clock position), using a sharp glass capillary needle (Supplementary Video 7). The fish was placed back into the tank for recovery. The adult zebrafish were grouped ($n = 3$) and injected with A β , A β with β Cas AuNPs, β Cas AuNPs alone and PBS. Buffer injected and untreated fish were considered as controls.

Behavioral pathology and cognitive function test of adult zebrafish. The adult zebrafish microinjected with the above described samples were monitored on a daily basis for any apparent change to their swimming activity. The swimming activity of the fish started to change 1-week post treatment and became significantly apparent at 2 weeks post treatment. The behavioral pathology of the fish was recorded with ZebraBox (Viewpoint), using a 1 L fish tank, and characterized for total distance traveled and movement frequency. The recording was performed for 1 min, 3 times for each fish at a 2-h interval.

Cognitive function test was performed by hypothetically dividing the 1 L fish tank into two halves, i.e., arenas 1 and 2 (Supplementary Fig. 17). A red colored paper was attached to the bottom of the tank to associate a color with arena 2. Fish were allowed to freely swim in the whole tank for 30 min and then trained for 20 min to avoid swimming into arena 2 by using an electric shock punishment. Whenever the fish swam into the red arena 2, it was punished by dipping the electrodes of 9 V in electric potential. After 20 min of training, the electric source was removed and the cognitive ability of the fish to avoid arena 2, while swimming in arena 1 was recorded for 2 min. The comparative distance traveled and movement frequency of the fish in arena 1 vs. 2 were recorded simultaneously. The recordings were made 3 times for each fish ($n = 3$) at 2 h intervals. The results were analyzed via EthnoVision X1. The analysis parameters were as follows; animal: adult zebrafish, arena: open field square template (divided into two-halves for the cognitive function test), tracking feature: central point, sample rate: 5 per second, detection setting level: sensitive enough to track the fish in the whole tank, threshold for movement frequency: 50° turn (clockwise or counter clockwise) and minimum 0.5 cm of travel.

IHC was performed on adult zebrafish brain sections. Adult zebrafish at 2 weeks post A β or A β + β Cas AuNPs treatment were euthanized by placing the animals in ice chilled tricaine (1% in Holtfreter's buffer for 1 min). The heads were separated from the bodies, at pectoral fin, with a sharp scalpel and fixed in 2.5% paraformaldehyde overnight. The heads were treated with 20% sucrose overnight, fixed in Tissue Trek OCT mounting medium at -20°C and sectioned into 20 μ M thick sections via cryostat. The sections were mounted on gelatinized glass slides, immunostained for A β as described above in the "Fluorescence imaging, IHC, and polarized light microscopy" section and imaged via a fluorescence microscope.

Statistical analysis. All the experiments in the manuscript were repeated three times, unless specified, and data was presented as mean \pm SD. For the zebrafish experiments, 20 larvae per group and 3 group per sample were used to minimize experimental error. The significance of results was determined by one-way ANOVA followed by Turkey's test and p values less than 0.05 were considered significant (presented with * in figures) while p values less than 0.005 were considered as highly significant (presented with ** in figures).

Reporting summary. Further information on research design is available in the Nature Research Reporting Summary linked to this article.

Data availability

Data supporting the findings of this paper are available from the corresponding authors upon reasonable request. Reporting summary of this article is available as Supplementary Information file. The raw data underlying the respective main text (Figs. 1–7) and Supplementary figures (Supplementary Figs. 1, 2, 8, 13, 14 and 15) are provided as Source Data File.

Received: 10 December 2018 Accepted: 4 August 2019

Published online: 22 August 2019

References

- Knowles, T. P., Vendruscolo, M. & Dobson, C. M. The amyloid state and its association with protein misfolding diseases. *Nat. Rev. Mol. Cell Biol.* **15**, 384 (2014).
- Hardy, J. A. & Higgins, G. A. Alzheimer's disease: the amyloid cascade hypothesis. *Science* **256**, 184–186 (1992).
- Sakono, M. & Zako, T. Amyloid oligomers: formation and toxicity of A β oligomers. *FEBS J.* **277**, 1348–1358 (2010).
- Benilova, I., Karran, E. & De Strooper, B. The toxic A β oligomer and Alzheimer's disease: an emperor in need of clothes. *Nat. Neurosci.* **15**, 349–357 (2012).
- Cummings, J. et al. Drug development in Alzheimer's disease: the path to 2025. *Alzheimers Res. Ther.* **8**, 39 (2016).
- Javed, I. et al. Probing the aggregation and immune response of human islet amyloid polypeptides with ligand-stabilized gold nanoparticles. *ACS Appl. Mater. Interfaces* **11**, 10462–10471 (2019).
- Rogers, J., Strohmeier, R., Kovelowski, C. & Li, R. Microglia and inflammatory mechanisms in the clearance of amyloid β peptide. *Glia* **40**, 260–269 (2002).
- Marsh, S. E. et al. The adaptive immune system restrains Alzheimer's disease pathogenesis by modulating microglial function. *Proc. Natl Acad. Sci. USA* **113**, E1316–E1325 (2016).
- What Causes Alzheimer's Disease? <https://www.nia.nih.gov/health/what-causes-alzheimers-disease> (2017).
- Peric, A. & Annaert, W. Early etiology of Alzheimer's disease: tipping the balance toward autophagy or endosomal dysfunction? *Acta Neuropathol.* **129**, 363–381 (2015).
- Gerakis, Y. & Hetz, C. Emerging roles of ER stress in the etiology and pathogenesis of Alzheimer's disease. *FEBS J.* **285**, 995–1011 (2018).
- Selfridge, J. E., Lezi, E., Lu, J. & Swerdlow, R. H. Role of mitochondrial homeostasis and dynamics in Alzheimer's disease. *Neurobiol. Dis.* **51**, 3–12 (2013).
- Itzhaki, R. F. et al. Microbes and Alzheimer's disease. *J. Alzheimers Dis.* **51**, 979–984 (2016).
- Ke, P. C. et al. Implications of peptide assemblies in amyloid diseases. *Chem. Soc. Rev.* **46**, 6492–6531 (2017).
- Steenhuyzen, J. Biogen Scraps Two Alzheimer Drug Trials, Wipes \$18 Billion from Market Value. <https://www.reuters.com/article/us-biogen-alzheimers/biogen-scraps-two-alzheimer-drug-trials-wipes-18-billion-from-market-value-idUSKCN1R213G> (2019).
- Doody, R. S. et al. Phase 3 trials of solanezumab for mild-to-moderate Alzheimer's disease. *N. Engl. J. Med.* **370**, 311–321 (2014).
- Salloway, S. et al. Two phase 3 trials of bapineuzumab in mild-to-moderate Alzheimer's disease. *N. Engl. J. Med.* **370**, 322–333 (2014).
- The Lancet. Alzheimer's disease: expedition into the unknown. *Lancet* **388**, 2713 (2016).
- Reardon, S. Frustrated Alzheimer's researchers seek better lab mice. *Nature* **563**, 611–612 (2018).
- Ke, P. C. et al. Mitigation of amyloidosis with nanomaterials. *Adv. Mater.* **1901690** (2019). <https://doi.org/10.1002/adma.201901690>.
- Luo, Q. et al. A self-destructive nanosweeper that captures and clears amyloid β -peptides. *Nat. Commun.* **9**, 1802 (2018).
- Lansbury, P. T. & Lashuel, H. A. A century-old debate on protein aggregation and neurodegeneration enters the clinic. *Nature* **443**, 774 (2006).
- Kim, D. et al. Graphene quantum dots prevent α -synucleinopathy in Parkinson's disease. *Nat. Nanotech.* **13**, 812 (2018).
- Javed, I. et al. In vivo mitigation of amyloidogenesis through functional-pathogenic double-protein coronas. *Nano Lett.* **18**, 5797–5804 (2018).
- Gao, N. et al. Transition-metal-substituted polyoxometalate derivatives as functional anti-amyloid agents for Alzheimer's disease. *Nat. Commun.* **5**, 3422 (2014).
- Faridi, A. et al. Mitigating human IAPP amyloidogenesis in vivo with chiral silica nanoribbons. *Small* **14**, 1802825 (2018).
- Bieschke, J. et al. Small-molecule conversion of toxic oligomers to nontoxic β -sheet-rich amyloid fibrils. *Nat. Chem. Biol.* **8**, 93 (2012).

28. Thorn, D. C., Ecroyd, H. & Carver, J. A. The two-faced nature of milk casein proteins: amyloid fibril formation and chaperone-like activity. *Aust. J. Dairy Technol.* **64**, 34 (2009).
29. Guha, S., Manna, T. K., Das, K. P. & Bhattacharyya, B. Chaperone-like activity of tubulin. *J. Biol. Chem.* **273**, 30077–30080 (1998).
30. Thorn, D. C. et al. Amyloid fibril formation by bovine milk κ -casein and its inhibition by the molecular chaperones α S- and β -casein. *Biochemistry* **44**, 17027–17036 (2005).
31. Librizzi, F., Carrotta, R., Spigolon, D., Bulone, D. & San Biagio, P. L. α -Casein inhibits insulin amyloid formation by preventing the onset of secondary nucleation processes. *J. Phys. Chem. Lett.* **5**, 3043–3048 (2014).
32. Carrotta, R. et al. Inhibiting effect of α 1-casein on A β 1–40 fibrillogenesis. *Biochim. Biophys. Acta* **1820**, 124–132 (2012).
33. Zhang, X. et al. Chaperone-like activity of β -casein. *Int. J. Biochem. Cell Biol.* **37**, 1232–1240 (2005).
34. Gladysz, A., Abel, B. & Risselada, H. J. Gold-induced fibril growth: the mechanism of surface-facilitated amyloid aggregation. *Angew. Chem. Int. Ed.* **55**, 11242–11246 (2016).
35. Proctor, E. A. & Dokholyan, N. V. Applications of discrete molecular dynamics in biology and medicine. *Curr. Opin. Struct. Biol.* **37**, 9–13 (2016).
36. Javed, I. et al. Cofibrillation of pathogenic and functional amyloid proteins with gold nanoparticles against amyloidogenesis. *Biomacromolecules* **18**, 4316–4322 (2017).
37. Francis, R. et al. α 1- and α 2- are required for Notch pathway signaling, γ -secretase cleavage of β APP, and presenilin protein accumulation. *Dev. Cell* **3**, 85–97 (2002).
38. Team, M. G. C. P. Generation and initial analysis of more than 15,000 full-length human and mouse cDNA sequences. *Proc. Natl Acad. Sci. USA* **99**, 16899–16903 (2002).
39. Newman, M., Ebrahimi, E. & Lardelli, M. Using the zebrafish model for Alzheimer's disease research. *Front. Genet.* **5**, 189 (2014).
40. Geling, A., Steiner, H., Willem, M., Bally-Cuif, L. & Haass, C. A γ -secretase inhibitor blocks Notch signaling in vivo and causes a severe neurogenic phenotype in zebrafish. *EMBO Rep.* **3**, 688–694 (2002).
41. Joshi, P., Liang, J. O., DiMonte, K., Sullivan, J. & Pimplikar, S. W. Amyloid precursor protein is required for convergent-extension movements during Zebrafish development. *Dev. Biol.* **335**, 1–11 (2009).
42. Xie, J., Farage, E., Sugimoto, M. & Anand-Apte, B. A novel transgenic zebrafish model for blood-brain and blood-retinal barrier development. *BMC Dev. Biol.* **10**, 76 (2010).
43. Fleming, A., Diekmann, H. & Goldsmith, P. Functional characterisation of the maturation of the blood-brain barrier in larval zebrafish. *PLoS ONE* **8**, e77548 (2013).
44. Santana, S., Rico, E. P. & Burgos, J. S. Can zebrafish be used as animal model to study Alzheimer's disease? *Am. J. Neurodegener. Dis.* **1**, 32 (2012).
45. García-Ayllón, M.-S. et al. Altered levels of acetylcholinesterase in Alzheimer plasma. *PLoS ONE* **5**, e8701 (2010).
46. Sáez-Valero, J., Sberna, G., McLean, C. A. & Small, D. H. Molecular isoform distribution and glycosylation of acetylcholinesterase are altered in brain and cerebrospinal fluid of patients with Alzheimer's disease. *J. Neurochem.* **72**, 1600–1608 (1999).
47. Roher, A. E. et al. Amyloid beta peptides in human plasma and tissues and their significance for Alzheimer's disease. *Alzheimer's Dement.* **5**, 18–29 (2009).
48. Pacheco-Quinto, J. et al. Hyperhomocysteinemic Alzheimer's mouse model of amyloidosis shows increased brain amyloid β peptide levels. *Neurobiol. Dis.* **22**, 651–656 (2006).
49. Avella, M. A. et al. Lactobacillus rhamnosus accelerates zebrafish backbone calcification and gonadal differentiation through effects on the GnRH and IGF systems. *PLoS ONE* **7**, e45572 (2012).
50. Lau, B. Y., Mathur, P., Gould, G. G. & Guo, S. Identification of a brain center whose activity discriminates a choice behavior in zebrafish. *Proc. Natl Acad. Sci. USA* **108**, 2581–2586 (2011).
51. Howe, K. et al. The zebrafish reference genome sequence and its relationship to the human genome. *Nature* **496**, 498 (2013).
52. Mathuru, A. S. & Jesuthasan, S. The medial habenula as a regulator of anxiety in adult zebrafish. *Front. Neural Circuits* **7**, 99 (2013).
53. Tomasiewicz, H. G., Flaherty, D. B., Soria, J. & Wood, J. G. Transgenic zebrafish model of neurodegeneration. *J. Neurosci. Res.* **70**, 734–745 (2002).
54. Van Bebber, F., Paquet, D., Hruscha, A., Schmid, B. & Haass, C. Methylene blue fails to inhibit Tau and polyglutamine protein dependent toxicity in zebrafish. *Neurobiol. Dis.* **39**, 265–271 (2010).
55. Lin, S. et al. High content screening in zebrafish speeds up hazard ranking of transition metal oxide nanoparticles. *ACS Nano* **5**, 7284–7295 (2011).
56. Smith, P. E. et al. Measurement of protein using bicinchoninic acid. *Anal. Biochem.* **150**, 76–85 (1985).
57. Javed, I. et al. Lecithin-gold hybrid nanocarriers as efficient and pH selective vehicles for oral delivery of diacerein—in-vitro and in-vivo study. *Colloids Surf. B* **141**, 1–9 (2016).
58. Whitmore, L. & Wallace, B. A. Protein secondary structure analyses from circular dichroism spectroscopy: methods and reference databases. *Biopolymers: Original Research on. Biomolecules* **89**, 392–400 (2008).
59. Pan, Y., Chatterjee, D. & Gerlai, R. Strain dependent gene expression and neurochemical levels in the brain of zebrafish: focus on a few alcohol related targets. *Physiol. Behav.* **107**, 773–780 (2012).
60. Richetti, S. K. et al. Acetylcholinesterase activity and antioxidant capacity of zebrafish brain is altered by heavy metal exposure. *Neurotoxicology* **32**, 116–122 (2011).

Acknowledgements

This work was supported by ARC Project No. CE140100036 (Davis), the NSFC grant #21607115 and #21777116 (Lin), NSF CAREER CBET-1553945 (Ding), and NIH MIRA R35GM119691 (Ding). Javed acknowledges the support of Monash International Post-graduate Research Scholarship (MIPRS) and Australian Government Research Training Program Scholarship. TEM imaging was performed at Bio21 Advanced Microscopy Facility, University of Melbourne and polarized light microscopy was performed at Monash Micro Imaging, Monash University. Javed and Lin thank Shanghai Science and Technology Commission “Belt and Road” initiative program, Grant no. 17230743000. The authors acknowledge the support from Profs. Ting Xu and Daqiang Yin on the Zebrafish instrument.

Author contributions

P.C.K., I.J., S.L. and T.P.D. designed the project. I.J. and P.C.K. wrote the paper. I.J. performed AuNP synthesis, TEM, CD, UV-SPR, fluorescence characterizations, larval, and adult zebrafish behavioral and cognitive assays, histology, and polarized light microscopy. I.J., M.Z. and T.Y. performed in vivo microinjection. I.J. and G.P. performed ICP-MS analysis. Y.X. and F.D. conducted DMD simulations. A.F. performed cell viability assay and HIM imaging. C.L.P. and A.K. provided inputs to the discussion of the paper. All authors agreed on the presentation of the paper.

Additional information

Supplementary Information accompanies this paper at <https://doi.org/10.1038/s41467-019-11762-0>.

Competing interests: The authors declare no competing interests.

Reprints and permission information is available online at <http://npg.nature.com/reprintsandpermissions/>

Peer review information: *Nature Communications* would like to thank Morgan Newman, George Perry, and other, anonymous, reviewers for their contributions to the peer review of this work. Peer review reports are available.

Publisher's note: Springer Nature remains neutral with regard to jurisdictional claims in published maps and institutional affiliations.



Open Access This article is licensed under a Creative Commons Attribution 4.0 International License, which permits use, sharing, adaptation, distribution and reproduction in any medium or format, as long as you give appropriate credit to the original author(s) and the source, provide a link to the Creative Commons license, and indicate if changes were made. The images or other third party material in this article are included in the article's Creative Commons license, unless indicated otherwise in a credit line to the material. If material is not included in the article's Creative Commons license and your intended use is not permitted by statutory regulation or exceeds the permitted use, you will need to obtain permission directly from the copyright holder. To view a copy of this license, visit <http://creativecommons.org/licenses/by/4.0/>.

© The Author(s) 2019

Supplementary Information

Inhibition of Amyloid Beta Toxicity in Zebrafish with A Chaperone-Gold Nanoparticle Dual Strategy

Javed *et al.*

List of Content

Supplementary Methods

Supplementary Tables 1,2

Supplementary Figures 1-17

Supplementary References

Supplementary Methods

Discrete molecular dynamics (DMD) simulations

DMD is a type of molecular dynamics algorithms where conventional continuous interaction potentials are replaced by optimized step-wise potential functions.^{1,2} Comprehensive description of the DMD algorithm was published elsewhere.⁴⁹ In brief, the united-atom model was used to represent all molecules where all heavy atoms and polar hydrogen atoms were explicitly modeled. An implicit solvent model was adopted in the current simulations. The interatomic interactions included *van der Waals*, solvation, electrostatic interactions and hydrogen bond. The solvation energy was adopted by the Lazaridis-Karplus implicit solvent model, EEF1.³ The distance- and angular-dependent hydrogen bond interactions were modeled using a reaction-like algorithm.⁴ Screened electrostatic interactions were computed by the Debye-Hückel approximation. A Debye length of 1 nm was used by assuming a water dielectric constant of 80 and a monovalent electrolyte concentration of 0.1 M. The Anderson's thermostat was used to maintain constant temperature.⁵

During the synthesis of AuNP, β Cas served as the capping agent. The only one cysteine residue in β Cas was not expected to form disulfide bridge under the reducing condition during synthesis. Hence, without chemical modifications β Cas adopted its thermodynamically stable conformations on the AuNP surface and the structure of the β Cas corona remained independent of the synthesis process of AuNPs. Since our focus was to study the capping of β Cas AuNPs and the subsequent ability of β Cas corona to bind with A β , we therefore modelled only the binding of β Cas with a pre-formed AuNP.

We adopted the recently developed Au molecular mechanics force field⁶ to model a spherical AuNP with a diameter of 40 Å comprising 1,865 Au atoms. The AuNP force field included both physical and chemical absorption, aromatic and “image” charge interactions. The polarization was modelled by attaching a charged virtual particle ($-0.3e$) to each metal ($0.3e$)

atom with a fixed bond length (1.0 Å) as implemented in the GōLP force field.⁶ Only electrostatic interaction was taken into account for the virtual particle.

The structural coordinates for βCas were obtained from the protein homology prediction server (<https://zhanglab.ccmb.med.umich.edu/I-TASSER/>). The structural coordinates for Aβ oligomer were obtained from the protein data bank (PDB code: 2NAO), which was a β-sheet rich hexamer structure. Structural coordinates for proteins, basic and acidic amino acids were assigned charges corresponding to their titration states at physiological conditions, i.e. Arg and Lys residues were assigned +1, Asp and Glu were assigned -1, while His was neutral. Counter ions (Cl⁻) were added to maintain the net charge of the systems zero and accounted for possible counter-ion condensation.⁷ All simulations were conducted at 300 K. The periodic boundary condition was applied in all simulations. For each molecular system, 20 independent simulations were performed with different initial inter-molecular distances and orientations to avoid bias. For data analysis, an inter-atomic distance cutoff of 5.0 Å was used to define an atomic contact.

We used a hierarchical clustering program, oc (www.compbio.dundee.ac.uk/downloads/oc), to group similar protein binding poses with the AuNP. Based on an input pair-wise distance matrix that was the center-of-mass distances of the proteins on the AuNP surface in our study, a hierarchical clustering algorithm iteratively joined the two closest clusters into one cluster according to the distances between two clusters. The “cluster distance” was computed based on all pairwise distances between the elements of the two corresponding clusters, which can be the minimum, maximum, or mean of all these values. In this study, we used the mean to compute the distance between two clusters. The centroid structure of each cluster was selected as the one with the smallest average distance to other elements in the cluster.

Supplementary Tables

Supplementary Table 1. Zeta potential, hydrodynamic diameter and polydispersity index (PDI) of β Cas AuNPs and β Cas, before and after incubation with A β .

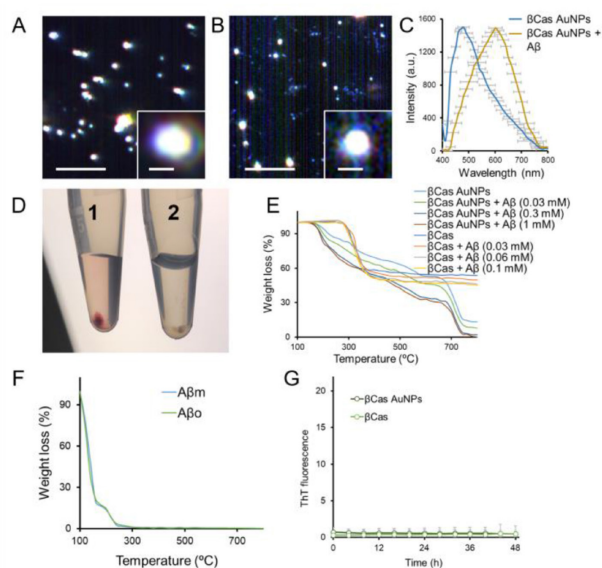
Sample	Zeta potential \pm SD (mV)	Hydrodynamic diameter \pm SD (nm)	PDI \pm SD
A β 0 h	-43.2 \pm 2.8	3.2 \pm 1.6	0.261 \pm 0.04
A β 48 h	-37.4 \pm 2.1	3565 \pm 846	0.634 \pm 0.13
β Cas AuNPs	-11.7 \pm 1.8	7.5 \pm 2.6	0.214 \pm 0.06
β Cas AuNPs+ A β	-33.7 \pm 2.1	39.3 \pm 5.4	0.345 \pm 0.08
β Cas	-19.9 \pm 2.7	156.3 \pm 34.4	0.324 \pm 0.07
β Cas + A β	-21.7 \pm 2.0	496.1 \pm 114	0.674 \pm 0.15

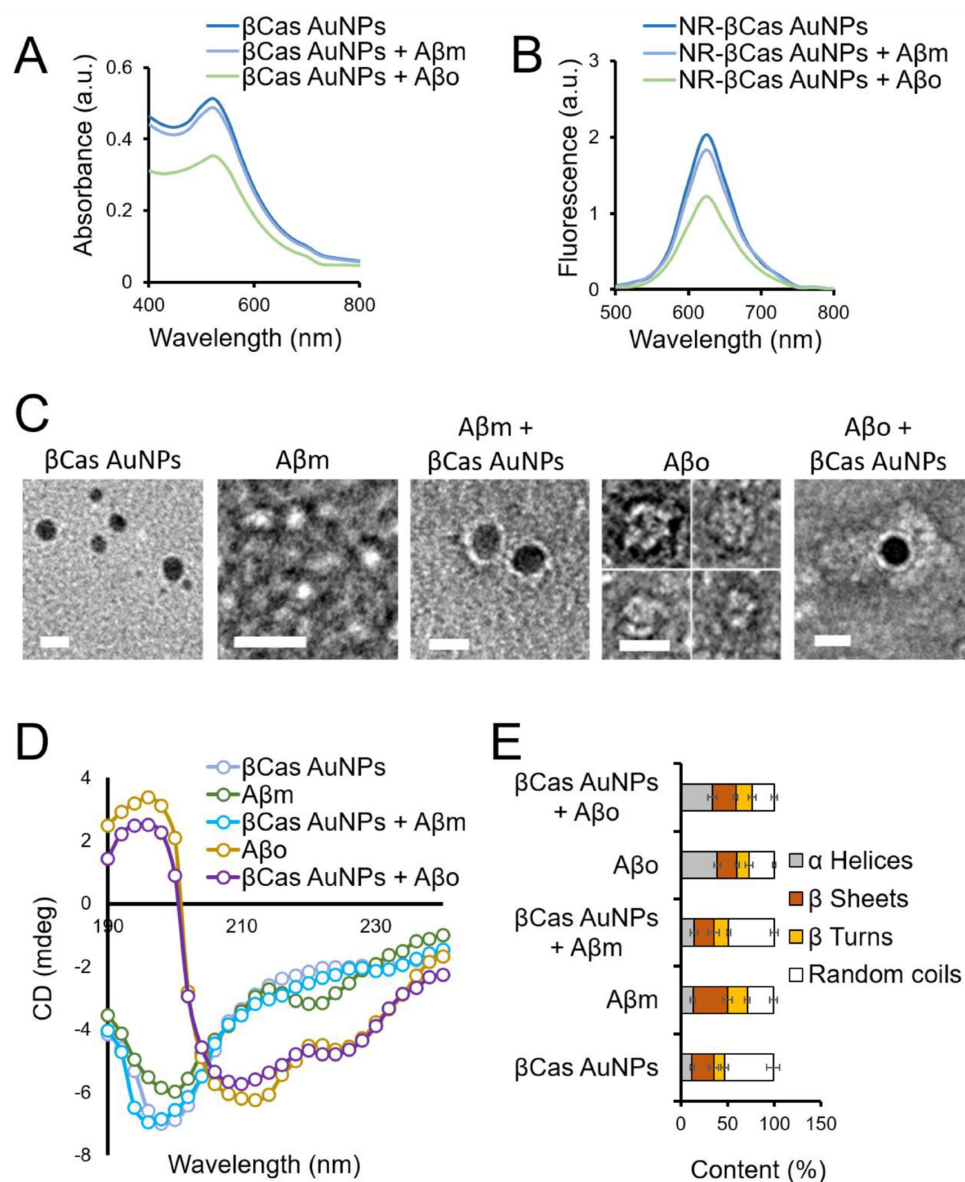
Supplementary Table 2. Estimation of protein-AuNP binding energies. The average potential energies of each molecular system were obtained from the corresponding equilibrated DMD simulations. The AuNP binding affinity difference between β Cas and A β was estimated based on the obtained average potential energies.

	$\langle E \rangle \pm$ SD (kcal \cdot mol $^{-1}$)
A β	-79.6 \pm 3.5
β Cas	-595.5 \pm 7.0
A β +AuNP	-97.3 \pm 4.0
β Cas+AuNP	-807.1 \pm 11.1

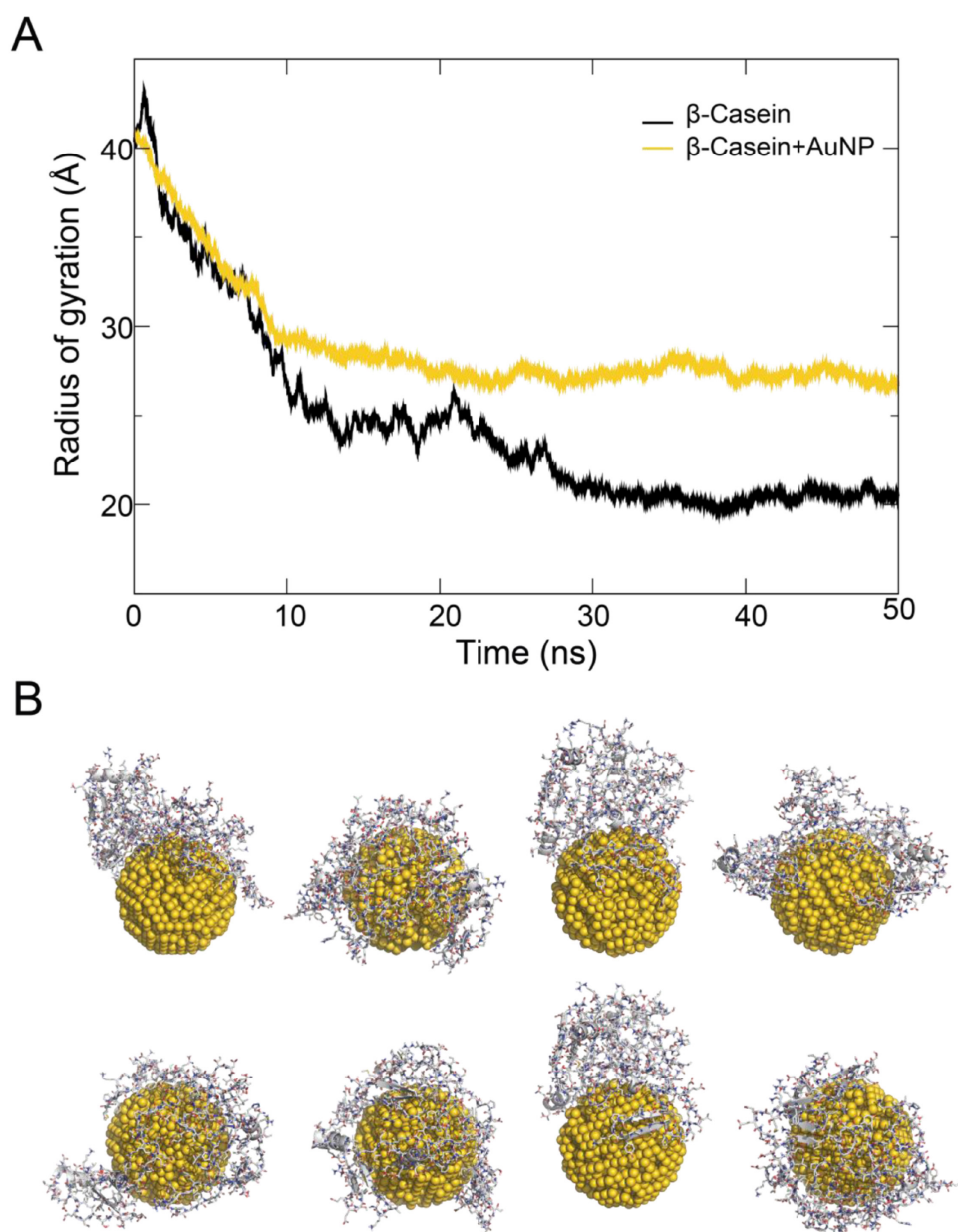
$$\Delta\Delta G \sim (\langle E_{\beta\text{Cas-AuNP}} \rangle - \langle E_{\text{A}\beta\text{-AuNP}} \rangle) - (\langle E_{\beta\text{Cas}} \rangle - \langle E_{\text{A}\beta} \rangle): -193.9 \text{ (kcal}\cdot\text{mol}^{-1}\text{)}$$

Supplementary Figures

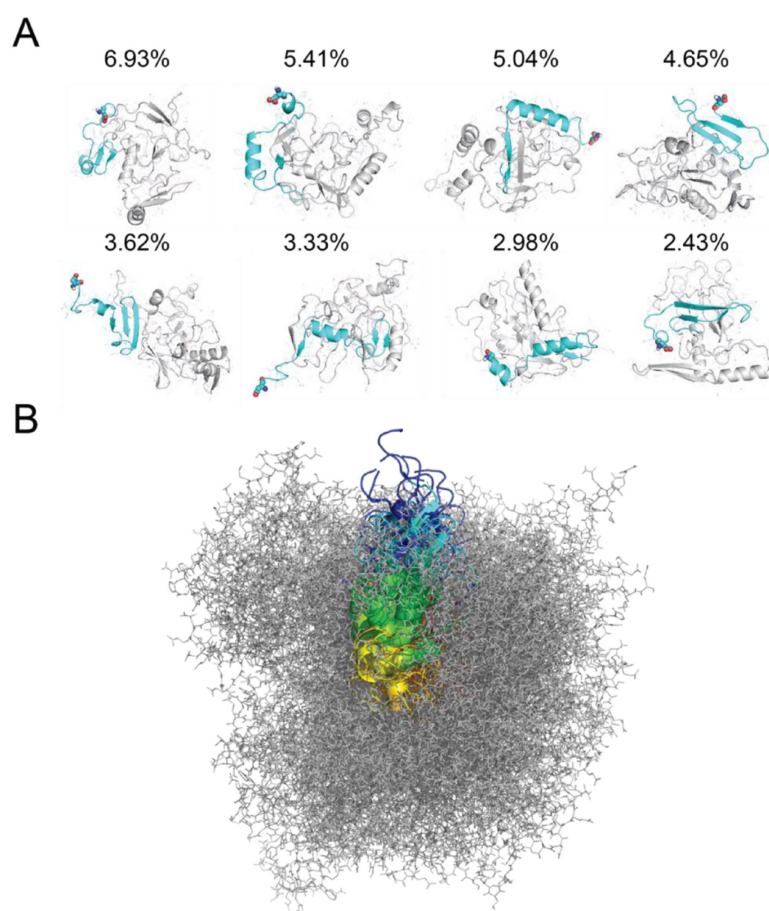




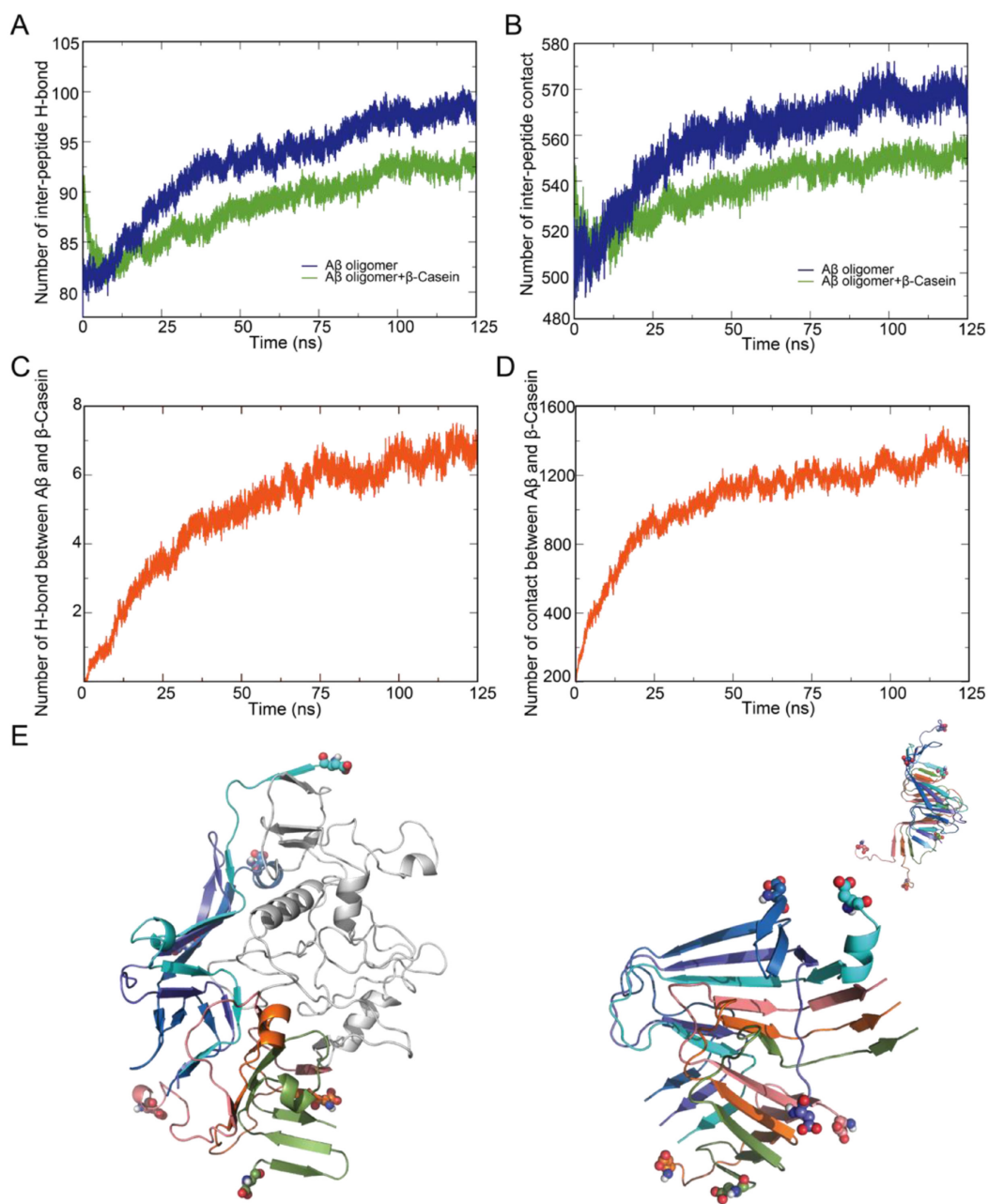
Supplementary Figure 2. Differential binding of β Cas AuNPs with A β m vs A β o. (A) The UV-SPR spectrum of β Cas AuNPs was suppressed significantly after binding with A β o as compared to A β m. (B) Similarly, the fluorescence spectrum of NR- β Cas AuNPs was significantly suppressed after binding with A β o. (C) TEM shows corona formation on β Cas AuNPs after incubation with A β o but not with A β m. (D) CD spectra and percentage secondary structure (E) of β Cas AuNPs before and after binding with A β m and A β o (n=3). β Cas AuNPs displayed a greater affinity for the A β o corona. Scale bars in TEM the images are 5 nm. Error bars represent the standard deviation. Source data are provided as a Source Data file.



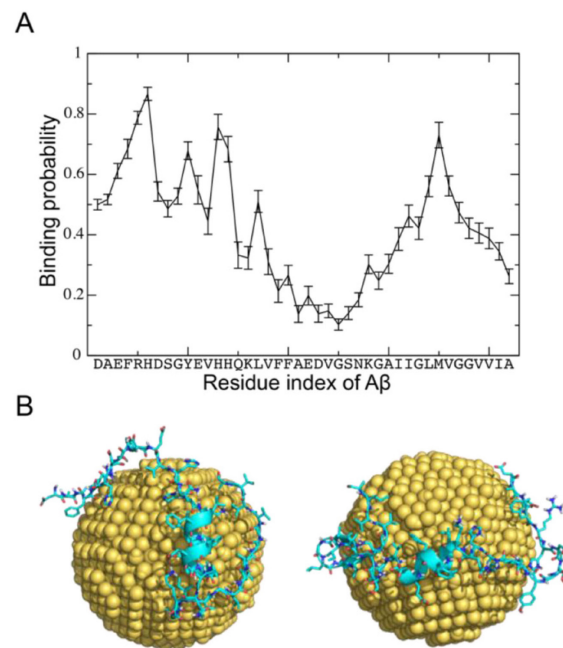
Supplementary Figure 3. DMD simulations of β Cas and AuNP. (A) Radius of gyration (R_g) of β Cas in the absence/presence of AuNP as a function of time. The thermo-fluctuations after 30 ns indicate the equilibrium of the simulation system and the larger R_g of β Cas in the presence of AuNP indicates extended conformation of β Cas. (B) Centroid structures of top 8 clusters of β Cas and AuNP complexes, obtained from multiple independent DMD simulations with clustering analysis.



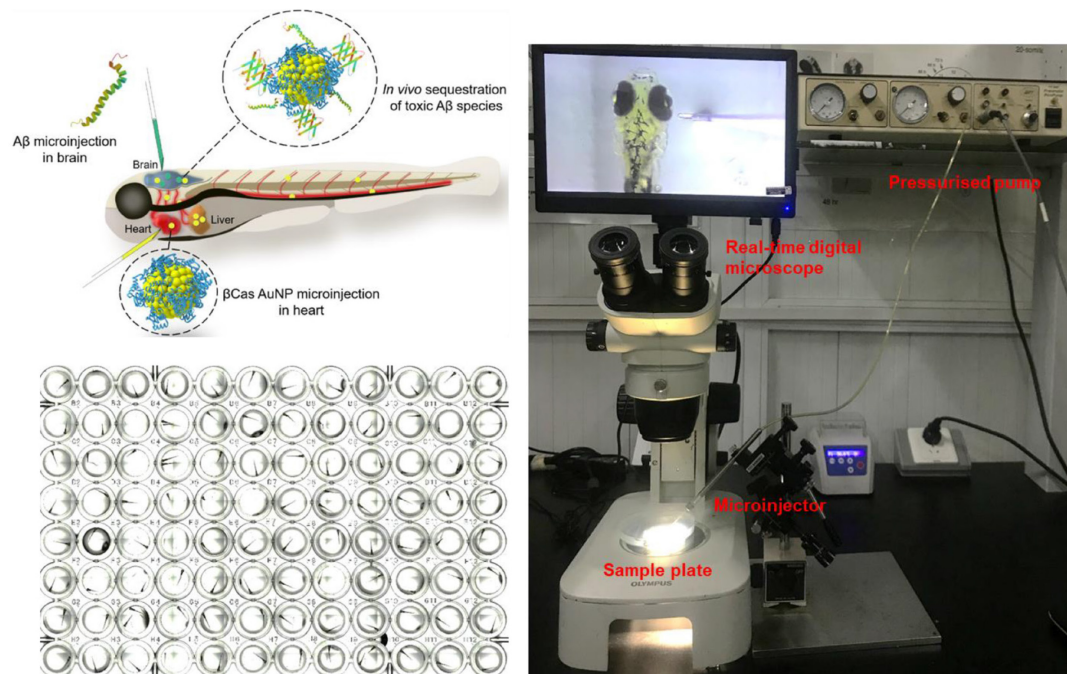
Supplementary Figure 4. DMD simulation of β Cas and A β monomer. (A) Centroid structures of top 8 clusters of β Cas and A β complexes. (B) Representative binding structures of A β (cartoon in rainbow color) and β Cas (sticks in gray) aligned according to A β . The complex structures were obtained from independent binding simulations of A β and β Cas monomers, and the centroid structures of top 50 clusters were used in the alignment.



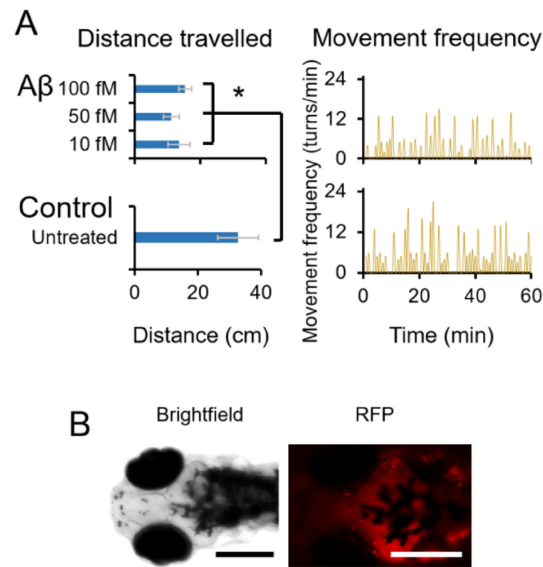
Supplementary Figure 5. DMD simulation of β Cas and A β oligomer. Number of A β inter-peptide H-bonding (A) and contact (B) ranging from residues 10 to 42 in the presence/absence of β Cas as a function of time. Number of H-bond (C) and contact (D) between A β oligomer and β Cas as a function of time. (E) Representative snapshots of A β oligomer in the presence (left) and absence (right) of β Cas (gray) after 125 ns of DMD simulations.



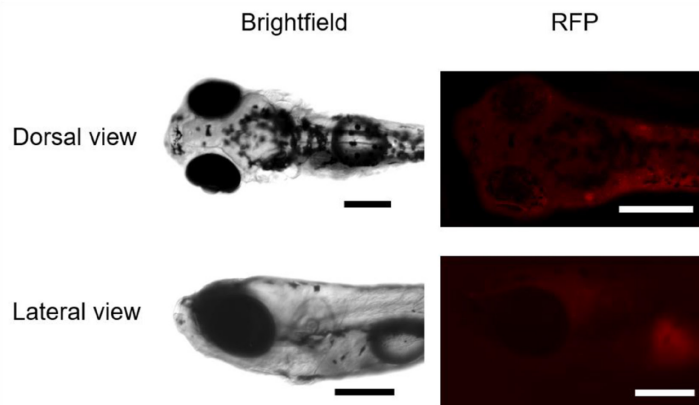
Supplementary Figure 6. binding of Aβ with a bare AuNP. (A) Binding probability of each Aβ residue with the AuNP. (B) Typical snapshots of Aβ binding with the AuNP.



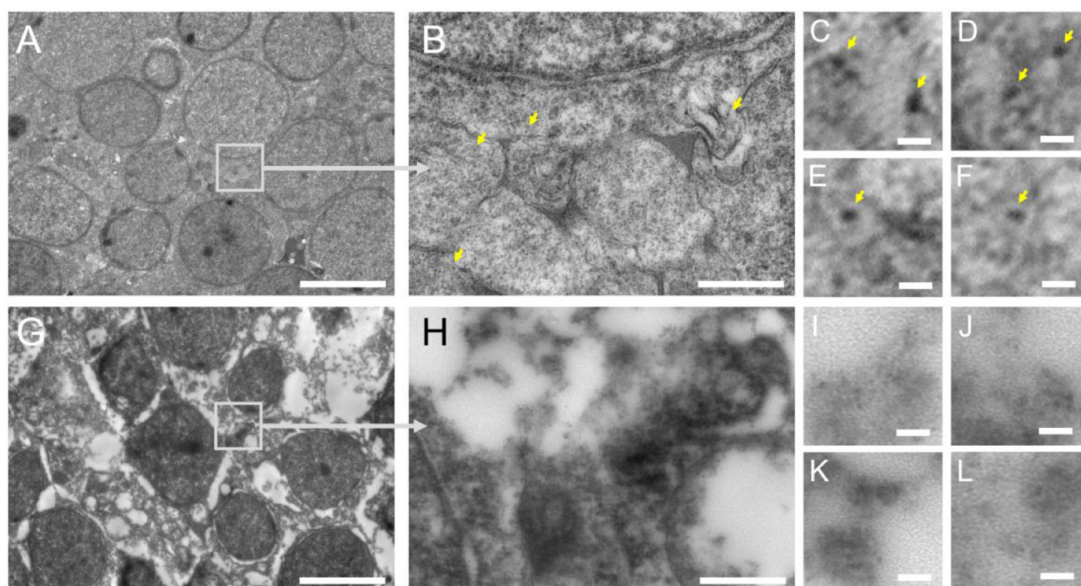
Supplementary Figure 7. High-throughput setup for Aβ microinjection with zebrafish larvae.



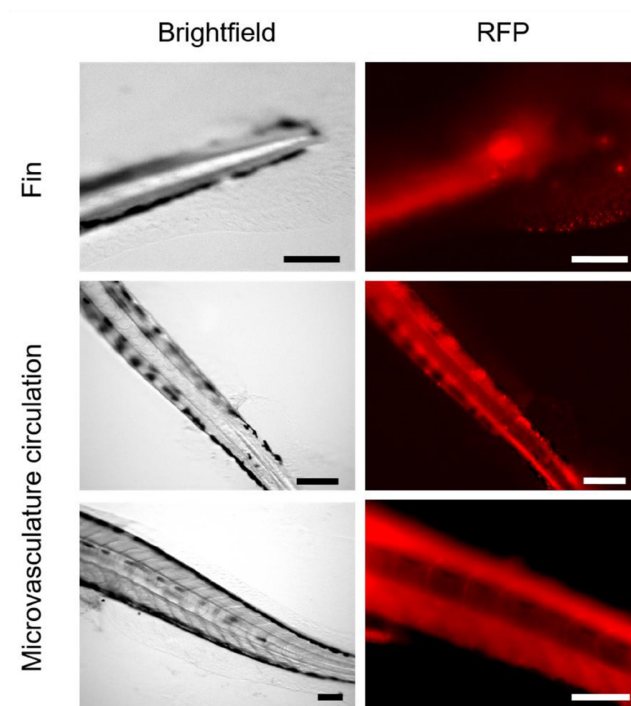
Supplementary Figure 8. Behavioral changes in zebrafish larvae on the 3rd day post A β treatment. (A) Zebrafish larvae swimming behavior was suppressed significantly ($p < 0.05$) on the 3rd day post A β treatment. Swimming distance was reduced to 13.5 ± 3.3 , 11.1 ± 2.4 and 15.4 ± 1.9 cm with 10, 50 and 100 fM A β as compared to 35.3 ± 4.3 cm of untreated control ($n=3$). (B) A β treated larvae were injected with Congo red dye on the 3rd day post A β treatment and slight retention of the dye was observed in the brain. Scale bars in the images are 300 μ m. Error bars represent the standard deviation. Source data are provided as a Source Data file.



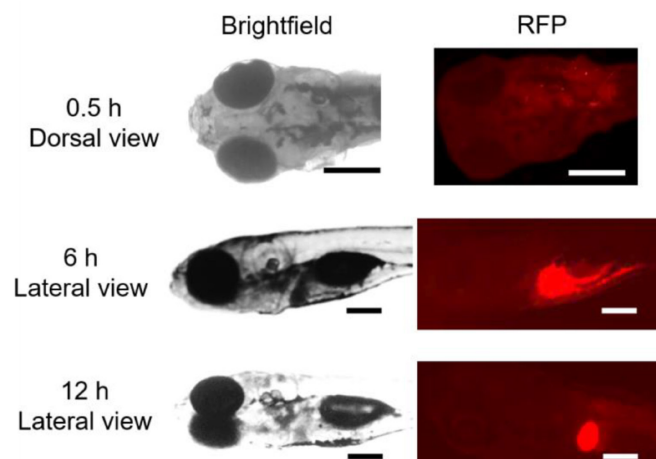
Supplementary Figure 9. Dorsal and lateral view of untreated zebrafish larvae under brightfield and RF channel of microscope. It indicates no background fluorescence in the larvae to interfere with the other fluorescence measurements. Scale bars in all images are 200 μ m.



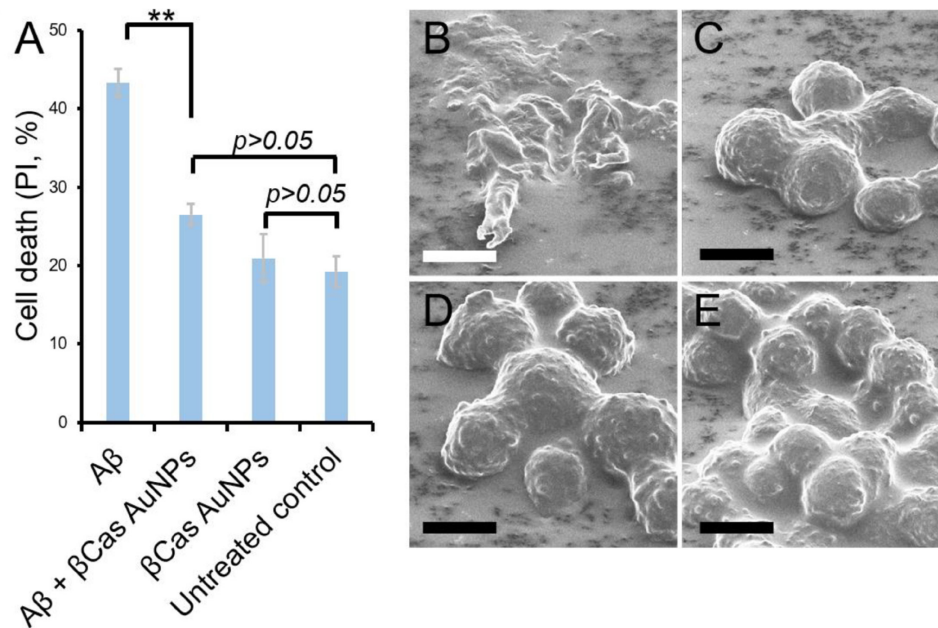
Supplementary Figure 10. TEM imaging of the brain tissues of zebrafish larvae containing β Cas AuNPs. Zebrafish larvae treated with intracardiac injection of 3 ng Au equivalent β Cas AuNPs were subjected to TEM analysis of the brain tissues for detection of AuNPs translocated across BBB. (A, B) TEM images of the brain tissues of β Cas AuNPs treated larvae. Presence of AuNPs in the interstitial spaces are highlighted and presented as zoomed images (C-F). (G, H) However, untreated control larvae did not show any presence of AuNPs in the tissue sections (I-L). Scale bars in A,G: 5 μ m; B,H: 500 nm and C-F,I-L: 10 nm.



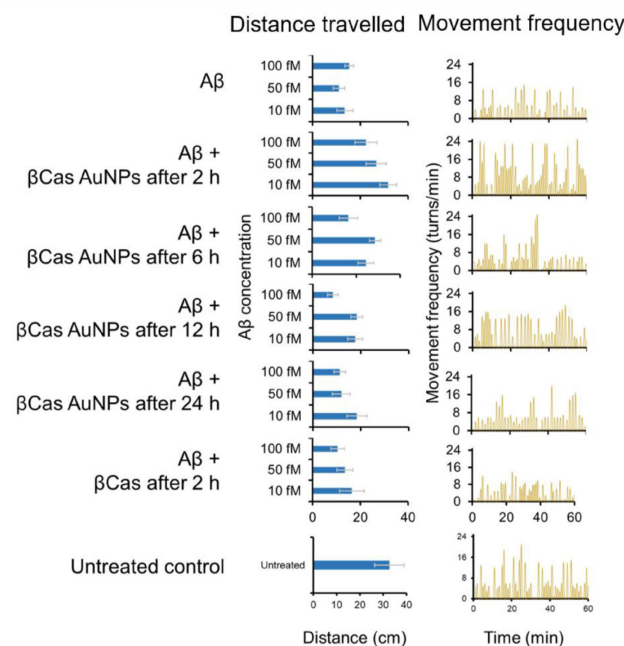
Supplementary Figure 11. Biodistribution of β Cas AuNPs. β Cas AuNPs were conjugated with neutral red and imaged for their biodistribution in zebrafish larvae. Red fluorescence of β Cas AuNPs was traced in microvasculature circulation and fins of the larvae. Scale bars in the images are 200 μ m.



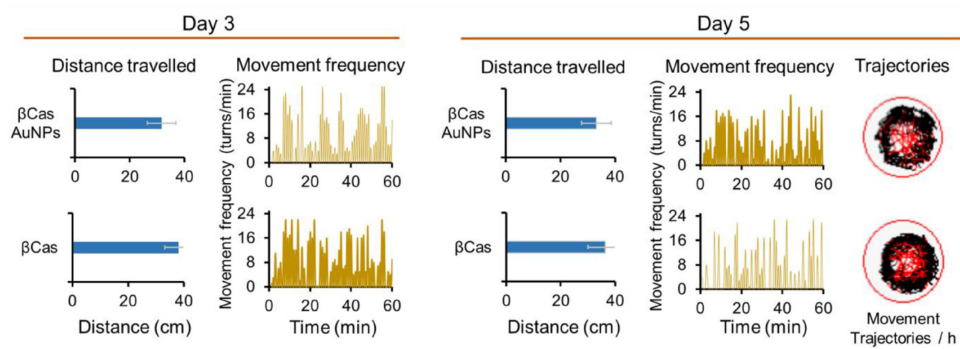
Supplementary Figure 12. Biodistribution of β Cas micelles in zebrafish larvae. β Cas micelles were conjugated with neutral red and imaged for their biodistribution in zebrafish larvae. No fluorescence was observed from the larval cerebral region in 0.5 h or later, indicating inability of large β Cas micelles (~ 100 nm) to translocate across the BBB. Red fluorescence was observed from the hepatic region of the larvae at 6 and 12 h, indicating slow elimination of β Cas micelles directly from the liver. Scale bars in images are 200 μ m.



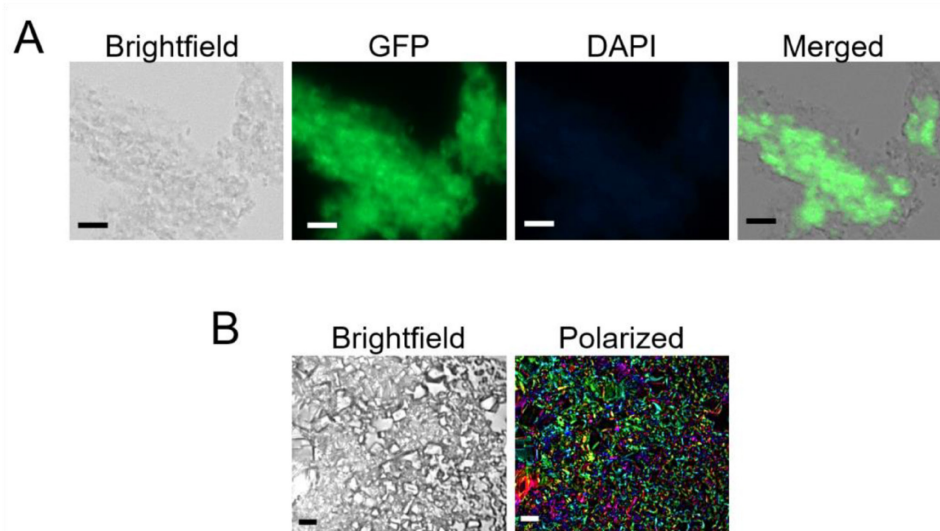
Supplementary Figure 13. Mitigation of Aβ-induced SH-SY5Y cytotoxicity with βCas AuNPs. (A) Cell viability assay (n=3) and helium ion microscopy (HIM) images of (B) Aβ treated (20 μM), (C) Aβ (20 μM) with βCas AuNPs (50 μM), (D) βCas AuNPs alone (50 μM) and (E) untreated control cells. Scale bars in TEM images are 4 μm. Error bars represent the standard deviation. Source data are provided as a Source Data file.



Supplementary Figure 14. Mitigation of Aβ induced behavioral abnormalities in zebrafish larvae by βCas AuNPs, on the 3rd day post Aβ treatment (n=10). Error bars represent the standard deviation. Source data are provided as a Source Data file.

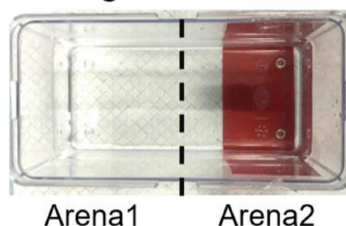


Supplementary Figure 15. β Cas AuNPs and β Cas did not influence the behavior of zebrafish larvae ($n=10$). Error bars represent the standard deviation. Source data are provided as a Source Data file.



Supplementary Figure 16. Immunohistochemistry IHC (A) and polarized light microscopy (B) of fibrillized A β deposited on glass slides, performed as positive controls for IHC and polarized light microscopy. Scale bars in all images are 50 μ m.

Fish tank for cognitive behavior analysis



Supplementary Figure 17. Fish tank (1L) used for cognitive behavior analysis of adult zebrafish. The tanks were hypothetically divided into two arenas. Whenever, fish swims into arena 2, electrodes of 9V battery were dipped in the arena 2 to shock the fish and train it to remain in arena 1. Arena 2 was labelled with red color to associate with the punishment. 20 min training was performed, followed by 2 min of observation period when the electric source was removed. Observations were performed 3 times for each fish, 2 h apart (n=3).

Supplementary References

- 1 Allen, M. P. & Tildesley, D. J. *Computer simulation of liquids*. (Oxford university press, 2017).
- 2 Rapaport, D. C. & Rapaport, D. C. R. *The art of molecular dynamics simulation*. (Cambridge university press, 2004).
- 3 Lazaridis, T. & Karplus, M. Effective energy functions for protein structure prediction. *Curr. Opin. Struc. Biol.* **10**, 139-145 (2000).
- 4 Ding, F., Borreguero, J. M., Buldyrey, S. V., Stanley, H. E. & Dokholyan, N. V. Mechanism for the α -helix to β -hairpin transition. *Proteins: Struct. Funct. Bioinf.* **53**, 220-228 (2003).
- 5 Andersen, H. C. Molecular dynamics simulations at constant pressure and/or temperature. *J. Chem. Phys.* **72**, 2384-2393 (1980).
- 6 Hughes, Z. E., Wright, L. B. & Walsh, T. R. Biomolecular adsorption at aqueous silver interfaces: first-principles calculations, polarizable force-field simulations, and comparisons with gold. *Langmuir* **29**, 13217-13229 (2013).
- 7 Manning, G. S. Limiting laws and counterion condensation in polyelectrolyte solutions I. Colligative properties. *J. Chem. Phys.* **51**, 924-933 (1969).

Chapter 5

Summary and future directions

5.1. Summary

My PhD research has accomplished the objectives as described in chapters 2, 3 and 4. It has provided a foundation for future research in the design and application of biomimetic nanomaterials against amyloid diseases. As described in the “cross-talk between amyloid proteins” section of the introduction, amyloid proteins can cross-interact and promote or inhibit their mutual fibrillization. Whey proteins, when extracted from milk and heated at low pH, can fibrillate into amyloid fibers with atomic and mesoscopic structures resembling pathogenic amyloids. First, in chapter 2, I prepared bLg AuNPs of ~8 nm size that was comparable to the thickness of an IAPP amyloid fibril, i.e., ~10 nm. bLg AuNPs were decorated with small fragments of bLg amyloids, thus provided a β -sheet rich interface. Upon introducing IAPP, I demonstrated for the first time a facile scheme of cross-talk or co-fibrillization between functional and pathogenic amyloids. The β -sheet rich corona on the surface of bLg AuNPs was able to intercalate AuNPs inside IAPP amyloids, as corroborated by CD spectroscopy and TEM/AFM imaging. Embedding bLg AuNPs in IAPP amyloids mitigated the IAPP toxicity against pancreatic β -cells and enabled darkfield (hyperspectral or HSI) imaging of bLg AuNPs-IAPP amyloid hybrids, even when the hybrids were covered with human plasma proteins. IAPP amyloids were not immunogenic, however, bLg AuNPs-IAPP amyloid hybrids were recognized and phagocytosed when exposed to human T-cells. AuNPs absorbed X-ray irradiation and dissipated the absorbed energy to their surroundings in the form of heat. When bLg AuNPs-IAPP amyloid hybrids were exposed to X-rays (exposure: 100 s; dose: 300 μ Sv/h), the embedded AuNPs were able to destroy IAPP amyloids and converted them from β -sheets rich fibrils to random coiled aggregates.

In chapter 3, I stabilised the bLg amyloid fragments on the surface of multiwalled CNTs (b_a CNTs). The hydrophobic surface of CNTs, coated with the β -sheets rich corona of bLg amyloid fragments, acted as a substrate and sequestered the toxic IAPP species *in vitro* and *in*

vivo. b_aCNTs inhibited the IAPP fibrillization and sequestered the peptide in the form of α -helical aggregates. *In vivo* translation of this inhibitory interaction was performed in zebrafish embryos. Zebrafish embryos, injected with b_aCNTs, showed no toxicity of the biomimetic NPs. When injected with IAPP or A β , the toxicity of these amyloid peptides was evident in terms of hampered hatching or abnormal development of zebrafish embryos. Upon co-injection of b_aCNTs and IAPP or A β , the amyloid toxicity was mitigated and zebrafish embryos were able to develop and hatch normally. This study established zebrafish embryos as an *in vivo* model for rapid screening the inhibitory potential of nanomaterials against amyloidosis. Furthermore, it was evident from a comparison of bLg AuNPs from chapter 1 (~8 nm diameters) and b_aCNTs from chapter 2 (~50 × 500 nm, width × length) that the same corona, i.e. β -sheet rich amyloid fragments, on the surface of nanomaterials with different shapes and aspect ratios could render different effects on amyloid fibrillization and toxicity.

Finally, in chapter 4, I used β -casein (β Cas) to synthesise AuNPs of 5 nm in diameter (β Cas AuNPs). Due to the malleable and flexible conformation and intermittent hydrophobic regions in the structure of β Cas, it acted as a chaperone and bound with a variety of unfolded monomeric and oligomeric proteins/peptides. This chaperone-like activity of β Cas was cloaked onto the surface of AuNPs and then exposed to A β . A β fibrillization was completely inhibited and β Cas AuNPs sequestered A β monomers and oligomers onto their surface with high affinity. For the *in vivo* translation of this inhibitory interaction, zebrafish larvae were developed as a transparent and high throughput animal model. Zebrafish larvae displayed Alzheimer's-like symptoms, i.e., distorted swimming behaviour and reduced swimming distance, one week after receiving a cerebroventricular injection of A β . The biodistribution of β Cas AuNPs revealed the transportation of NPs to the brain within 0.5 h of intracardiac injection. β Cas NPs were subsequently eliminated from the brain and liver, 12 h post-injection. When β Cas AuNPs and A β were co-introduced to the zebrafish larvae via intracardiac and cerebroventricular injections, respectively, β Cas AuNPs rescued the larvae from A β toxicity and prevented it from developing

behavioral pathology. The chaperone-like potential of β Cas AuNPs against A β was further implicated in adult zebrafish by examining the animals' memory function. The cognitive memory of zebrafish was deteriorated upon A β treatment and was largely rescued when co-injected with β Cas AuNPs. This final chapter in my PhD thesis revealed the *in vivo* potential of biomimetic nano-chaperone β Cas AuNPs and supported the use of zebrafish as a new lab rat to study amyloid diseases.

A key knowledge gained from this thesis is the corona-mediated amyloidosis inhibition or co-fibrillization with nanomaterials. Such interactions depended primarily upon the secondary structure of the functional surface corona as well as aspect ratio of the underlying nanoparticle core. bLg amyloid-fragments co-fibrillated with IAPP when decorated on small AuNPs, but sequestered IAPP and prevented their amyloidosis and toxicity when displayed on CNTs. Furthermore, when the corona was changed from bLg to β Cas, which possessed a molten and random conformation in its monomeric form, a chaperone-like activity was observed for β Cas AuNPs against A β . This implies that biomimetic ligands can be tailored to render their nanoparticle cores potent anti-amyloidosis nanomedicines. Another intellectual contribution from this thesis is the establishment of zebrafish models for amyloid research. Zebrafish at different stages of development can be utilized to examine the various aspects of amyloid diseases - zebrafish embryos can be used for studying nano-bio interactions between amyloid proteins and nanoparticles, larvae for disease modelling and imaging, while adult zebrafish for examining the neurochemical and behavioural pathologies of neuronal disorders.

5.2. Future directions

Based on the observations made during the research of this PhD project, these established biomimetic nanomaterials hold a great potential against protein misfolding diseases. The corona-driven interactions between the NPs and amyloid fibers may be controlled via the surface properties of the NPs. Once interfaced with amyloid species, such NPs-amyloid hybrids

may be exploited for photothermal destruction, dark-field imaging and physiological clearance of amyloid plaques. This biomimetic approach may also be used to target nanomedicines to the site of amyloid deposition. Biomimetic nanomaterials, crafted from functional amyloids like bLg and casein, may be used to understand and exploit the functional-pathological protein cross-talk. This proposition is based on the facts that cross-talk across the pathogenic amyloid proteins is driven by β -sheet stacking and functional amyloids possess similar cross- β spine but are non-toxic.

There has been recent clinical evidence that co-relate incidence of AD and PD with patient's history for bacterial infections and oral microbiota profiles. Therefore, future research beyond the context of this thesis may examine promising anti-amyloid nanomedicines and unravel the etiological factors of AD and PD, based on functional-pathological cross-talks between A β / α S and FapC/CsgA amyloids from bacterial biofilms.

Furthermore, there is a need to fill the gap between *in vitro* and *in vivo* experimental conditions in the fields of nanomedicine and amyloid research. Anti-amyloid therapies that showed promising results *in vitro* failed to show similar potential *in vivo* and therapeutic strategies that succeeded *in vivo*, failed in the 2nd or 3rd stage of human clinical trials. This implies a gap between *in vitro* studies and *in vivo* translation of nanomedicines. The disease pathology in human is far more complex and involves multiple pathophysiological pathways for the onset and progression of the disease, particularly amyloid diseases such as T2D, AD and PD that are associated with age and take decades to present their clinical symptoms. There is a urgent need for developing animal models that can provide faster disease modelling with simultaneous involvement of multiple pathogenic pathways. Zebrafish as a transparent animal model can be developed to induce disease pathologies with a short period of time, as demonstrated in the 3rd chapter of this thesis. For example, adult zebrafish took 2 weeks to develop Alzheimer's-like symptoms as compared to 0.5-2 years in rat models. Zebrafish embryos can provide a high

throughput quasi *in vivo* model system, acting as a link between *in vitro* cell cultures and *in vivo* disease conditions. The complex perivitelline space between the chorionic membranes and embryonic cells is abundant with ions, proteins and cytokines that are dynamically controlled by the underlying developing embryonic cells. The zebrafish larvae can provide a transparent and imaging friendly animal model. Future research directions can further exploit zebrafish to develop neurodegenerative or metabolic disorders with simultaneous involvement of multiple pathophysiological pathways.